Advanced 3-D Ultrasound Imaging.

3-D Synthetic Aperture Imaging and Row-column Addressing of 2-D Transducer Arrays

Rasmussen, Morten Fischer; Jensen, Jørgen Arendt

Publication date:
2014

Document Version
Publisher's PDF, also known as Version of record

Ph.D. Thesis

Advanced 3-D Ultrasound Imaging

3-D Synthetic Aperture Imaging and Row-column Addressing of 2-D Transducer Arrays

Morten Fischer Rasmussen

Supervised by: Prof. Jørgen Arendt Jensen, PhD, Dr. Techn.

Technical University of Denmark
Kgs. Lyngby, Denmark 2014

Technical University of Denmark
Department of Electrical Engineering
Center for Fast Ultrasound Imaging (CFU)
Ørsteds Plads 349
2800 Kgs. Lyngby
DENMARK
Tel: (+45) 4525 3031
Fax: (+45) 4588 1295
Web: www.cfu.elektro.dtu.dk
E-mail: info@elektro.dtu.dk

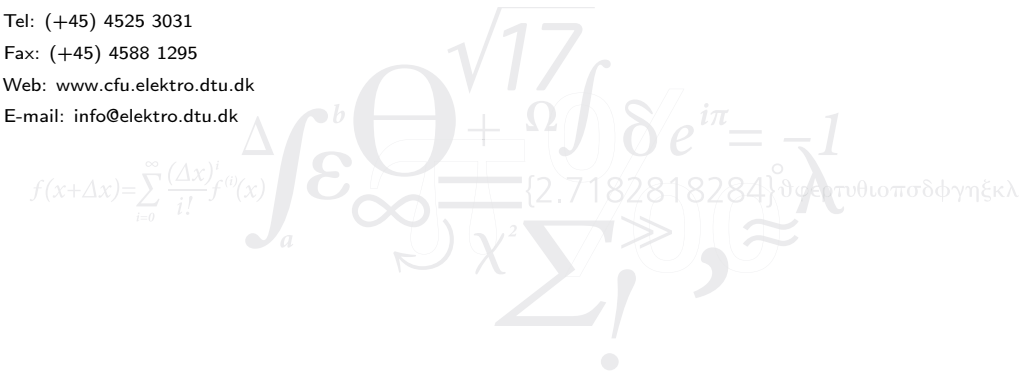

Contents

Summary vii

Resumé ix

Preface xi

Acknowledgements xiii

List of Figures xv

List of Tables xix

Abbreviations xxi

1 Introduction 1
- 1.1 Publications in the thesis . . . 2
- 1.2 Publications not included in the thesis . . . 4
- 1.3 Other Contributions . . . 6
- 1.4 Outline . . . 6

2 3-D Synthetic Aperture Imaging 7
- 2.1 Introduction . . . 7
- 2.2 The Fair Comparison . . . 10
- 2.3 Image Quality Metrics . . . 11
- 2.4 The Reference: Parallel Beamforming . . . 13
- 2.5 Synthetic Aperture Imaging . . . 16
- 2.6 Results . . . 21
- 2.7 Summary of Papers . . . 25
- 2.8 Discussion and Conclusions . . . 27
- References . . . 27

3 Row-Column Addressed Arrays 31

3.1 Literature Survey . . . 34
3.2 Edge Effects . . . 35
3.3 Implementation of Integrated-Apodization . . . 38
3.4 A New Apodization Layout . . . 44
3.5 Beamforming with line elements . . . 47
3.6 Imaging Results . . . 49
3.7 Summary of Papers on Row-column Addressing of 2-D Arrays . . . 50
3.8 Conclusion . . . 53
References . . . 54

4 Conclusion and Perspectives 57

Papers 59

Paper A Preliminary Comparison of 3D Synthetic Aperture Imaging with Explososcan 61
A.1 Introduction . . . 62
A.2 Performance Metrics . . . 63
A.3 Methods . . . 64
A.4 Simulation setup . . . 67
A.5 Results . . . 68
A.6 Discussion and conclusion . . . 70
References . . . 71

Paper B Comparison of 3D Synthetic Aperture Imaging and Explososcan using Phantom Measurements 73
B.1 Introduction . . . 74
B.2 Methods . . . 74
B.3 Measurement setup . . . 77
B.4 Results . . . 79
B.5 Discussion and conclusion . . . 79
References . . . 81

Paper C Comparison of 3-D Synthetic Aperture Phased Array Ultrasound Imaging and Parallel Beamforming 83
C.1 Introduction . . . 84
C.2 Methods . . . 86
C.3 Simulations . . . 95
C.4 Measurements . . . 99
C.5 Discussion and Conclusions . . . 105
References . . . 106

Paper D 3D Ultrasound Imaging Performance of a Row-column Addressed 2D Array Transducer: A Simulation Study 111
D.1 Introduction . . . 112
D.2 Methods/Theory . . . 113
D.3 Simulation setup . . . 118
D.4 Results . . . 119
D.5 Conclusion and perspectives . . . 120
References . . . 123

Paper E 3-D Ultrasound Imaging Performance of a Row-Column Addressed 2-D Array Transducer: A Measurement Study 125
E.1 Introduction . . . 126
E.2 Methods . . . 126
E.3 Experimental Setup . . . 131
E.4 Results . . . 132
E.5 Conclusion . . . 133
References . . . 133

Paper F Row-Column Addressed 2-D CMUT Arrays with Integrated Apodization 135
F.1 Introduction . . . 135
F.2 Transducer Design . . . 136
F.3 Transducer Fabrication . . . 138
F.4 Measurement and Simulation Setup . . . 139
F.5 Results . . . 140
F.6 Conclusions . . . 141
References . . . 143

Paper G 3-D Imaging with Row-Column Addressed Arrays: Transducer-Integrated Apodization and Line-element Beamforming 145
G.1 Introduction . . . 146
G.2 Edge effects . . . 148
G.3 Simulation and Measurement Setup . . . 153
G.4 Transducer-Integrated Apodization . . . 154
G.5 Beamforming with Line Sources . . . 160
G.6 Image Quality . . . 164
G.7 Discussion and Conclusion . . . 168
References . . . 169

Paper H 3-D Imaging using Row-Column Addressed Arrays with Integrated Apodization: Transducer Fabrication and Experimental Results 173

H.1 Introduction . . . 174
H.2 Array Design, Fabrication, and Interconnect Electronics . . . 175
H.3 Transducer Characterization . . . 182
H.4 Imaging . . . 189
H.5 Conclusions . . . 193
References . . . 194

Patent 199

Patent A Ultrsound Imaging Transducer Array with Integrated Apodization 201
A.1 Technical Field . . . 201
A.2 Background . . . 201
A.3 Summay . . . 203
A.4 Brief Description of the Drawings . . . 203
A.5 Detailed Description . . . 204
A.6 Claims . . . 215
A.7 Abstract . . . 218
A.8 Drawings . . . 220

Combined Bibliography 233
References from Chapter 2 . . . 233
References from Chapter 3 . . . 235
References from Paper A . . . 237
References from Paper B . . . 238
References from Paper C . . . 239
References from Paper D . . . 242
References from Paper E . . . 244
References from Paper F . . . 245
References from Paper G . . . 246
References from Paper H . . . 249

Summary

The main purpose of the PhD project was to develop methods that increase the 3-D ultrasound imaging quality available for the medical personnel in the clinic. Acquiring a 3-D volume gives the medical doctor the freedom to investigate the measured anatomy in any slice desirable after the scan has been completed. This allows for precise measurements of organs dimensions and makes the scan more operator independent.

Real-time 3-D ultrasound imaging is still not as widespread in use in the clinics as 2-D imaging. A limiting factor has traditionally been the low image quality achievable using a channel limited 2-D transducer array and the conventional 3-D beamforming technique, Parallel Beamforming.

The first part of the scientific contributions demonstrate that 3-D synthetic aperture imaging achieves a better image quality than the Parallel Beamforming technique. Data were obtained using both Field II simulations and measurements with the ultrasound research scanner SARUS and a 3.5 MHz 1024 element 2-D transducer array. In all investigations, 3-D synthetic aperture imaging achieved a smaller main-lobe, lower side-lobes, higher contrast, and better signal to noise ratio than parallel beamforming. This is achieved partly because synthetic aperture imaging removes the limitation of a fixed transmit focal depth and instead enables dynamic transmit focusing.

Lately, the major ultrasound companies have produced ultrasound scanners using 2-D transducer arrays with enough transducer elements to produce high quality 3-D images. Because of the large matrix transducers with integrated custom electronics, these systems are extremely expensive. The relatively low price of ultrasound scanners is one of the factors for the widespread use of ultrasound imaging. The high price tag on the high quality 3-D scanners is limiting their market share.

Row-column addressing of 2-D transducer arrays is a low cost alternative to fully addressed 2-D arrays, for 3-D ultrasound imaging. Using row-column addressing, the number of transducer elements is dramatically reduced. This reduces the interconnection cost and removes the need to integrate custom made electronics into the probe. A downside of row-column addressing 2-D arrays is the creation of secondary temporal lobes, or ghost echoes, in the point spread function.

In the second part of the scientific contributions, row-column addressing of 2-D arrays was investigated. An analysis of how the ghost echoes can be attenuated was presented.

Attenuating the ghost echoes were shown to be achieved by minimizing the first derivative of the apodization function. In the literature, a circular symmetric apodization function was proposed. A new apodization layout that addresses the drawbacks of the circular symmetric apodization function was proposed and described. The new layout was shown to be effective in both simulations and with measurements on in-house produced CMUT arrays. The measurements included both intensity measurements of the edge waves and imaging of a wire phantom. New methods of integrating arbitrary apodization functions into the transducer array were proposed.

The main part of the thesis consists of eight scientific papers submitted for international conferences and journals during the PhD project.

Resumé

(Summary in Danish)

Hovedformålet med dette ph.d.-projekt var at udvikle metoder der øger billedkvaliteten af 3-D ultralyd til rådighed for personalet i klinikkerne. Skanning af et 3-D volumen giver lægen frihed til at undersøge den målte anatomi i ethvert ønskeligt snit, efter skanningen er afsluttet. Dette giver mulighed for præcise målinger af organernes størrelse, og gør skanningen mere operatør uafhængig.

Sandtids 3-D ultralydsskanning er stadig ikke lige så udbredt i brug i klinikkerne som 2-D skanninger er. En begrænsende faktor har traditionelt været en lav billedkvalitet, som opstår p.g.a. brug af et kanalbegrænset 2-D transducerarray og brug af den konventionelle 3-D fokuseringsteknik, Parallel Fokusering.

I den første del af de videnskabelige bidrag i denne afhandling blev det vist, at 3-D syntetisk blænde billeddannelse opnår en bedre billedkvalitet end Parallel Fokusering. Undersøgelsen blev lavet ved hjælp af både Field II simuleringer og målinger med en eksperimentel ultralydskanner, SARUS, og et 3,5 MHz 1024 element 2-D transducerarray. I alle undersøgelser opnåede 3-D syntetisk blænde billeddannelse en mindre hoved-sløjfe, lavere side-sløjfe, højere kontrast og bedre signal støjforhold end Parallel Fokusering gjorde. Dette blev opnået, til dels fordi syntetisk blænde billeddannelse fjerner begrænsningen af en fast sende fokus dybde og i stedet gør det muligt dynamisk at fokusere sendeskuddet.

På det seneste har de store ultralydsselskaber produceret ultralydsskannere, der anvender 2-D transducerarrays med nok transducerelementer til at opnå en høj kvalitet i deres 3-D billeder. På grund af de store matrix transducere med specialdesignet, integreret elektronik er disse systemer ekstremt dyre. Den relativt lave pris på ultralydsskannere er en af de faktorer, der har hjulpet ultralydsbilleddannelse med at blive så udbredt . Den høje pris på kvalitets 3-D-skannerne er en begrænsende faktor på deres markedsandel.

Række-søjle adressering af 2-D transducerarrays er et billigt alternativ til fuldt adresserede 2-D arrays, til 3-D ultralydsbilleddannelse. Ved brug af række-søjle adressering, er antallet af transducerelementer dramatisk reduceret. Dette reducerer omkostningerne til integrering med transducerhovedet, og det fjerner helt behovet for at skulle integrere specialfremstillet elektronik med transducerhovedet. En ulempe ved række-søjle adressering af 2-D arrays er skabelsen af spøgelses ekkoer i punktspredningsfunktionen.

I den anden del af de videnskabelige bidrag fra denne afhandling, blev række-søjle adressering af 2-D arrays undersøgt. En analyse af, hvordan spøgelses ekkoer kan dæmpes blev præsenteret. Det blev vist at dæmpning af spøgelses ekkoer kunne opnås ved at minimere den første afledte af apodiseringsfunktionen. I litteraturen blev det foreslået at bruge en cirkulær symmetrisk apodiseringsfunktion. Et nyt apodiseringslayout, der løser ulemperne ved den tidligere foreslåede apodisering blev beskrevet. Ved hjælp af både simuleringer og målinger udført med to internt producerede CMUT arrays, viste det nye layout sig at være effektivt til at dæmpe kantbølgerne. Der blev i afhandlingen også foreslået nye metoder til at integrere apodiseringen med selve transducerarray'et.

Den væsentligste del af afhandlingen består af otte videnskabelige artikler indsendt til internationale konferencer og tidsskrifter i løbet af ph.d.-projektet.

Preface

This PhD thesis has been submitted to the Department of Electrical Engineering at the Technical University of Denmark in partial fulfillment of the requirements for acquiring the PhD degree. The research providing the foundation for the thesis has been conducted over a period of three years from April 15th, 2011 to June 14th, 2014 at the Center for Fast Ultrasound Imaging (CFU), the Biomedical Engineering Group, Department of Electrical Engineering, Technical University of Denmark. The project was funded by grant 024-2008-3 from the Danish Advanced Technology Foundation and BK Medical Aps, Denmark. The thesis recapitulates the conducted research and included are three journal papers four conference papers, and one extended abstract. During my work I have had the opportunity to attend conferences in San Diego, Orlando, Artimino, Dresden and Prague to present my research, and it has let to many fruitful discussions. Traveling to these conferences has been a huge privilege, and the experiences have broadened my horizon of both the technical and the clinical side of medical ultrasound as well as within acoustics in general. Additionally, the conferences have given me the opportunity to nurture and expand my professional as well as social networks. I have also enjoyed and learned a lot from teaching and tutoring students in medical imaging systems, and I especially value the experience of co-supervising two bachelor's and one master's project. It has been a pleasure to share my knowledge within ultrasound imaging with professors, colleagues, and students at the Biomedical Engineering Group.

Morten Fischer Rasmussen
Copenhagen, June 2014

Acknowledgements

During the last 3 years working on this PhD project, I have met many interesting people from all over the world. They are invaluable connections that undoubtedly will have an impact on my future professional life.

I would like to thank my supervisor Professor Jørgen Arendt Jensen, PhD, Dr. Techn., from the Center for Fast Ultrasound Imaging (CFU) at the Technical University of Denmark. Thank you for believing in me and for choosing me for this PhD project. You have given me invaluable guidance, helped with new ideas, and supported me throughout my PhD.

I would like to thank Thomas Lehrmann Christiansen for the many fruitful discussions on the possibilities and limitations of row-column addressed CMUT arrays, which have so forth let to one patent application.

I would also like to thank my other fellow PhD students Michael Johannes Pihl and Jacob Bjerring Olesen, you have both been good friends and colleagues.To my former and current office mates Joachim Hee Rasmussen, PhD, and Martin Christian Hemmsen, PhD, goes my warmest regards. We have spend many hours together engaged in concentrated silence, intriguing theoretical discussions, or sharing everyday life experiences.

I would also like to thank all the other PhD students at CFU, past and present. They have created a great working environment where ideas could be shared and discussed, and have always been available for help and discussions on ultrasound and on life in general.

Without the help from the following people, my ability to concentrate on research would have been significantly hampered. Matthias Bo Stuart, PhD, and Borislav Gueorguiev Tomov, PhD, for their hard work on making the SARUS system functional. Elna Sørensen, you have always been ready to provide help with administrative matters and issues in general. Nina Kjærsgaard, you have always had a positive attitude and been very helpful with proof reading of manuscripts. Furthermore, I appreciate all the technical help I have received from Henrik Laursen, who never hesitated to help. Also Jens Chr. Jensen has provided technical assistance and has helped constructing several measurement set-ups.

I would also like to thank my fellow PhD students Niels Christian Jerichau Clausen and Ulrik Nielsen, with whom our individual ups and downs of the last 3 years were shared and discussed.

Last, but definitely not least, I would like to express my sincerest thanks to my family and my girlfriend Mirja Riewe, who have lovingly supported me throughout the project and for understanding my high commitment and engagement to the project.

The thesis is typeset using LaTeX, and the drawings are done in XFig. Most of the tools used in my everyday work are a product of the open source software community. This PhD project was financially supported by grant 024-2008-3 from the Danish Advanced Technology Foundation and by BK Medical ApS.

List of Figures

2.1 Synthetic transmit focusing. 8
2.2 Virtual sources. 9
2.3 Cystic resolution illustration. 12
2.4 Parallel Beamforming illustration. 14
2.5 Parallel beamforming transmit apertures. 15
2.6 Parallel beamform boxing effect compensation. 17
2.7 The synthetic aperture virtual element setup. 19
2.8 The synthetic aperture imaging transmit and receive apertures. 20
2.9 Synthesized transmit aperture. 21
2.10 SARUS. 22
2.11 The 32×32 element phased array ultrasound probe. 22
2.12 Simulated PSF for PB and SAI. 23
2.13 The measured 3-D line spread function. 24
2.14 Cyst phantom measurement. 26

3.1 Row-column addressing illustration. 32
3.2 Scaling of row-column vs fully addressed arrays. 33
3.3 Edge effect illustration. 35
3.4 Edge wave sources and drains. 37
3.5 Time of flight for edge waves. 37
3.6 Mask layout of a $32+32$ row-column addressed array. 39
3.7 A wafer with conventional and fixed-area apodized. 40
3.8 Illustration of dynamic area apodization. 41
3.9 Bias voltage apodization. 43
3.10 PSF with different discretization levels. 45
3.11 Illustration of the circular symmetric apodization. 46
3.12 Illustration of Roll-off region apodization. 47
3.13 Beamforming illustration. 48
3.14 B-mode of anechoic blood vessel. 50
3.15 Measured and simulated line spread function. 51

A.1 Explososcan boxing effect compensation. 65
A.2 SAI virtual source setup. 66
A.3 FWHM as a function of depth. 69
A.4 The cystic resolution. 69
A.5 PSF of Explososcan vs. SAI. 72

B.1 Explososcan TX and RX aperture. 76
B.2 SAI TX aperture. 77
B.3 PSF of Explososcan and SAI. 78
B.4 CTR from PSF 80
B.5 Speckle comparison. 80

C.1 Geometry for determining the aperture width. 88
C.2 Four different transmit apertures with 256 active elements. 90
C.3 The receive aperture for parallel beamforming. 91
C.4 Imaging quality metrics extracted from simulated PSFs. 91
C.5 The synthetic aperture imaging transmit and receive apodization. . . . 94
C.6 Optimizing the transmit focal depth and the max transmit-beam angle of synthetic aperture imaging. 95
C.7 The setup for a single emission. 96
C.8 Simulated C-scans of the 3-D PSFs. 97
C.9 The main-lobe size is seen as a function of depth. 98
C.10 The Cystic Resolution sampled at 20 dB intensity difference. 99
C.11 The 32×32 element phased array ultrasound probe used for the measurements. 100
C.12 The measured 3-D line spread function. 101
C.13 The measured FWHM on the wire phantom. 102
C.14 The measured cystic resolution on the wire phantom. 102
C.15 Parallel beamforming and synthetic aperture imaging. 103
C.16 The estimated contrast to noise ratio. 104
C.17 Using synthetic aperture imaging increases the SNR at all depths. . . . 105

D.1 Row-column addressing illustration. 113
D.2 Beamforming illustration. 114
D.3 Projection of point on line. 114
D.4 Scaling of row-column addressing vs fully addressing. 116
D.5 Edge effect illustration. 117
D.6 Time of flight for edge waves. 119
D.7 Effect of apodizing on PSF. 121
D.8 PSF comparison. 122

E.1 Row-column addressing illustration. 127

E.2 Beamforming illustration. 128
E.3 LSF of a row-column addressed array vs fully addressed array. 131
E.4 Resolution scaling. 132

F.1 Mask layout of the row-column addressed $32+32$ CMUT transducers. 137
F.2 Process flow of the cleanroom fabrication. 138
F.3 Picture of the experimental setup. 140
F.4 Simulated and measured pressure field. 142
F.5 Measured and simulated pressure. 143

G.1 Row-column addressing of 2-D transducer array illustration. 147
G.2 Spatial impulse response of long thin line-elements. 150
G.3 Illustration of a pulse-echo simulation setup 152
G.4 Time of flight of edge waves. 152
G.5 Circular symmetric integrated apodization. 155
G.6 New integrated-apodization layout. 155
G.7 Maximum received echo intensity from a single scatter. 156
G.8 Maximum ghost-echo intensity of a single scatterer. 157
G.9 Mask layout of the $32+32$ prototype CMUT array with integrated apodization. 159
G.10 The measurement setup. 160
G.11 The measured and simulated sound field pressures. 161
G.12 Time of flight (ToF) illustration of a focused emission. 162
G.13 Projection of the point $\mathbf{p}$ onto the line segment $\mathbf{ab}$. 163
G.14 PSF at $(x,y,z) = (8,3,30)$ mm. 165
G.15 Maximum intensity of the PSFs. 165
G.16 B-mode images of a slice through the center of an anechoic blood vessel. 166
G.17 Peak pressure distribution of a phased row-column addressed array. . . 167

H.1 3-D illustration of the CMUT row-column addressed transducer array. . 176
H.2 Array mask layout. 178
H.3 The row-column addressed CMUT array mounted and wire-bonded on the carrier board. 179
H.4 Process flow of the cleanroom fabrication. 180
H.5 Sketch of the front end electronics as seen by a column element. . . . 182
H.6 Impedance magnitude and phase. 183
H.7 Resonance frequency in air. 185
H.8 Pulse-echo impulse response. 187
H.9 Measured and simulated line spread function. 191
H.10 3-D beamformed image of a wire. 193

List of Tables

A.1 Transducer parameters 67

B.1 Transducer parameters 76

C.1 Transducer, simulation and measurement parameters 92

D.1 Simulation parameters 118

E.1 Ultrasound probe parameters. 130

G.1 Simulation parameters. 148
G.2 Transducer parameters common for both CMUT arrays. 158

H.1 Transducer dimensional parameters 177
H.2 Transducer impedance characterization parameters 186
H.3 Transducer acoustical characterization parameters 186
H.4 Imaging results 190

Abbreviations

1-D	One Dimensional
2-D	Two Dimensional
3-D	Three Dimensional
apo	Apodization
CMUT	Capacitive Micromachined Ultrasonic Transducer
CNR	Contrast to Noise Ratio
CTR	Clutter to Total energy Ratio
DRF	Dynamic receive focusing
ems	Emission
$f_\#$	f-number, equal to the focal length divided by the aperture diameter
FWHM	Full Width at Half Maximum
FWTM	Full Width at Tenth Maximum
HRI	High Resolution Image
HWHM	Half Width at Half Maximum
HWTM	Half Width at Tenth Maximum
IQ	In-phase and quadrature-phase (A phase shift of: 0° and 90°.)
LRI	Low Resolution Image
LSF	Line Spread Function
PA	Phased Array
PB	Parallel Beamforming
PRF	Pulse Repetition Frequency
PSF	Point Spread Function
RC	Row-column
RF	Radio Frequency
RI	Relative Intensity
RMS	Root Mean Square
SA	Synthetic Aperture
SAI	Synthetic Aperture Imaging
SARUS	Synthetic aperture real-time ultrasound system
SASB	Synthetic aperture Sequential Beamforming
SAR	Synthetic Aperture Radar

SNR	Signal to Noise Ratio
STF	Synthetic Transmit Focusing
ToF	Time of Flight
US	Ultrasound
USI	Ultrasound Imaging
VS	Virtual Source

CHAPTER 1

Introduction

Medical ultrasound imaging is one of the most used diagnostic imaging techniques for visualizing internal body organs. It has gained its popularity by being a safe imaging modality with no known side-effects. It can image soft tissue in real-time, which gives sonographers and radiologists a dynamic view of the anatomy. Ultrasound imaging is relatively cheap and does not require special facilities like most of the other imaging modalities, such as X-ray, PET, SPECT, CT and MRI. At the same time, most ultrasound scanners are portable and can run on batteries, which is useful in emergency situations.

Ultrasound imaging was first developed in the late 1940s and originated from ideas developed in the radar and sonar community. In the beginning only a single acoustic scan line was measured and presented to the operator as a function of depth. This is known as the A-mode, or amplitude mode. Later the A-mode lines were stacked next to each other to create the B-mode, or brightness mode. 2-D B-modes is today the standard in all ultrasound scanners. Some scanners can also create 3-D B-modes, enabling full visualization of entire organs.

In modern ultrasound scanners the 2-D B-modes are made using a 1-D array of ultrasound transducers. The B-mode image displays a slice of the anatomy below the transducer array. The image significantly changes its appearance when the orientation of the transducer array is changed, making it harder to recognize the features of the 3-D anatomy. This complicates the diagnosis of the pathology.

Using 3-D imaging, entire organs can be imaged and visualized. In obstetrics, 3-D imaging is usually made using a mechanically scanned 1-D array. This way, if the fetus is lying still a high quality 3-D image can be reconstructed. For real-time 3-D imaging a 2-D transducer array is needed to steer the transmit and receive beams in two dimensions. Acquiring a 3-D volume gives the medical doctor the freedom to investigate the measured anatomy in any slice desirable after the scan has been completed. This allows for precise measurements of organs dimensions and makes the scan more operator independent.

A problem for conventional 3-D imaging is that it only has one fixed transmit focal depth, compared to in receive where dynamic focusing can be performed. This reduces the image quality at other depths than the focal depth. It is always desirable to increase the image quality, which makes the diagnosing process for the medical doctors easier. It could also potentially enable the medical doctors to detect more diseases at an earlier state and could reduce the cost of each investigation if less scans must be completed on the same patient. It is therefore desirable to achieve as good an image quality as possible at all depths.

A method that enables dynamic focusing also for the transmit beams, is the synthetic aperture imaging (SAI) technique. Ideally, SAI would achieve full dynamic focusing in transmit with a frame rate high enough to be used for cardiac imaging. The subject for the first part of this PhD project was to investigate if synthetic aperture 3-D imaging could increase the imaging quality compared to conventional 3-D imaging and still achieve a frame rate usable for cardiac imaging.

The disadvantage of real-time 3-D imaging using large 2-D arrays is a huge increase in the complexity and cost of the ultrasound scanner. 2-D matrix arrays with "enough" elements to create a 3-D volume with imaging quality equal to the current best achievable 2-D imaging is extremely expensive. This high 3-D imaging quality has recently been achieved by several of the leading ultrasound companies, by integrating electronics directly into the ultrasound probe. These probes are very expensive, often on par with entire 2-D ultrasound scanners. Some of the large 2-D matrix probes also require water cooling.

A low cost alternative to the large 2-D matrix transducers is to row-column address the 2-D array. When using row-column addressing, the 2-D array is effectively converted to two perpendicular 1-D arrays., This reduces the number of elements on a $N \times N$ 2-D transducer array from N^2 to $2N$, which greatly reduces cost of the ultrasound probe. Imaging with row-column addressed 2-D arrays was the second topic of this PhD project.

1.1 Publications in the thesis

This thesis is based on the following publications. The publication letter refers to the appendix name containing the corresponding paper.

3-D Phased Array Synthetic Aperture Imaging

3-D Synthetic Aperture Imaging (SAI) was in two conference papers and one journal paper compared to the Parallel Beamforming (PB) technique (in the two first papers referred to as Explososcan.)

Paper A

M. F. Rasmussen, G. Férin, R. Dufait, and J. A. Jensen. (2012).
"Preliminary comparison of 3D synthetic aperture imaging with Explososcan".
Published in: *Proceedings of SPIE Med. Imag.* Vol. 8320. pp. 1–9.

Paper B

M. F. Rasmussen, J. M. Hansen, G. Férin, R. Dufait, and J. A. Jensen (2012).
"Comparison of 3D Synthetic Aperture Imaging and Explososcan using Phantom Measurements".
Published in: *Proceedings of IEEE Ultrason. Symp.* pp. 113–116.

Paper C

M. F. Rasmussen and J. A. Jensen (2014).
"Comparison of 3-D Synthetic Aperture Phased Array Ultrasound Imaging with Parallel Beamforming".
Accepted on June 4, 2014 for publication in: *IEEE Trans. Ultrason., Ferroelec., Freq. Contr.*

3-D Imaging with Row-column addressed 2-D arrays

The pros and cons of row-column addressing 2-D ultrasound transducer arrays was described in three conference papers and two journal papers.

Paper D

M. F. Rasmussen and J. A. Jensen (2013).
"3D ultrasound imaging performance of a row-column addressed 2D array transducer: a simulation study".
Published in: *Proceedings of SPIE Med. Imag.* 86750C, pp. 1–11.

Paper E

M. F. Rasmussen and J. A. Jensen (2013).
"3-D Ultrasound Imaging Performance of a Row-Column Addressed 2-D Array Transducer: A Measurement Study".
Published in: *Proceedings of IEEE Ultrason. Symp.* pp. 1460–1463.

Paper F

T. L. Christiansen, **M. F. Rasmussen**, J. A. Jensen and E. V. Thomsen. (2014).
"Row-Column Addressed 2-D CMUT Arrays with Integrated Apodization".
Accepted for publication in: *Proceedings of IEEE Ultrason. Symp.*

Paper G

M. F. Rasmussen, T. L. Christiansen, E. V. Thomsen, and J. A. Jensen (2014).
"3-D Imaging with Row-Column Addressed Arrays: Transducer-Integrated Apodization and Line-element Beamforming".
Submitted to: *IEEE Trans. Ultrason., Ferroelec., Freq. Contr.*.

Paper H

T. L. Christiansen, **M. F. Rasmussen**, J. A. Jensen, and E. V. Thomsen (2014).
"3-D Imaging using Row-Column Addressed Arrays with Integrated Apodization: Transducer Fabrication and Experimental Results".
Submitted to: *IEEE Trans. Ultrason., Ferroelec., Freq. Contr.*

Patent on Apodization of Ultrasound Transducer Arrays

One patent was taken on how to integrate apodization into ultrasound transducer arrays.

Patent A

M. F. Rasmussen, T. L. Christiansen, E. V. Thomsen, and J. A. Jensen "Ultrasound Imaging Transducer Array with Integrated Apodization".
Filed on December 19, 2013, Number PCT/IB2013/002838.

1.2 Publications not included in the thesis

Five co-authored conference papers and two co-authored journal papers are not included in this thesis.

External Paper I

3-D Synthetic Aperture Sequential Beamforming (SASB) was in a conference paper compared to Parallel Beamforming. It was in the work demonstrated that 3-D SASB could achieve the same imaging quality as Parallel Beamforming, but using only one output channel.

M. C. Hemmsen, **M. F. Rasmussen**, M. B. Stuart and J. A. Jensen (2014). "Simulation study of real time 3-D Synthetic Aperture Sequential Beamforming for Ultrasound imaging". In: *Proceedings of SPIE Med. Imag.* In press.

External Paper II

The Synthetic Aperture Real-time Ultrasound System (SARUS) for acquiring and processing synthetic aperture data for research purposes was in this journal paper described. The specifications and design of the system were detailed, along with its performance for SA, nonlinear, and 3-D flow estimation imaging. SARUS acquires individual channel data simultaneously for up to 1024 transducer elements for a couple of heart beats, and is capable of transmitting any kind of excitation.

J. A. Jensen, H. Holten-Lund, R. T. Nilsson, M. Hansen, U. D. Larsen, R. P. Domsten, B. G. Tomov, M. B. Stuart, S. I. Nikolov, M. J. Pihl, Y. Du, J. H. Rasmussen, and **M. F. Rasmussen** (2013). "SARUS: A Synthetic Aperture Real-time Ultrasound System". In: *IEEE Trans. Ultrason., Ferroelec., Freq. Contr.* 60.9, pp. 1838-1852.

External Paper III

This conference paper presented 3-D vector flow images obtained using the 3-D Transverse Oscillation (TO) method. The method employed a 2-D transducer and estimated the three velocity components simultaneously, which is important for visualizing complex flow patterns. Data were acquired using the experimental ultrasound scanner SARUS on a flow rig system with steady flow. It was shown that the ultrasound method is suitable for real-time data acquisition as opposed to magnetic resonance imaging (MRI). The results demonstrated that the 3-D TO method is capable of performing 3-D vector flow imaging.

M. J. Pihl, M. B. Stuart, B. G. Tomov, J. M. Hansen, **M. F. Rasmussen**, and J. A. Jensen (2013). "Preliminary examples of 3D vector flow imaging". In: *Proceedings of SPIE Med. Imag.* Vol. 8675, In press.

External Paper IV

This journal paper is the second part of two papers on the subject of the 3-D Transverse Oscillation (TO) method. 3-D TO was investigated through flow rig experiments and measurements of the synthesized TO fields and estimated 3-D velocity vectors were presented. Simulated data were generated using Field II for comparison. The experimental results validated the results obtained through simulations and verified that the 3-D TO method estimates the full 3-D velocity tensors simultaneously, as well as the correct velocity magnitudes.

M. J. Pihl, M. B. Stuart, B. G. Tomov, **M. F. Rasmussen**, and J. A. Jensen (2014). "A Transverse Oscillation Approach for Estimation of Three-Dimensional Velocity Vectors. Part II: Experimental Validation". In: *IEEE Trans. Ultrason., Ferroelec., Freq. Contr.* Accepted.

External Paper V

Measuring how close an emission sequence is to the FDA limits is often cumbersome, since the scan sequence has to broken apart, measurements conducted for the individually emitted beams, and the final intensity levels calculated by combining the intensities from the individual beams. In this conference paper a fast measurement scheme using the multi-line sampling capability of modern scanners and research systems was suggested. The approach has several advantages: the scanner does not have to be re-programmed and can use the scan sequence without modification. A single emission sequence was employed for testing and calibrating the approach. The measurements, using either the intensity measurement system AIMS III or SARUS, agreed within a relative standard deviation of 0.24 %.

J. A. Jensen, **M. F. Rasmussen**, M. B. Stuart, and B. G. Tomov (2014). "Rapid Measurements of Intensities for Safety Assessment of Advanced Imaging Sequences". In: *Proceedings of SPIE Med. Imag.* In Press.

External Paper VI

This conference paper is the successor to the previous paper, External Paper V. For advanced imaging sequences it can be difficult to predict the position of maximum intensity (MI) and peak negative pressure values. This paper investigated how both the magnitude of the intensities as well as the placement of the peak values can be predicted by simulations. The sequence is defined through the normal setup routines for the SARUS scanner, and Field II is then used to simulate both intensity and MI. The method was shown be useful for predicting the intensity field of advanced imaging sequences.

J. A. Jensen, **M. F. Rasmussen**, M. B. Stuart, and B. G. Tomov (2014). "Simulation and Efficient Measurements of Intensities for Complex Imaging Sequences". In: *Proceedings of IEEE Ultrason. Symp.* Abstract accepted.

1.3 Other Contributions

Besides the papers published, several software projects were developed for the benefit of the colleagues at the center for fast ultrasound imaging (CFU).

An interface to control the positioner of the intensity measurement system AIMS-3 by Onda Corporation was programmed during this PhD project. The software can control the positioner either from within MATALB or from a stand-alone C program. The C-program uses a control library that could be compiled into any other C program.

A collection of MATLAB and bash scripts that solves often appearing problems when working with ultrasound imaging were programmed. Collectively the scripts are called the "CFUtools". Excluding all external scripts, CFUtools consists of more than 9000 lines of code. The scripts can be used for measuring point spread function metrics, metrics from cysts, easing the task of creating prettier plots from MATLAB, PDF conversion, creation of high quality video from MATLAB figures, match filtering, dynamically averaging of measurements, plotting raw data of new measurements, synchronization of parallel jobs on multiple nodes, several coordinate transformations, easy definition of 1-D and 2-D transducer arrays for Field II and SARUS, calculating delays and apodizations for defined transducer arrays, and much more.

A collection of scripts and LaTeX files were produced and gathered as CFUlatex. The scripts define poster, pre-print, report and thesis layouts. It also includes scripts that converts PDFs to anti-alization PNGs and many other tasks. CFUlatex consists of more than 2000 lines of code.

A delay-and-sum beamformer that can handle row-column addressed 2-D arrays was programmed and made available online. The beamformer can be downloaded at `rc-beamformer.mofi.dk`.

1.4 Outline

The outline of the remaining part of this thesis is as follows. The next chapter contains a resume of the results achieved with 3-D synthetic aperture imaging. In Chapter 3, the research conducted on the subject row-column addressing of 2-D arrays is presented. This is followed by a perspectivation in Chapter 4. The main part of this thesis consists of the papers published on the subject of 3-D synthetic aperture imaging and row-column addressing of 2-D arrays. The papers are included as appendices named Paper A though Paper H. At the very end is included a patent application related to row-column addressing of 2-D arrays.

The main results and conclusions are conveyed through Chapter 2 and 3, and the three journal papers, Paper C, G, and H.

CHAPTER 2

3-D Synthetic Aperture Imaging

As this research project started, one of the goals was to investigate if the results achieved by the research community for 2-D synthetic aperture imaging could be extended to 3-D imaging. The results being that synthetic aperture imaging improves the imaging quality compared to conventional imaging.

In this chapter, the research carried out on 3-D synthetic aperture imaging is presented. The analyses and results included in this chapter are based on the work presented in the papers A (included on page 61), B (included on page 73) and C (included on page 83). A different setup was used for synthetic aperture imaging in all three papers. The setup presented in this chapter is the one used in the journal paper C. First, the previous literature is briefly described, afterwards the basis for the comparison between synthetic aperture imaging and the reference of conventional 3-D imaging is given. Then, the reference technique and the synthetic aperture technique are introduced, followed by the results of the simulations and the measurements. Concluding is a description of the published papers and a conclusion.

2.1 Introduction

Synthetic aperture imaging (SAI) originates from radar systems as synthetic aperture radar (SAR) (Sherwin et al. 1962). SAR is usually an airborne modality where the imaging platform is translated across the imaged scene, either on board an airplane or a satellite. By post processing of the acquired data, a larger aperture can be synthesized leading to increased lateral resolution. SAR was in the 1950s adapted to ultrasound imaging (Burckhardt et al. 1974).

The first implementations of synthetic aperture ultrasound imaging was the mono-static synthetic aperture imaging (Bennett et al. 1982; Peterson and Kino 1984; Ylitalo and Ermert 1994), which is a copy of the airborne SAR. In mono-static SAI, only a single element is used for transmitting and receiving the ultrasound waves at a time. This is a natural limitation for a moving platform SAR, but not for ultrasound imaging where large arrays of transducer elements are usually available.

Synthetic aperture imaging enables dynamic transmit focusing (Burckhardt et al. 1974; Kino et al. 1980). If the receive aperture consists of an array of transducer elements, as opposed to the mono-static SAI, dynamic focusing can also be carried out in receive. Measured ultrasound data can be focused by to estimating the position of the emitted wavefront and its reflections at any given time. This way one can calculate the time-of-

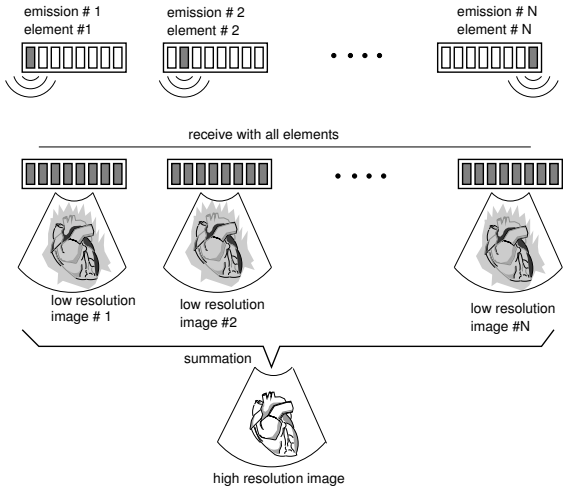

Figure 2.1: Synthetic transmit focusing by summation of low resolution images. The figure is from (Nikolov and Jensen 2002).

flight (ToF) from the transmitting transducer element, to the point of interest, and back to each element in the receiving array. When assuming a constant speed of sound, the time of flight is the distance traveled divided by the speed of sound, which can be written as

$$\mathrm{ToF}(\mathbf{p},n,i) = \frac{\|\mathbf{p}-\mathbf{s}_n\| + \|\mathbf{r}_i - \mathbf{p}\|}{c}\,, \tag{2.1}$$

where $\mathbf{p}$ is the coordinate of the point of interest being focused, c the speed of sound, $\mathbf{s}_n$ the transmit element with index n, and $\mathbf{r}_i$ the receive element with index i. Using this equation for focusing and recording the echoes from a single emission, an entire image can be beamformed. Only using a single emission will result in a low image quality. This is often termed the low resolution image (LRI). On the other hand, by repeatedly changing the position of the transmit element, $\mathbf{s}_n$, and each time focusing a new LRI, followed by a summation of all LRIs, a high resolution image (HRI) is created. The high resolution image is now dynamically transmit focused at all points in the image. This is illustrated in Fig. 2.1. The process of using the synthetic aperture technique for transmit focusing is also termed synthetic transmit focusing (STF) (Bae and Jeong 2000; Flaherty et al. 1967; Frazier and O'Brien 1998; Karaman, Li, et al. 1995; Pedersen et al. 2004; Ylitalo 1995).

Only emitting with a single element limits the amount of energy delivered to the body or object being imaged, due to the restricted size of each element. This also limits the achievable signal to noise ratio (SNR). Equation (2.1) assumes the emitted wavefront has the shape of a sphere. If several transmit elements are grouped together and their combined wavefront still has the shape of a sphere, then Eq. (2.1) still holds. The apparent

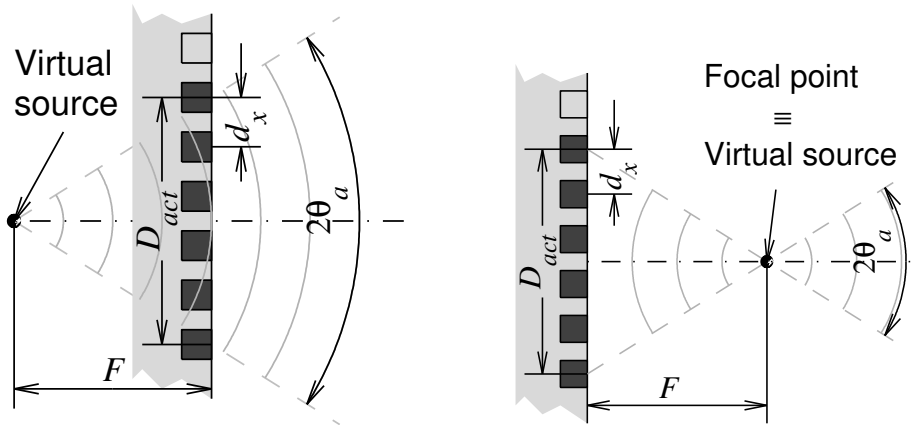

(a) Virtual source behind the array.

(b) Virtual source in front of the array.

Figure 2.2: Virtual sources. Several transmit elements are emulating a spherical wavefront that appears to be originating from the behind the transducer array (a) or in front of the array (b). The figures are from (Nikolov and Jensen 2002). The focal depth in (a) is defined as a negative focal depth and in (b) as a positive focal depth.

source of the wavefront is then termed the virtual source, or the virtual element (Bae and Jeong 2000; Karaman, Li, et al. 1995; Nikolov and Jensen 2002). Two virtual sources are illustrated in Fig. 2.2, where the dark squares illustrate the active transmit elements and the dashed cones the acceptance angle of the virtual sources. When using virtual sources, the coordinate of the virtual source is used as $\mathbf{s}_n$ in Eq. (2.1). The acceptance angle of a virtual source describes the maximum angle within which the assumption of the spherical wavefront holds. Using synthetic aperture imaging gives a higher flexibility in the beamforming process, but comes with the disadvantage of increases the processing requirements.

A thorough investigation of 2-D synthetic aperture phased array imaging was made by Johnson, Karaman, et al. (2005) and Johnson, Oralkan, et al. (2005). They showed that to achieve an optimal image quality when the number of active elements are limited, the active subarray must be translated between the emissions.

Achieving high frame rate 3-D synthetic aperture imaging by mechanically sweeping a 1-D phased array was investigated by Lockwood et al. (1998). Nikolov and Jensen (2000) used the elevation focal point as a virtual source in the elevation direction with a mechanically scanned 1-D transducer array. High frame rate 3-D imaging with a 2-D

phased array was investigated via simulations by Kim and Song (2008).

In the first part of this thesis, it is investigated whether 3-D synthetic aperture phased array imaging improves the imaging quality compared to conventional 3-D phased array imaging. In the following, it is first investigated how a fair comparison between the two techniques can be made.

2.2 The Fair Comparison

When evaluating the image quality of a new imaging technique, a reference imaging technique is needed in order to evaluate whether the new imaging technique is an improvement. A common ground, or set of restrictions, must be laid for the comparison of the two techniques to be fair. May the two ultrasound imaging techniques for instance use an indefinite amount of active transducer elements and beamformer channels? If so, then the comparison between the two techniques would not be clinically relevant, since none of the solutions would be implementable in a clinical scanner. The restrictions used and their motivation are covered in the following.

The first restriction laid on the two techniques is that they must be implementable on the available 32×32 element transducer array available for the measurements. In the first conference paper on synthetic aperture 3-D imaging, paper A, the goal of the two techniques was to achieve the best possible image quality with the available 2-D array and using all 1024 channels. In the next two papers, paper B and C, the available active elements and beamformer channels were restricted. Even though the available computational power is exponentially increasing, the actual cable connecting the ultrasound probe with the ultrasound scanner will, in the near future only very slowly improve its diameter and weight per channel used. If the cable is too heavy, the operator will risk injuring his or her wrist when scanning on a daily basis. To limit the cable size, the amount of transducer elements sampled must therefore be limited. Both techniques are therefore, in this comparison, limited to 256 active channels at a time during both transmitting and receiving. Multiplexing electronics in the handle that selects the active transducer elements are assumed available, and are in this study otherwise neglected.

The two imaging techniques are designed for cardiac imaging, which requires imaging down to 15 cm and a frame rate f_r of at least 20 Hz. To be comparable with products from the medical ultrasound industry, a volume scan spanning 90° in both the azimuth and elevation direction is chosen.

With a maximum scan depth r_{max} of 15 cm and a speed of sound c equal to approximately 1540 m/s, the maximum pulse repetition frequency is

$$f_{prf} = \frac{c}{2\,r_{max}} = 5.133\,\text{kHz}\,. \tag{2.2}$$

The possible number of emission per frame then becomes

$$N_{ems} = \frac{5.133\,\text{kHz}}{20\,\text{Hz}} \approx 256\,. \tag{2.3}$$

Using 256 emissions per frame allows for resolving the azimuth and elevation directions with $\sqrt{256} = 16$ emissions each.

2.3 Image Quality Metrics

To evaluate the image quality, an image quality metric is needed. Unfortunately, no single metric can describe what a good image quality is. Instead, several metrics are used, each describing a different facet of the image quality.

For the detail resolution, in other words how small details can be distinguished in the image, the classic full-width-at-half-maximum (FWHM) is used. The FWHM is measured on the point spread function (PSF). In the following the three other image quality metrics are introduced.

2.3.1 Cystic Resolution

On the PSF, the cystic resolution is also measured, which describes how well dark regions surrounded by bright tissue can be identified. This mimics an often seen situation in medical ultrasound where the object of interest is a weakly reflecting medium, such as blood or a cyst, surrounded by a stronger back-scattering medium. Specifically, it describes the ability to detect an anechoic cyst in a uniform scattering medium (Vilkomerson et al. 1995). The cystic resolution gives the intensity at the center of an anechoic cyst of a given size relative to its surrounding uniformly back-scattering medium. This setup is seen in Fig. 2.3 on the following page. The lower the intensity at the center of the cyst, i.e. the darker it appears in the image for a given cyst size, the better the imaging performance of the system. The relative intensity (RI) of the anechoic cyst was shown by Ranganathan and Walker (Ranganathan and Walker 2007), to be quantized as the clutter energy to total energy ratio,

$$\mathrm{RI}(R) = \sqrt{\frac{E_{out}(R)}{E_{tot}}} = \sqrt{1 - \frac{E_{in}(R)}{E_{tot}}}\,, \tag{2.4}$$

where E_{in} is the signal energy inside a circular region with radius R centered on the peak of the point spread function, E_{tot} is the total point spread function energy, and E_{out} is the point spread function energy outside the circular region. To achieve a single number from the $\mathrm{RI}(R)$-curve, one either determines the relative intensity for a single cyst radius, or determines the required radius to achieve a certain relative intensity, e.g. the cyst radius at which the intensity at center of the cyst is 20 dB lower than its surroundings, written as $R_{20\mathrm{dB}}$.

2.3.2 Contrast-to-Noise Ratio

The real test of how well dark regions surrounded by tissue is detected is the contrast-to-noise ratio (CNR). Where the cystic resolution is calculated on the PSF the CNR is

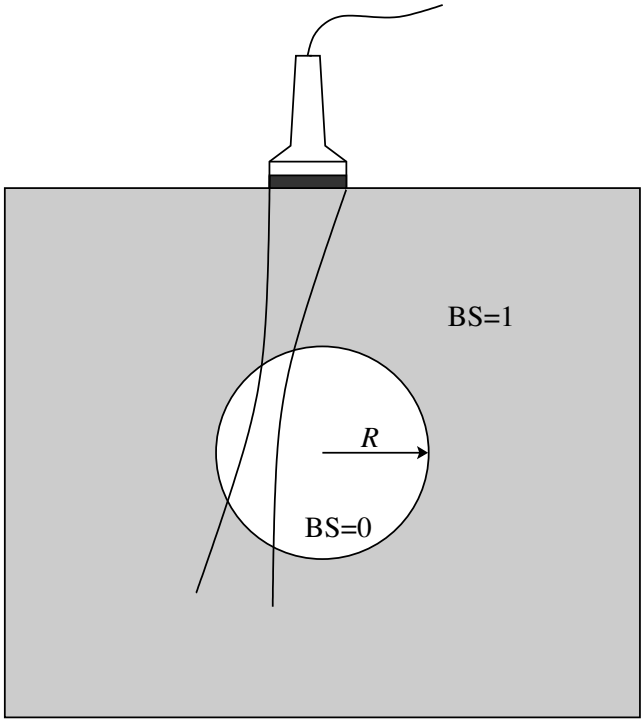

Figure 2.3: Cystic resolution illustration. BS is the back scattering coefficient, here meaning how large a fraction of the energy hitting a scatterer is reflected. The circle with radius R is anechoic, the surrounding medium is continuously back scattering. The darker the image is at the center of the cyst, the better is the cystic resolution.

calculated on real cysts embedded in a tissue mimicking material. The darker the cysts are compared to their surroundings, the better is the imaging quality and the CNR metric. The imaging performance of the cysts is estimated using the contrast-to-noise ratio (CNR) which is calculated as

$$\mathrm{CNR} = \frac{\mu_s - \mu_c}{\sqrt{\sigma_s^2 + \sigma_c^2}}\,, \tag{2.5}$$

where μ_c and μ_s are the mean intensities of a cyst region and a speckle region. σ_c^2 and σ_s^2 are the variances of the cyst and speckle data. The CNR is calculated from spherical regions of the envelope-detected data before it is log-compressed.

2.3.3 Signal-to-Noise Ratio

The SNR can be used to estimate the penetration depth. The SNR is measured by scanning a tissue mimicking phantom only containing randomly distributed scatterers. To estimate the signal and noise components, N frames are acquired. The signal component is estimated by averaging the N measurements. Subtracting the signal component from each frame produces N noise estimates. The SNR is estimated for each voxel in the IQ-beamformed volume by taking the ratio of the signal power and the noise power. The SNR is thereby estimated on a complex data set. The RMS-power of a complex signal when assuming a unit load is

$$P_{\text{RMS}} = V_{\text{RMS}} \times I^*_{\text{RMS}} = |V_{\text{RMS}}|^2 \ , \tag{2.6}$$

where * denotes complex conjugated. Using (2.6) the SNR is calculated by

$$\text{SNR}(\mathbf{x}) = \frac{\left|\sqrt{\frac{1}{N}\sum_{n=1}^{N}\text{E}[s(\mathbf{x})]^2}\right|^2}{\left|\sqrt{\frac{1}{N}\sum_{n=1}^{N}(s_n(\mathbf{x}) - \text{E}[s(\mathbf{x})])^2}\right|^2} \tag{2.7a}$$

$$= \frac{\left|\text{E}[s(\mathbf{x})]\right|^2}{\text{var}[s(\mathbf{x})]} \ , \tag{2.7b}$$

where $\mathbf{x} = (x, y, z)$ is the voxel coordinate, $\text{E}[\cdot]$ the expectation operator, $\text{var}[\cdot]$ the variance operator, s the set of all IQ-beamformed frames, and s_n a single image frame with index n.

2.4 The Reference: Parallel Beamforming

To estimate how well SAI performs, a reference is needed for comparison. The first real-time 3-D scanning system, made by Smith, von Ramm and colleagues at Duke in the 1980s, used Explososcan as its beamforming technique. Explososcan is a parallel beamforming technique using less resources. Parallel beamforming is illustrated in Fig. 2.4 on the next page. Instead of using one beamformer per receive line, only a single beamformer is used. The delays for the other receive lines are approximated using the delays calculated by the full beamformer. Extensive patent lawsuits in the 1980s showed that all the major ultrasound companies were using Explososcan in their 3-D scanners. Because of the increase in available computational power, using a full beamformer for each receive line is today not an issue. The modern version of Explososcan, parallel beamforming, was chosen as a reference for comparison of image quality.

For 3-D imaging, parallel beamforming makes $N \times N$ receive lines per emission. From trial and error, $N = 4$ scan lines per dimension were determined as an adequate spatial sampling frequency to represent the PSF at the focal point.

As determined earlier, the maximum f_{prf} allows for 16 emissions per steering angle, leading to $16 \times 4 = 64$ scan lines to be beamformed per steering angle per emission. The

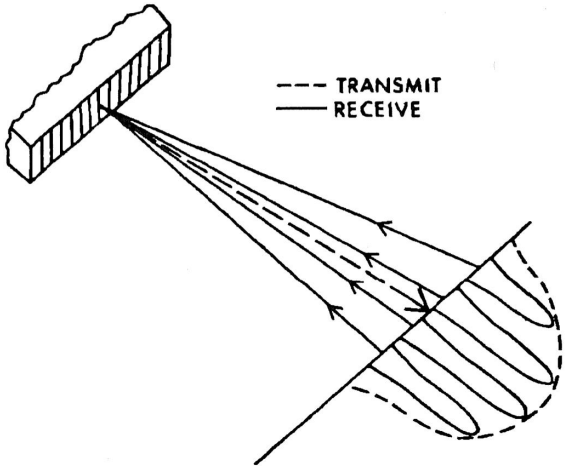

Figure 2.4: Parallel Beamforming illustration. Multiple receive lines are beamformed within the area insonified by the transmit beam. The figure is from the paper (Smith et al. 1991).

transmit beam should therefore be four times as wide as the receive beams. In paper C, the aperture width that results in a beamwidth of approximately $90°/16 = 5.63°$ was determined to 5.22 mm or approximately 17 transducer elements on the Vermon probe. A circular aperture with a diameter of 17 elements contains approximately 226 elements, however 256 active channels are available for the scanner in both transmit and receive. If the diameter of the circular aperture is increased to 18 elements, it contains approximately 256 elements. The circular aperture with 256 active elements is shown in Fig. 2.5(a). Since the transducer array is made of four stacked piezo crystals, the array contains three joints where no elements are present.

It has been shown (Karaman, Wygant, et al. 2009; Smith et al. 1991) that when the number of active channels is restricted and a wide aperture is needed, the simple sparse cross array results in one of the best ratios between detail resolution and the number of active elements used. Three possible transmit cross array apertures of differing widths are shown in Fig. 2.5(b)-(d). Since all shown transmit apertures in Fig. 2.5 are wider than 17 elements, their transmit beam width will be too narrow. To compensate for this, the effective width of the apertures is reduced by applying an apodization function. The apodization functions are in paper C optimized to have equal main-lobe size. The radiation pattern at the focal point and in the far field can be approximated by the Fourier transform of the active aperture (Steinberg 1976, p.12), (Hoctor and Kassam 1990). The 1-D Fourier transform of the center row of each transmit array is plotted in Fig. 2.5(e). The Fourier transform of a 17 element wide rectangular array is plotted as a reference. The main-lobes of the four transmit apertures are seen to be practically identical. The

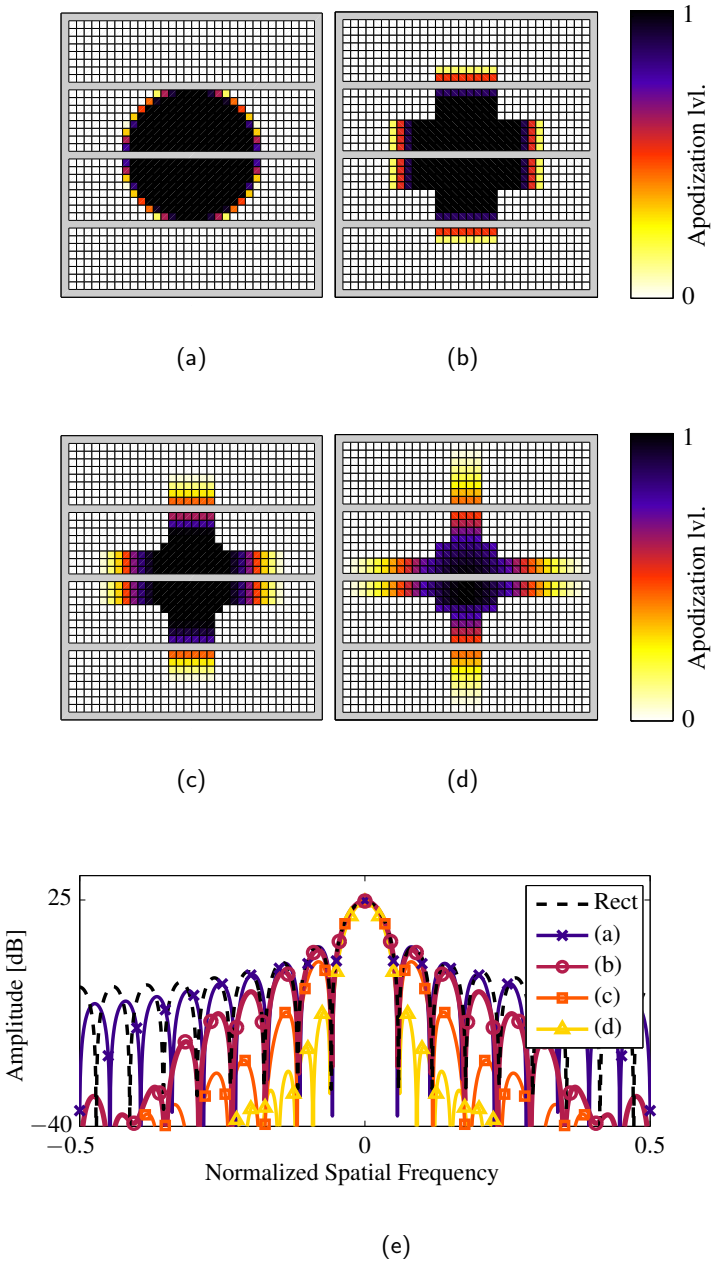

Figure 2.5: In (a)-(d), four different transmit apertures with 256 active elements and approximately the same main-lobe width are shown. In (e) the 1-D Fourier transform of each of the four transmit apertures are shown. The transmit aperture shown in (b) is chosen as the compromise between emitted energy and low side-lobe levels. The transmit aperture is used for all 256 emissions it takes to sample the volume. The figure is from paper C.

side-lobes are seen to decrease faster for the wider apertures, e.g., aperture (c) and (d), compared with the narrower apertures, e.g., aperture (a) and (b). On the other hand, the wider the aperture and the more the aperture is apodized, the less energy is emitted. As a trade-off between emitted energy and side-lobe performance, the 24 element wide cross array, seen in Fig. 2.5(b), is chosen as the transmit aperture.

To beamform the 4×4 lines per emission, the receive aperture should be almost four times as wide as the transmit aperture. This is not possible on the 32×32 element array. The widest possible array, a cross array along the diagonals, is chosen as receive aperture. Because the receive aperture is still too narrow, it is apodized with a Tukey function with a ψ parameter close to zero. The receive aperture is shown in paper C in Fig. C.3.

The second last parameter to be determined for the parallel beamforming technique is its focal depth. The influence of the focal depth on the imaging quality was investigated via simulations of the PSF using the ultrasound simulation program Field II. The result of parameter study is showed in paper C, it showed a clear optimum at a focal length of 30 mm.

When using parallel beamforming, which lines that were beamformed from the same emission is often visible in the final image. This is seen in Fig. 2.6(a). It is sometimes termed the boxing effect or the parallel beamforming artifact. Different advanced measures have previously been pursued to minimize the parallel beamforming artifact (Augustine 1987; Hergum et al. 2007; Liu et al. 2002). A simple measure to compensate for the boxing effect is to beamform more lines than are needed per emission, and let the outer beamformed lines overlap with the lines beamformed from the neighboring emission beams. In Fig. 2.6 on the facing page, the effect of the simple boxing effect compensation is seen on a C–scan measurement of a tissue mimicking phantom. The C–scans contain the same number of resulting lines in all four sub–figures, but the number of lines overlapping differs. In Fig. 2.6(a), the C–scan is seen without compensation and in Fig. 2.6(b)–2.6(d) the compensation is increased one step at a time. The figure is from paper A, and the setup used is therefore not the same as the setup used for parallel beamforming in this chapter. As the correlation compensation increases, the C–scan gets more blurred and the dynamic range decreases. In paper A, the visually attractive first level of compensation (Fig. 2.6(b)) was used. The method turned out to decrease the CNR performance on cyst measurements, and no compensation was therefore applied in paper C and therefore also not in this chapter.

2.5 Synthetic Aperture Imaging

To avoid grating lobes within the $\pm 45°$ beamformed volume, the pitch of the transducer array should not be larger than $\lambda/2$. The center frequency of the Vermon probe is 3.5 MHz and the pitch is 300 µm, which corresponds to $0.68\,\lambda$. As a compromise between the transducer efficiency in converting electrical to mechanical energy, and grating-lobe levels, the center frequency of the emission is set to 3.0 MHz.

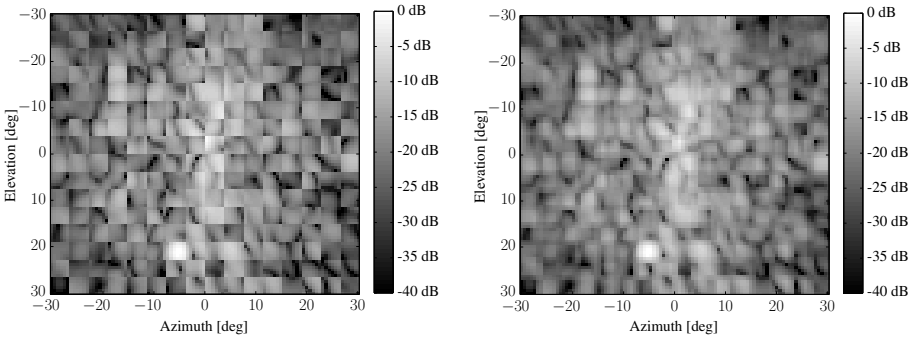

(a) No boxing effect compensation; 6×6 lines beamformed per emission.

(b) 1st level of boxing effect compensation; 8×8 lines beamformed per emission.

(c) 2nd level of boxing effect compensation; 10×10 lines beamformed per emission.

(d) 3rd level of boxing effect compensation; 12×12 lines beamformed per emission.

Figure 2.6: Parallel beamforming boxing effect compensation showed on a C–scan of a tissue mimicking phantom. The figures are from paper A.

When using synthetic transmit focusing, a virtual transmit aperture is synthesized. One virtual element is synthesized in the synthetic aperture for each focal point. Since 256 emissions are used, 256 virtual elements are synthesized. The relations between aperture array design and the PSF also apply to the synthesized aperture array (Frazier and O'Brien 1998). Especially the width of the synthesized array and the pitch of the virtual elements must be considered. The location of the virtual elements also influences the distribution of the emitted energy and thereby the signal-to-noise ratio (SNR) within the imaged volume.

The synthetic aperture can be synthesized in three different ways: by having a static transmit aperture and steering the transmit beam angle for each emission, by translating transmit aperture and not applying beam steering as is seen in Fig. 2.7(a), or by both translating the transmit aperture and applying beam steering as is seen in Fig. 2.7(b).

In Fig. 2.7 on the next page the synthesized array from different transmit beams is shown. The synthesized elements are marked with blue boxes and the maximum width of the synthesized array is with a blue arrow. Only at points where all transmit beams overlap will the width of the synthesized aperture achieve its maximum width. If a static transmit aperture with beam steering is used, the focal distance must be large, either in front or behind the array, for the width of the synthesized aperture to become large enough. This leads to a large f-number, and, thus, a narrow beam. A narrow beam implies only little overlap between the insonified regions of each transmit beam. Thereby, only a small aperture is synthesized for any given point in the imaged volume. Usually, this leads to inferior image quality. If the active aperture is translated and no beam steering is applied, the width of the synthesized array is independent of the transmit f-number. In this case, the synthesized array is narrower than the physical array, as is illustrated by the red arrows in Fig. 2.7. When no beam steering is applied, the energy of all transmit beams are emitted straight down. For phased array imaging, this leads to the SNR being higher in front of the array, compared with the sides of the imaged volume. The third possibility is to both translate the physical array and to apply transmit beam steering. This has the advantage that even when the transmit f-number is kept low, a wide aperture can be synthesized. It is therefore chosen to both translate the active aperture and to apply beam steering of the transmit beam.

To enable the translation of the active aperture, it needs to be small in order to fit on the physical array and still leave room for translation. The active aperture could either be a 16×16 square or a circle with radius of approximately 9 elements. To increase the circular symmetry of the PSF, the circular shape is chosen as the active aperture.

To ensure an even SNR performance within the pyramidal volume, the active aperture is translated on a square with a side length of 16 elements. The centers of all translated transmit apertures are shown as a dot in Fig. 2.8(a). The cross is the center of the shown active aperture. The beam steering is controlled proportionally to the position of the active aperture. That is

$$\phi(x) = \kappa_x x \tag{2.8a}$$

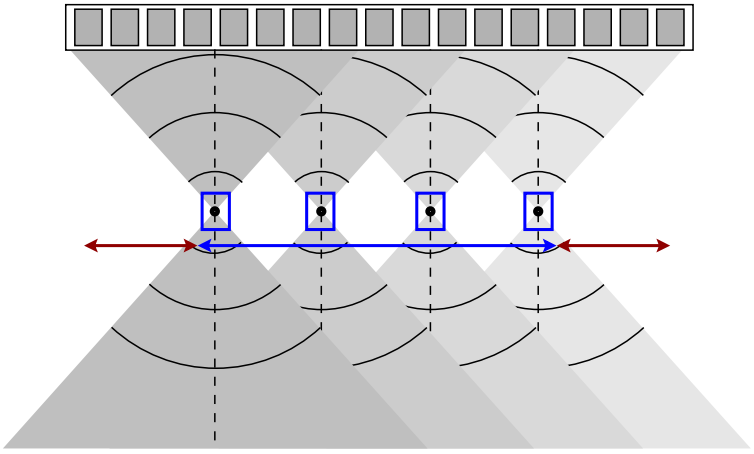

(a) Traditional synthetic aperture. The virtual source is centered on each sub–aperture.

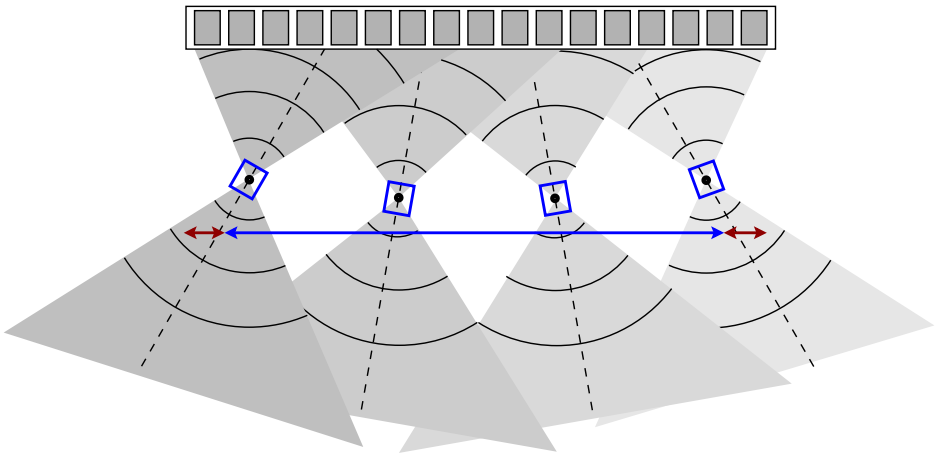

(b) Synthetic aperture with beam steering. The virtual source is tilted to the sides when the active aperture is translated.

Figure 2.7: The synthetic aperture virtual element setup. The gray array in the top is the physical aperture, the thick dots the focal points, and the blue boxes the virtual elements in the synthesized aperture. Four emissions are shown, each with eight active elements. The blue arrow indicates the synthesized aperture size and the gray cones the acceptance angle of each virtual element.. The figures are from the presentation of Paper A given at SPIE Medical Imaging 2012.

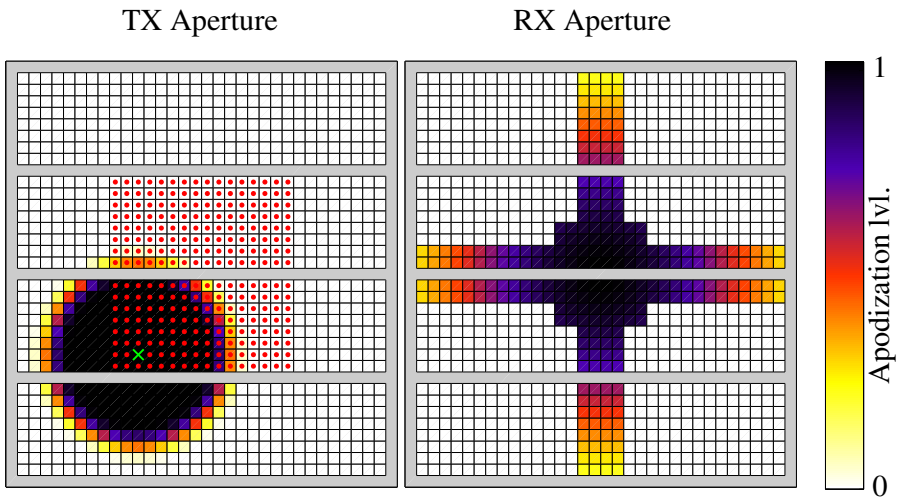

Figure 2.8: The synthetic aperture imaging transmit and receive apertures as implemented on the 32×32 element transducer array. The transmit aperture translates between each emission. The center of the current aperture is illustrated with a cross and the centers of the 255 remaining emissions are shown with a dot. The receive aperture is static during all 256 emissions. The figures are from paper C.

$$\theta(y) = \kappa_y y \,, \tag{2.8b}$$

where ϕ is the angle in the z-x plane, θ the angle in the z-y plane, x and y the (x,y) coordinate of the center of the active aperture, and κ_x and κ_y are scaling constants. κ_x and κ_y then set the maximum transmit beam angle.

The resulting synthesized aperture is shown in Fig. 2.9. The transmit beam for the shown emission is illustrated with an arrow. The source of the beam is the active virtual source, shown with a circle. For each emission, a low resolution volume is beamformed. Each point in the low resolution volume is then weighted by a virtual source apodization. The virtual source apodization has the shape of a cone centered around the transmit beam and with its apex located at the active virtual source, as is illustrated with gray in Fig. 2.7. The angular width of the cone depends on the focal distance of the active transducer array. The closer the virtual source is to the transducer surface, the wider is the cone. In this work, the cone angular width is 50°. The beamformed points located outside of the cone is weighted by 0. The points inside of the cone is weighted by a Hann window, centered

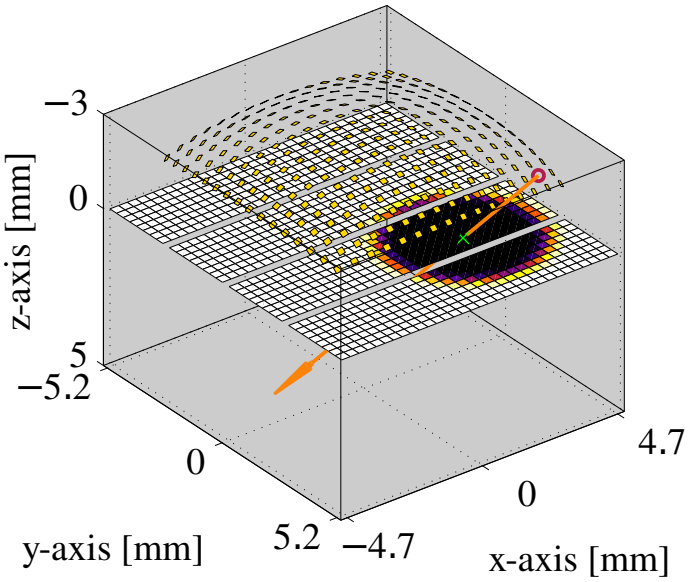

Figure 2.9: The setup for a single emission is shown, which synthesizes one virtual element (shown as a circle) in the synthetic aperture. The remaining virtual elements of the sequence are shown as squares raised above the physical aperture. The virtual sources are located behind the aperture and the sound is emitted downwards, in the direction of the arrow. The cross marks the center of the active aperture and the colors of the physical elements represent their apodization value.

on the transmit beam. The weight of a point within the cone then depends on its angular distance to the transmit beam. This procedure removes beamformed points which were not insonified by the transmit beam. After the points are weighted, the low resolution volumes are summed to create one high resolution volume.

2.6 Results

In this section, the results of the comparison between synthetic aperture imaging and parallel beamforming are presented. All results originate from paper C. The measurements were carried out using the 1024 channel experimental ultrasound scanner SARUS, which is seen in Fig. 2.10 on the following page. The 2-D probe used in both simulations and in the measurements is seen in Fig. 2.11.

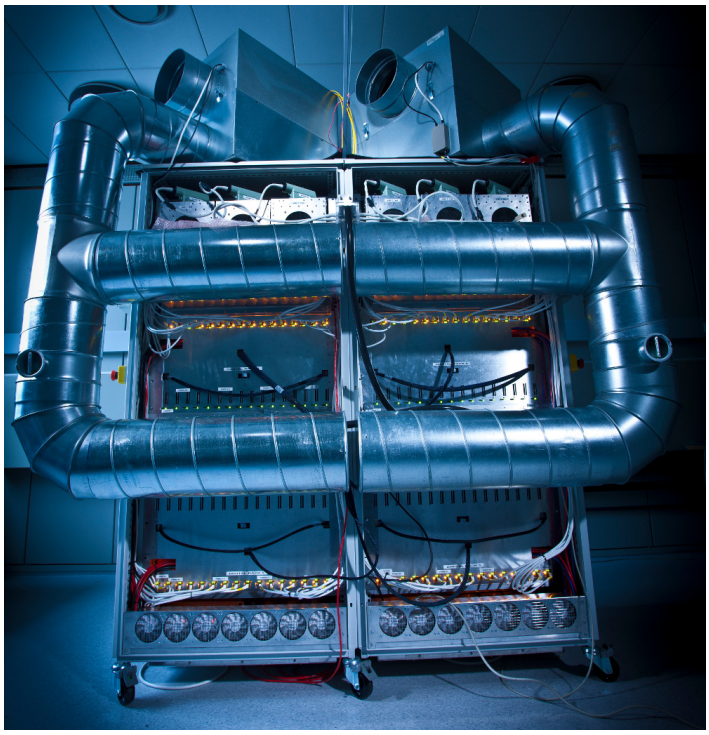

Figure 2.10: SARUS, the 1024 channel experimental ultrasound scanner used for the measurements. This image is from external paper II.

Figure 2.11: The 32×32 element phased array ultrasound probe used for the measurements and modeled in the simulations. The image is from paper C.

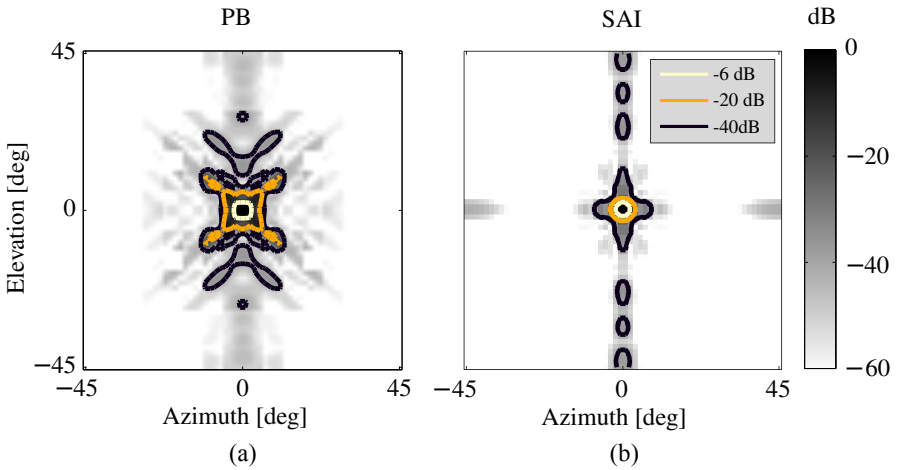

Figure 2.12: Simulated C-scans of the 3-D PSFs of parallel beamforming and synthetic aperture imaging at a depth of 60 mm. The dynamic range of the gray scale is 60 dB. The main-lobe width is seen to be similar for the two techniques. The side-lobes, especially at −20 dB, are lower for synthetic aperture imaging. The −20 dB isocurve in (a) is seen to have four distinct corners. The figures are from paper C.

2.6.1 The Simulated Point Spread Function

In Fig. 2.12, the PSF C-scan of both parallel beamforming and synthetic aperture imaging at a depth of 60 mm are shown with dynamic range of 60 dB. The main-lobes of the two techniques are seen to be similar in both the elevation and azimuth directions. The side-lobe levels are clearly lower for synthetic aperture imaging than for parallel beamforming. The side-lobes are seen to be asymmetrical, as they are wider in the elevation direction than in the azimuth direction. The asymmetric PSF is due to the asymmetry of the transducer array used. The discontinuities in the probe cause the increased side-lobe levels in the elevation direction. Grating-lobes are visible in the azimuth direction of the synthetic aperture imaging PSF. This is probably due to the pitch of both the physical and synthesized arrays being larger than $\lambda/2$. In the elevation direction it is hard to separate the side-lobes from grating-lobes.

2.6.2 Line Spread Function

The line spread function (LSF) is measured using a wire phantom. The wire runs parallel to the transducer surface at depths of 20, 40, 60, and 80 mm. In Fig. 2.13, 2-D B-modes perpendicular to the wire at 40 mm and 80 mm of depth are shown. The B-mode images are sliced perpendicular to the wire direction. They have a dynamic range of 60 dB over which isocurves at –40 dB, –20 dB, and –6 dB are marked. The images in Fig. 2.13(a) and

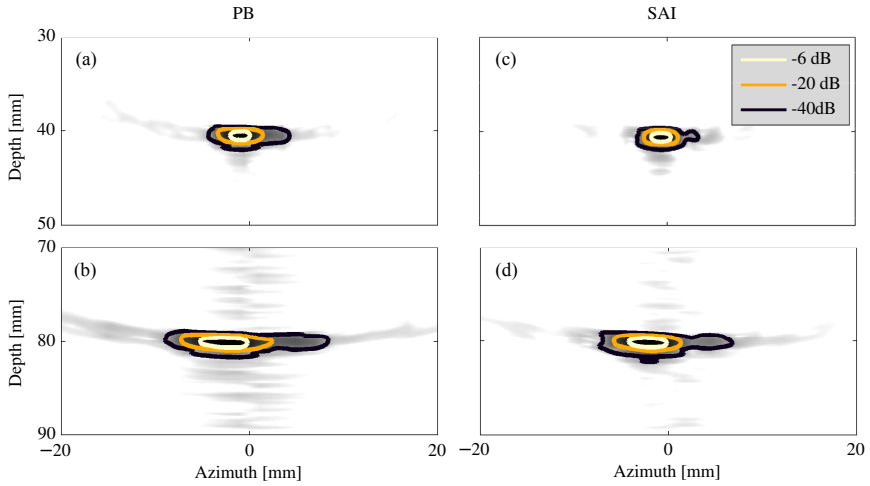

Figure 2.13: The measured 3-D line spread function of Parallel beamforming (a and b) and synthetic aperture imaging (c and d) sliced in a 2-D plane. The wire runs parallel to the transducer surface at depths of 40 mm and 80 mm. The 2-D gray level images have a dynamic range of 60 dB. The side-lobes of parallel beamforming are seen to be clearly larger than the side-lobes of synthetic aperture imaging.

2.13(b) are made with parallel beamforming and in Fig. 2.13(c) and 2.13(d) with synthetic aperture imaging. The wire is placed a little off-center which results in slightly asymmetric LSFs. Comparing the LSFs of synthetic aperture imaging and parallel beamforming, the −6 dB contour widths differ 0.4 mm (16 %) at 40 mm of depth and 1.0 mm (20 %) at 80 mm, in favor of synthetic aperture imaging. The side-lobe levels are clearly lower for synthetic aperture imaging than for parallel beamforming, both at −20 dB and at −40 dB.

The received energy at the ultrasound probe surface is lower for deeper wire placements in the water tank. This results in a relative increase in the noise floor originating from electronic noise within the experimental ultrasound scanner. The noise floor is seen to be higher for parallel beamforming in Fig. 2.13(b) than for synthetic aperture imaging in Fig 2.13(d). The noise appears at the center of the B-mode image, because the noise is in phase in the raw data on all receive channels and only sums up coherently during the delay-and-sum beamforming of points close to the center line pointing straight down. Even though the noise is almost in-phase on all channels, it is not static and therefore changes from emission to emission. Parallel beamforming does not sum any beamformed lines and the noise is therefore only sampled once. Synthetic aperture imaging is coherently adding the beamformed signal, which there for increases in amplitude faster than the incoherently summed noise. Synthetic aperture imaging therefore effectively suppressed the noise.

2.6.3 Cysts Embedded in Tissue Mimicking Phantom

In Fig. 2.14, a 2-D slices of the cyst phantom is shown. Fig. 2.14(a) and (c) are made with parallel beamforming and Fig. 2.14(b) and (d) with synthetic aperture imaging. The cysts are clearly more apparent when imaged with synthetic aperture imaging than with parallel beamforming. The cyst statistics are measured from a sphere with a radius of 6 mm located at the center of each cyst. The speckle statistics are estimated on the exact same spheres but on the tissue mimicking phantom containing only random scatterers. The CNR was better for synthetic aperture imaging at all depths compared with parallel beamforming. When ignoring the first cyst, the CNR for both synthetic aperture imaging and parallel beamforming cysts decreased approximately linearly. The CNR of parallel beamforming decreases faster than the CNR for synthetic aperture imaging.

The estimated SNR is calculated from stochastic data and a limited amount of data is available due to the depth dependent SNR. Therefore averaging has to be employed to reduce the variance of the estimates. The noisy estimates are low-pass filtered with a 3-D FIR filter. The SNR of synthetic aperture imaging is higher than the SNR of parallel beamforming. The penetration depth, where the SNR crosses 0 dB, is by linear regression estimated to be 88 mm for parallel beamforming and 109 mm for synthetic aperture imaging. In other words, synthetic aperture imaging increases the penetration depth by approximately 24 % with the same amount of energy emitted.

2.7 Summary of Papers

Paper A: Preliminary Comparison of 3D Synthetic Aperture Imaging with Explososcan

This is the first conference paper that compares synthetic aperture imaging to parallel beamforming. The paper is based on Field II simulations. The implementation of the two beamformer techniques were allowed to used the full 2-D array and all 1024 channels. The PB implementation used 1024 channels and the SAI implementation used 256 channels. Both techniques used 289 emissions and beamformed lines within $\pm 30°$. The comparison found the image quality of SAI to be best at all depths except at the focal depth of PB. The comparison was made at the center of the volume.

Paper B: Comparison of 3D Synthetic Aperture Imaging and Explososcan using Phantom Measurements

This is the second conference paper that compares synthetic aperture imaging to parallel beamforming. In this paper, the two beamformer techniques were channel limited to 316 channels and could use 256 emissions. The paper was based on wire phantom measurements. This comparison was also made at the center of the beamformed volume. With the channel limited setup, the imaging quality of SAI was better than PB at all locations within the beamformed volume.

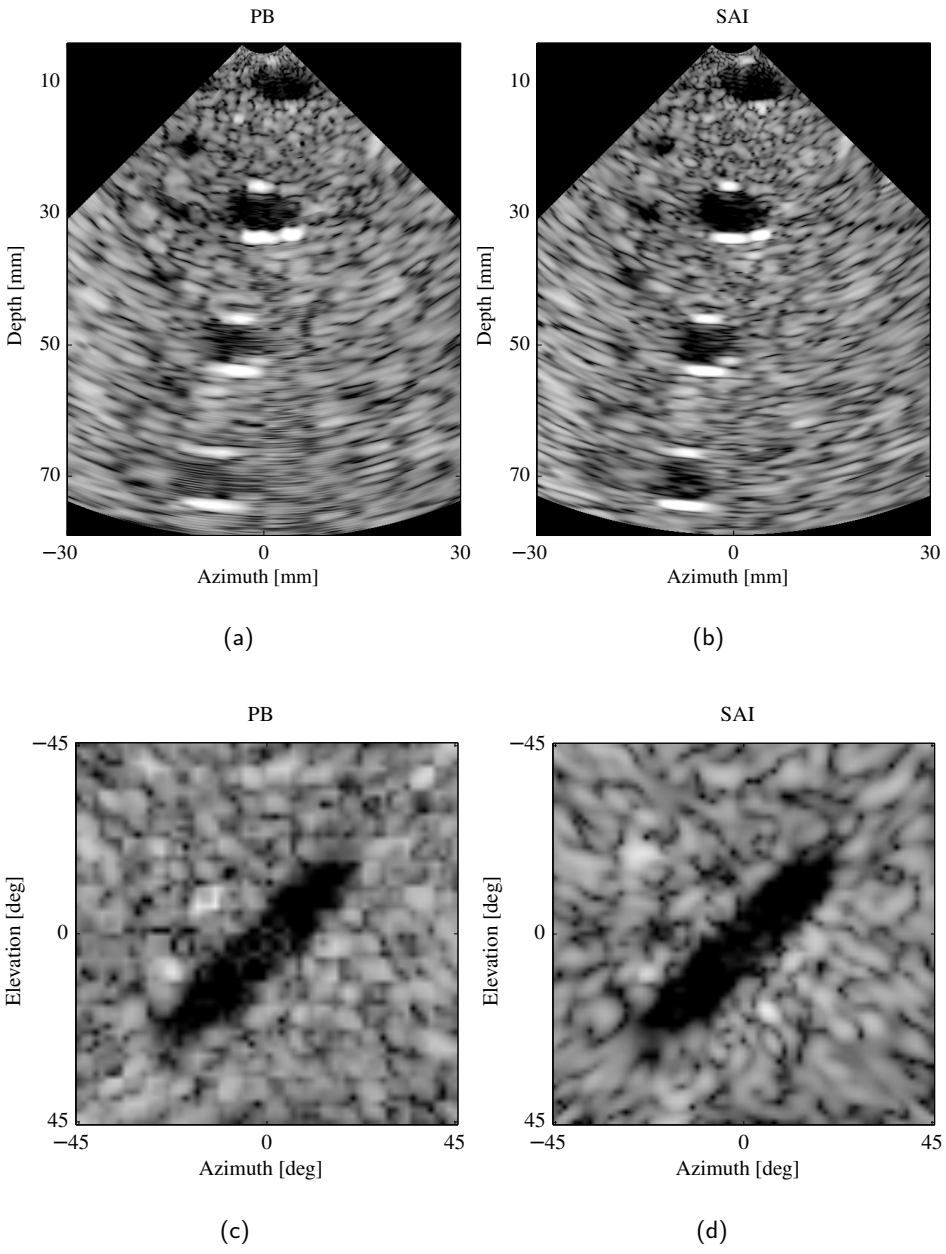

Figure 2.14: Parallel beamforming (a and c) and synthetic aperture imaging (b and d) of anechoic cysts embedded in a tissue-mimicking phantom. The dynamic range is 40 dB. The large cysts have a diameter of 8 mm and the small cysts 4 mm. (a) and (b) are vertical scan planes and (c) and (d) are C-scans with a constant distance to the array center. The cysts are water-filled pipes aligned 45° to the vertical scan plane.

Paper C: Comparison of 3-D Synthetic Aperture Phased Array Ultrasound Imaging and Parallel Beamforming

This Journal paper summarizes and expands on the work done in the two previous papers. This comparison is also based on a channel limited setup. 256 active channels and 256 emissions are allowed by the two techniques. The signal-to-noise ratio was by optimizations greatly improved compared to the previous measurement paper, paper B. The greater SNR enabled measurements of a cyst phantom and a speckle phantom. The imaging quality is this time investigated both as a function of depth and angle. SAI performs in all metrics better than PB at all positions investigated.

2.8 Discussion and Conclusions

Two conference papers and one journal paper was published on the subject of 3-D synthetic aperture imaging.

The setup and most of the results from the journal paper, Paper C, was described in this chapter. A comparison of real-time 3-D synthetic aperture imaging and parallel beamforming using only 256 active channels was presented. The comparison was based on both Field II simulations and measurements with the experimental ultrasound scanner SARUS.

From measurement, the imaging quality was investigated by use of wire and cyst phantoms. The wire phantom measurements were carried out at a low steering angle and showed the same tendency as the simulations. Synthetic aperture imaging increased both the resolution and the contrast. The FWHM was improved by 20 % at 80 mm depth. The cyst phantom measurement confirmed that synthetic aperture imaging increases the contrast at all depths, compared with parallel beamforming. The CNR was improved by 22 % at 70 mm depth. Measurements on a tissue mimicking phantom indicated that the penetration depth is deeper for synthetic aperture imaging compared with parallel beamforming. Synthetic aperture had a higher SNR than parallel beamforming at all depths and the increased SNR resulted in a penetration depth increase of 24 %. The penetration depth did not reach the design goal of 15 cm. This was likely due to the small transducer array surface area, limited by the restriction of 256 active channels. It is most likely that the low SNR of the experimental scanner used also limited the penetration depth.

References

Augustine, L. J. (1987). *High resolution multiline ultrasonic beamformer*. U.S. Patent 4,644,795 (cit. on p. 16).

Bae, M. H. and M. K. Jeong (2000). “A study of synthetic-aperture imaging with virtual source elements in B-mode ultrasound imaging systems”. In: *IEEE Trans. Ultrason., Ferroelec., Freq. Contr.* Vol. 47, pp. 1510–1519 (cit. on pp. 8, 9).

Bennett, S., D. K. Peterson, D. Corl, and G. S. Kino (1982). "A real-time synthetic aperture digital acoustic imaging system". In: *Acoust. Imaging*. Ed. by P. Alais and A. F. Metherell. Vol. 10, pp. 669–692 (cit. on p. 7).

Burckhardt, C. B., P.-A. Grandchamp, and H. Hoffmann (1974). "An Experimental 2 MHz Synthetic Aperture Sonar System Intended for Medical Use". In: *IEEE Trans. Son. Ultrason.* 21.1, pp. 1–6 (cit. on p. 7).

Flaherty, J. J., K. R. Erikson, and V. M. Lund (1967). *Synthetic Aperture Ultrasound Imaging Systems*. United States Patent, US 3,548,642. United States Patent, US 3,548,642, 1967, Published 22 Dec 1970 (cit. on p. 8).

Frazier, C. H. and W. D. O'Brien (1998). "Synthetic aperture techniques with a virtual source element". In: *IEEE Trans. Ultrason., Ferroelec., Freq. Contr.* 45, pp. 196–207 (cit. on pp. 8, 18).

Hergum, T., T. Bjåstad, K. Kristoffersen, and H. Torp (2007). "Parallel Beamforming Using Synthetic Transmit Beams". In: *IEEE Trans. Ultrason., Ferroelec., Freq. Contr.* 54.2, pp. 271–280 (cit. on p. 16).

Hoctor, R. T. and S. A. Kassam (1990). "The unifying role of the coarray in aperture synthesis for coherent and incoherent imaging". In: *IEEE Proc.* Vol. 78, pp. 735–752 (cit. on p. 14).

Johnson, J., M. Karaman, and B. Khuri-Yakub (2005). "Coherent-array imaging using phased subarrays. Part I: basic principles". In: *IEEE Trans. Ultrason., Ferroelec., Freq. Contr.* 52.1, pp. 37–50. DOI: 10.1109/TUFFC.2005.1397349 (cit. on p. 9).

Johnson, J., O. Oralkan, S. Ergun, U. Demirci, M. Karaman, and B. Khuri-Yakub (2005). "Coherent array imaging using phased subarrays. Part II: simulations and experimental results". In: *IEEE Trans. Ultrason., Ferroelec., Freq. Contr.* 52.1, pp. 51–64. DOI: 10.1109/TUFFC.2005.1397350 (cit. on p. 9).

Karaman, M., P. C. Li, and M. O'Donnell (1995). "Synthetic aperture imaging for small scale systems". In: *IEEE Trans. Ultrason., Ferroelec., Freq. Contr.* 42, pp. 429–442 (cit. on pp. 8, 9).

Karaman, M., I. O. Wygant, O. Oralkan, and B. T. Khuri-Yakub (2009). "Minimally Redundant 2-D Array Designs for 3-D Medical Ultrasound Imaging". In: *IEEE Trans. Med. Imag.* 7, pp. 1051–1061 (cit. on p. 14).

Kim, J.-J. and T.-K. Song (2008). "Real-Time 3D Imaging Methods using 2D Phased Arrays Based on Synthetic Focusing Techniques". In: *Ultrasonic Imaging* 30.3, pp. 169–188 (cit. on p. 10).

Kino, G. S., D. Corl, S. Bennett, and K. Peterson (1980). "Real Time Synthetic Aperture Imaging System". In: *Proc. IEEE Ultrason. Symp.* Pp. 722–731 (cit. on p. 7).

Liu, D.-L. D., J. C. Lazenby, Z. Banjanin, and B. A. McDermott (2002). *System and method for reduction of parallel beamforming artifacts*. U.S. Patent 6447452 (cit. on p. 16).

Lockwood, G. R., J. R. Talman, and S. S. Brunke (1998). "Real-time 3-D ultrasound imaging using sparse synthetic aperture beamforming". In: *IEEE Trans. Ultrason., Ferroelec., Freq. Contr.* 45, pp. 980–988 (cit. on p. 9).

Nikolov, S. I. and J. A. Jensen (2000). “3D synthetic aperture imaging using a virtual source element in the elevation plane”. In: *Proc. IEEE Ultrason. Symp.* Vol. 2, pp. 1743–1747 (cit. on p. 9).

— (2002). “Virtual ultrasound sources in high-resolution ultrasound imaging”. In: *Proc. SPIE - Progress in biomedical optics and imaging*. Vol. 3, pp. 395–405 (cit. on pp. 8, 9).

Pedersen, M. H., K. L. Gammelmark, and J. A. Jensen (2004). “Preliminary in-vivo evaluation of convex array synthetic aperture imaging”. In: *Proc. SPIE - Progress in biomedical optics and imaging*, pp. 33–43 (cit. on p. 8).

Peterson, D. K. and G. S. Kino (1984). “Real-Time Digital Image Reconstruction: A Description of Imaging Hardware and an Analysis of Quantization Errors”. In: *IEEE Trans. Son. Ultrason.* 31, pp. 337–351 (cit. on p. 7).

Ranganathan, K. and W. F. Walker (2007). “Cystic Resolution: A Performance Metric for Ultrasound Imaging Systems”. In: *IEEE Trans. Ultrason., Ferroelec., Freq. Contr.* 54.4, pp. 782–792 (cit. on p. 11).

Sherwin, C. W., J. P. Ruina, and D. Rawcliffe (1962). “Some early developements in synthetic aperture radar systems”. In: *IRE Trans. Mil. Elect.* MIL-6.2, pp. 111–115 (cit. on p. 7).

Smith, S. W., H. G. Pavy, and O. T. von Ramm (1991). “High speed ultrasound volumetric imaging system – Part I: Transducer design and beam steering”. In: *IEEE Trans. Ultrason., Ferroelec., Freq. Contr.* 38, pp. 100–108 (cit. on p. 14).

Steinberg, B. D. (1976). *Principles of aperture and array system design*. New York: John Wiley & Sons (cit. on p. 14).

Vilkomerson, D., J. Greenleaf, and V. Dutt (1995). “Towards a Resolution Metric for Medical Ultrasound Imaging”. In: *Proc. IEEE Ultrason. Symp.* Pp. 1405–1410 (cit. on p. 11).

Ylitalo, J. T. (1995). “Synthetic aperture ultrasound imaging using a convex array”. In: *Proc. IEEE Ultrason. Symp.* Pp. 1337–1340 (cit. on p. 8).

Ylitalo, J. T. and H. Ermert (1994). “Ultrasound synthetic aperture imaging: Monostatic approach”. In: *IEEE Trans. Ultrason., Ferroelec., Freq. Contr.* 41, pp. 333–339 (cit. on p. 7).

CHAPTER 3

Row-Column Addressed Arrays

The previous chapter investigated the achievable imaging quality of two imaging techniques using a 32×32 element 2-D matrix transducer. The transducer array had 1024 channels and still neither the imaging quality nor the penetration depth achieved was on par with that typically achieved by commercial 2-D imaging systems. The limitation lies in the small aperture side-length of the 2-D array compared to that of a typical 1-D transducer array. The equation

$$\text{FWHM} = \lambda f_{\#} = \frac{\lambda d}{w} , \tag{3.1}$$

from Fraunhofer diffraction theory, shows that the upper limit of achievable imaging quality scales linear with the f-number which is the focal length divided by the aperture diameter. To increase the imaging quality of the 2-D transducer array, either the frequency, the aperture diameter, or both, therefore has to be increased. Increasing the frequency has the disadvantage of decreasing the penetration depth. Increasing the aperture width would increase both the imaging quality and the transducer surface area, which could be used to increase the penetration depth. The disadvantage of increasing the side length is a dramatic increase in the number of transducer elements in the array. Often 1-D arrays feature 128 or more transducer elements. A 2-D array with 128×128 elements would contain 16 384 transducer elements. It is a tremendous challenge to make a connection to this amount of transducer elements, let alone to process this amount of information.

One method to reduce the number transducer elements, but not the aperture side-length, is to use sparse or thinned arrays (Austeng and Holm 2002; Brunke and Lockwood 1997; Davidsen et al. 1994; Karaman et al. 2009; Yen, Steinberg, et al. 2000). One of the drawbacks of sparse arrays is the lower emitted energy from the reduced number of elements. This leads to a lower SNR in the recorded ultrasound image. The sparse arrays also have higher side-lobes and can introduce grating lobes in the field.

A different approach is to integrate microbeamformers into the ultrasound probe. This way, both the aperture width is kept high, the transducer array is dense, and the number of connections out of the ultrasound probe is kept low (Blaak et al. 2009; Halvorsrod et al. 2005; Savord and Solomon 2003). The disadvantage is the need for expensive specialized electronics that are hard to integrate with the very large transducer array. The integrated electronics may also require water cooling to remove the excessive heat.

A low cost alternative to microbeamformers that maintain the aperture width and surface area is to row-column address the 2-D array. In a row-column addressed array,

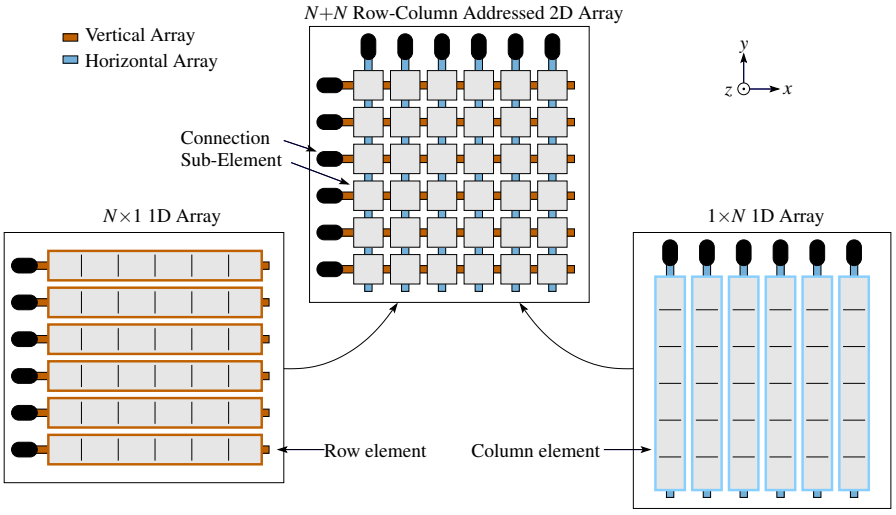

Figure 3.1: A row-column addressed 2-D array can be interpreted as two orthogonal 1D arrays: One array consisting of row-elements and one array consisting of column elements. The Figure is from paper D.

the elements are accessed by their row index in transmit and by their column index in receive, or vice versa. This is illustrated in Figure 3.1. Thus, instead of addressing a single element, an entire row or column of elements is addressed. This effectively reduces the number of elements on a $N \times N$ 2-D transducer array from N^2 to $2N$. This reduces the interconnection cost and removes the need to integrate beamformers into the probe.

The new line elements, shown in the bottom left and bottom right array in Figure 3.1, are referred to as row and column elements. The individual physical elements, making up the row and column elements, are referred to as sub-elements or physical elements. Focusing in the lateral direction is then performed with the 1-D receive array, and focusing in the elevation direction is performed with the 1-D transmit array.

A naive comparison of row-column addressing is made with the fully addressed 2-D array and the sparse 2-D cross array. In Figure 3.2(a) a rough estimate of full width at half maximum (FWHM) for each array is plotted. This prediction is only for the main-lobe size and says nothing about the side-lobe levels. The estimate builds on Eq. (3.1) which assumes focusing in both transmit and receive. Since the row-column addressed array only focuses one-way in each dimension, a rough estimate is made that its main-lobe size is 35 % wider than predicted by Eq. (3.1). The row-column addressed array is seen to perform almost as good as the cross array and much better than the fully addressed 2-D array for the same amount of beamformer channels and elements.

In Figure 3.2(b), the active area of the row-column addressed array, the fully addressed

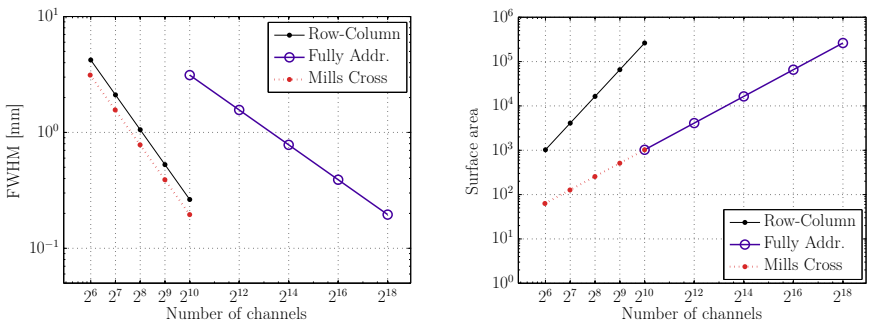

(a) Detail resolution comparison.

(b) Surface area comparison.

Figure 3.2: Comparison of three transducer layouts. The marked points on each line indicate an aperture diameter equivalent to that of a 32×32, 64×64, 128×128, 256×256 or 512×512 element 2-D array, respectively. The row-column addressed array is seen to achieve both a good detail resolution and have a high surface area compared to the sparse cross array and the fully addressed array. The figure is from paper D.

array and the Cross array is plotted with double logarithmic axes. The cross array consists of $2N-1$ elements on a $N \times N$ 2-D array, the fully addressed array of N^2 elements and the row-column addressed array of $2N$ elements. As expected, the surface area per channel is much larger for the row-column array than for the two other arrays. The row-column addressed array is seen to have a more than 10 larger surface area than a cross array for a 32×32 element array. When using 1024 (2^{10}) channels, the surface area of the row-column addressed array is more than 100 times larger than the surface area of the two other arrays. The row-column addressed array connected to a channel-limited imaging system can therefore emit far more energy than the cross array, or any other of the sparse arrays. That the row-column addressed array has both a large surface area and promises to achieve a high resolution per active channel, is what makes it a very interesting candidate for real-time 3-D imaging.

A literature survey of existing publications on the subject of row-column addressed arrays is presented in the next section. In the subsequent sections, the main results from the research on the subject of row-column addressing arrays carried out in this project are presented. The results presented here are also presented in the papers D, E, G, G and patent application A. To minimize repetitions from the papers, the sections are kept short and to the point. The purpose of a patent is not to publish new results or ideas, but instead to be interpreted by patent lawyers. It therefore takes an extra effort for laymen to read and comprehend patents. Section 3.3 includes most of the ideas from the patent

application on how to implement transducer-integrated apodization and is therefore more extensive than the other sections.

3.1 Literature Survey

Several groups have worked on what we refer to as "row-column addressed transducer arrays". The first work that *almost* presented row-column addressing of transducer arrays is (Bates 1995). Bates proposed to use one control line per row and column in the array, thereby reducing the number of control lines to a N×N element array from N^2 to 2N. Using integrated electronics, including two frequency mixers per transducer element, the proposed 3-D imaging system was enabled to achieve two-way focusing in both dimensions.

Row-column addressing of the transducer elements was first introduced as "crossed electrode 2-D array" by Morton and Lockwood (Morton and Lockwood 2003). They reduced not only the number of control lines, but also the number of elements in the array from $N \times N$ elements to $2N$. The reduction in the number of elements in the array comes with the prize of only being able to focus one-way in each dimension. The main advantage compared to the solution proposed by Bates is that no integrated electronics in the probe is necessary. Later Démoré (née Morton) and colleagues published a paper on row-column addressing (Démoré et al. 2009). Here they show that a disadvantage of row-column addressing transducer arrays is the creation of range secondary lobes, also termed ghost echoes. They propose to apply a fixed physical apodization by introducing an attenuating layer with varying thickness over the aperture area. This way the signal amplitude is smoothly reduced towards the ends of the aperture.

Jesse T. Yen's group has also done extensive research on the subject. They termed the name "row-column addressing of 2-D arrays" and started out with a simulation study using synthetic aperture techniques on a rectilinear array (Daher and Yen 2004). In a later paper (Daher and Yen 2006), imaging with a $256+256$ element row-column addressed transducer array is investigated by simulations. The same year the group presented the first experimental verification row-column addressing 2-D arrays, using a $64+64$ element array (Seo and Yen 2006). In the following papers, they presented experimental results of a row-column addressed $256+256$ element piezo transducer (Seo and Yen 2007, 2008, 2009). Yen's group also introduced an alternative approach to row-column addressed arrays, where the piezo crystal of two 1-D arrays are stacked on top of each other and aligned orthogonal to each other. They published four conference papers and a journal paper on this subject (Y. Chen et al. 2010, 2011; Jeong et al. 2007; Yen et al. 2008, 2009). In a recent paper, Yen describes how the imaging quality of row-column addressed arrays can be increased by applying spatially matched filters (Yen 2013).

The group led by Yeow is a third active group within the field of row-column addressing 2-D arrays. The group was the first to produce a row-column addressed CMUT array (Logan, Wong, A. I. H. Chen, et al. 2011; Logan, Wong, and Yeow 2009). In (A. I. H.

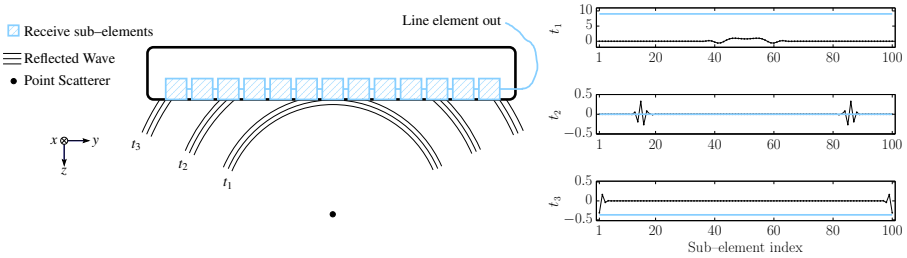

(a) Receiving the reflected wave at the three time instants: t_1, t_2 and t_3.

(b) The measured signal. The response of each sub-element is shown in black and the output of the line element is shown in light blue.

Figure 3.3: Edge effect illustration. The three plots in (b) corresponds to the measured signal in (a) at the three time instants t_1, t_2 and t_3. The amplitudes in (b) are normalized to the maximum of the sub-element signals. The Figure is from paper D.

Chen et al. 2011) they demonstrate real-time measurements with a row-column addressed array and an FPGA based ultrasound imaging system.

Finally, Roger Zemp's group has published on the subject of row-column addressing 2-D CMUT arrays. They use the term top-orthogonal-bottom-electrode (TOBE) for row-column addressing. Using CMUT arrays they show how sending on a single sub-element at a time, instead of an entire row or column of elements, the imaging resolution could be increased (Sampaleanu et al. 2014; Zemp et al. 2011). This enables focusing in two directions in transmit, but comes at the cost of reducing the frame rate and SNR.

3.2 Edge Effects

Despite all the promises of row-column addressing 2-D arrays, such arrays have an inherent drawback: The long elements produce prominent edge effects leading to ghost echoes in the measured signal. Row column addressed arrays are quite different acoustically from fully addressed arrays. Due to the row-column addressing, each line-element may have a length that is hundreds of times longer than the lengths of the square elements used in a fully addressed array. The long length of the line-elements results in prominent edge effects. This issue was first observed by Démoré et al. (2009) and later described in further detail in paper D and G.

The edge effect is easiest to describe when a reflected wave is received. When an emitted waveform is reflected by a point scatterer, the reflected wave will take the shape of a sphere. Just as the reflected spherical wave intersects with the receiving line element, only the first part of the wave interacts with the sub-elements within the line element, corresponding to time t_1 in Figure 3.3(a). The measured signal from the line element is the sum of the sub-element signals. At time t_1, where the signals from the sub-elements are mostly in phase, the line element will output a strong signal as illustrated with a blue line in the top plot of Figure 3.3(b). A short time later, the entire reflected wave intersects with the line element at two locations. This is illustrated as the wave at time t_2. The amplitude of the transmit waveform used in medical ultrasound is usually symmetric around zero and the integration of the waveform is therefore close to zero as illustrated in the center plot in Figure 3.3(b). This situation will prevail until the front of the waveform crosses the edge of the line element at time t_3. At this time, the integrated signal is no longer zero, and the line element therefore has a small output as shown in the bottom plot in Figure 3.3(b). If the scatterer is not located at the center of the array, three responses will be recorded. The pulse-echo spatial impulse response is the convolution of the transmit and receive impulse responses and therefore contains up to nine responses (Jensen 1991).

Paper G contains in Section G.2 a mathematical stringent explanation. The following equation states the proportionality of acoustic pressure for a single line-element aperture at the point $\mathbf{p}$:

$$p(\mathbf{p},t) \propto \begin{cases} v(t) * \frac{\mathrm{d}}{\mathrm{d}t} a_l(l(t)) \ , & \text{if } t \geq t_1 \\ 0 \ , & \text{else} \ , \end{cases} \tag{3.2}$$

where v is the excitation function, a_l is the line-element apodization function, and l is the length coordinate as a function of time. The details and derivation of this equation are given in paper G. This shows that the edge effect originates from discontinuities in the aperture function at the edges of the long element. It also shows that to decrease the edge effect, the first derivative of the aperture function must be minimized.

In Figure 3.4, a row-column addressed array is seen with a scatterer in front of it at the point $\mathbf{p}$. When observing the pressure at point $\mathbf{p}$, the three wavefronts appears to originate from $\mathbf{s}_1$, $\mathbf{s}_2$ and $\mathbf{s}_3$. The receive line-element behaves as if it measures at the three discrete points $\mathbf{r}_1$, $\mathbf{r}_2$ and $\mathbf{r}_3$. That nine echoes are measured from a single scatterer can be tested by a single line-element pulse-echo simulation. Figure 3.5 shows the signals received by a 128+128 element row-column addressed array from a single scatter located at the point $\mathbf{p} = (5,4,3)$ mm, when exciting the center line-element with a two-cycle sinusoidal 5 MHz pulse. As expected, nine echoes are received. Overlaid on the gray level receive echoes are the expected echo arrival time combinations of the three sources and the three receive points of Figure 3.4. The echo arrival time, also termed the time-of-flight (ToF), is calculated as

$$\mathrm{ToF}(\mathbf{p},n,i) = \frac{\|\mathbf{p}-\mathbf{s}_n\| + \|\mathbf{r}_i - \mathbf{p}\|}{c} \ , \tag{3.3}$$

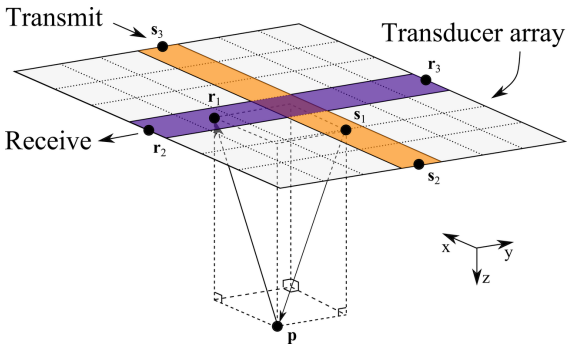

Figure 3.4: Illustration of a pulse-echo simulation setup with one line-element transmitting and one line-element receiving. A scatterer is located at the point $\mathbf{p}$, $\mathbf{s}_1$ is the closest point on the transmit element to $\mathbf{p}$, and $\mathbf{r}_1$ is the closest point on the receive element to $\mathbf{p}$. $\mathbf{s}_2$, $\mathbf{s}_3$ and $\mathbf{r}_2$, $\mathbf{r}_3$ are the edges of the transmit and receive line-elements, respectively. The Figure is from paper G.

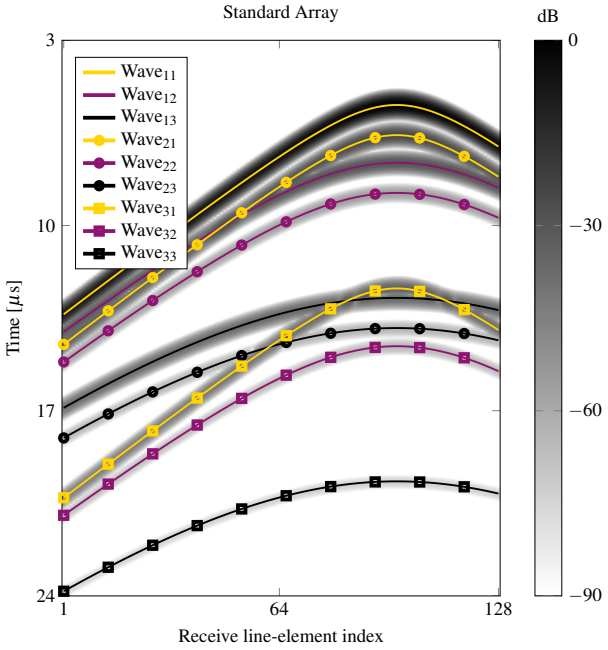

Figure 3.5: Nine echoes are received from a single line-element emission reflected by a scatter located at $(x,y,z) = (5,4,3)$ mm. The gray-scale image is the envelope of the received signals and the overlaid lines are predicted time-of-flights. The Figure is from paper G.

where both n and i are indices between 1 and 3. The wavefronts are named wave_{ni}, where n and i refers to the indexes in Eq. (3.3). It is seen that the arrival time at each receive line-element of all received echoes are perfectly predicted, and the location assumption of the transmitter and receiver of each wavefront, shown in Figure 3.4, must therefore be correct.

It is only the first echo, wave_{11} that can be used for imaging, as the amplitudes of the other ghost echoes are too weak. Even though the ghost echoes cannot be used for imaging, they still degrade the image quality. It is seen from (3.2) that to reduce the edge waves, and thereby the ghost echoes, the derivative of the apodization function must be kept as small as possible. The apodization function of the line elements therefore has to converge to zero when approaching the edges. This cannot be achieved by the usual electronic apodization, since this does not change the line-element apodization value along the length of it. Instead, the apodization must be integrated into the transducer array itself.

3.3 Implementation of Integrated-Apodization

Démoré and colleagues suggested implementing the apodization as a attenuating layer between the transducer array and the medium (Démoré et al. 2009). The following two subsections, the two conceptually different techniques for implementing apodization directly into the line elements are described. The first applies the apodization by varying the active area, while the second uses DC bias voltages to achieve varying output pressures and sensitivities of the individual transducer sub-elements. While the former is applicable to both piezoelectric transducers and capacitive micromachined ultrasonic transducers (CMUTs), the second technique can only be used with CMUT technology.

3.3.1 Area-Controlled Integrated-Apodization

This apodization scheme uses variations in the active area of the individual sub-elements to define the pressure output from a given sub-element.

From Equation (G.1a) and (G.1b) in paper G it is seen that if parts of the active aperture is removed, the output pressure will decrease proportional to the fraction of the aperture that was removed. A different way to state this is, if a transducer element having an area A is actuated by a given excitation, then that element will generate an acoustical wave with a given pressure, p. If the area of the element is multiplied by a factor α, then the transmitted pressure will be αp. The argument can be carried out in receive as well, such that for a given acoustical wave impinged on the element surface, the signal generated by this element will scale with α. Thus, it is clear that the individual elements can be apodized by varying their respective areas.

This technique can be applied to both piezoelectric transducers and CMUTs. In the case of conventionally fabricated piezoelectric transducers, in which the individual elements are diced out, varying the area of each individual element might complicate

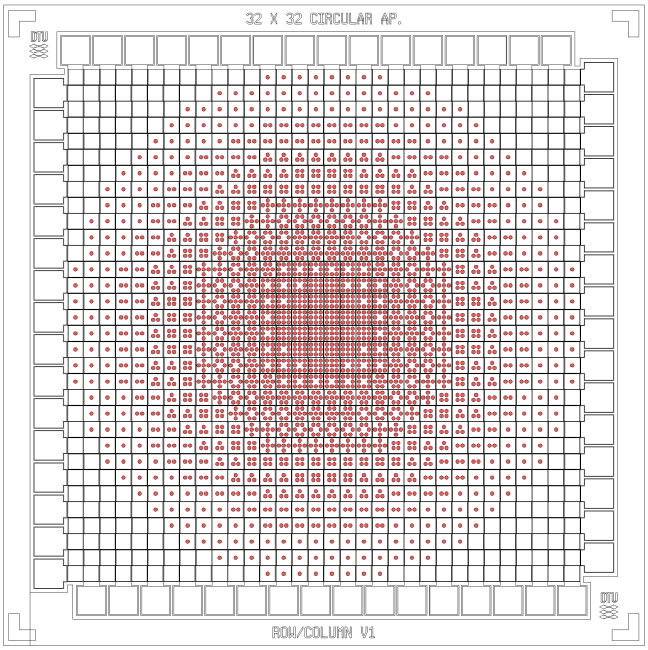

Figure 3.6: Mask layout of a $32+32$ row-column addressed array in which each element has been assigned a given number of CMUT cells (shown in red) ranging from 1 to 9. The apodization is a circular symmetric Hann function.

the fabrication process depending on the apodization layout. Alternatively, piezoelectric transducers can also be manufactured through screen-printing, where the layout of each cell is defined by a mask, making it possible to freely vary the area of each individual element. As the resonance frequency of piezo-elements are given by their height, the area can be freely adjusted without altering the operating frequency of each element.

The same is the case for CMUTs, where the lithographic definition of the elements makes variations of the active area in a given element trivial, since it is only a matter of mask layout. Each sub-element in a CMUT will contain a number of capacitive membranes, from here on referred to as cells, the size of which are determined by the desired fundamental resonant frequency of the transducer. Therefore, the active area of an sub-element is in this case adjusted by varying the number of cells per sub-element. A given transducer element pitch and cell pitch defines the maximum number of cells per sub-element, and the apodization profile must therefore be discretized into a number of levels equal to the maximum number of cells per sub-element. In Figure 3.6, the mask layout of a 2-D row-column addressed CMUT array where a circular symmetric Hann apodization is integrated into the array is seen. Nine cells constitute a single sub-

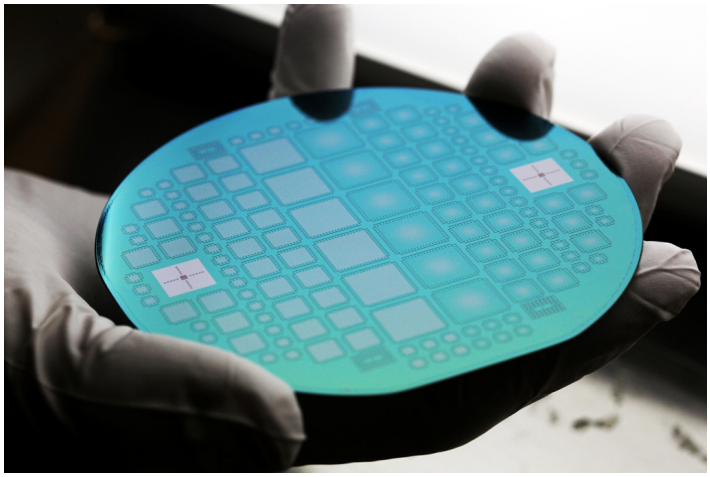

Figure 3.7: A wafer with $6+6$, $16+16$ and $32+32$ conventional (to the left) and fixed-area apodized (to the right) CMUT transducer arrays.

element and nine discrete apodization levels can therefore be used. The final wafer with row-column addressed CMUTs without integrated apodization (left) and with integrated apodization (right) is seen in Figure 3.7. The mask layout and the wafer was produced by Thomas Lehrmann Christiansen using the Danchip clean room facilities at the Technical University of Denmark.

The area-controlled apodization can be implemented in both a fixed and a dynamic version. The principle of varying the active area as described above inherently provides a fixed apodization, and is the simplest way of integrating an apodization. However, dynamic area-controlled apodization is also possible, providing that switches – either purely electrical switches such as MOSFETs or electromechanical switches such as MEMS contact switches – are used. To explain the principle behind this, consider the example of a CMUT transducer with nine cells per sub-element arranged in a 3×3 matrix as illustrated in Figure 3.8. If the row and column electrodes are each divided into three sub-electrodes, and a single switch is placed at the end of each sub-row and sub-column, the number of active cells per sub-element can be reconfigured by enabling or disabling a given number of cells in an sub-element. If the number of enabled switches in row i is denoted k_i and the number of enabled switches in column j is denoted k_j, the area apodization A of sub-element (i, j) is

$$A(i, j) = k_i \times k_j \, . \tag{3.4}$$

Hence, any separable 2-D function can be implemented as an apodization function. Due to this product relationship, the number of switches per row or column for $k \times k$ cells per

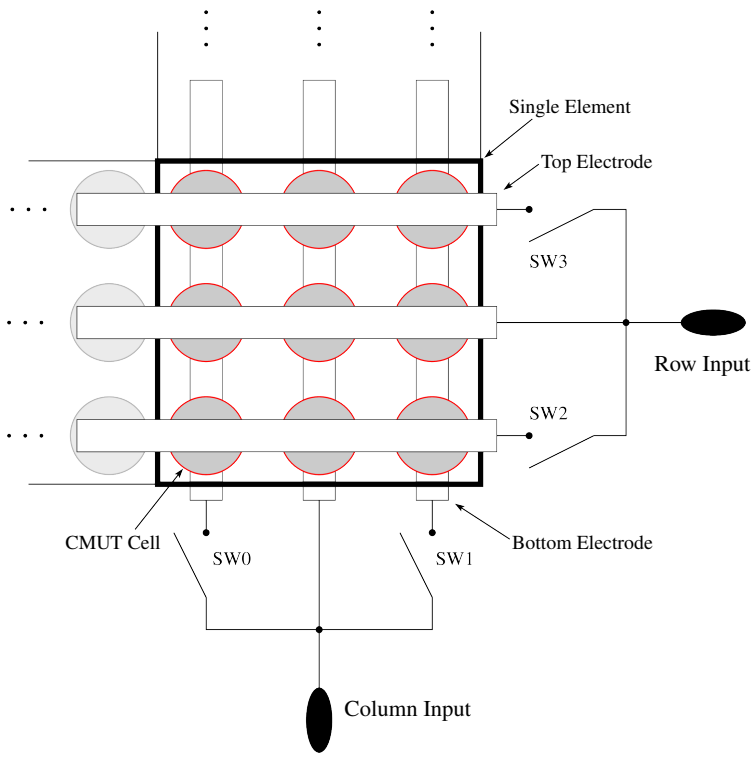

Figure 3.8: Illustration of dynamic area apodization of a single transducer sub-element using switches. In this example, nine CMUT cells are used per transducer sub-element. The sub-element can be apodized in seven levels: {0,1,2,3,4,6,9}, by opening or shortening the four switches.

sub-element can in principle be reduced to $2k-2$, as this – together with the possibility of not reading out the signal from a row or column – allows any number of cells in a given sub-element to be active.

Dynamic area-controlled apodization is directly applicable to existing piezoelectric transducer manufacturing technologies, as the active area of the individual sub-elements can be controlled by external switches. It does require further dicing of the sub-elements, which may limit the yield.

3.3.2 Bias-Controlled Apodization

The previous section described how the active area of a single sub-element can be manipulated to achieve both fixed and dynamic apodization. This section demonstrates how to exploit the operating principle of CMUTs to achieve arbitrary apodizations in two

dimensions, both fixed and dynamic, by using DC bias voltages. Furthermore, it is noted that slowly ramped DC bias voltages can be used as a time gain compensation directly on the transducer.

The operating principle of CMUTs offers a unique way of adjusting both the output power and the sensitivity of the cells in the CMUT sub-element. CMUTs are operated by applying a DC bias voltage in series with an AC voltage to the capacitor plates. The DC voltage serves two purposes: It suppresses the second harmonic of the AC signal and it reduces the effective stiffness of the deformable capacitor plate.

The first purpose is illustrated by considering the energy of a capacitor, which is given by:

$$E = \frac{1}{2} C(w_0) V^2 \,, \tag{3.5}$$

where V is the applied voltage and $C(w_0)$ is the capacitance of the capacitor, which is a function of the center deflection w_0 of the deformable capacitor plate. The force acting on the plate in case of voltage control is therefore (Senturia 2004)

$$F = -\frac{\partial E}{\partial w_0} = -\frac{1}{2} \frac{\partial C(w_0)}{\partial w_0} V^2 \,. \tag{3.6}$$

As the force is seen to scale with the voltage squared, a pure AC voltage will generate a force with the double frequency. By applying a DC bias, the force becomes proportional to $F \propto (V_{AC} + V_{DC})^2 = V_{AC}^2 + V_{DC}^2 + 2V_{AC}V_{DC}$. Thus, if the magnitude of the DC bias voltage is significantly larger than the magnitude of the AC voltage, the V_{AC}^2 term, and hence the double frequency component, becomes negligible.

The second purpose of the DC bias voltage is to lower the effective stiffness of the deformable capacitor plate. As the restoring mechanical force of the plate scales linearly with the center displacement of the plate and the electrostatic force scales with the voltage squared, the magnitude of the electrostatic force relative to the magnitude of the restoring mechanical force will increase with increasing voltage. This trend continues until the voltage reaches a critical value, the pull-in voltage, at which the electrostatic force overpowers the mechanical restoring force, and the deformable plate snaps down to the fixed bottom plate of the capacitor.

If the DC bias voltage is kept below the pull-in voltage, the effect of these two counteracting forces is a more compliant top plate as the DC bias voltage is increased. Thus, for a given AC voltage, the CMUT cell will increase its acoustical output if the DC bias voltage is increased. Equivalently, the electrical signal generated by the CMUT cell for a given acoustical wave will increase with the DC bias voltage. More formally, the electromechanical coupling coefficient of the CMUT describing the conversion between electrical power and mechanical power (and hence acoustical power) can be adjusted through the DC bias voltage. The exact scaling between DC bias voltage and electromechanical coupling coefficient is dependent on the particular geometry of the CMUT cells

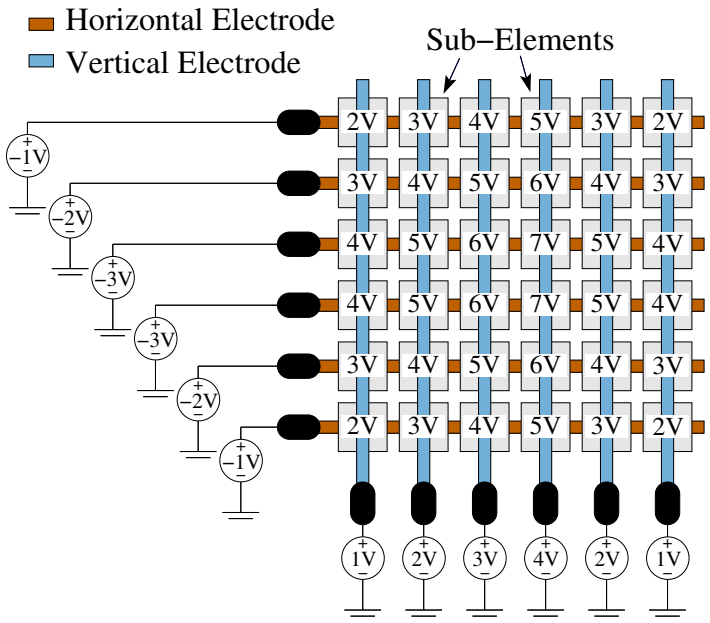

Figure 3.9: Since the oscillation amplitudes of the cells in the CMUT are increased for increasing DC bias voltages, the individual sub-elements can be apodized by assigning them different bias voltages. The figure shows an example of how the bias voltages can be adjusted by applying a given bias profile along the rows and columns. Note that the applied voltages are only illustrative; usually, higher DC bias voltages are used for operating CMUTs.

and their operating frequency, so although the previously described trend is the same for all CMUT geometries, the exact conversion factor between apodization and DC bias voltage is therefore determined by the given transducer.

The above described effect can be used to apodize the individual sub-elements in a CMUT array. In Figure 3.9, this concept is sketched by showing the effect of applying DC bias profiles along the rows and columns, respectively. Notice how the DC voltages generate a map of voltage differences over the sub-elements of the 6×6 array. The DC bias voltage for a given sub-element is the difference between its row and column voltage.

As the apodization of the individual sub-elements in terms of power scaling is a function of only $V_{DC}(i, j)$ for a given operating frequency, DC bias control allows application of any apodization profile over the entire 2-D array that can be described as the sum of two arbitrary discrete 1-D functions. Since the number apodization levels are not limited by the number of cells per sub-element, the DC bias voltage is not restricted to discrete levels.

As with area-controlled apodization, bias-controlled apodization can be implemented

as either a fixed or a dynamic apodization. In the first case, a simple voltage divider circuit can be implemented next to the transducer, providing simple means of implementing the solution. In this way, the apodization profile is fixed, but the apodization levels are continuous. If a dynamic DC bias is wanted, a slightly more complicated electronic circuit has to be designed.

A last note on the possibilities offered by dynamic DC bias voltage control is the potential of integrating part of the time gain compensation directly into the transducer. By ramping up the DC bias voltage during receive, the signals from the transducer are partly time-gain compensated.

3.3.3 Influence of Apodization Discretization Levels

The easiest integrated-apodization to implement is the area-controlled apodization. The area-controlled apodization discretizes the intended continuous apodization function. The result of a PSF-simulation with different apodization quantification levels is seen in Figure 3.10. A $128 + 128$ element row-column addressed array with a center frequency of 3.5 MHz and a pitch equal to $\lambda/2$ is used.

The worst response is clearly when no integrated apodization is applied, which is equivalent to one apodization level. The more apodization levels that are used, the better is the ghost echo attenuated. It is therefore desirable to have as many CMUT cells per sub-element as possible.

A natural question to ask, is how trustworthy the simulations of integrated apodization are? In Paper F it is demonstrated that simulations of the integrated apodization predicts the results from the measurements. The simulations should therefore be accurate.

3.4 A New Apodization Layout

Apodizing both the row and column line-elements with a Hann function in the entire length of the line-elements is very effective at suppressing the ghost echoes (Démoré et al. 2009; Rasmussen and Jensen 2013). A Hann apodized row-column addressed array is shown in Figure 3.11, where the top graph shows the apodization of a single line-element. Since the row and column line-elements are overlapping, so are their apodization functions. At each position on the transducer surface, two apodization functions are overlapping, one from a row element and one from a column element. The effective apodization is the multiplication of the two apodization functions. The vertical line-elements close to the edges are multiplied by values close to zero by the horizontal apodization function. Similarly, the horizontal line-elements at the edges are multiplied by values close to zero by the vertical apodization function. The sensitivity of the edge line-elements are therefore highly limited. The only location where this apodization function allows the row-column addressed array to perform well, is straight down at the center of the array. Even if the array angles the transmit beam to the sides, like a phased array transducer, the echoes returning to the transducer surface will be significantly attenuated.

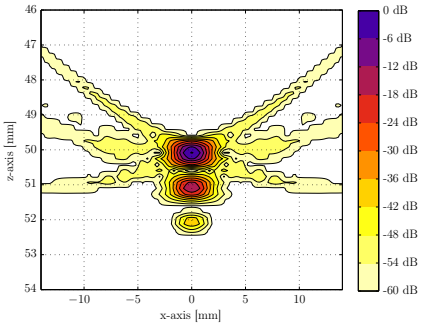

(a) No apodization applied.

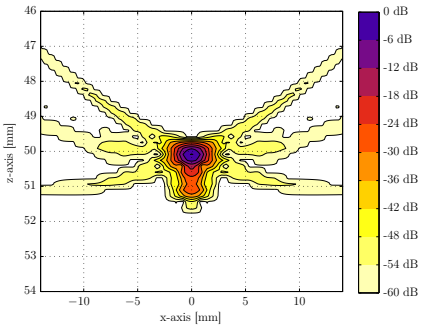

(b) 4 apodization levels.

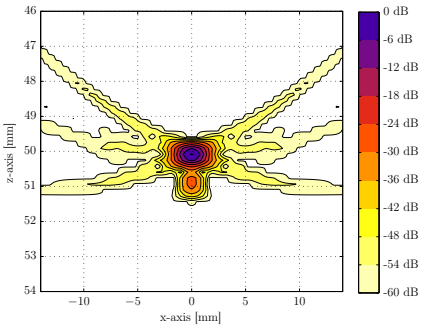

(c) 9 apodization levels.

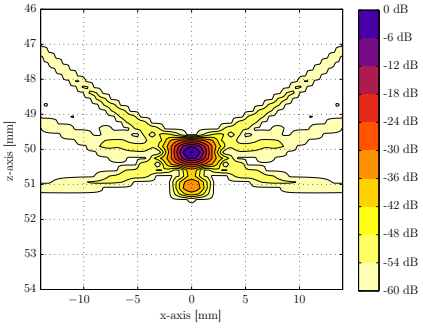

(d) 16 apodization levels.

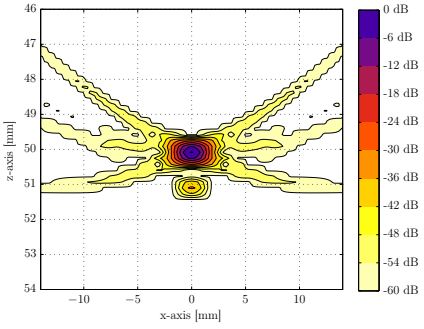

(e) Continuous apodization levels.

Figure 3.10: PSF with five different apodization discretization levels. The apodization function is a circular symmetric Hamming apodization on a 128+128 element transducer array.

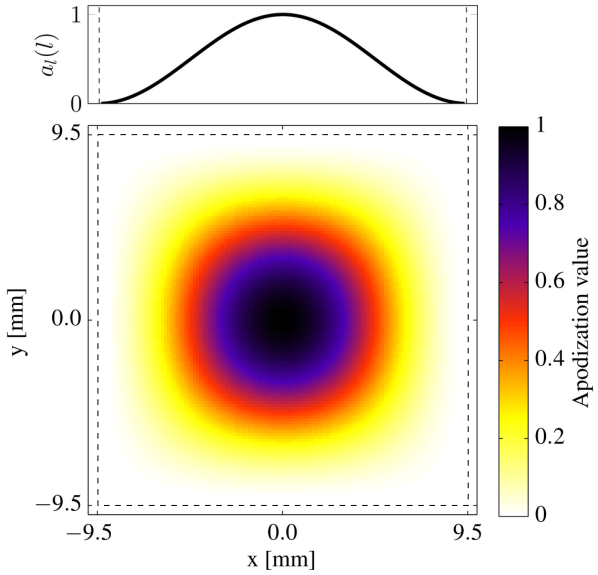

Figure 3.11: The row-column addressed array with a transducer-integrated Hann apodization. The graph at the top shows the Hann apodization of a single line-element as a function of the position along the line-element, l. The bottom figure shows the Hann apodization of the full transducer array. The dashed lines mark the edge of the line-elements and the row-column addressed array. The size of the area within the dashed lines is identical to that of the area within the dashed lines in Figure 3.12.

An alternative to the overlapping apodizations is to not apodize the central part of the transducer surface, but instead adding a roll-off region on both sides of all line-elements as shown in Figure 3.12. This roll-off region is used for the apodization function to converge smoothly to zero. This way, the central region of the aperture surface has a uniform apodization value of 1, and there is no overlapping of the apodization functions where they are less than one. At the same time, the discontinuities at the edges have been removed. If the added roll-off region is short, then the derivative of the aperture function will be high, and if the roll-off region is wide, the derivative will be low. From Eq. (3.2), it then follows that a wider roll-off region is better at suppressing the edge waves. Each line-element thereby becomes longer, but there are the same number of row- and column-elements in the array. This apodization thereby does not affect the electronics, interconnections, or the data processing.

There is an upper limit on the edge apodization width. A very large footprint results

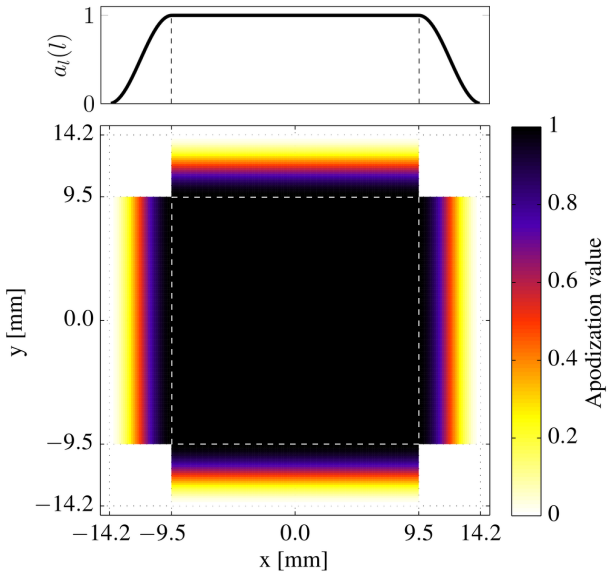

Figure 3.12: New integrated-apodization layout where a roll-off region is added to the ends of the line-elements. The central region, marked with dashed lines, has an apodization value of one. The size of the area within the dashed lines is identical to that of the area within the dashed lines in Figure 3.11.

in difficulties getting a good acoustical contact between the aperture and the human body. For a discussion on the influence of the edge width, see paper G. An edge width of 16 λ is chosen in this work.

3.5 Beamforming with line elements

Delay-and-sum beamformers usually assumes the geometry the sound sources and receivers to be points. The emitted wavefront of a line-element has the shape of a cylinder surface: it is a plane wave in the plane aligned along the line-element and a circle arc in the plane orthogonal to the line-element. Assuming the geometry of the line-elements to be points is therefore a poor approximation. A better approximation assumes the line-elements to be line segments. When an array of line-elements is focused, the geometry of the focal zone is also a line segment. Calculating the distances between the line-elements and a given point should therefore be calculated as the distance between a line segment and a point.

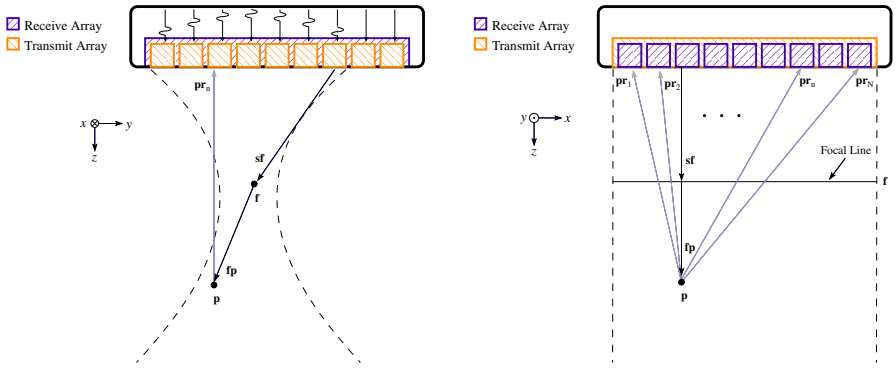

(a) ToF in y–dimension. (b) ToF in x–dimension.

Figure 3.13: Time of flight (ToF) illustration of a focused emission. The vector **sf** connects the first source line-element that is excited with the focal line **f**. **fp** is the vector from the nearest point on the focal line to the point being beamformed (**p**), and $\mathbf{pr}_i$ is the vector from **p** to the nearest point on the receive line-element $\mathbf{r}_i$. In (a) the setup is sliced orthogonal to the transmitting line-elements and parallel with the receiving line elements. In (b) the setup is sliced parallel with the transmitting line-elements and orthogonal to the receiving line elements. In (a) the focal zone **f** looks like a focal point, but in (b) it is seen to be a focal line.

The vectors **fp** and $\mathbf{pr}_n$, seen in Figure 3.13, connects the point **p** to the closest point on respectively the focal line **f** and the receiving element $\mathbf{r}_n$. **sf** is the vector from the source line-element **s** to the focal line **f**. Since the source elements and the focal line are parallel, determining the distance between them can be solved in the z-y plane.

The time of flight of a wavefront is given by the shortest distance from the source **s** through the focal line **f** to the point being focused **p** and back to the receiving element $\mathbf{r}_n$, divided by the speed of sound. Using the notation from Figure 3.13, this can be written as:

$$\mathrm{ToF}_m(\mathbf{p},n) = \frac{\|\mathbf{sf}\| \pm \|\mathbf{fp}\| + \left\|\mathbf{pr}_n\right\|}{c}\,, \tag{3.7}$$

where c is the speed of sound in the medium, n is an index from 1 to the number of receive line-elements N and m is the emission index. Only one value of ToF_m is calculated per emission. If the point being focused is closer to the transducer array than the focal line, then the case of $-\|\mathbf{fp}\|$ is used, otherwise $+\|\mathbf{fp}\|$ is used.

In Section G.5 in paper G it is shown that there are three cases when calculating the distance between a point and a line source or receiver. The correct case is chosen based

on the parameter $\hat{l}$, indicating whether the point is in front of the source or off to one of the sides. The following determines the minimum distance between the point $\mathbf{p}$ and the line segment $\mathbf{ab}$:

$$d(\mathbf{ab},\mathbf{p}) = \begin{cases} \dfrac{\|\mathbf{ab}\times\mathbf{ap}\|}{\|\mathbf{ab}\|} & \text{if } 0 \le \hat{l} \le 1 \\ \|\mathbf{ap}\| & \text{if } \hat{l} < 0 \\ \|\mathbf{bp}\| & \text{if } \hat{l} > 1\,, \end{cases} \tag{3.8}$$

where

$$\hat{l} = \frac{\mathbf{ap}\cdot\mathbf{ab}}{\|\mathbf{ab}\|^2}\,. \tag{3.9}$$

Using (3.8), the distances $\|\mathbf{fp}\|$ and $\left\|\mathbf{pr}_n\right\|$ can now be determined as

$$\|\mathbf{fp}\| = d(\mathbf{f},\mathbf{p}) \quad \text{and} \quad \left\|\mathbf{pr}_n\right\| = d(\mathbf{r}_n,\mathbf{p})\,. \tag{3.10}$$

A MATLAB beamformer that uses (3.8) was programmed in order to beamform data from row-column addressed arrays. The beamformer can IQ-beamform 250 000 voxels from a complex data set of 1.5 MiB from 128 receive line-elements in approximately 11.4 s on a PC with a 3.4 GHz Intel Core i7-3770 CPU. The beamformer can therefore not achieve a frame rate useful for real-time applications, but the frame rate is adequate for research purposes.

3.6 Imaging Results

In Figure 3.14 the result of a simulation study that investigated the appearance an anechoic blood vessel embedded in tissue is shown. In the left figure, a standard row-column addressed array is used and in the right figure a roll-off apodized row-column addressed array is used. The blood vessel diameter is seen to be smaller when not applying integrated-apodization. By applying integrated-apodization the blood vessel diameter at -10 dB is increased from 2.0 mm to 2.4 mm. In the papers D and G, the point spread function with and without integrated-apodization is also investigated. In the papers E and H the line spread function (LSF) is investigated using both simulations and measurements.

In Figure 3.15 the result of both a measurement and a simulation using a $62+62$ element row-column addressed array is shown. In the two left figures, no apodization is integrated into the array, and in the figures to the right, apodization is integrated into the arrays. The ghost echo is clearly seen to be attenuated in both the simulations and measurements. The maximum ghost echo intensity is attenuated by 15.8 dB in the measurements and by 11.5 dB in the simulations.

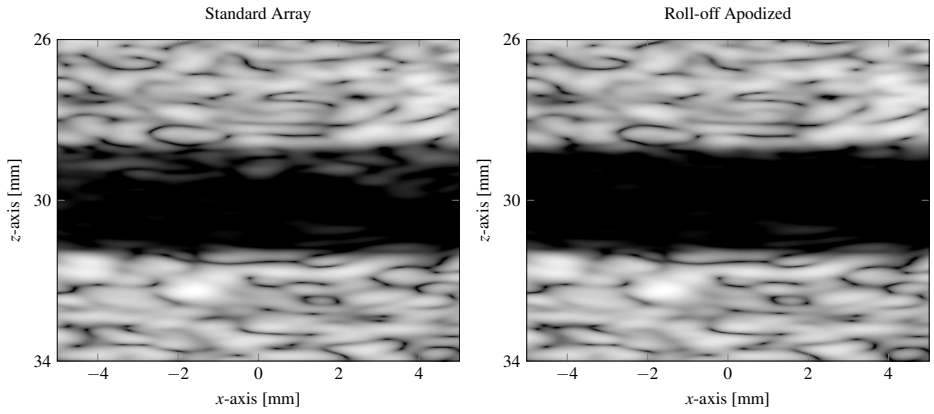

Figure 3.14: B-mode images of a slice through the center of an anechoic blood vessel with a diameter of 3 mm located at 30 mm depth. (a) is made with a standard array and (b) with the roll-off apodized array. The dynamic range is 40 dB for both images. Because of ghost echoes in the PSF for the standard array, the blood vessel in (a) appears to be smaller than the blood vessel in (b).

3.7 Summary of Papers on Row-column Addressing of 2-D Arrays

Three conference papers and two journal papers that are either published or submitted are in the following briefly described.

Paper D: 3D Ultrasound Imaging Performance of a Row-column Addressed 2D Array Transducer: A Simulation Study

The first paper on 3-D imaging with row-column addressed arrays we published, was a simulation comparison of the achievable image quality between a fully addressed 2-D and a row-column addressed 2-D array. In the comparison the two transducer arrays had the same pitch, center frequency and number of active elements.

Before the image quality comparison was made, it was shown how the delay-and-sum beamformer equation must be changed to beamform signals from a row-column addressed array. The presented beamformer equation can handle single element emissions. It was also shown that row-column addressing had a downside of creating ghost echoes in the point spread function. This had previously been shown by Démoré et al. (2009), but was investigated in greater detail in this paper.

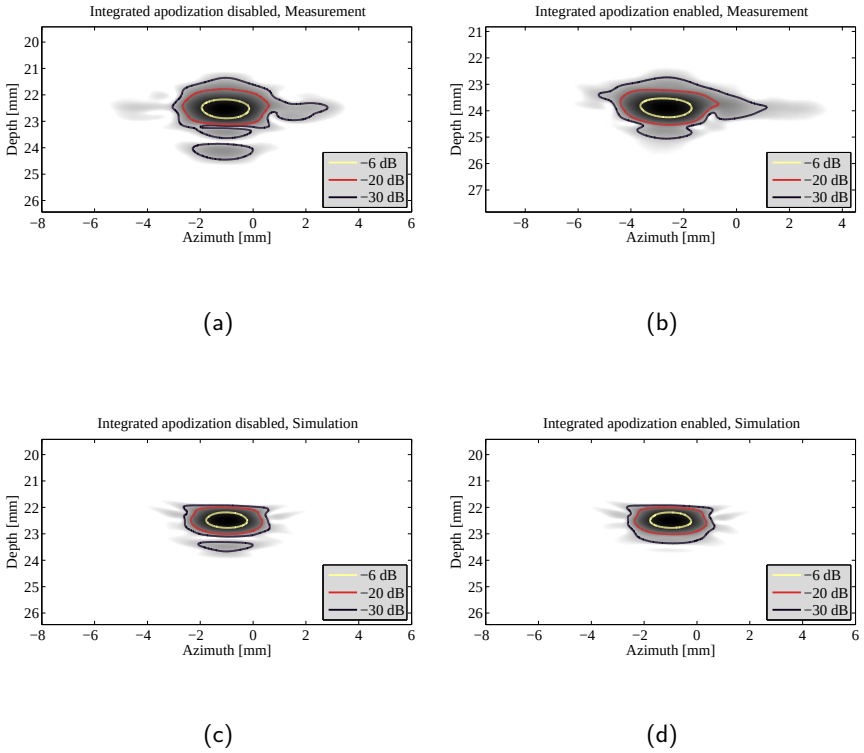

Figure 3.15: Measured (a and b) and simulated (c and d) line spread function at a depth of 2.3 cm using dynamic range of 40 dB. a and c show the result with the integrated apodization disabled, while b and d show the result with the integrated apodization enabled. The line spread function was acquired using a line of point scatterers in the simulation, while a 0.3 mm diameter steel wire was used for the measurements. The image was beamformed using full synthetic aperture imaging with 62 single element emissions and data received by 62 receive elements for each emission. The azimuth zero-point is positioned at the center of the array.

For both groups it was clear that the solution to the ghost echo problem is to apply apodization. Démoré and colleagues proposed to integrate the apodization into the ultrasound probe as a attenuating layer between the lens and the transducer elements. We proposed to integrate the apodization into the transducer elements. Since our sponsor wanted to apply for a patent based on this solution, the paper was not specific on how to apply the apodization.

An apodization of the entire active area was chosen, leading to a ghost echo damping of 22 dB.

Paper E: 3-D Ultrasound Imaging Performance of a Row-Column Addressed 2-D Array Transducer: A Measurement Study

In the second conference paper on row-column addressing, our first measurements with a row-column addressed array are performed and presented. The focus of this paper was the image quality of row-column addressed arrays compared to fully addressed arrays and how their image quality scales with the number of active beamformer channels.

On the 32×32 element Vermon probe a $32 + 32$ element row-column addressed array was emulated. A comparison was then made between the 32×32 element array and the $32 + 32$ element array. The row-column addressed array used a single row element per transmission and all 32 column elements in receive. The fully addressed array used all 1024 elements in both transmit and receive, 256 emissions was used to sample the 3-D volume. Even though the fully addressed array used 8 times as many emissions and 32 times as many elements and beamformer channels, the achieved main-lobe size was similar for the two arrays. The side-lobes, on the other hand, were higher for the row-column addressed array than for the fully addressed array.

A simulations study on how the imaging quality of the fully addressed array and row-column addressed array scales with the number of active elements was also presented. For any given number of active elements, the row-column addressed array achieved a better detail resolution and cystic resolution than the fully addressed array.

Paper F: Row-Column Addressed 2-D CMUT Arrays with Integrated Apodization

In this paper, measurements with two in-house produced $32 + 32$ element row-column addressed arrays were presented and compared to simulations. One transducer array has an integrated circular symmetric Hann apodization, the other array is not apodized. The apodization is applied by varying the density of CMUT cells in the array with the objective of attenuating the edge waves originating from the element ends. Measurements of the emitted pressure field from the array with integrated apodization showed a reduction in edge wave energy of SI85% compared to the array without integrated apodization. Simulations in Field II yielded a corresponding reduction of 95 %. The simulations were able to replicate the measured pressure field, proving the predictability of the technique.

Paper G: 3-D Imaging with Row-Column Addressed Arrays: Transducer-Integrated Apodization and Line-element Beamforming

This was our first journal paper on row-column addressing of 2-D transducer arrays. It included and extended the results from the previous conference papers. The graphical edge-effect explanation from paper D was in this paper superseded by a mathematical stringent version. The extra responses in the spatial impulse response were shown to originate from discontinuities in the aperture function. The edge effect was shown to be minimized when the derivative of the apodization function was minimized.

As a solution to minimizing the first derivative of the apodization function, different ways of integrating apodization into a transducer array was presented. The apodization of the entire active aperture, as used in the conference papers and by Démoré et al. (2009), was shown not to be a good solution. A new apodization scheme with roll-off regions on the sides of the array is proposed as a solution. Measurements from an in-house produced CMUT array with and without integrated apodization were presented and compared. The apodized array attenuated the edge waves compared to the conventional row-column addressed array. Simulations of the same setup gave the same result and verified that row-column addressed arrays with integrated-apodization can be simulated using Field II. The effect of the new apodization scheme was through simulations shown on both the PSF and an anechoic blood vessel.

The beamformer equation from paper D was expanded to also handle multi-element focused or unfocused emissions. A row-column suitable beamformer that implements the presented delay-and-sum equation was implemented and made available online.

Paper H: 3-D Imaging using Row-Column Addressed Arrays with Integrated Apodization: Transducer Fabrication and Experimental Results

The second journal paper on row-column addressing of 2-D arrays presents the fabrication, characterization, and imaging results of a $62+62$ element row-column addressed 2-D CMUT array. The $62+62$ element array is designed with the roll-off apodization presented in paper G. For the experimental setup, custom front-end electronics with the ability to send and receive on all 124 elements was produced. The imaging was carried out with 62 single element emissions.

A simulation that mimicked the measurement setup and the transducer arrays was also presented. The dominant ghost echo was reduced in both the measurements and the simulations. The main response was practically unaffected by the integrated apodization. This demonstrated that the proposed apodization roll-off layout works in an experimental measurement setup and not only in simulations.

3.8 Conclusion

The origin of ghost echoes when imaging with row-column addressed arrays was analyzed. The ghost echoes were shown to originate from the edge effects appearing at the

discontinuity of the aperture. Attenuating the ghost echoes was shown to be achieved by minimizing the first derivative of the apodization function.

A new apodization layout that addresses the drawbacks of the previously used apodization was published. The new layout was shown to be effective in both simulations and with measurements on in-house produced CMUT arrays. New methods of integrating the apodization into the transducer array were proposed.

The assumptions used in the conventional delay-and-sum beamformer does not hold for row-column addressed arrays. In order to correct this, an expanded delay-and-sum equation was presented. The updated equation was implemented in a MATLAB beamformer and made available on-line, for others to download and use.

References

Austeng, A. and S. Holm (2002). "Sparse 2-D arrays for 3-D phased array imaging - design methods". In: *IEEE Trans. Ultrason., Ferroelec., Freq. Contr.* 49.8, pp. 1073–1086 (cit. on p. 31).

Bates, K. N. (1995). "A high acuity 3-D acoustic imaging system". In: *Proc. IEEE Ultrason. Symp.* Pp. 1245–1250 (cit. on p. 34).

Blaak, S., Z. Yu, G. Meijer, C. Prins, C. Lancee, J. Bosch, and N. de Jong (2009). "Design of a micro-beamformer for a 2D piezoelectric ultrasound transducer". In: *Proc. IEEE Ultrason. Symp.* Pp. 1338–1341. DOI: 10.1109/ULTSYM.2009.5441534 (cit. on p. 31).

Brunke, S. S. and G. R. Lockwood (1997). "Broad-bandwidth radiation patterns of sparse two-dimensional vernier arrays". In: *IEEE Trans. Ultrason., Ferroelec., Freq. Contr.* 44.5, pp. 1101–1109 (cit. on p. 31).

Chen, A. I. H., L. L. Wong, A. S. Logan, and J. T. W. Yeow (2011). "A CMUT-based real-time volumetric ultrasound imaging system with row-column addressing". In: *Proc. IEEE Ultrason. Symp.* Pp. 1755–1758 (cit. on p. 34).

Chen, Y., M. Nguyen, and J. T. Yen (2010). "Recent results from dual-layer array transducers for 3-D imaging". In: *Proc. IEEE Ultrason. Symp.* Pp. 2400–2403 (cit. on p. 34).

— (2011). "Real-time rectilinear volumetric acquisition with a 7.5 MHz dual-layer array transducer - Data acquisition and signal processing". In: *Proc. IEEE Ultrason. Symp.* Pp. 1759–1761 (cit. on p. 34).

Daher, N. M. and J. T. Yen (2004). "Rectilinear 3-D ultrasound imaging using synthetic aperture techniques". In: *Proc. IEEE Ultrason. Symp.* Vol. 2, pp. 1270–1273 (cit. on p. 34).

— (2006). "2-D Array for 3-D Ultrasound Imaging Using Synthetic Aperture Techniques". In: *IEEE Trans. Ultrason., Ferroelec., Freq. Contr.* 53.5, pp. 912–924 (cit. on p. 34).

Davidsen, R. E., J. A. Jensen, and S. W. Smith (1994). "Two-Dimensional Random Arrays for Real Time Volumetric Imaging". In: *Ultrasonic Imaging* 16.3, pp. 143–163 (cit. on p. 31).

Démoré, C. E. M., A. Joyce, K. Wall, and G. Lockwood (2009). "Real-time volume imaging using a crossed electrode array". In: *IEEE Trans. Ultrason., Ferroelec., Freq. Contr.* 56.6, pp. 1252–1261 (cit. on pp. 34, 35, 38, 44, 50, 53).

Halvorsrod, T., W. Luzi, and T. Lande (2005). "A log-domain µbeamformer for medical ultrasound imaging systems". In: *IEEE Trans. Circuits Syst. I, Reg. Papers* 52.12, pp. 2563–2575. DOI: 10.1109/TCSI.2005.857544 (cit. on p. 31).

Jensen, J. A. (1991). "A Model for the Propagation and Scattering of Ultrasound in Tissue". In: *J. Acoust. Soc. Am.* 89, pp. 182–191 (cit. on p. 36).

Jeong, J. S., C. H. Seo, and J. T. Yen (2007). "Dual-Layer Transducer Array for 3-D Imaging". In: *Proc. IEEE Ultrason. Symp.* Pp. 2371–2374 (cit. on p. 34).

Karaman, M., I. O. Wygant, O. Oralkan, and B. T. Khuri-Yakub (2009). "Minimally Redundant 2-D Array Designs for 3-D Medical Ultrasound Imaging". In: *IEEE Trans. Med. Imag.* 7, pp. 1051–1061 (cit. on p. 31).

Logan, A. S., L. L. P. Wong, A. I. H. Chen, and J. T. W. Yeow (2011). "A 32 x 32 element row-column addressed capacitive micromachined ultrasonic transducer". In: *IEEE Trans. Ultrason., Ferroelec., Freq. Contr.* 58.6, pp. 1266–1271 (cit. on p. 34).

Logan, A. S., L. L. P. Wong, and J. T. W. Yeow (2009). "2-D CMUT wafer bonded imaging arrays with a row-column addressing scheme". In: *Proc. IEEE Ultrason. Symp.* Pp. 984–987 (cit. on p. 34).

Morton, C. E. and G. R. Lockwood (2003). "Theoretical assessment of a crossed electrode 2-D array for 3-D imaging". In: *Proc. IEEE Ultrason. Symp.* Pp. 968–971 (cit. on p. 34).

Rasmussen, M. F. and J. A. Jensen (2013). "3D ultrasound imaging performance of a row-column addressed 2D array transducer: a simulation study". In: *Proc. SPIE Med. Imag.* 86750C, pp. 1–11 (cit. on p. 44).

Sampaleanu, A., P. Zhang, A. Kshirsagar, W. Moussa, and R. Zemp (2014). "Top-orthogonal-to-bottom-electrode (TOBE) CMUT arrays for 3-D ultrasound imaging." In: *IEEE Trans. Ultrason., Ferroelec., Freq. Contr.* 61.2, pp. 266–276. DOI: 10.1109/TUFFC.2014.6722612 (cit. on p. 35).

Savord, B. and R. Solomon (2003). "Fully sampled matrix transducer for real time 3D ultrasonic imaging". In: *Proc. IEEE Ultrason. Symp.* Vol. 1, pp. 945–953 (cit. on p. 31).

Senturia, S. D. (2004). *Microsystem Design*. 6th ed. Kluwer Academic Publishers (cit. on p. 42).

Seo, C. H. and J. T. Yen (2006). "64 x 64 2-D array transducer with row-column addressing". In: *Proc. IEEE Ultrason. Symp.* Vol. 1, pp. 74–77 (cit. on p. 34).

— (2007). "256 x 256 2-D array transducer with row-column addressing for 3-D imaging". In: *Proc. IEEE Ultrason. Symp.* Pp. 2381–2384 (cit. on p. 34).

Seo, C. H. and J. T. Yen (2008). “Recent results using a 256 x 256 2-D array transducer for 3-D Rectilinear Imaging”. In: *Proc. IEEE Ultrason. Symp.* Vol. 1-4, pp. 1146–1149 (cit. on p. 34).

— (2009). “A 256 x 256 2-D array transducer with row-column addressing for 3-D rectilinear imaging”. In: *IEEE Trans. Ultrason., Ferroelec., Freq. Contr.* 56.4, pp. 837–847 (cit. on p. 34).

Yen, J. T., C. H. Seo, S. I. Awad, and J. S. Jeong (2008). “A PZT-P[VDF-TrFE] dual-layer transducer for 3-D rectilinear imaging”. In: *Proc. IEEE Ultrason. Symp.* Pp. 1138–1141 (cit. on p. 34).

— (2009). “A dual-layer transducer array for 3-D rectilinear imaging”. In: *IEEE Trans. Ultrason., Ferroelec., Freq. Contr.* 56.1, pp. 204–212 (cit. on p. 34).

Yen, J. T., J. P. Steinberg, and S. W. Smith (2000). “Sparse 2-D array design for real time rectilinear volumetric imaging”. In: *IEEE Trans. Ultrason., Ferroelec., Freq. Contr.* 47.1, pp. 93–110 (cit. on p. 31).

Yen, J. T. (2013). “Beamforming of sound from two-dimensional arrays using spatial matched filters”. In: *J. Acoust. Soc. Am.* 134.5, pp. 3697–704. DOI: 10.1121/1.4821988 (cit. on p. 34).

Zemp, R. J., W. Zheng, and P. Zhang (2011). “Feasibility of Top-Orthogonal-to-Bottom Electrode (TOBE) 2D CMUT arrays for low-channel-count 3D imaging”. In: *Proc. IEEE Ultrason. Symp.* Pp. 498–502 (cit. on p. 35).

CHAPTER 4

Conclusion and Perspectives

The subject of the first part was 3-D synthetic aperture imaging, on which two conference papers and one journal paper was published. Using both simulations and measurements, it was shown that 3-D synthetic aperture imaging increases the image quality compared with parallel beamforming. The wire phantom measurements showed the same tendency as the simulations. Synthetic aperture imaging increased both the resolution and the contrast. Measurements on a tissue mimicking phantom indicated that the penetration depth is deeper for synthetic aperture imaging compared with parallel beamforming. Synthetic aperture had a higher SNR than parallel beamforming at all depths and the increased SNR resulted in a penetration depth increase of 24 %.

The setup of synthetic aperture imaging was made using extensive parameter studies. There still is a need for the theory of synthetic aperture imaging to be updated to ease the optimization of the synthetic aperture imaging setup. Some of the questions still to be answered are: Can the image quality be predicted using only the synthesized transmit aperture and the receive aperture? If the synthetic aperture is to be interpreted as a physical aperture, how are the dimensions of the synthesized elements, and how does the physical transmit apodization influence them? And how should the synthesized aperture be interpreted when the focal distance is approaching infinity, resulting in plane wave imaging?

3-D synthetic aperture imaging was compared to 3-D parallel beamforming, which used to be the 'gold standard' of 3-D ultrasound imaging. The leading 2-D matrix probes contain a very large amount of transducer elements, and still only the standard amount cables to connect the probe to the scanner is used. This clearly indicates that parallel beamforming is not being used by the most modern 3-D ultrasound scanners. The ultrasound companies that have published about which beamformer techniques they use today, state they use microbeamformers (Savord and Solomon 2003). The microbeamformer technique could therefore be implemented as a future reference for investigations of 3-D synthetic aperture imaging. Combining microbeamformers with the synthetic aperture technique would also be interesting, perhaps increasing the image quality of the large 2-D arrays even further.

An interesting research subject is to increase the frame rate of 3-D synthetic aperture imaging by using multiple transmit beams. Multiple virtual elements would then be synthesized per emission, thereby increasing the frame rate, or possibly the image quality.

The subject of the second part was row-column addressing of 2-D arrays. On that subject three conference papers and two journal papers were submitted. The origin of

ghost echoes when imaging with row-column addressed arrays was analyzed. The ghost echoes were shown to originate from the edge effects appearing at the discontinuity of the aperture. Attenuating the ghost echoes was shown to be achieved by minimizing the first derivative of the apodization function.

With simulations and measurements it was demonstrated that integrated apodization attenuates the ghost echoes and increases the image quality. It was also shown that increasing the number of apodization levels increases the ghost attenuation.

A future research subject could be to determine the optimum length of the proposed roll-off regions and also their optimum apodization curve. Is their optimum apodization curve for instance a Hann function, Gaussian function or just a straight line? It would also be interesting to demonstrate that large row-column addressed arrays can achieve a clinical relevant image 3-D imaging quality.

Flow imaging is essential on a modern ultrasound scanner. Some new ultrasound scanners also provide vector flow imaging. How to achieve vector flow estimation with a row-column addressed array should also be researched.

Papers

To ease the reading of the following publications they have been reformatted to fit the layout of this thesis. No contextual editing of the papers since their publication has taken place.

PAPER A

Preliminary Comparison of 3D Synthetic Aperture Imaging with Explososcan

Authors: Morten Fischer Rasmussen[a], Jens Munk Hansen[a], Guillaume Férin[b], Rémi Dufait[b] and Jørgen Arendt Jensen[a].

Published in: *Proceedings of SPIE Medical Imaging* Vol. 8320, pp. 1–9, (2012).

Abstract

Explososcan is the 'gold standard' for real-time 3D medical ultrasound imaging. In this paper, 3D synthetic aperture imaging is compared to Explososcan by simulation of 3D point spread functions. The simulations mimic a 32x32 element prototype transducer. The transducer mimicked is a dense matrix phased array with a pitch of 300 µm, made by Vermon. For both imaging techniques, 289 emissions are used to image a volume spanning 60° in both the azimuth and elevation direction and 150 mm in depth. This results for both techniques in a frame rate of 18 Hz. The implemented synthetic aperture technique reduces the number of transmit channels from 1024 to 256, compared to Explososcan. In terms of FWHM performance, was Explososcan and synthetic aperture found to perform similar. At 90 mm depth is Explososcan's FWHM performance 7 % better than that of synthetic aperture. Synthetic aperture improved the cystic resolution, which expresses the ability to detect anechoic cysts in a uniform scattering media, at all depths except at Explososcan's focus point. Synthetic aperture reduced the cyst radius, $R_{20\text{dB}}$, at 90 mm depth by 48 %. Synthetic aperture imaging was shown to reduce the number of transmit channels by four and still, generally, improve the imaging quality.

Keywords: medical ultrasound, three-dimensional imaging, synthetic aperture, explososcan

[a]Center for Fast Ultrasound Imaging, Dept. of Elec. Eng. Bldg. 349, Technical University of Denmark, DK-2800 Kgs. Lyngby, Denmark.

[b]Vermon S.A., Avenue du Général Renault, 37000 Tours, France.

A.1 Introduction

In conventional ultrasound, images are produced by sequentially acquiring and beamforming scan lines, followed by a scan line conversion. For at setup using N scan lines per image the achievable frame rate, f_r, when acquiring to a depth of D, is then

$$f_r = \frac{c}{2DN}\,. \tag{A.1}$$

In 3D ultrasound imaging, an entire volume is imaged. The extension from 2D to 3D greatly increases the number of lines to be acquired, e.g. from 100 to 100^2 lines. This increase leads to a proportional decrease in frame rate. Using conventional imaging, the achievable frame rate is too low to capture the dynamics of the anatomy, e.g. the heart. This was addressed by von Ramm and Smith (Ramm et al. 1991; Shattuck et al. 1984; Smith et al. 1991) by applying a parallel beamforming technique, dubbed Explososcan, to 3D imaging.

In Explososcan, multiple lines are beamformed per transmission, thus increasing the achievable frame rate. If, for instance, 6×6 lines are beamformed per transmission instead of just one, the frame rate increases by a factor of 36. Besides increasing the frame rate, Explososcan introduces some undesirable effects. In order to cover the extra scan lines, must the emission beam insonify a larger volume, and a less focused beam is therefore needed. This leads to a larger point spread function main lobe. The further away from an emission beam a line is beamformed, the less energy the beamformed area receives from the emission beam, and the darker it appears in the image. This is an amplitude modulation of the image lines, with peak intensity at lines co-aligned with emission beams, and lower intensity further away from the emission beams. A second effect can be observed. Scan lines beamformed from a the same emission exhibit higher correlation with one another, than do lines not beamformed from a the same emission. Together these two effects are termed the “boxing effect”.

An alternative technique called synthetic aperture (Burckhardt et al. 1974; Flaherty et al. 1967; Jensen, Nikolov, et al. 2006; Nagai 1985; Soumekh 1999), exists. The synthetic aperture technique synthesizes a larger aperture from measurements carried out using apertures located at different positions. Synthetic aperture can be divided into two major groups; the synthetic receive aperture, where a larger receive aperture is synthesized, and the synthetic transmit aperture (Chiao et al. 1997), where a larger transmit aperture is synthesized. The basic principle of synthetic transmit aperture is that a single point source emits a spherical wave, insonifying the entire image region. This is repeated for all available sources, each located at different locations. After each transmission, all elements in the receive aperture are sampled. Each sampled data set is used for beamforming a low resolution image, which is dynamically receive focused. Summing all low resolution images results in a fully focused high resolution image. The high resolution image is, thus, dynamically focused in both receive and transmit. The end effect is a synthesized transmit aperture, with the point sources as elements and a dynamic transmit focus. In

this paper is synthetic transmit implemented and synthetic aperture will refer to synthetic transmit aperture.

The imaging quality of synthetic aperture is compared to Explososcan, when doing 3D imaging with a 2D phased array transducer. The comparison of the two imaging techniques is based on performance metrics applied to their respective point spread function.

The organization of this paper is as follows: First, the applied performance metrics are introduced. Next, it is described how Explososcan and synthetic aperture are implemented and the simulation setup is described. In the results section, a visual comparison of two point spread functions is made and the acquired performance metrics as a function of depth are presented. Finally, some concluding remarks are given.

A.2 Performance Metrics

Metrics quantifying different quality features can be used to compare the two imaging techniques. In this paper, both a detail resolution and a cystic resolution metric are applied to the point spread functions. Both are introduced in detail in the following.

A.2.1 Detail resolution

The detail resolution is how close two identical point scatters in a non–reflective medium can be located to each other and still be distinguished. An often used measure for when two scatterer can be resolved is the size of the point spread function main lobe, i.e. the full width at half maximum (FWHM).

The FWHM is determined in both the azimuth and elevation direction of the point spread function C–scan. A single number is achieved by averaging the two measures.

A.2.2 Cystic resolution

The cystic resolution describes the ability to detect an anechoic cyst in a uniform scattering medium. Specifically, the cystic resolution gives the intensity at the center of an anechoic cyst of a given size relative to its surrounding uniformly back-scattering medium (Vilkomerson et al. 1995). The lower the intensity at the center of the cyst, i.e. the darker it appears in the image for a given cyst size, the better imaging performance of the system. This metric mimics an often seen situation in medical ultrasound where the object of interest is a weakly reflecting tissue, such as a blood vessel or a cyst, in a back-scattering medium. For this reason, is cystic resolution assumed to be a more important performance metric than the FWHM. The relative intensity (RI) of the anechoic cyst was shown by Ranganathan and Walker (Ranganathan and Walker 2007), to be

quantized as the clutter energy to total energy ratio,

$$\mathrm{RI}(R) = \sqrt{\frac{E_{out}(R)}{E_{tot}}} = \sqrt{1 - \frac{E_{in}(R)}{E_{tot}}}, \tag{A.2}$$

where E_{in} is the signal energy inside a circular region with radius, R, centered on the peak of the point spread function, E_{tot} is the total point spread function energy, and E_{out} is the point spread function energy outside the circular region. To achieve a single number from the $\mathrm{RI}(R)$–curve, one either determines the relative intensity for a single cyst radius, or determines the required radius to achieve a certain relative intensity, e.g. the cyst radius at which the intensity at center of the cyst is 20 dB lower than its surroundings, written as $R_{20\mathrm{dB}}$.

The cystic resolution is in this work measured in the point spread function C–scan and is presented both as a full $\mathrm{RI}(R)$–curve and as a single cyst radius giving a relative intensity of 20 dB, $R_{20\mathrm{dB}}$.

A.3 Methods

A.3.1 Explososcan

As described in the introduction, the procedure of beamforming several lines per emission introduces an undesirable boxing effect consisting of two effects; firstly, an intensity modulation of the beamformed image lines, and secondly, scan lines beamformed from the same emission exhibit a higher correlation with one another, than do lines not beamformed from the same emission. If the line intensity modulation factor is known it can be compensated for. The intensity modulation factor could be estimated from simulations, but this is not implemented. The correlation effect can to some extent be compensated for by overlapping lines beamformed from neighboring emissions. When overlapping scan lines, each line has to be weighted in order to ensure a uniform intensity in the image. It is intuitive to have the largest scan line weight when the scan line and its emission beam are parallel, and a lower weight as the angle between them increases. In this work, it is chosen to have the weight of each scan line to be inversely proportional with the angle difference between the scan line and its emission beam. If we define the distance measure

$$\mathrm{d}(\ell, e) = \sqrt{(\theta_\ell - \theta_e)^2 + (\phi_\ell - \phi_e)^2}, \tag{A.3}$$

where ℓ is a scan line in a given direction, e is the emission beam from which ℓ was beamformed, ϕ is the azimuth angle and θ the elevation angle of the line, the weight function then becomes

$$w(\ell, e) = \begin{cases} 1 & \text{if} \quad \mathrm{d}(\ell, e) = 0 \\ \dfrac{1/\mathrm{d}(\ell, e)}{Z(\ell)} & \text{else} \end{cases}, \tag{A.4}$$

where $Z(\ell)$ is a normalization factor, which makes sure the weights of all lines overlapping with line ℓ sums to one.

In Fig. A.1, the effect of the implemented correlation compensation is seen on a C–scan measurement of a tissue mimicking phantom. In all four sub–figures contains the C–scans the same number of resulting lines, but the number of lines overlapping differs. In Fig. A.1A.1(a) the C–scan is seen without correlation compensation and in

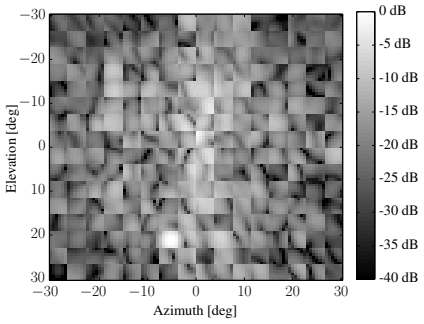

(a) No correlation compensation; 6×6 lines beamformed per emission.

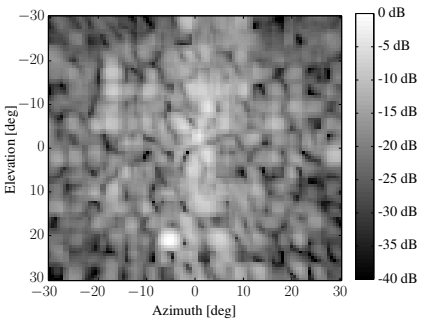

(b) 1st level of correlation compensation; 8×8 lines beamformed per emission.

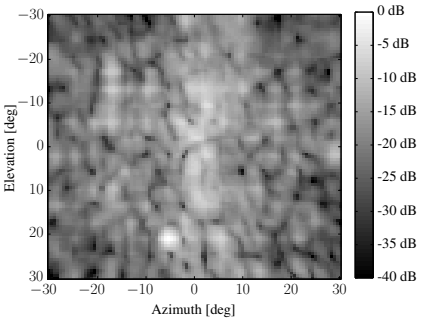

(c) 2nd level of correlation compensation; 10×10 lines beamformed per emission.

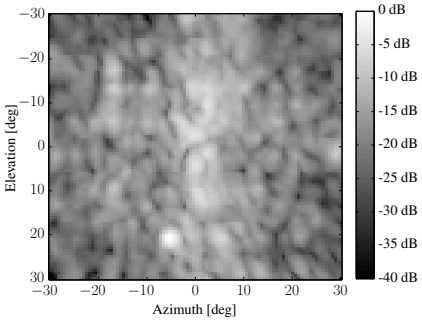

(d) 3rd level of correlation compensation; 12×12 lines beamformed per emission.

Figure A.1: Explososcan correlation compensation for a C–scan measurement of a tissue mimicking phantom. The transducer parameters can be seen in Table A.1.

Fig. A.1A.1(b)–A.1(d) the correlation compensation is increased one step at a time. Each step of correlation compensation is dubbed 1st level, 2nd level and 3rd level of correlation compensation, respectively. The number of lines beamformed per emission is increased from 6×6 in Fig. A.1A.1(a), through 8×8, 10×10 and 12×12, in Fig. A.1A.1(b)–A.1(d). As the correlation compensation increases, the C–scan gets more blurred and the dynamic range decreases. For the Explososcan implementation, the 1st level of correlation compensation is chosen. The 1st level of correlation compensation is a compromise between a very evident boxing effect, when no correlation compensation is applied, and a blurry image when the 3rd level of correlation compensation is applied.

Adding extra scan lines goes against the original Explososcan idea of decreasing the number of beamformers. But the new scan lines could be beamformed by using the parallel beamforming approximation, described by von Ramm and colleagues in (Ramm et al. 1991), and thereby keeping the computational cost low.

A.3.2 Synthetic aperture

In the standard version of synthetic aperture, each source emits an unfocused spherical wave. By using multiple transducer elements in transmit, a virtual source can be imitated at the focus point. This leads to an increase in emitted energy and penetration depth. If the virtual source is located directly in front of the active aperture, the synthesized transmit aperture is smaller than the physical transducer. This is illustrated in Fig. A.2A.2(a). The larger the sub–aperture, the smaller the synthesized aperture. For 2D imaging, the

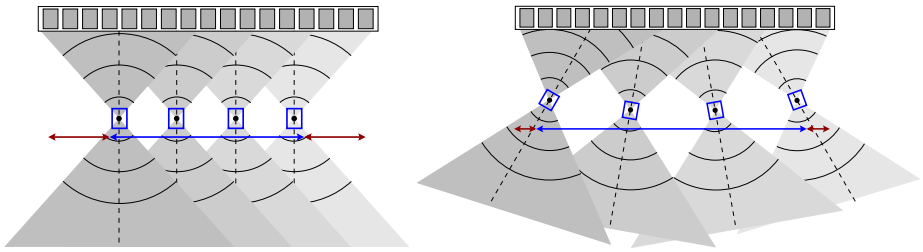

(a) Traditional synthetic aperture. The virtual source is centered on each sub–aperture.

(b) Synthetic aperture with beam steering. The virtual source is tilted to the sides when the active aperture is translated.

Figure A.2: Synthetic aperture virtual source setup. The gray array in the top is the physical aperture, the thick dots the virtual sources, and the array of boxes around the virtual sources the synthesized aperture. Four emissions are shown, each with eight active elements. The center arrow indicates the synthesized aperture size.

maximum number of synthesized transmit sources can be found by the following relation,

$$N_{\text{vs}} = N_{\text{phys}} - N_{\text{act}} + 1 \ , \tag{A.5}$$

where N_{vs} is the number of virtual sources in the synthesized transmit aperture, N_{phys} is the number of physical elements, and N_{act} is the number of active physical elements used for the emissions. If 16 elements are used for each dimension of the sub–aperture and the physical transducer has a size of 32x32 elements, the synthesized transmit aperture contains 17×17 elements. This is little more than half the size of the physical transducer, and the transmit f–number is therefore approximately doubled, compared to a full 32x32 element transmission.

A method to partially compensate for the smaller synthesized transmit aperture is to spread the virtual sources apart by tilting the emission beam proportionally with the active aperture location on the transducer. This way, the synthesized aperture is increased in size. This illustrated in Fig. A.2A.2(b).

Synthetic aperture imaging is in this work implemented with emission beam steering.

A.4 Simulation setup

All simulations are carried out using Field II (Jensen 1996; Jensen and Svendsen 1992) and beamformed using BFT3 (Hansen et al. 2011). The transducer used in the simulations mimics a prototype transducer soon to be used for 3D synthetic aperture measurements. It is a 2D phased array transducer, made by Vermon, (Vermon S.A., Tours, France), with a layout of 35x32 elements, of which row 9,18 and 27 are inactive, effectively giving 32x32 elements. The transducer parameters can be seen in Table A.1. The point spread

Table A.1: Transducer parameters

Parameter name	Notation	Value
Center frequency	f_c	3.5 MHz
Transducer pitch –x	d_x	300 µm
Transducer pitch –y	d_y	300 µm
Total number of elements –x	N_{tot_x}	32
Total number of elements –y	N_{tot_y}	35
Inactive rows	–	9,18,27
Number of active elements –x	N_x	32
Number of active elements –y	N_y	32

function is simulated by imaging a volume containing a single point scatter. The point scatterers are placed in front of the transducer at depths ranging from 40 mm to 150 mm. The emission beam is controlled similarly to what is used for phased array imaging, and

the coordinate system used is the one defined by Smith et al. (Smith et al. 1991). For both Explososcan and synthetic aperture, the transmit aperture is apodized with a Tukey window, and for receive apodization, a Hanning window is applied.

A.4.1 Explososcan

The implemented Explososcan technique uses, in both transmit and receive, all 1024 available elements of the 32x32 element transducer. Explososcan is implemented with 17 emissions in both the azimuth and elevation direction, which results in 289 emissions per imaged volume. As discussed in Sec. A.3.1, to counteract the boxing effect of Explososcan, some of the scan lines are overlapped. 8×8 lines are beamformed per emission, but 6×6 lines appear in the volume, resulting in 102×102 total lines in the volume. The beamformed lines span from $-30°$ to $30°$ in both directions, and the emission beams are spread evenly within this span. The focus point is placed at 40 mm range, which gives a transmit f–number ranging from 4.2 to 4.8, depending on the emission beam angle.

A.4.2 Synthetic aperture

For synthetic aperture, there is for each emission used an active aperture of 16×16 elements in transmit, and all 1024 elements in receive. This results in 256 active elements in transmit, which is one fourth of what is used for the Explososcan implementation. The active aperture is translated between each emission, one element in either the x– or y–direction. The active aperture is therefore translated 17 times in both the x– and the y–direction, giving a total of 289 emissions. This is the same number of emissions per volume as for the Explososcan implementation. The emission beam is tilted from $-15°$ to $15°$, proportional to the active aperture position on the transducer. The virtual source is placed at 10 mm range, which gives a transmit f–number ranging from 2.0 to 2.2. For each emission 102×102 scan lines are beamformed, spanning from $-30°$ to $30°$ in both directions. This is the same as the number of resulting lines in the Explososcan implementation.

When imaging to a depth of 150 mm, the 289 emission per volume results for both synthetic aperture and Explososcan in a frame rate of approximately 18 Hz.

A.5 Results

In Fig. A.5, a point spread function example of Explososcan and synthetic aperture is seen, and can be visually inspected and compared. The point spread function is located at 90 mm depth and $0°$ azimuth and elevation tilt angle. In the azimuth plane are the side–lobes larger than in the elevation plane. This is due to three inactive rows of elements on the transducer, all parallel to the elevation plane. Synthetic and Explososcan appears to have approximately the same main lobe size, but synthetic aperture clearly has smaller side–lobes. This is especially evident in the elevation plane.

In Fig. A.3 is the FWHM as a function of depth seen. Even though Explososcan uses four times more transmit channels than synthetic aperture, is the FWHM performance of the two techniques similar. Explososcan is seen to perform a little better than synthetic aperture at all depths. The largest performance difference occurs at Explososcan's focus point and the smallest at the deepest depth, 150 mm. At 90 mm is the FWHM of synthetic aperture 4.7 mm and 4.36 mm for Explososcan. In percentage, this is a difference of 7 %.

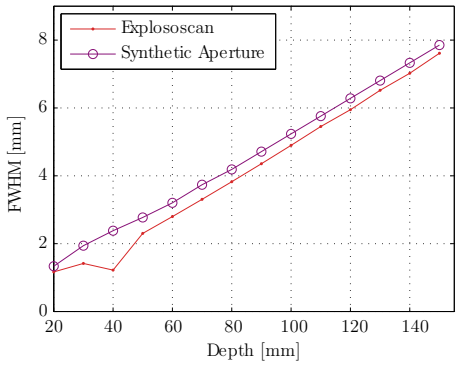

Figure A.3: FWHM as a function of depth.

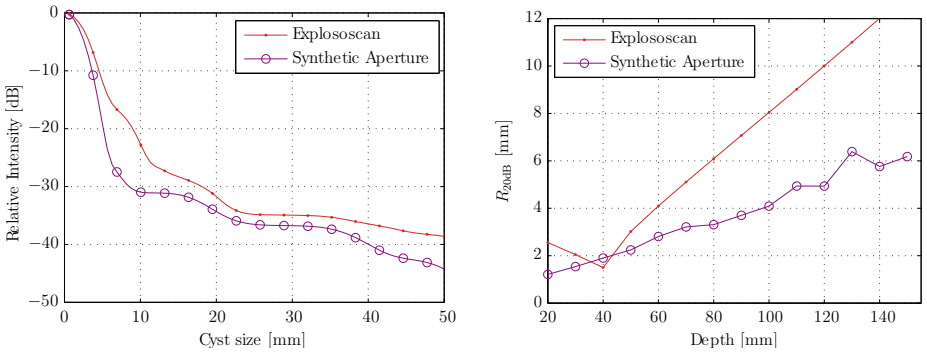

(a) Cystic resolution at 120 mm depth.

(b) R_{20dB} as a function of depth.

Figure A.4: The cystic resolution.

In Fig. A.4 is the cystic resolution at 120 mm depth and the R_{20dB} as a function of depth shown. In Fig. A.4A.4(a) is synthetic aperture seen to give a better relative intensity

at the cyst center, for all cyst sizes. This means, all anechoic cysts appears darker when imaged with synthetic aperture imaging than with Explososcan. As an example, a 10 mm anechoic cyst has a relative intensity of −31 dB when imaged with synthetic aperture and −23 dB when imaged with Explososcan.

The $R_{20\text{dB}}$ in Fig. A.4A.4(b), increases for both techniques approximately linearly with depth. Explososcan deteriorates more than twice as fast width depth as synthetic aperture, but performs at its focus point a little better than synthetic aperture. Everywhere else outperforms synthetic aperture Explososcan. At 90 mm depth is the $R_{20\text{dB}}$ of synthetic aperture 3.7 mm, and 7.07 mm for Explososcan. In percentage, decreases synthetic aperture the 20 dB cyst radius at 90 mm depth by 48 % compared to Explososcan.

A.6 Discussion and conclusion

3D synthetic aperture imaging was compared with Explososcan by simulating 3D point spread functions. The implemented Explososcan is partly compensated for its boxing effect. The implemented synthetic aperture technique uses one fourth the number of transmit channels of Explososcan. Both techniques scans a volume to 150 mm depth with a frame rate of 18 Hz.

In terms of FWHM, performs Explososcan and synthetic aperture almost the same. At 90 mm depth is Explososcan's FWHM performance 7 % better than that of synthetic aperture. At Explososcan's focus point performed Explososcan better than synthetic aperture, measured in both FWHM and cystic resolution.

Synthetic aperture was found to generally have a better cystic performance than Explososcan. At 120 mm depth achieves synthetic aperture a better cystic resolution, for all cyst sizes, than Explososcan. The $R_{20\text{dB}}$ performance of synthetic aperture was clearly better than Explososcan at all depths except at Explososcan's focus point. Synthetic aperture decreased $R_{20\text{dB}}$ at 90 mm depth by 48 %, compared to Explososcan.

There are still many variables to be optimized for the implemented synthetic aperture, including the f–number, the active sub–aperture size, the number of emissions, and amount of emission beam tilt.

From the simulated point spread functions, it is estimated that synthetic aperture achieves a better imaging quality for medical imaging, than Explososcan. This is based mainly on synthetic aperture's better cystic resolution performance.

ACKNOWLEDGMENTS

This work was financially supported by grant 024-2008-3 from the Danish Advanced Technology Foundation and from BK Medical (BK Medical ApS, Herlev, Denmark).

References

Burckhardt, C. B., P.-A. Grandchamp, and H. Hoffmann (1974). "An Experimental 2 MHz Synthetic Aperture Sonar System Intended for Medical Use". In: *IEEE Trans. Son. Ultrason.* 21.1, pp. 1–6 (cit. on p. 62).

Chiao, R. Y., L. J. Thomas, and S. D. Silverstein (1997). "Sparse array imaging with spatially-encoded transmits". In: *Proc. IEEE Ultrason. Symp.* Pp. 1679–1682 (cit. on p. 62).

Flaherty, J. J., K. R. Erikson, and V. M. Lund (1967). *Synthetic Aperture Ultrasound Imaging Systems*. United States Patent, US 3,548,642. United States Patent, US 3,548,642, 1967, Published 22 Dec 1970 (cit. on p. 62).

Hansen, J. M., M. C. Hemmsen, and J. A. Jensen (2011). "An object-oriented multi-threaded software beamformation toolbox". In: *Proc. SPIE Med. Imag.* Vol. 7968, pages. URL: http://dx.doi.org/10.1117/12.878178 (cit. on p. 67).

Jensen, J. A. (1996). "Field: A Program for Simulating Ultrasound Systems". In: *Med. Biol. Eng. Comp.* 10th Nordic-Baltic Conference on Biomedical Imaging, Vol. 4, Supplement 1, Part 1, pp. 351–353 (cit. on p. 67).

Jensen, J. A., S. Nikolov, K. L. Gammelmark, and M. H. Pedersen (2006). "Synthetic Aperture Ultrasound Imaging". In: *Ultrasonics* 44, e5–e15 (cit. on p. 62).

Jensen, J. A. and N. B. Svendsen (1992). "Calculation of Pressure Fields from Arbitrarily Shaped, Apodized, and Excited Ultrasound Transducers". In: *IEEE Trans. Ultrason., Ferroelec., Freq. Contr.* 39, pp. 262–267 (cit. on p. 67).

Nagai, K. (1985). "A New Synthetic-Aperture Focusing Method for Ultrasonic B-Scan Imaging by the Fourier Transform". In: *IEEE Trans. Son. Ultrason.* SU-32.4, pp. 531–536 (cit. on p. 62).

Ramm, O. T. von, S. W. Smith, and H. G. Pavy (1991). "High speed ultrasound volumetric imaging system – Part II: Parallel processing and image display". In: *IEEE Trans. Ultrason., Ferroelec., Freq. Contr.* 38, pp. 109–115 (cit. on pp. 62, 66).

Ranganathan, K. and W. F. Walker (2007). "Cystic Resolution: A Performance Metric for Ultrasound Imaging Systems". In: *IEEE Trans. Ultrason., Ferroelec., Freq. Contr.* 54.4, pp. 782–792 (cit. on p. 63).

Shattuck, D. P., M. D. Weinshenker, S. W. Smith, and O. T. von Ramm (1984). "Explososcan: A parallel processing technique for high speed ultrasound imaging with linear phased arrays". In: *J. Acoust. Soc. Am.* 75, pp. 1273–1282 (cit. on p. 62).

Smith, S. W., H. G. Pavy, and O. T. von Ramm (1991). "High speed ultrasound volumetric imaging system – Part I: Transducer design and beam steering". In: *IEEE Trans. Ultrason., Ferroelec., Freq. Contr.* 38, pp. 100–108 (cit. on pp. 62, 68).

Soumekh, M. (1999). *Synthetic aperture radar. Signal processing with MATLAB algorithms*. New York: John Wiley & Sons, Inc. (cit. on p. 62).

Vilkomerson, D., J. Greenleaf, and V. Dutt (1995). "Towards a Resolution Metric for Medical Ultrasound Imaging". In: *Proc. IEEE Ultrason. Symp.* Pp. 1405–1410 (cit. on p. 63).

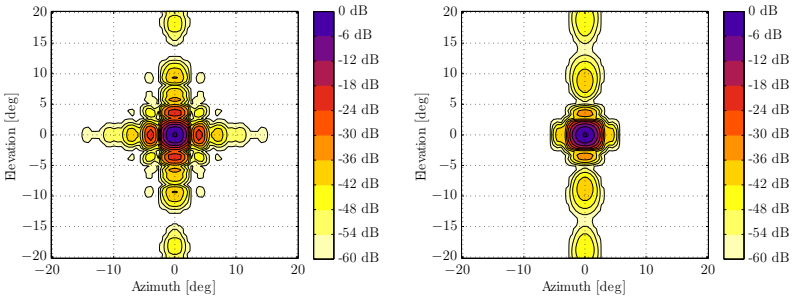

(a) Explososcan C–scan.

(b) Synthetic aperture C–scan.

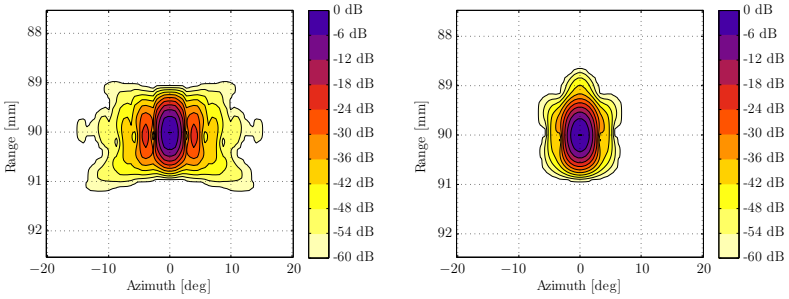

(c) Explososcan azimuth plane.

(d) Synthetic aperture azimuth plane.

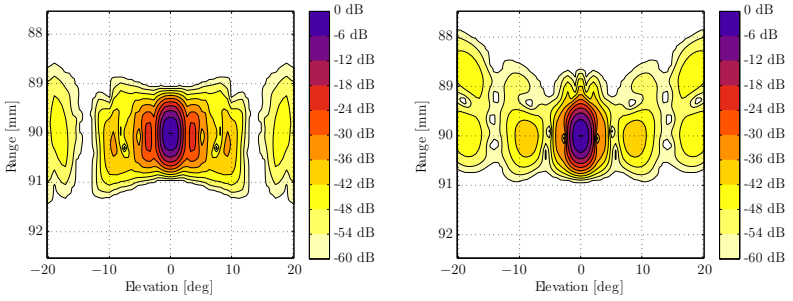

(e) Explososcan elevation plane.

(f) Synthetic aperture elevation plane.

Figure A.5: Explososcan and synthetic aperture 3D point spread function sliced into three 2D planes. The point spread functions are observed at 90 mm depth and 0° azimuth and elevation tilt angle. The left column is Explososcan and the right column is synthetic aperture.

PAPER B

Comparison of 3D Synthetic Aperture Imaging and Explososcan using Phantom Measurements

Authors: Morten Fischer Rasmussen[a], Guillaume Férin[b], Rémi Dufait[b] and Jørgen Arendt Jensen[a].

Published in: *Proceedings of IEEE Ultrasonic Symposium* pp. 113–116, (2012).

Abstract

In this paper, initial 3D ultrasound measurements from a 1024 channel system are presented. Measurements of 3D Synthetic aperture imaging (SAI) and Explososcan are presented and compared. Explososcan is the 'gold standard' for real-time 3D medical ultrasound imaging. SAI is compared to Explososcan by using tissue and wire phantom measurements. The measurements are carried out using a 1024 element 2D transducer and the 1024 channel experimental ultrasound scanner SARUS. To make a fair comparison, the two imaging techniques use the same number of active channels, the same number of emissions per frame, and they emit the same amount of energy per frame. The measurements were performed with parameters similar to standard cardiac imaging, with 256 emissions to image a volume spanning $90° \times 90°$ and 150 mm in depth. This results in a frame rate of 20 Hz. The number of active channels is set to 316 from the design of Explososcan. From wire phantom measurements the point spread functions of both techniques were measured. At 40 mm depth Explososcan achieves a main lobe width (FWHM) of 2.5 mm while SAI's FWHM is 2.2 mm. At 80 mm the FWHM is 5.2 mm for Explososcan and 3.4 mm for SAI, which is a difference of 35 %. Another metric used on the PSF is the cystic resolution, which expresses the ability to detect anechoic cysts in a uniform scattering media. SAI improved the cystic resolution, $R_{20\text{dB}}$, at 40 mm depth from 4.5 mm to 1.7 mm, compared to Explososcan. The speckle pattern looked better for SAI compared to Explososcan's spatial shift variant speckle pattern.

[a]Center for Fast Ultrasound Imaging, Dept. of Elec. Eng., Technical University of Denmark, 2800 Kgs. Lyngby, Denmark.

[b]Vermon S.A., Avenue du Général Renault, 37000 Tours, France.

B.1 Introduction

Ultrasound imaging has since the 1950s improved from advancements made in integrated electronics, computing power and transducer technology. This have led to an increase in both detail and dynamic resolution and has enabled advanced visualisations like color flow map and vector flow estimation. Although these technology advancements has led to high quality 2D imaging, a real-time 3D imaging system has not yet been implemented with a quality on par with 2D imaging.

Two major obstacles has delayed the implementation of real-time 3D imaging systems: the large amount of active channels needed to scan the volume with a 2D array transducer and the low frame rate achievable when scanning a full volume.

Explososcan is the gold standard of real-time 3D ultrasound imaging, developed by Smith, von Ramm and colleagues in the 1980s (Ramm et al. 1991; Shattuck et al. 1984). It is a parallel beamforming technique which addresses the frame rate problem by beamforming multiple lines per emission. A broad transmit beam is emitted and multiple receive beams are focused in parallel during receive. This leads to a lower resolution and the amplitude of the outer receive beams are lower than the center ones.

The paper therefore investigates whether 3D synthetic aperture imaging (SAI) can improve resolution, contrast and remove the beam modulation artifact. Several versions of SAI exist. In this paper, SAI refers to synthetic transmit focusing (STF) where a transmit aperture is synthesized. Using STF the entire volume can be focused at all depths in transmit, in the same way as all depths can be in focus by using dynamic focus in receive.

Earlier work by the authors investigated the performance of 3D SAI and Explososcan using simulations (Rasmussen et al. 2012). In this paper, the imaging quality of SAI and Explososcan is investigated and compared using phantom measurements.

B.2 Methods

There are many degrees of freedom in the design of both Explososcan and SAI. Some constraints on the design process therefore have to be enforced. Both techniques are restricted to use only a fixed amount of active channels. The number of active channels and number of emissions used per imaged volume is determined by the design of Explososcan and then enforced on the design of synthetic aperture imaging. The design choices made during the implementation of the two techniques compared are described in this section.

B.2.1 Explososcan

The Explososcan system is designed with cardiac imaging in mind, which demands a wide scan area and a deep scan depth. A scan area of $90° \times 90°$ and a scan depth of 15 cm are chosen to be usable for cardiac imaging.

To limit the degrees of freedom in the design process of the imaging system, the number of beamformers is chosen to be 16, beamforming 4x4 lines per emission. This

gives a frame rate increase of 16 times compared to classic phased array imaging and is a standard choice in commercial systems. The imaged volume is scanned in 16 emissions per dimension, resulting in 256 emissions and 64x64 lines being beamformed in total. When scanning down to 15 cm a pulse repetition frequency, f_{prf}, of 5 kHz can be used, which leads to a frame rate of 20 Hz. Since 16 emissions are used to scan 90° per dimension, each transmit beam must have a main lobe width of $2\alpha = 90°/16 = 5.6°$. The beamwidth at the focal point is found as:

$$\text{FWHM} = 2r\tan\alpha \ , \tag{B.1}$$

where r is the distance from the aperture to the focal point and FWHM is the full width at half max. Eq. (B.1) comes from solving for the opposite side in the triangle made of the three points: the center of the transducer, the focal point and the point at the same depth as the focal point but offset by half the beamwidth (FWHM/2) to the side. The width of an aperture that has the FWHM from (B.1) is approximately:

$$w = \frac{r\lambda}{\text{FWHM}} = \frac{\lambda}{2\tan\alpha} \ , \tag{B.2}$$

where λ is the wavelength of the emitted wave and w is the aperture width[1]. Inserting the values for λ and α in (B.2) gives an aperture width of 5.22 mm, or approximately 20 transducer elements. A circle with a diameter of 20 has an area of 314, but because symmetry is desired, 316 elements are used in the transmit aperture. The edge of the active transmit aperture is rounded by a Tukey window, to reduce side lobes. The resulting transmit aperture and its apodization is seen in Fig. B.1(a).

In receive, 4x4 lines must be beamformed within each transmit beam. The beamwidth in receive should therefore be one fourth of the transmit beamwidth, requiring the receive aperture to be four times as wide as the transmit aperture. This gives an 80x80 element large receive aperture, which can not be implemented on the available 32x32 element transducer. Different aperture layouts have been analyzed in (Karaman et al. 2009; Smith et al. 1991). In this work, the receive aperture is chosen as two crosses with a width of 32 elements and a total of 316 active elements. The receive aperture is shown in Fig. B.1(b). The focus point is placed at a distance of 50 mm, giving an F# of 8.3.

B.2.2 Synthetic aperture imaging

The SAI system inherits from the Explososcan design the number of active channels and the number of emissions it may use to image one volume.

Where Explososcan uses the same aperture for each emission, SAI slides the active aperture between each emission on the transducer surface. For each emission, SAI synthesizes a virtual source (VS) which is an element in the synthesized aperture. The synthesized aperture therefore has 256 elements, ordered as a circle with a diameter of

[1] It is here used that $\text{FWHM} = \lambda F\# = \lambda r/w$.

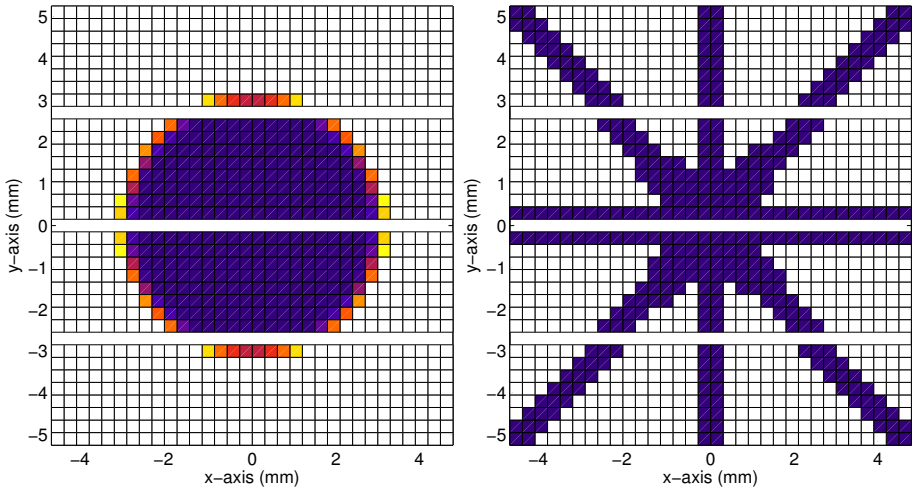

(a) TX aperture with apodization. (b) RX aperture with apodization.

Figure B.1: The layout and apodization of Explososcan's transmit and receive aperture.

approximately 18 elements. This is illustrated in Fig. B.2, where the synthesized virtual source is shown with a yellow cross. By comparing with Exploscan's transmit aperture, which has a diameter of 20 elements, it is seen that SAI's synthesized transmit aperture is slightly smaller. The virtual source is placed at 5 mm depth, giving an F# of 0.83.

Table B.1: Transducer parameters

Parameter name	Notation	Value
Center frequency	f_0	3.5 MHz
Transducer pitch –x	d_x	300 µm
Transducer pitch –y	d_y	300 µm
Active number of elements –x	N_{act_x}	32
Active number of elements –y	N_{act_y}	32
Inactive rows	–	9,18,27

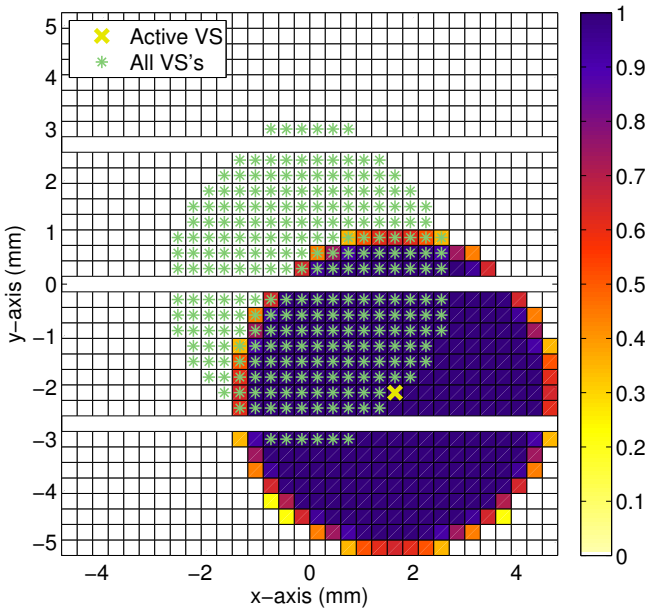

Figure B.2: The apodization of one of SAI's transmit apertures. The virtual source being synthesized in this emission is indicated with a yellow cross. The synthesized aperture consists of all the green stars.

B.3 Measurement setup

All measurements are carried out using the 1024 channel experimental scanner *synthetic aperture real-time ultrasound system* (SARUS). SARUS can acquire data on all 1024 individual channels for a couple of heart beats, and is capable of transmitting any kind of excitation. It samples with 70 MHz in 12 bit. The ultrasound probe used in the measurements is a piezocomposite matrix transducer with 1024 elements, made by Vermon S.A., Tours, France. The probe is composed of four 2D sub-apertures, that each contains 8x32 elements. The sub-apertures are joined into one 2D array. On the junction between sub-apertures, there is an inactive row with a width of one pitch. The transducer elements are, thus, organized as 35x32 elements, and inactive rows are placed at rows 9, 18 and 27. The transducer parameters are listed in Table B.1, and the inactive elements are shown as white stripes in Fig. B.1 and B.2.

The wire phantom used consists of thin cobber wires with a diameter of 0.07 mm. The wires are located at 40 mm and 80 mm depth. The tissue phantom used is model 571 made by Danish Phantom Service, which mimics the properties of real tissue.

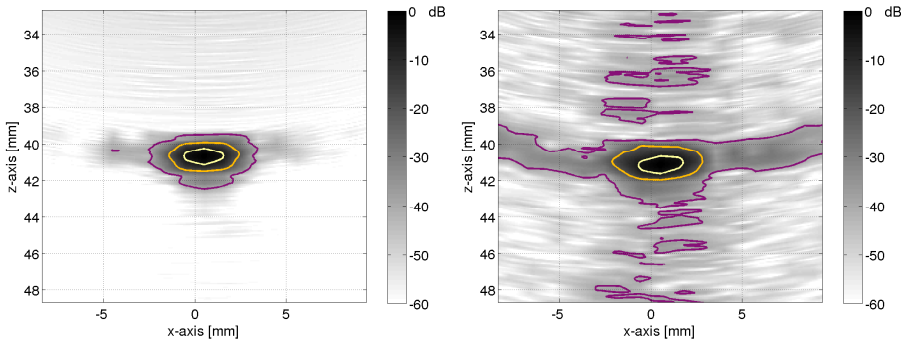

(a) SAI, wire at 40 mm depth.

(b) Explososcan, wire at 40 mm depth.

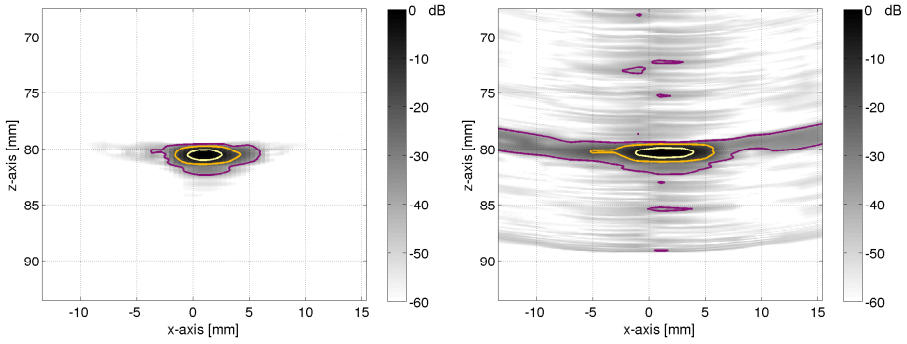

(c) SAI, wire at 80 mm depth.

(d) Explososcan, wire at 80 mm depth.

Figure B.3: 2D slices of SAI's and Explososcan's 3D PSF. The left column is made with SAI and the right with Explososcan. The x-axis is the same as used in Fig. B.1 and B.2, and the z-axis is orthogonal to the transducer surface. To ease the comparison, three isocurves at −6 dB, −20 dB and −40 dB are overlaid on the PSFs.

B.4 Results

When slicing a volume measurement of a wire orthogonal to the wire direction, a 2D slice of the 3D point spread function (PSF) is observed. Fig. B.3 shows the measured PSF of both SAI and Explososcan at approximately 40 mm and 80 mm depth with a 60 dB dynamic range. At both depths, the PSF of SAI is seen to have lower side lobes and be more circular symmetric than the PSF of Explososcan. At 40 mm depth, which is close to Explososcan's focal point, the main lobe size of the two techniques are similar. The FWHM is at 40 mm depth measured to 2.2 mm for SA imaging against 2.5 mm for the Explososcan technique. At 80 mm depth, which is far away from Explososcan's focal point, the main lobe is 3.4 mm for SAI and 5.2 mm for Explososcan. The noise floor is seen to be higher in both of Explososcan's PSFs than for SAI's PFSs. A low peak value at the center of Explososcan's PSF is causing the relative high noise floor. The wire used is very thin and reflects therefore little energy. Explososcan only has a single emission where the main lobe is reflected by the wire. In contrast, in SAI all 256 broad emission beams get reflected by the wire and are coherently summed after the beamforming. The low SNR in the Explososcan measurements are probably the reason for its high side lobe levels.

From the PSFs shown in Fig. B.3 the clutter to total energy ratio (CTR) (Ranganathan and Walker 2007; Vilkomerson et al. 1995) is calculated and shown in Fig. B.4. The CTR predicts the contrast between the center of an anechoic cyst embedded in a continuously back scattering media and its surroundings, and is given by:

$$\mathrm{CTR}(R) = \sqrt{\frac{E_{out}(R)}{E_{tot}}}\,, \tag{B.3}$$

where E_{out} is the signal energy outside a circular region with radius, R, centered on the peak of the PSF and E_{tot} is the total PSF energy. This can be used to predict how well an imaging system can detect small cysts. As seen from Fig. B.4 will a small cyst appear darker in a SAI image than in an Explososcan image. The $R_{20\mathrm{dB}}$ is how large a cyst has to be to obtain an intensity difference of 20 dB. The smaller the cyst radius, the better. At 40 mm depth the $R_{20\mathrm{dB}}$ is for SAI 1.7 mm and for Explososcan it is 4.5 mm, and at 80 mm depth $R_{20\mathrm{dB}}$ has increased to 2.8 mm and 8.3 mm, respectively.

In Fig. B.5 two C-scans of the tissue mimicking phantom at a depth of 30 mm is seen. The spatial variance, or "block artifact", is visible in the Explososcan C-scan in Fig. B.5(b), whereas it is not visible in the SAI C-scan in Fig. B.5(a).

B.5 Discussion and conclusion

3D measurements made with both SAI and with Explososcan was presented. SAI was found to have a smaller main lobe, lower side lobes and better SNR than Explososcan. At 40 mm depth, which is close to Explososcan's focal point, their main lobe sizes

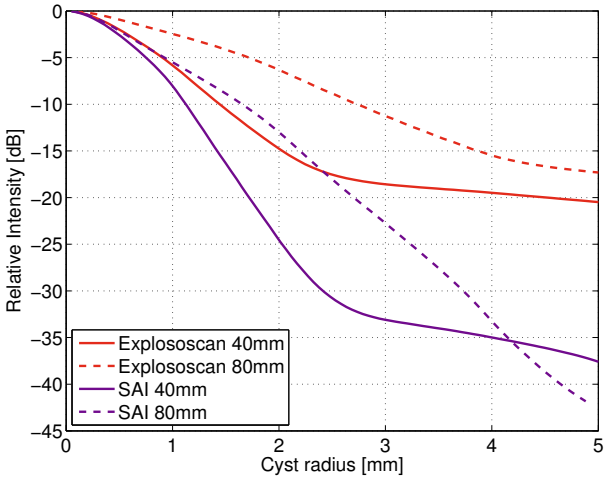

Figure B.4: Clutter to total energy ratio extracted from the PSFs in Fig. B.3.

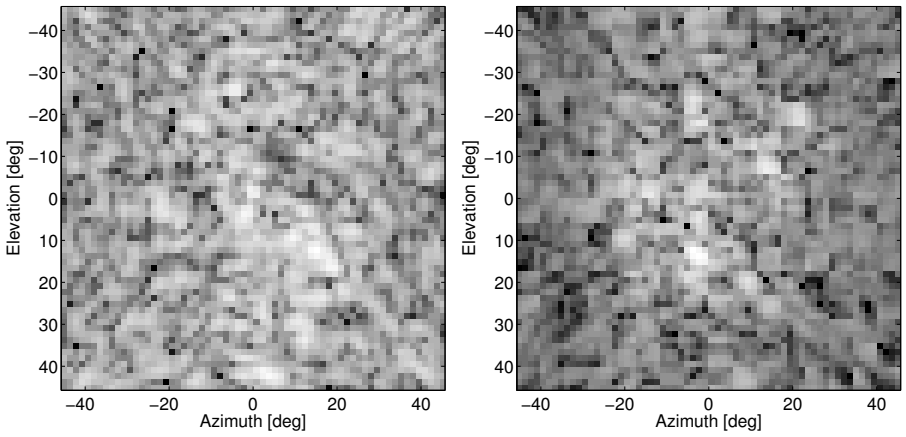

(a) SAI C-scan.

(b) Explososcan C-scan.

Figure B.5: Explososcan and SAI C-scan of speckle in a tissue mimicking phantom. The C-scan is made at a depth of 30 mm and the dynamic range is 40 dB. Each of the 64×64 pixels represents one scan line.

were similar, but at 80 mm depth, which is far away from Explososcan's focal point, SAI outperformed Explososcan. SAI was shown to have a better cystic resolution than Explososcan. The speckle pattern was for SAI more pleasant to look at than the boxed speckle pattern of Explososcan.

Acknowledgments

This work was financially supported by grant 024-2008-3 from the Danish Advanced Technology Foundation and from BK Medical ApS, Herlev, Denmark.

References

Karaman, M., I. O. Wygant, O. Oralkan, and B. T. Khuri-Yakub (2009). "Minimally Redundant 2-D Array Designs for 3-D Medical Ultrasound Imaging". In: *IEEE Trans. Med. Imag.* 7, pp. 1051–1061 (cit. on p. 75).

Ramm, O. T. von, S. W. Smith, and H. G. Pavy (1991). "High speed ultrasound volumetric imaging system – Part II: Parallel processing and image display". In: *IEEE Trans. Ultrason., Ferroelec., Freq. Contr.* 38, pp. 109–115 (cit. on p. 74).

Ranganathan, K. and W. F. Walker (2007). "Cystic Resolution: A Performance Metric for Ultrasound Imaging Systems". In: *IEEE Trans. Ultrason., Ferroelec., Freq. Contr.* 54.4, pp. 782–792 (cit. on p. 79).

Rasmussen, M. F., J. M. Hansen, G. Férin, R. Dufait, and J. A. Jensen (2012). "Preliminary comparison of 3D synthetic aperture imaging with Explososcan". In: *Proc. SPIE Med. Imag.* Ed. by J. G. Bosch and M. M. Doyley. Vol. 8320. 83200F. SPIE, pp. 1–9 (cit. on p. 74).

Shattuck, D. P., M. D. Weinshenker, S. W. Smith, and O. T. von Ramm (1984). "Explososcan: A parallel processing technique for high speed ultrasound imaging with linear phased arrays". In: *J. Acoust. Soc. Am.* 75, pp. 1273–1282 (cit. on p. 74).

Smith, S. W., H. G. Pavy, and O. T. von Ramm (1991). "High speed ultrasound volumetric imaging system – Part I: Transducer design and beam steering". In: *IEEE Trans. Ultrason., Ferroelec., Freq. Contr.* 38, pp. 100–108 (cit. on p. 75).

Vilkomerson, D., J. Greenleaf, and V. Dutt (1995). "Towards a Resolution Metric for Medical Ultrasound Imaging". In: *Proc. IEEE Ultrason. Symp.* Pp. 1405–1410 (cit. on p. 79).

PAPER C

Comparison of 3-D Synthetic Aperture Phased Array Ultrasound Imaging and Parallel Beamforming

Authors: Morten Fischer Rasmussen and Jørgen Arendt Jensen.

Accepted for publication in: *IEEE Transactions on Ultrasonics, Ferroelectrics, and Frequency Control*, June 4, 2014.

Abstract

This paper demonstrated that synthetic aperture imaging (SAI) can be used to achieve real-time 3-D ultrasound phased array imaging. It was investigated whether SAI increases the image quality compared with the parallel beamforming (PB) technique for real-time 3-D imaging. Data were obtained using both Field II simulations and measurements with the ultrasound research scanner SARUS and a 3.5 MHz 1024 element 2-D transducer array from Vermon S.A. (Tours, France). To limit the probe cable thickness, 256 active elements were used in transmit as well as receive for both techniques. The two imaging techniques were designed for cardiac imaging, which requires sequences designed for imaging down to 15 cm of depth and a frame rate of at least 20 Hz. The imaging quality of the two techniques was investigated through simulations as a function of depth and angle. SAI improved the full-width-at-half-maximum (FWHM) at low steering angles by 35 %, and the 20 dB cystic resolution by up to 62 %. The FWHM of the measured line spread function (LSF) at 80 mm depth showed a difference of 20 % in favor of SAI. SAI reduced the cyst radius at 60 mm depth by 39 % in measurements. SAI improved the contrast-to-noise ratio measured on anechoic cysts embedded in a tissue mimicking material by 29 % at 70 mm depth.

Manuscript received February 13, 2014; accepted June 4, 2014. This research was financially supported by grant 024-2008-3 from the Danish Advanced Technology Foundation, by the Technical University of Denmark, and by BK Medical ApS, Denmark.

The authors are with the Center for Fast Ultrasound Imaging, Department of Electrical Engineering at the Technical University of Denmark, Kgs. Lyngby, Denmark. E-mail of corresponding author: research@mofi.dk.

Digital Object Identifier: xxxx

The estimated penetration depth on the same tissue mimicking phantom showed SAI increased the penetration by 24 % compared with PB. Neither SAI nor PB achieved the design goal of 15 cm penetration depth. This is likely due to the limited transducer surface area and a low SNR of the experimental scanner used.

C.1 Introduction

Since the 1950s the usability and quality of ultrasound imaging has improved due to advancements made in integrated electronics, algorithms, computing power, and transducer technology (Bennett et al. 1982; Burckhardt et al. 1974; Wild 1950). This has led to an increase in resolution, contrast and penetration depth. These technology advancements have led to high quality 2-D and 3-D imaging systems. The state of the art 3-D imaging systems have up to more that 9000 active elements, beamformers integrated directly in the ultrasound probe and some requires water cooling. These ultrasound systems are therefore very expensive to both develop and produce. The purpose of this paper is to investigate the achievable 3-D image quality possible with a modest amount of active elements. It is investigated which beamforming technique of synthetic aperture imaging (SAI) (Burckhardt et al. 1974; Flaherty et al. 1967; Karaman and O'Donnell 1998; Karaman, Ş. Bilge, et al. 1998; Ylitalo and Ermert 1994) and parallel beamforming (PB) (Delannoy et al. 1979; Shattuck et al. 1984) that achieves the best image quality. Earlier work by the authors investigated the performance of 3-D synthetic aperture imaging and parallel beamforming using simulations (M. F. Rasmussen, Hansen, et al. 2012) and phantom studies (M. F. Rasmussen, Férin, et al. 2012). In this paper, a more realistic setup is used, using only 256 active elements and beamformer channels as opposed to 1024 active elements and beamformers. The measurements are also expanded, now including cysts and tissue-mimicking phantom measurements.

Two major obstacles have delayed the implementation of real-time 3-D imaging systems: the large amount of channels on a 2-D array transducer to scan the volume and the low frame rate often achievable when scanning a full volume. Parallel beamforming addresses the frame rate problem by broadening the transmit beam and focusing multiple receive beams in parallel. This increases the frame rate proportional to the number of lines beamformed per emission. The downside compared to emitting a focused beam for each receive-beamformed line is a lower resolution and an amplitude modulation artifact of the beamformed lines. Different measures have previously been pursued to minimize the parallel beamforming artifact (Augustine 1987; Hergum et al. 2007; Liu et al. 2002), these are not investigated or applied in this work. Parallel beamforming was, in the form of Explososcan (Ramm et al. 1991; Shattuck et al. 1984) implemented in hardware by Smith, von Ramm and colleagues as early as the 1980s.

Several versions of SAI exist (Gammelmark and Jensen 2003b; Karaman and O'Donnell 1998; Nock and Trahey 1992; Ylitalo and Ermert 1994). In this paper, SAI refers to synthetic transmit focusing, where a virtual transmit aperture is synthesized (M. H. Bae and Jeong 2000; Frazier and O'Brien 1998; Karaman, Li, et al. 1995). Using synthetic

transmit focusing an entire volume can be dynamically focused in transmit, whereas conventional transmit focusing only has a fixed focal depth in transmit.

Related work was carried out by Karaman et al., who increased the SNR of synthetic aperture imaging by transmitting from multiple elements to emulate a single powerful virtual transmit element (Karaman, Li, et al. 1995). Achieving high frame rate 3-D synthetic aperture imaging by mechanically sweeping a 1-D phased array was investigated by Lockwood et al. (Lockwood et al. 1998). Nikolov and Jensen (Nikolov and Jensen 2000) used the elevation focal point as a virtual source in the elevation direction with a mechanically scanned 1-D transducer array. A thorough investigation of 2-D synthetic aperture phased array imaging was made by Johnson et al (Johnson, Karaman, et al. 2005; Johnson, Oralkan, et al. 2005). They showed that for optimal image quality when the number of active elements are limited, the active subarray must be translated between the emissions. High frame rate 3-D imaging with a 2-D phased array was investigated via simulations by Kim et al. (Kim and Song 2008).

Synthetic aperture imaging is susceptible to tissue motion artifacts, which degrades the image quality. Previous literature has demonstrated tissue motion compensation in the axial direction (Bilge et al. 1996; Karaman, Ş. Bilge, et al. 1998; Trahey and Nock 1992) and in two dimensions (Gammelmark and Jensen 2003a, 2014; Ho et al. 2013). Since the tissue inherently moves in 3-D, tissue motion compensation should ideally be carried out in all three dimensions when performing 3-D imaging. To our knowledge, reliable 3-D tissue motion compensation has yet to be demonstrated. 3-D tissue motion compensation is therefore not investigated nor applied in this work.

Tissue harmonic imaging is routinely applied when performing conventional clinical cardiac imaging. Synthetic aperture tissue harmonic imaging has been demonstrated by Bae et al. (M. Bae et al. 2008), who bandpass filtered the second harmonic before beamforming, and by Rasmussen et al. (J. H. Rasmussen et al. 2013), who applied pulse inversion. Generating the second harmonics requires sufficient acoustic pressure. This demonstrates that Tissue Harmonic imaging can be performed with both parallel beamforming and synthetic aperture imaging. In this paper the image quality is investigated for the fundamental harmonic.

In the next section, the two techniques are further introduced and the imaging sequences are designed and optimized. In Section C.3, the imaging quality is investigated by simulations of the point spread function (PSF) at a large number of positions within the imaged volume. The PSF simulations show that synthetic aperture imaging improves the detail resolution at small steering angles, compared to parallel beamforming. With larger steering angles, the detail resolution performance of the two techniques are similar. The contrast resolution is significantly improved by synthetic aperture imaging at all positions in the entire imaged volume. In Section C.4, the imaging quality is investigated using wire and cyst phantom measurements. The wire phantom measurements are carried out at a low steering angle and show the same tendency as the simulations; synthetic aperture imaging increases resolution as well as contrast. The cyst phantom measurement confirms that synthetic aperture imaging increases the contrast at all depths, compared to parallel

beamforming. Measurements on a tissue mimicking phantom indicate that the penetration depth is deeper for synthetic aperture imaging compared to parallel beamforming. Conclusion and Discussion follow in Section C.5.

C.2 Methods

In this section, the implementations of the two techniques are described. Certain restrictions must be imposed for the comparison to be realistic, such as the width of the aperture, the number of active channels used, and the use of multiplexing. First, these restrictions are determined, then an image quality metric, "cystic resolution", is introduced, and finally, implementation and optimization of both techniques are carried out using simulations.

The two imaging techniques are designed for cardiac imaging, which requires imaging down to 15 cm and a frame rate f_r of at least 20 Hz. To be comparable with products from the medical ultrasound industry, a volume scan spanning 90° in both the azimuth and elevation direction is chosen.

With a maximum scan depth r_{max} of 15 cm and a speed of sound c equal to approximately 1540 m/s, the maximum pulse repetition frequency is

$$f_{prf} = \frac{c}{2\,r_{max}} = 5.133\,\text{kHz}\ . \tag{C.1}$$

The possible number of emission per frame then becomes

$$N_{ems} = \frac{5.133\,\text{kHz}}{20\,\text{Hz}} \approx 256\ . \tag{C.2}$$

Using 256 emissions per frame allows for resolving the azimuth and elevation directions with $\sqrt{256} = 16$ emissions each.

Due to the constant increase in processing power of ultrasound scanners, the amount of ultrasound channels that can be processed increases with time. A limiting factor is the diameter and weight of the cable connecting the ultrasound probe with the ultrasound system. If the cable is too heavy, the operator will risk injuring his or her wrist when scanning on a daily basis. To impose a limit on the cable size, both techniques are therefore limited to 256 active channels at a time during both transmitting and receiving. Multiplexing electronics in the handle that selects the active transducer elements are assumed available, and are in this study otherwise neglected.

C.2.1 An Image Quality Metric: Cystic Resolution

Two quality metrics are used for evaluating the images. The *full-width-at-half-maximum* (FWHM) and the *cystic resolution*. The cystic resolution describes the ability to detect an anechoic cyst in a uniform scattering medium (Vilkomerson et al. 1995). Specifically, the cystic resolution gives the intensity at the center of an anechoic cyst of a given size relative to its surrounding uniformly back-scattering medium. The lower the intensity at the center

of the cyst, i.e. the darker it appears in the image for a given cyst size, the better the imaging performance of the system. This metric mimics an often seen situation in medical ultrasound where the object of interest is a weakly reflecting medium, such as blood or a cyst, surrounded by a stronger back-scattering medium. The relative intensity (RI) of the anechoic cyst was shown by Ranganathan and Walker (Ranganathan and Walker 2007), to be quantized as the clutter energy to total energy ratio,

$$\mathrm{RI}(R) = \sqrt{\frac{E_{out}(R)}{E_{tot}}} = \sqrt{1 - \frac{E_{in}(R)}{E_{tot}}}\,, \tag{C.3}$$

where E_{in} is the signal energy inside a circular region with radius R centered on the peak of the point spread function, E_{tot} is the total point spread function energy, and E_{out} is the point spread function energy outside the circular region. To achieve a single number from the $\mathrm{RI}(R)$-curve, one either determines the relative intensity for a single cyst radius, or determines the required radius to achieve a certain relative intensity, e.g. the cyst radius at which the intensity at center of the cyst is 20 dB lower than its surroundings, written as $R_{20\mathrm{dB}}$. In this work the cystic resolution is presented as the cyst radius $R_{20\mathrm{dB}}$.

C.2.2 Parallel Beamforming

For 3-D imaging, parallel beamforming makes $N \times N$ receive lines per emission. From trial and error, $N = 4$ scan lines per dimension were determined as an adequate spatial sampling frequency to represent the PSF at the focal point. As determined in the previous section, the maximum f_{prf} allows for 16 emissions per steering angle, leading to $16 \times 4 = 64$ scan lines to be beamformed per dimension per emission. Beamforming 4×4 lines in parallel per emission gives a frame rate increase of 16 times compared with conventional phased array imaging.

The transmit beam should therefore be four times as wide as the receive beams. In Fig. C.1, a transducer array which focuses its transmit beam at the marked focal point is shown. The transmit beam width in radians is α, the aperture width is w and the focal depth r. Ideally, the transmit beam should have a main-lobe width of $\alpha = 90°/16 = 5.63°$. As seen in Fig. C.1, when the focus point is directly under the center of the transducer, a right-angled triangle can be drawn from the three points: the center of the active aperture, the focal point and the half-width-at-half-maximum (HWHM) of the transmit beam at the focus depth. Using this triangle and that $\mathrm{HWHM} = \mathrm{FWHM}/2 \approx f_{\#}\lambda/2$, the following approximate relation can be written

$$\tan\frac{\alpha}{2} = \frac{\mathrm{HWHM}}{r} \approx \frac{f_{\#}\lambda}{2r} = \frac{\lambda}{2w} \tag{C.4a}$$

$$\Updownarrow$$

$$w \approx \frac{\lambda}{2\tan\frac{\alpha}{2}}\,, \tag{C.4b}$$

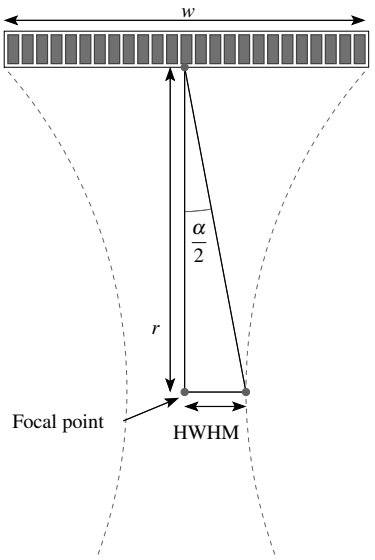

Figure C.1: Geometry for determining which aperture width w, which approximately relates to a given beam width α. r is the distance from the transducer surface to the focal point.

where λ is the wavelength of the emitted wave and $f_\# = r/w$ is the f-number. In (C.4) $\tan\frac{\alpha}{2}$ is assumed nonzero, implying that the main-lobe width is always nonzero. Inserting the values for λ and α into (C.4b) gives an aperture width of $w = 5.22\,\text{mm}$. Table C.1 shows the parameters of the 32×32 element 2-D transducer array used for both simulations and measurements. The pitch is 300 µm in both directions. Therefore, an aperture width of 5.22 mm corresponds approximately to a 17 element wide aperture. A circular aperture with a diameter of 17 elements contains approximately 226 elements, however 256 active channels are available for the scanner in both transmit and receive. If the diameter of the circular aperture is increased to 18 elements, it contains approximately 256 elements. The circular aperture with 256 active elements is shown in Fig. C.2(a). Since the transducer array is made of four stacked piezo crystals, the array contains three joints where no elements are present.

It has been shown (Karaman, Wygant, et al. 2009; Smith et al. 1991) that when the number of active channels is restricted and a wide aperture is needed, the simple sparse cross array results in one of the best ratios between imaging quality and the number of active elements used. Three possible transmit cross array apertures of differing widths are shown in Fig. C.2(b)-(d).

Since all shown transmit apertures in Fig. C.2 are wider than w from (C.4b), their transmit beam width will be too narrow. To compensate for this, the effective width of

the apertures is reduced by applying an apodization function. The Tukey apodization function has a parameter ψ that changes the apodization continuously from a rectangular apodization ($\psi = 0$) to a Hann apodization ($\psi = 1$). The ψ parameter of the Tukey apodization, which leads to the correct width, is determined by numerical optimization. The optimization routine determines the ψ parameter, which results in an area of the Tukey apodization function equal to the area of the rectangular apodization function. The expression optimized is thereby

$$\arg\min_{\psi} f(\psi) = \left(\sum_{n=1}^{N} \text{Tukey}(n;\psi) - \sum_{m=1}^{M} \text{rect}(m) \right)^2 . \tag{C.5}$$

Four different transmit apertures are shown in Fig. C.2(a)-(d). They are optimized using (C.5) to have equal main-lobe size. The radiation pattern at the focal point and in the far field can be approximated by the Fourier transform of the active aperture (Steinberg 1976, p.12), (Hoctor and Kassam 1990). The 1-D Fourier transform of the center row of each transmit array is calculated and plotted in Fig. C.2(e). The Fourier transform of the 17 element wide rectangular array is plotted as a reference.

The main-lobes of the four transmit apertures are seen to be practically identical, which shows the applicability of (C.5). The side-lobes are seen to decrease faster for the wider apertures, e.g., aperture (c) and (d), compared with the narrower apertures, e.g., aperture (a) and (b). On the other hand, the wider the aperture and the more the aperture is apodized, the less energy is emitted. As a trade-off between emitted energy and side-lobe performance, the 24 element wide cross array, seen in Fig. C.2(b), is chosen as the transmit aperture.

To get a wide receive aperture and thereby a narrow receive beam main-lobe, the cross array is also used in receive. In receive, 64 lines are beamformed per dimension giving a main-lobe width of $\alpha_{RX} = 90°/64 = 1.41°$. Inserting α_{RX} in (C.4b) gives an aperture width of 17.9 mm or approximately 60 elements. Since the available ultrasound probe is $32 \times 0.3\,\text{mm} = 9.6\,\text{mm}$ wide in each dimension, and $32 \times 0.3\,\text{mm} \times \sqrt{2} = 13.6\,\text{mm}$ along the diagonals, this receive aperture cannot be implemented. The widest possible array, a cross array along the diagonals, is chosen as receive aperture. Because the receive aperture is too narrow, it is apodized with a Tukey function with a ψ parameter close to zero. The receive aperture is shown in Fig. C.3.

The last parameter to be determined for the parallel beamforming technique is its focal depth. The influence of the focal depth on the imaging quality is investigated via simulations of the PSF using the ultrasound simulation program Field II (Jensen 1996; Jensen and Svendsen 1992). The PSF is investigated at a zero degree beam steering angle (straight down) at depths of 60, 90, 120 and 150 mm, while the transmit focal depth is varied from 5 mm to 120 mm. The result of the parameter study is shown in Fig. C.4. The main-lobe width in Fig. C.4(a) is almost independent of the focal depth; it only improves locally in the region around the focal depth. In Fig. C.4(b), the cystic resolution $R_{20\text{dB}}$ is shown to be highly dependent on the focal depth, and it obtains a global minimum close

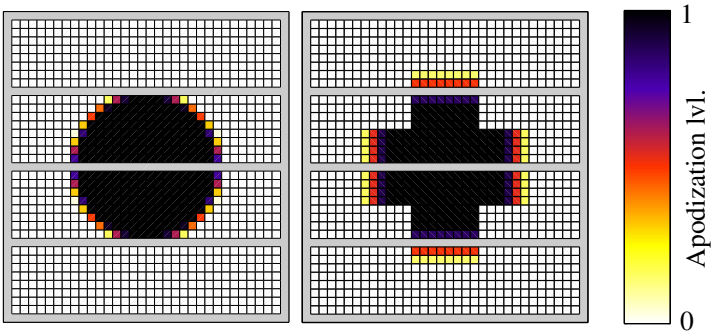

(a) (b)

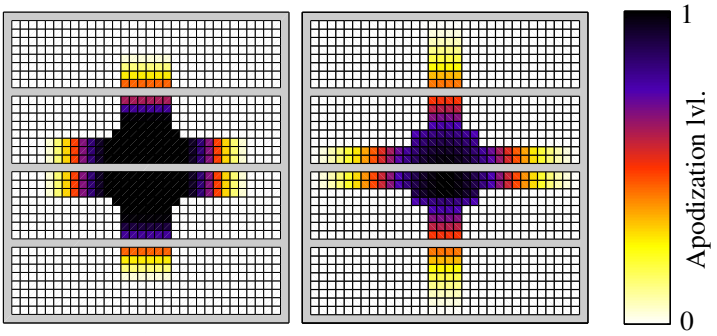

(c) (d)

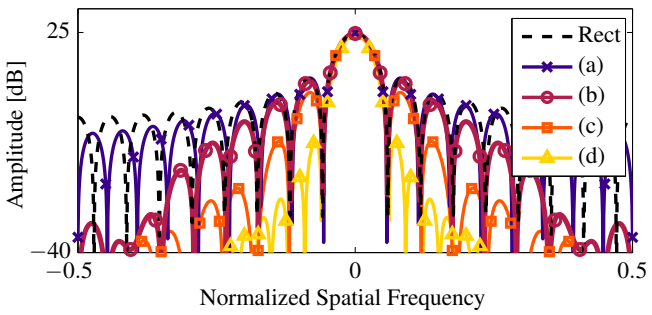

(e)

Figure C.2: In (a)-(d), four different transmit apertures with 256 active elements and approximately the same main-lobe width are shown. In (e) the 1-D Fourier transform of each of the four transmit apertures are shown. The transmit aperture shown in (b) is chosen as the compromise between emitted energy and low side-lobe levels. The transmit aperture is used for all 256 emissions it takes to sample the volume.

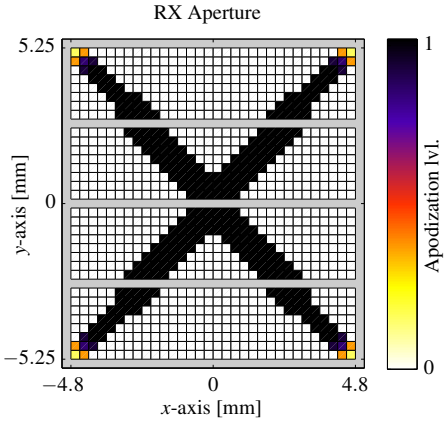

Figure C.3: The receive aperture for parallel beamforming is the widest possible cross array implementable on the 32×32 element array. It contains 256 active elements and is used for all 256 emissions.

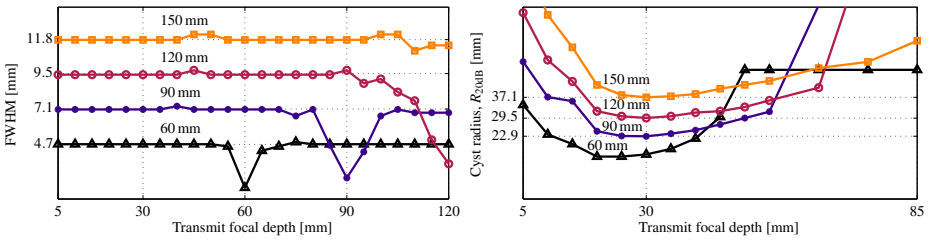

(a) (b)

Figure C.4: Imaging quality metrics extracted from simulated PSFs. In (a), the main-lobe width is shown to be almost independent of the transmit focal depth. In (b) the cystic resolution R_{20dB} is shown to be highly dependent on the transmit focal depth, and it obtains a near global minimum at 30 mm of depth.

to 30 mm of depth. The transmit focal depth of parallel beamforming is therefore chosen to be 30 mm.

This optimized setup of parallel beamforming is used for the rest of this paper.

Table C.1: Transducer, simulation and measurement parameters

Parameter name	Notation	Value	Unit
General Parameters			
Frame rate	f_r	20	Hz
Pulse repetition frequency	f_{prf}	5.133	kHz
Emissions per frame	N_{ems}	256	–
Number of active elem.	N_{act}	256	–
Scan depth (max range)	r_{max}	15	cm
Emission center freq.	f_0	3.0	MHz
Emission cycles	N_{cyc}	4	–
Emission window	W_{ems}	Hann	–
Ultrasound Probe Param.			
Center frequency	f_c	3.5	MHz
Relative bandwidth	BW	66	%
Transducer pitch – x	d_x	300	µm
Transducer pitch – y	d_y	300	µm
Number of elements – x	N_x	32	–
Number of elements – y	N_y	35	–
Number of wired elem.	N_{tot}	1024	–
Inactive rows	–	9,18,27	–
Simulation Parameters			
Sampling frequency	f_{s_sim}	120	MHz
Speed of sound	c_{sim}	1540	m/s
Measurement Parameters			
Sampling frequency	f_{s_meas}	70	MHz
TX Voltage	V_{TX}	±100	V
Sound speed in water	c_{w}	1482	m/s
Sound speed in phantom	c_{pht}	1548	m/s
Attenuation in phantom	α	0.51	$\frac{\mathrm{dB}}{\mathrm{MHz \cdot cm}}$
Wavelength in water	λ_{w}	494	µm
Wavelength in phantom	λ_{pht}	516	µm

C.2.3 Synthetic Aperture Imaging

To avoid grating lobes within the $\pm 45°$ beamformed volume, the pitch of the transducer array should not be larger than $\lambda/2$. The center frequency of the transducer array is 3.5 MHz and the pitch is 300 µm, which corresponds to $0.68\,\lambda$. As a compromise between the transducer efficiency in converting electrical to mechanical energy, and grating-lobe levels the center frequency is set to 3.0 MHz.

Synthetic aperture imaging synthesizes a virtual transmit aperture. One element is synthesized in the synthetic aperture for each focus point. Since 256 emissions are used, 256 virtual elements are synthesized. The relations between aperture array design and the PSF also apply to the synthesized aperture array (Frazier and O'Brien 1998). Especially the width of the synthesized array and the pitch of the virtual elements must be considered. The location of the virtual elements also influences the distribution of the emitted energy and thereby the signal-to-noise ratio (SNR) within the imaged volume.

The synthetic aperture can be synthesized in three different ways: by having a static transmit aperture and steering the transmit beam angle for each emission, by translating transmit aperture and not applying beam steering, or by both translating the transmit aperture and applying beam steering. If a static transmit aperture with beam steering is used, the focal distance must be large, either in front or behind the array, for the width of the synthesized aperture to become large enough. This leads to a large f-number, and, thus, a narrow beam. A narrow beam implies only little overlap between each transmit beam. Thereby only a small aperture is synthesized for any given point in the imaged volume. Usually, this leads to an inferior image quality. If the active aperture is translated and no beam steering is applied, the width of the synthesized array is independent of the transmit f-number. In this case the synthesized array is narrower than the physical array. When no beam steering is applied, the energy of all transmit beams are emitted straight down. For phased array imaging, this leads to the SNR being higher in front of the array, compared with the sides of the imaged volume. The third possibility is to both translate the physical array and to apply transmit beam steering. This has the advantage that even when the transmit f-number is kept low a wide aperture can be synthesized. It is therefore chosen to both translate the active aperture and to apply beam steering of the transmit beam.

To enable the translation of the active aperture, it needs to be small in order to fit on the physical array and still leave room for translation. The active array could either be a 16×16 square or a circle with radius of approximately 9 elements. To increase the circular symmetry of the PSF, the circular shape is chosen as active aperture.

A synthesized wide cross array would result in a small PSF but also in an unequal SNR performance with respect to steering angle. To assure an even SNR performance in all directions, within the pyramidal volume, the active aperture is translated around a square aperture with a side length of 16 elements. The centers of all translated transmit apertures are shown with a dot in Fig. C.5(a). The cross is the center of the shown active aperture. The beam steering is controlled proportionally to the position of the active

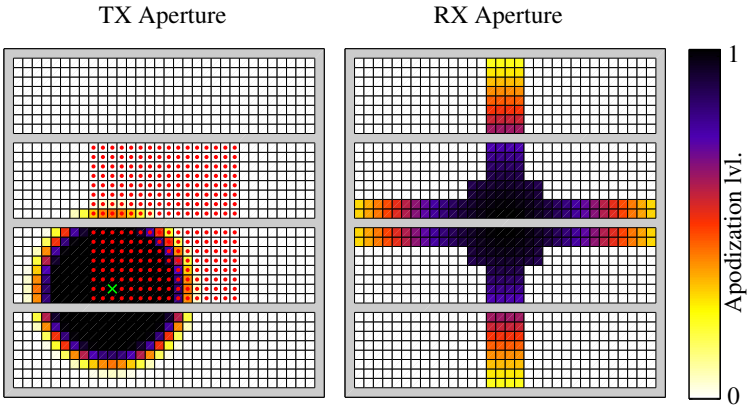

Figure C.5: The synthetic aperture imaging transmit and receive apodization implemented on the 32×32 element array. The transmit aperture translates between each emission. The center of the shown aperture is illustrated with a cross and the centers for the 255 remaining emissions are shown with a dot. The receive aperture is static during all 256 emissions.

aperture. That is

$$\phi(x) = \kappa_x x \tag{C.6a}$$
$$\theta(y) = \kappa_y y\,, \tag{C.6b}$$

where ϕ is the angle in the z-x plane, θ the angle in the z-y plane, x and y the (x,y) coordinate of the center of the active aperture, and κ_x and κ_y are scaling constants. κ_x and κ_y set the maximum transmit beam angle.

The focal depth of the transmit beam and the maximum transmit beam steering angle is determined by a parameter study using Field II. The detail resolution and cystic resolution are investigated at 60 mm depth at angles of $(\phi,\theta) = (0°,0°)$ and $(\phi,\theta) = (30°,30°)$. The result of the parameter study is shown in Fig. C.6. If the maximum transmit beam steering is low, then the image quality is good in the center and poor at 30°. For large transmit beam steering angles and large focal depths, it is the opposite result. As a compromise, the focal depth is chosen to be −6 mm and the maximum beam steering angle to 30°. The negative focal depth means that the focal point is located behind the transducer.

The resulting synthesized aperture is shown in Fig. C.7. The transmit beam for the shown emission is illustrated with an arrow. The source of the beam is the active virtual

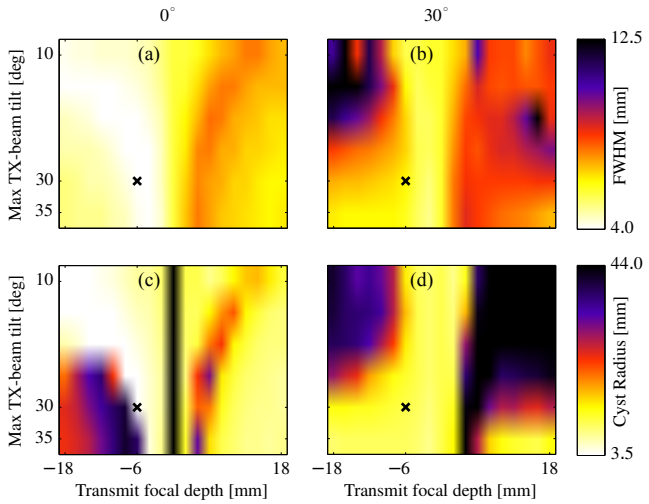

Figure C.6: Optimizing the transmit focal depth and the max transmit-beam angle of synthetic aperture imaging. In (a) and (c) the scatterer is located at an azimuth and elevation angle of $(\phi,\theta) = (0°,0°)$, in (b) and (d) the azimuth and elevation angle is $(\phi,\theta) = (30°,30°)$. In both cases the depth of the scatterer is 60 mm. The chosen parameter combination of a maximum transmit beam angle of 30° and a focal depth of −6 mm is marked with a cross.

source, shown with a circle. For each emission a low resolution volume is beamformed. Each point in the low resolution volume is then weighted by a virtual source apodization. After the weighting the low resolution volumes are summed to create the high resolution volume. The virtual source apodization has the shape of a cone centered around the transmit beam and with its apex located at the active virtual source. The angular width of the cone depends on the focal distance of the active transducer array. The closer the virtual source is to the transducer surface, the wider is the cone. In this work the cone angular width is 50°. The beamformed points located outside of the cone is weighted by 0. The points inside of the cone is weighted by a window function. In this work a Hann-window is applied. The weight of a point within the cone depends on its angular distance to the transmit beam. This procedure removes the noise from the beamformed points which were not insonified by the transmit beam. This optimized setup of synthetic aperture imaging is used for the remainder of this paper.

C.3 Simulations

In this section, the image quality of the two techniques are investigated via simulations. The PSF at different spatial positions, as a function of depth and angle, are simulated.

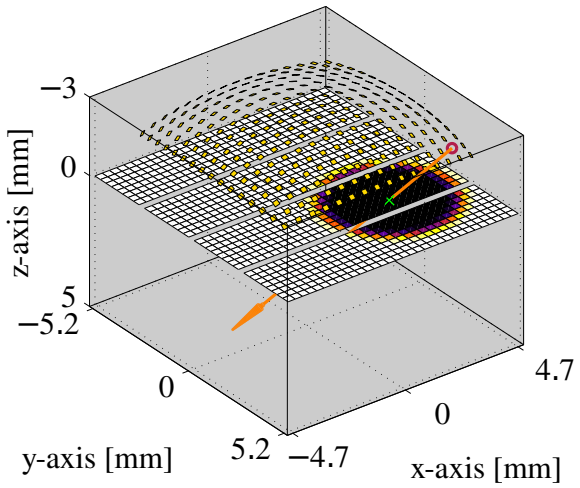

Figure C.7: The setup for a single emission is shown, which synthesizes one virtual element (shown as a circle) in the synthetic aperture. The remaining virtual elements of the sequence are shown as squares raised above the physical aperture. The virtual sources are located behind the aperture and the sound is emitted downwards, in the direction of the arrow. The cross marks the center of the active aperture and the colors of the physical elements represent their apodization value.

C.3.1 Simulation Setup

The ultrasound simulation program Field II is used for the simulation study. A 2-D phased array ultrasound probe, made by Vermon S.A. (Tours, France) with parameters as shown in Table C.1, is emulated. The 2-D transducer has 35×32 elements, of which rows 9, 18 and 27 are inactive, effectively giving 32×32 individually controllable elements.

A single scatter is placed in front of the transducer array and then imaged using the optimized imaging sequences described in the previous section. The simulated receive signals are Hilbert-transformed, and the analytic samples are beamformed. After the Hilbert transform, the samples contain both the in-phase and the quadrature components of the signal and are now referred to as *IQ-samples* or the *IQ data set*. The image quality metrics are applied on a 2-D slice of the 3-D PSF. The PSF in the axial direction is mostly dependent on the emission pulse, whereas in the ϕ- and θ-directions it is mostly dependent on the imaging method. The PSFs are therefore sliced into a C-Scan, a 2-D plane the shape of a spherical surface with a constant distance to the center of the transducer array. The two dimensions in the C-scan are the two angles ϕ and θ, which are also termed the azimuth and elevation angles, respectively.

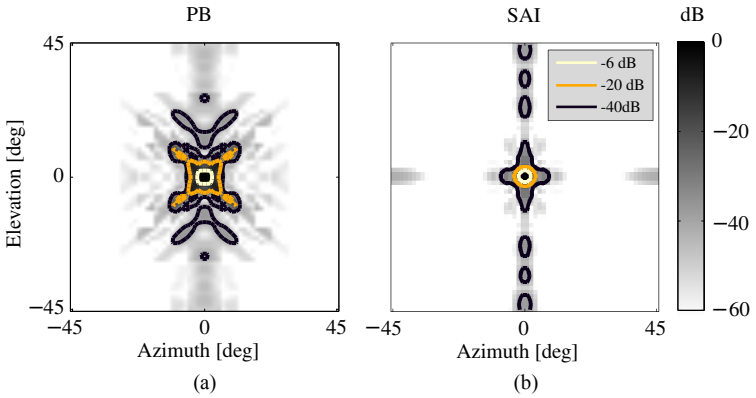

Figure C.8: Simulated C-scans of the 3-D PSFs of parallel beamforming and synthetic aperture imaging at a depth of 60 mm. The dynamic range of the gray scale is 60 dB. The main-lobe width is seen to be similar for the two techniques. The side-lobes, especially at −20 dB, are lower for synthetic aperture imaging. The −20 dB isocurve in (a) is seen to have four distinct corners.

C.3.2 Simulation Results

In Fig. C.8 the PSF C-scan of both parallel beamforming and synthetic aperture imaging at a depth of 60 mm are shown as gray scale images with dynamic range of 60 dB. The main-lobes of the two techniques are seen to be similar in both the elevation and azimuth directions. The side-lobe levels are clearly lower for synthetic aperture imaging than for parallel beamforming. The side-lobes are seen to be asymmetrical, as they are wider in the elevation direction than in the azimuth direction. The asymmetric PSF is due to the asymmetry of the transducer array used. The transducer array contains three inactive rows of elements. These discontinuities cause the increased side-lobe levels in the elevation direction. Low intensity grating-lobes are visible in the azimuth direction of the synthetic aperture imaging PSF. This is probably due to the pitch of both the physical and synthesized arrays being larger than $\lambda/2$. In the elevation direction it is hard to separate the side-lobes from grating-lobes.

The FWHM of the simulated PSFs in Fig. C.9(a) is seen to be slightly better for synthetic aperture imaging than for parallel beamforming, at all depths. The difference between the two techniques increases with depth. The FWHM increases linearly with depth, which is expected for a phased array system with a constant active aperture width. Parallel beamforming has a slightly increased FWHM performance at its transmit focal depth at 30 mm, which is not expected. In the parallel beamforming PSF at 60 mm depth, shown in Fig. C.8(a), the −20 dB isocurve is seen to have four distinct corners. The intensity of the PSF at the four corners increases abruptly around 30 mm depth to above −6 dB intensity. This directly influences the FWHM measure and is the reason for the

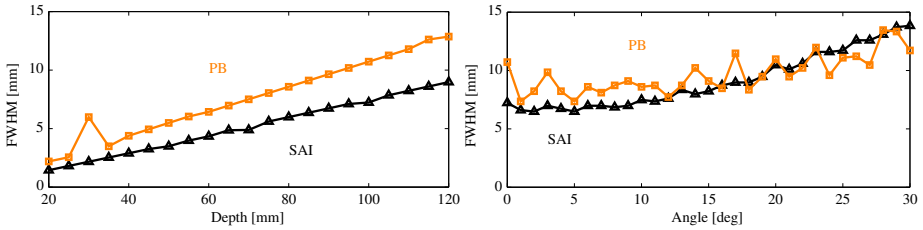

(a) (b)

Figure C.9: The main-lobe size in (a) is seen as a function of depth with no tilt angle ($(\phi,\theta) = (0°,0°)$), and in (b) as a function of angle ($(\phi,\theta) = (\text{angle}, \text{angle})$) at 100 mm of depth. For all depths in (a), the FWHM of the PSFs is seen to be slightly better for synthetic aperture imaging than for parallel beamforming. In (b) the FWHM performance improvement of synthetic aperture imaging is seen to be limited to angles up to about 10°-15°. At larger angles, the FWHM of parallel beamforming and synthetic aperture imaging are almost equal.

FWHM peak in Fig. C.9(a). Since synthetic aperture imaging is transmit focused at all depths, it has no specific depth with an unusually increased FWHM performance. Fig. C.9(b) shows the FWHM at a depth of 100 mm as a function of steering angle. The FWHM increases slightly with increasing steering angle. This is also as expected, since the effective aperture width decreases with increasing steering angle. Parallel beamforming is seen to have a slightly better FWHM at increasing angles compared with synthetic aperture imaging.

In Fig. C.10(a) the calculated cystic resolution described in Section C.2.1 is plotted as a function of depth. The cystic resolution is seen to be significantly better for synthetic aperture imaging than for parallel beamforming. The difference between the two techniques increases with depth. The cystic resolution as a function of beam steering angle is plotted in Fig. C.10(b). The difference in cystic resolution performance is largest when no beam steering angle is applied and decreases with increasing angle. It is also seen that the imaging performance of parallel beamforming oscillates once for each emission. The angles of the parallel beamforming transmit beams are illustrated with vertical dashed lines. Parallel beamforming performs better close to its transmit beams and worse in between them. The synthetic aperture imaging sequence uses unfocused emissions, and no distinct performance oscillation is present.

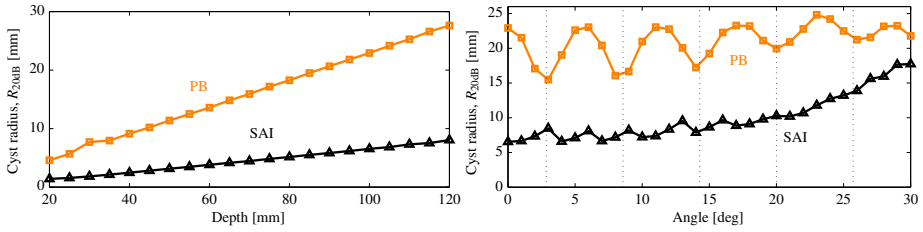

(a) (b)

Figure C.10: The Cystic Resolution sampled at 20 dB intensity difference is in (a) seen as a function of depth with no tilt angle ($(\phi,\theta) = (0°,0°)$), and in (b) as a function of angle ($(\phi,\theta) = (\text{angle},\text{angle})$) at 100 mm of depth. In (b) the angle of the parallel beamforming transmit beams are marked with vertical dashed lines. The smaller the cyst radius the better. The cystic resolution of parallel beamforming is seen to be improved near the transmit beams.

C.4 Measurements

In this section, measurements made with synthetic aperture imaging and parallel beamforming are presented and compared.

C.4.1 Measurement Setup

All measurements are carried out using the 1024 channel experimental ultrasound scanner *synthetic aperture real-time ultrasound system* (SARUS) (Jensen, Holten-Lund, et al. 2013) and a 32×32 element phased array probe made by Vermon S.A. (Tours, France) shown in Fig. C.11. The measured and simulated RF-data are beamformed using the Beam Formation Toolbox 3 (Hansen et al. 2011). For the measurements, two phantoms are used. The first phantom is a line spread phantom consisting of a thin copper wire submerged in a water tank. The copper wire is mounted on the *x*-*y*-*z* positioning system "AIMS III" made by Onda Corporation (Sunnyvale, CA, USA) and can be placed precisely at any given depth. The second phantom is a cyst phantom, model 571 from Danish Phantom Design (Frederikssund, Denmark). The speed of sound c_{pht} and attenuation α of the cyst phantom are listed in Table C.1. The cysts are made of water filled pipes orientated horizontally and with an angle of 45° in the *x*-*y*-plane with respect to the scan plane. Two sizes of cysts are present in the phantom, cysts with a diameter of 8 mm, spaced 20 mm apart, and cysts with a diameter of 4 mm, spaced 10 mm apart. The contrast-to-noise ratio (CNR) is measured on the 8 mm cysts. The cysts are only present in the center of the phantom. The region without cysts contains only tissue mimicking material and is used for estimating the SNR for both imaging techniques.

Figure C.11: The 32×32 element phased array ultrasound probe used for the measurements and modeled in the simulations.

C.4.2 Line Spread Function

The line spread function (LSF) is measured using the described wire phantom. The wire runs parallel to the transducer surface at depths of 20, 40, 60, and 80 mm. In Fig. C.12, 2-D B-modes of the wire at 40 mm and 80 mm of depth are shown. The B-mode images are sliced perpendicular to the wire direction. They have a dynamic range of 60 dB over which isocurves at −40 dB, −20 dB, and −6 dB are marked. The images in Fig. C.12(a) and C.12(b) are made with parallel beamforming and in Fig. C.12(c) and C.12(d) with synthetic aperture imaging. The wire is placed a little off-center which resulting in slightly asymmetric LSFs. Comparing the LSFs of synthetic aperture imaging and parallel beamforming, the −6 dB contour widths differ 0.4 mm(16 %) at 40 mm of depth and 1.0 mm(20 %) at 80 mm, in favor of synthetic aperture imaging. The FWHM of the LSF is shown in Fig. C.13. The side-lobe levels are clearly lower for synthetic aperture imaging than for parallel beamforming, both at −20 dB and at −40 dB. The received energy at the ultrasound probe surface is lower for deeper wire placements in the water tank. This results in a relative increase in the noise floor originating from electronic noise within the experimental ultrasound scanner. The noise floor is seen to be higher for parallel beamforming in Fig. C.12(b) than for synthetic aperture imaging in Fig C.12(d). The noise appears at the center of the B-mode image, because the noise is in phase in the raw data on all receive channels and only sums up coherently during the delay-and-sum beamforming of points close to the center line pointing straight down.

In Fig. C.13, the FWHM measured on the wire phantom at depths of 20, 40, 60, and 80 mm are shown. The FWHM increases linearly and the difference between the two techniques becomes larger with depth. The measured LSFs at 20 mm depth have a FWHM of 1.1 mm for synthetic aperture imaging vs. 1.3 mm for the parallel beamforming technique. At 60 mm the FWHM has increased to 3.1 mm for synthetic aperture imaging

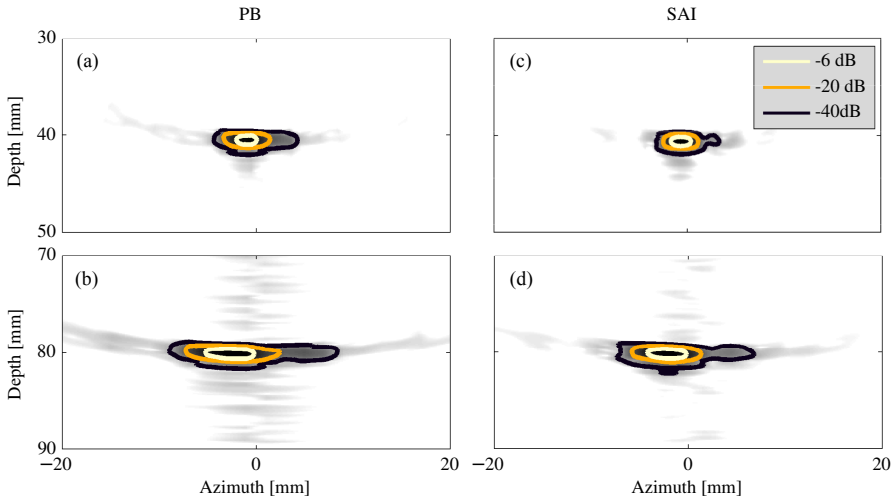

Figure C.12: The measured 3-D line spread function of Parallel beamforming ((a),(b)) and synthetic aperture imaging ((c),(d)) sliced in a 2-D plane. The wire runs parallel to the transducer surface at depths of 40 mm and 80 mm. The 2-D gray level images have a dynamic range of 60 dB. The side-lobes of parallel beamforming are seen to be clearly larger than the side-lobes of synthetic aperture imaging.

vs 3.9 mm for parallel beamforming.

From the measured LSF the cystic resolution is calculated and shown in Fig. C.14, where a large difference between the imaging performance of the two techniques is apparent. At 20 mm depth, synthetic aperture imaging needs a cyst with a radius of 1.1 mm and parallel beamforming 1.3 mm for the center of the cyst to be 20 dB darker than its surroundings. At 60 mm depth, the required cyst size has increased to 2.5 mm for synthetic aperture imaging vs 4.1 mm for parallel beamforming. Relatively, synthetic aperture imaging thereby improves the cystic resolution by 15 % at 20 mm and 39 % at 60 mm.

In Fig. C.15, a 2-D slice of the cyst phantom is shown. Fig. C.15(a) is made with synthetic aperture imaging and Fig. C.15(b) with parallel beamforming. The cysts are clearly more apparent when imaged with synthetic aperture imaging than with parallel beamforming.

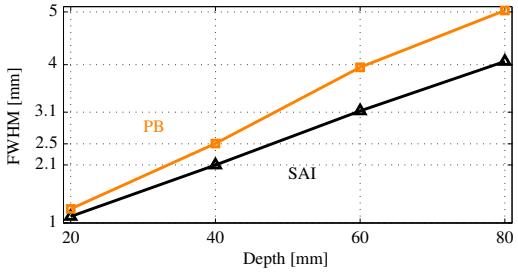

Figure C.13: The measured FWHM on the wire phantom shown as a function of wire depth. Synthetic aperture imaging has a smaller main-lobe size than parallel beamforming at all depths. The FWHM increases linearly with depth, as predicted by the simulations.

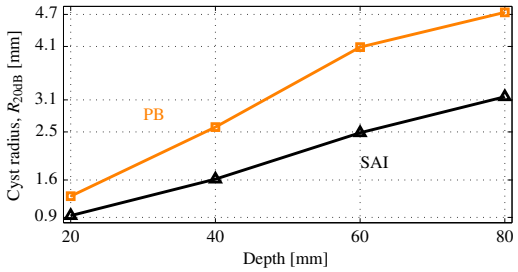

Figure C.14: The measured cystic resolution on the wire phantom shown as a function of wire depth. Synthetic aperture imaging is seen to achieve a better cystic resolution than parallel beamforming at all depths. The $R_{20\text{dB}}$ values increase approximately linearly with depth, and they increase faster for parallel beamforming than for synthetic aperture imaging. This is in agreement with the simulation predictions.

C.4.3 Contrast-to-Noise Ratio

The imaging performance of the cysts is estimated using the contrast-to-noise ratio (CNR) which was calculated as

$$\text{CNR} = \frac{\mu_s - \mu_c}{\sqrt{\sigma_c^2 + \sigma_s^2}}\,, \tag{C.7}$$

where μ_c and μ_s are the mean intensities of a cyst region and a speckle region. σ_c^2 and σ_s^2 are the variances of the cyst and speckle data. The CNR is calculated from spherical regions of the envelope-detected data before it is log-compressed. The cyst statistics is measured from a sphere with a radius of 6 mm located at the center of each cyst. The speckle statistics are estimated on the exact same spheres but on the tissue mimicking

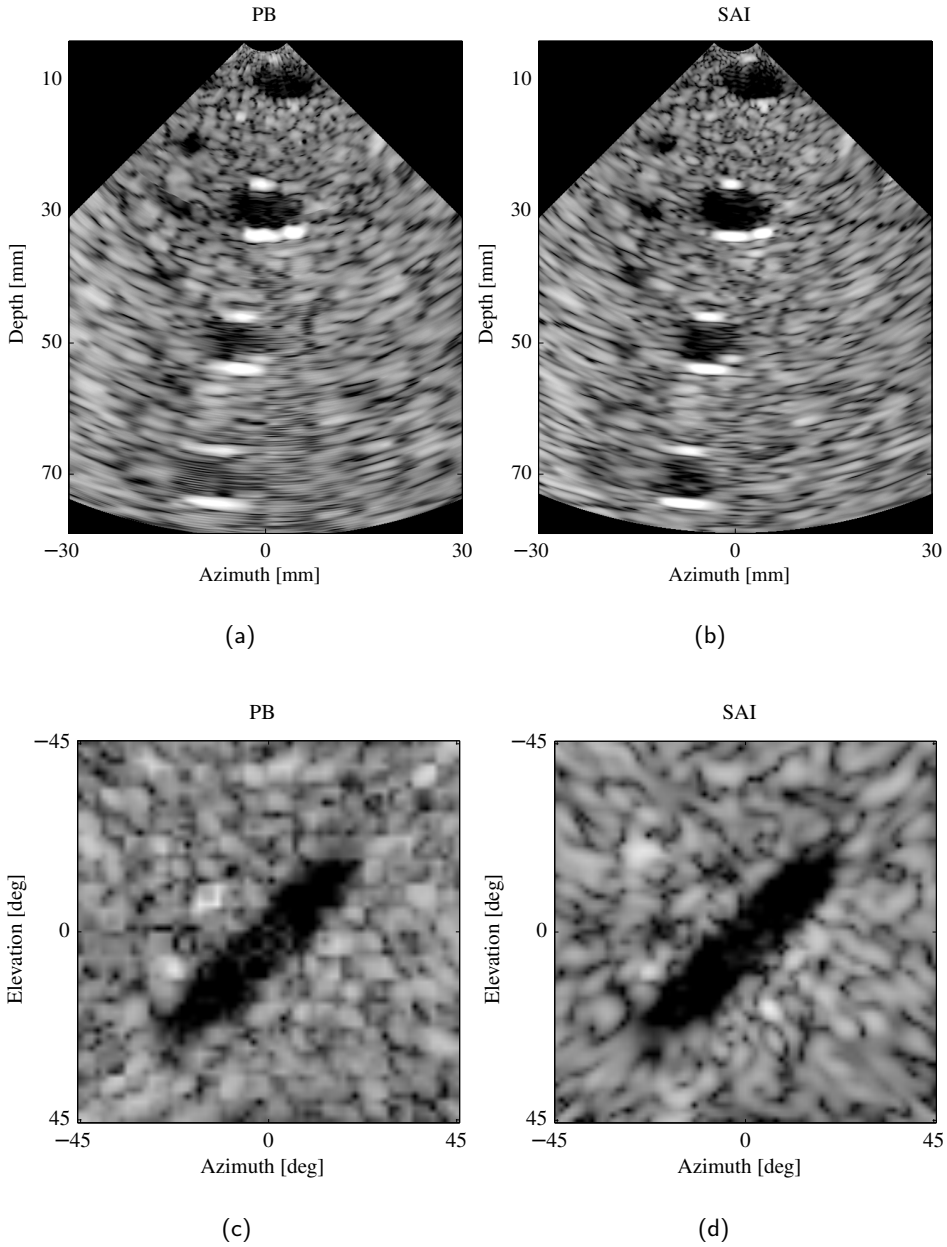

Figure C.15: Parallel beamforming (a and c) and synthetic aperture imaging (b and d) of anechoic cysts embedded in a tissue-mimicking phantom. The dynamic range is 40 dB. The large cysts have a diameter of 8 mm and the small cysts 4 mm. (a) and (b) are vertical scan planes and (c) and (d) are C-scans with a constant distance to the array center. The cysts are water-filled pipes aligned 45° to the vertical scan plane.

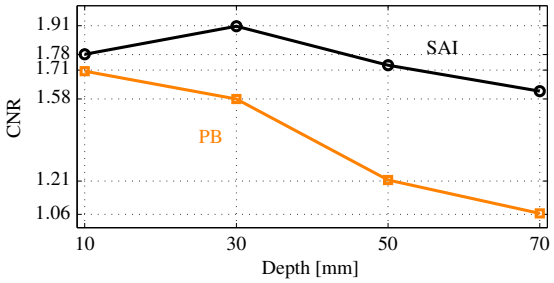

Figure C.16: The estimated contrast to noise ratio of the 8 mm cysts are shown. When ignoring the cyst at 10 mm, this shows the same tendency as in the simulations in Fig. C.10(a), the contrast decreases linearly with depth and the contrast for parallel beamforming decreases faster than for synthetic aperture imaging. The cyst at 10 mm depth is an outlier. This is probably because of reverberations from the phantom to transducer interface.

phantom containing only random scatterers. In Fig. C.16, the results of the CNR calculations from the 8 mm cysts are shown. The CNR is seen to be better for synthetic aperture imaging at all depths compared with parallel beamforming. When ignoring the first cyst, the CNR for both synthetic aperture imaging and parallel beamforming cysts are seen to decrease approximately linearly. The CNR of parallel beamforming decreases faster than the CNR for synthetic aperture imaging. This is as expected, when compared with the linearly decreasing contrast performance of the LSF, shown in Fig. C.14 and the simulated cystic resolution, shown in Fig. C.10(a). The decreased CNR performance of the top cyst could be because of excessive clutter close to the transducer.

C.4.4 Signal-to-Noise Ratio

The SNR can be used to estimate the penetration depth. The SNR is measured by scanning a tissue mimicking phantom only containing randomly distributed scatterers. To estimate the signal and noise components, 12 frames were acquired. The signal component is estimated by averaging the 12 measurements. Subtracting the signal component from each frame produces 12 noise estimates. The SNR is estimated for each voxel in the IQ-beamformed volume by taking the ratio of the signal power and the noise power. The SNR is thereby estimated on a complex data set. The RMS-power of a complex signal when assuming a unit load is

$$P_{\mathrm{RMS}} = V_{\mathrm{RMS}} \times I^{*}_{\mathrm{RMS}} = |V_{\mathrm{RMS}}|^2 \ , \tag{C.8}$$

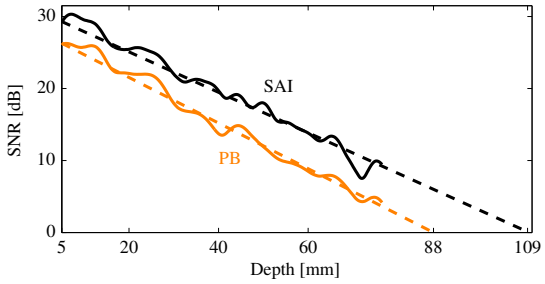

Figure C.17: Using synthetic aperture imaging increases the SNR at all depths. The penetration depth is estimated to 109 mm for synthetic aperture imaging and 88 mm for parallel beamforming.

where * denotes complex conjugated. Using (C.8) the SNR is calculated by

$$\mathrm{SNR}(\mathbf{x}) = \frac{\left|\sqrt{\frac{1}{N}\sum_{n=1}^{N}\mathrm{E}[s(\mathbf{x})]^2}\right|^2}{\left|\sqrt{\frac{1}{N}\sum_{n=1}^{N}(s_n(\mathbf{x})-\mathrm{E}[s(\mathbf{x})])^2}\right|^2} \tag{C.9a}$$

$$= \frac{\left|\mathrm{E}[s(\mathbf{x})]\right|^2}{\mathrm{var}[s(\mathbf{x})]}\,, \tag{C.9b}$$

where $\mathbf{x} = (x,y,z)^\top$ is the voxel coordinate, N the number of image frames, $\mathrm{E}[\cdot]$ the expectation operator, $\mathrm{var}[\cdot]$ the variance operator, s the set of all IQ-beamformed frames, s_n a single image frame with index n. The SNR estimated is calculated from stochastic data and a limited amount of data is available due to the depth dependent SNR. Therefore averaging has to be employed to reduce the variance of the estimates. The noisy estimates are low-pass filtered with a 3-D FIR filter. The FIR filter is applied before scan line conversion and its cut-off frequency for the three dimensions is $\frac{1}{6^\circ} \times \frac{1}{6^\circ} \times 0.15/\mathrm{mm}$. A single scan line is extracted and plotted in Fig. C.17. The SNR of synthetic aperture imaging is seen to be higher than the SNR of parallel beamforming. The penetration depth, where the SNR crosses 0 dB, is by linear regression estimated to be 88 mm for parallel beamforming and 109 mm for synthetic aperture imaging. In other words, synthetic aperture imaging increases the penetration depth by approximately 24 % with the same amount of energy emitted.

C.5 Discussion and Conclusions

A comparison of real-time 3-D synthetic aperture imaging and parallel beamforming using only 256 active channels was made with both Field II simulations and measurements from

the experimental ultrasound scanner SARUS.

Simulations were used to optimize both techniques before comparison. Simulations of the PSF at a large number of positions within the imaged volume showed synthetic aperture imaging improved the detail resolution at small steering angles compared with parallel beamforming. With larger steering angles, the detail resolution performance of the two techniques was similar. The contrast resolution was significantly improved by synthetic aperture imaging at all positions in the entire imaged volume.

From measurement, the imaging quality was investigated by use of wire and cyst phantoms. The wire phantom measurements were carried out at a low steering angle and showed the same tendency as the simulations. Synthetic aperture imaging increased both the resolution and the contrast. The FWHM was improved by 20 % at 80 mm depth. The cyst phantom measurement confirmed that synthetic aperture imaging increases the contrast at all depths, compared with parallel beamforming. The CNR was improved by 22 % at 70 mm depth. Measurements on a tissue mimicking phantom indicated that the penetration depth is deeper for synthetic aperture imaging compared with parallel beamforming. Synthetic aperture had a higher SNR than parallel beamforming at all depths and the increased SNR resulted in a penetration depth increase of 24 %. The penetration depth did not reach the designed 15 cm. This was likely due to the small transducer array surface area, limited by the restriction of 256 active channels. It is most likely, that the low SNR of the experimental scanner used also limited the penetration depth.

It was shown that using synthetic aperture imaging on a channel limited 3-D ultrasound system can achieve a high image quality at a low cost.

References

Augustine, L. J. (1987). *High resolution multiline ultrasonic beamformer*. U.S. Patent 4,644,795 (cit. on p. 84).

Bae, M. H. and M. K. Jeong (2000). “A study of synthetic-aperture imaging with virtual source elements in B-mode ultrasound imaging systems”. In: *IEEE Trans. Ultrason., Ferroelec., Freq. Contr.* Vol. 47, pp. 1510–1519 (cit. on p. 84).

Bae, M., H. Lee, S. B. Park, R. Yoon, M. H. Jeong, D. G. Kim, M. Jeong, and Y. Kim (2008). “A new ultrasonic synthetic aperture tissue harmonic imaging system”. In: *Proc. IEEE Ultrason. Symp.* Pp. 1258–1261 (cit. on p. 85).

Bennett, S., D. K. Peterson, D. Corl, and G. S. Kino (1982). “A real-time synthetic aperture digital acoustic imaging system”. In: *Acoust. Imaging*. Ed. by P. Alais and A. F. Metherell. Vol. 10, pp. 669–692 (cit. on p. 84).

Bilge, H. S., M. Karaman, and M. O’Donnell (1996). “Motion estimation using common spatial frequencies in synthetic aperture imaging”. In: *Proc. IEEE Ultrason. Symp.* Pp. 1551–1554 (cit. on p. 85).

Burckhardt, C. B., P.-A. Grandchamp, and H. Hoffmann (1974). "An Experimental 2 MHz Synthetic Aperture Sonar System Intended for Medical Use". In: *IEEE Trans. Son. Ultrason.* 21.1, pp. 1–6 (cit. on p. 84).

Delannoy, B., R. Torguet, C. Bruneel, E. Bridoux, J. M. Rouvaen, and H. Lasota (1979). "Acoustical image reconstructions in parallel-processing analog electronic systems". In: *J. Appl. Phys.* 50, pp. 3153–3159 (cit. on p. 84).

Flaherty, J. J., K. R. Erikson, and V. M. Lund (1967). *Synthetic Aperture Ultrasound Imaging Systems*. United States Patent, US 3,548,642. United States Patent, US 3,548,642, 1967, Published 22 Dec 1970 (cit. on p. 84).

Frazier, C. H. and W. D. O'Brien (1998). "Synthetic aperture techniques with a virtual source element". In: *IEEE Trans. Ultrason., Ferroelec., Freq. Contr.* 45, pp. 196–207 (cit. on pp. 84, 93).

Gammelmark, K. L. and J. A. Jensen (2003a). "Duplex Synthetic Aperture Imaging with Tissue Motion Compensation". In: *Proc. IEEE Ultrason. Symp.* Pp. 1569–1573 (cit. on p. 85).

— (2003b). "Multielement Synthetic Transmit Aperture Imaging using Temporal Encoding". In: *IEEE Trans. Med. Imag.* 22.4, pp. 552–563 (cit. on p. 84).

— (2014). "2-D Tissue Motion Compensation of Synthetic Transmit Aperture Images". In: *IEEE Trans. Ultrason., Ferroelec., Freq. Contr.* Pp. 594–610. DOI: http://dx.doi.org/10.1109/TUFFC.2014.2948 (cit. on p. 85).

Hansen, J. M., M. C. Hemmsen, and J. A. Jensen (2011). "An object-oriented multithreaded software beamformation toolbox". In: *Proc. SPIE Med. Imag.* Vol. 7968, pages. URL: http://dx.doi.org/10.1117/12.878178 (cit. on p. 99).

Hergum, T., T. Bjåstad, K. Kristoffersen, and H. Torp (2007). "Parallel Beamforming Using Synthetic Transmit Beams". In: *IEEE Trans. Ultrason., Ferroelec., Freq. Contr.* 54.2, pp. 271–280 (cit. on p. 84).

Ho, K.-Y., Y.-H. Chen, C.-Z. Zhan, and A.-Y. Wu (2013). "VLSI implementation of real-time motion compensated beamforming in synthetic transmit aperture imaging". In: *IEEE Int. Symp. Circ. & Sys.* Pp. 1893–1896 (cit. on p. 85).

Hoctor, R. T. and S. A. Kassam (1990). "The unifying role of the coarray in aperture synthesis for coherent and incoherent imaging". In: *IEEE Proc.* Vol. 78, pp. 735–752 (cit. on p. 89).

Jensen, J. A. (1996). "Field: A Program for Simulating Ultrasound Systems". In: *Med. Biol. Eng. Comp.* 10th Nordic-Baltic Conference on Biomedical Imaging, Vol. 4, Supplement 1, Part 1, pp. 351–353 (cit. on p. 89).

Jensen, J. A., H. Holten-Lund, R. T. Nilsson, M. Hansen, U. D. Larsen, R. P. Domsten, B. G. Tomov, M. B. Stuart, S. I. Nikolov, M. J. Pihl, Y. Du, J. H. Rasmussen, and M. F. Rasmussen (2013). "SARUS: A Synthetic Aperture Real-time Ultrasound System". In: *IEEE Trans. Ultrason., Ferroelec., Freq. Contr.* 60.9, pp. 1838–1852 (cit. on p. 99).

Jensen, J. A. and N. B. Svendsen (1992). "Calculation of Pressure Fields from Arbitrarily Shaped, Apodized, and Excited Ultrasound Transducers". In: *IEEE Trans. Ultrason., Ferroelec., Freq. Contr.* 39, pp. 262–267 (cit. on p. 89).

Johnson, J., M. Karaman, and B. Khuri-Yakub (2005). "Coherent-array imaging using phased subarrays. Part I: basic principles". In: *IEEE Trans. Ultrason., Ferroelec., Freq. Contr.* 52.1, pp. 37–50. DOI: 10.1109/TUFFC.2005.1397349 (cit. on p. 85).

Johnson, J., O. Oralkan, S. Ergun, U. Demirci, M. Karaman, and B. Khuri-Yakub (2005). "Coherent array imaging using phased subarrays. Part II: simulations and experimental results". In: *IEEE Trans. Ultrason., Ferroelec., Freq. Contr.* 52.1, pp. 51–64. DOI: 10.1109/TUFFC.2005.1397350 (cit. on p. 85).

Karaman, M., P. C. Li, and M. O'Donnell (1995). "Synthetic aperture imaging for small scale systems". In: *IEEE Trans. Ultrason., Ferroelec., Freq. Contr.* 42, pp. 429–442 (cit. on pp. 84, 85).

Karaman, M. and M. O'Donnell (1998). "Subaperture processing for ultrasonic imaging". In: *IEEE Trans. Ultrason., Ferroelec., Freq. Contr.* 45, pp. 126–135 (cit. on p. 84).

Karaman, M., H. Ş. Bilge, and M. O'Donnell (1998). "Adaptive multi-element synthetic aperture imaging with motion and phase aberation correction". In: *IEEE Trans. Ultrason., Ferroelec., Freq. Contr.* 42, pp. 1077–1087 (cit. on pp. 84, 85).

Karaman, M., I. O. Wygant, O. Oralkan, and B. T. Khuri-Yakub (2009). "Minimally Redundant 2-D Array Designs for 3-D Medical Ultrasound Imaging". In: *IEEE Trans. Med. Imag.* 7, pp. 1051–1061 (cit. on p. 88).

Kim, J.-J. and T.-K. Song (2008). "Real-Time 3D Imaging Methods using 2D Phased Arrays Based on Synthetic Focusing Techniques". In: *Ultrasonic Imaging* 30.3, pp. 169–188 (cit. on p. 85).

Liu, D.-L. D., J. C. Lazenby, Z. Banjanin, and B. A. McDermott (2002). *System and method for reduction of parallel beamforming artifacts*. U.S. Patent 6447452 (cit. on p. 84).

Lockwood, G. R., J. R. Talman, and S. S. Brunke (1998). "Real-time 3-D ultrasound imaging using sparse synthetic aperture beamforming". In: *IEEE Trans. Ultrason., Ferroelec., Freq. Contr.* 45, pp. 980–988 (cit. on p. 85).

Nikolov, S. I. and J. A. Jensen (2000). "3D synthetic aperture imaging using a virtual source element in the elevation plane". In: *Proc. IEEE Ultrason. Symp.* Vol. 2, pp. 1743–1747 (cit. on p. 85).

Nock, L. F. and G. E. Trahey (1992). "Synthetic receive aperture imaging with phase correction for motion and for tissue inhomogenities - part I: basic principles". In: *IEEE Trans. Ultrason., Ferroelec., Freq. Contr.* 39, pp. 489–495 (cit. on p. 84).

Ramm, O. T. von, S. W. Smith, and H. G. Pavy (1991). "High speed ultrasound volumetric imaging system – Part II: Parallel processing and image display". In: *IEEE Trans. Ultrason., Ferroelec., Freq. Contr.* 38, pp. 109–115 (cit. on p. 84).

Ranganathan, K. and W. F. Walker (2007). "Cystic Resolution: A Performance Metric for Ultrasound Imaging Systems". In: *IEEE Trans. Ultrason., Ferroelec., Freq. Contr.* 54.4, pp. 782–792 (cit. on p. 87).

Rasmussen, J. H., M. C. Hemmsen, S. S. Madsen, P. M. Hansen, M. B. Nielsen, and J. A. Jensen (2013). "Preliminary study of synthetic aperture tissue harmonic imaging

on in-vivo data". In: *Proc. SPIE Med. Imag.* Vol. 8675, pp. 1–10. DOI: dx.doi.org/10.1117/12.2006363 (cit. on p. 85).

Rasmussen, M. F., G. Férin, R. Dufait, and J. A. Jensen (2012). "Comparison of 3D Synthetic Aperture Imaging and Explososcan using Phantom Measurements". In: *Proc. IEEE Ultrason. Symp.* Pp. 113–116. DOI: 10.1109/ULTSYM.2012.0028 (cit. on p. 84).

Rasmussen, M. F., J. M. Hansen, G. Férin, R. Dufait, and J. A. Jensen (2012). "Preliminary comparison of 3D synthetic aperture imaging with Explososcan". In: *Proc. SPIE Med. Imag.* Ed. by J. G. Bosch and M. M. Doyley. Vol. 8320. 83200F. SPIE, pp. 1–9 (cit. on p. 84).

Shattuck, D. P., M. D. Weinshenker, S. W. Smith, and O. T. von Ramm (1984). "Explososcan: A parallel processing technique for high speed ultrasound imaging with linear phased arrays". In: *J. Acoust. Soc. Am.* 75, pp. 1273–1282 (cit. on p. 84).

Smith, S. W., H. G. Pavy, and O. T. von Ramm (1991). "High speed ultrasound volumetric imaging system – Part I: Transducer design and beam steering". In: *IEEE Trans. Ultrason., Ferroelec., Freq. Contr.* 38, pp. 100–108 (cit. on p. 88).

Steinberg, B. D. (1976). *Principles of aperture and array system design*. New York: John Wiley & Sons (cit. on p. 89).

Trahey, G. E. and L. F. Nock (1992). "Synthetic receive aperture imaging with phase correction for motion and for tissue inhomogenities - part II: effects of and correction for motion". In: *IEEE Trans. Ultrason., Ferroelec., Freq. Contr.* 39, pp. 496–501 (cit. on p. 85).

Vilkomerson, D., J. Greenleaf, and V. Dutt (1995). "Towards a Resolution Metric for Medical Ultrasound Imaging". In: *Proc. IEEE Ultrason. Symp.* Pp. 1405–1410 (cit. on p. 86).

Wild, J. J. (1950). "The use of ultrasonic pulses for the measurement of biologic tissues and the detection of tissue density changes". In: *Surgery* 27, pp. 183–188 (cit. on p. 84).

Ylitalo, J. T. and H. Ermert (1994). "Ultrasound synthetic aperture imaging: Monostatic approach". In: *IEEE Trans. Ultrason., Ferroelec., Freq. Contr.* 41, pp. 333–339 (cit. on p. 84).

PAPER D

3D Ultrasound Imaging Performance of a Row-column Addressed 2D Array Transducer: A Simulation Study

Authors: Morten Fischer Rasmussen and Jørgen Arendt Jensen.

Published in: *Proceedings of SPIE Medical Imaging* Vol. 86750C, pp. 1–11, (2013).

Abstract

This paper compares the imaging performance of a 128+128 element row-column addressed array with a fully addressed 16×16 2D array. The comparison is made via simulations of the point spread function with Field II. Both arrays have lambda-pitch, a center frequency of 3.5 MHz and use 256 active elements. The row-column addressed array uses 128 transmit channels and 128 receive channels, whereas the fully addressed array uses 256 channels in both transmit and receive. The large size of the emulated row and column elements in the row-column addressed array causes ghost echoes to appear. The ghost echoes are shown to be suppressed when the sub-elements within each of the emulated row and column elements are apodized. The maximum ghost intensity is suppressed by 22.2 dB compared to using no apodization. With apodization applied, the full-width-at-half-maximum in the lateral direction for the fully addressed array is 2.81 mm, and 1.01 mm for the row-column addressed array. This shows that the detail resolution can be more than doubled using the row-column addressed array instead of the fully addressed array. The row column addressed array achieves a $R_{20\text{dB}}$ cystic resolution of 0.76 mm, compared to 3.16 mm for the fully addressed array. The significantly smaller $R_{20\text{dB}}$-value for the row-column addressed

Center for Fast Ultrasound Imaging, Dept. of Electrical Engineering Technical University of Denmark, 2800 Lyngby, Denmark.

"F"urther author information: Send correspondence to M. F. Rasmussen. E-mail: mofi@elektro.dtu.dk

array indicates that it can achieve a much higher contrast resolution than the fully addressed array.

Keywords: row-column addressing, beamforming, low channel count 3D imaging, 2D array transducer, synthetic aperture imaging, medical ultrasound

D.1 Introduction

For ultrasonic 3D imaging, 2D array transducers are needed to achieve real-time scanning of a volume(Ramm et al. 1991; Turnbull and Foster 1991). The number of elements in a fully addressed $N \times N$ 2D array scales with N^2. In 2D imaging, a 1D array using more than 100 elements is often used. Using a fully addressed 2D array, this would correspond to an array with more than 10 000 elements. To control the individual elements in the array, a connection has to be made to each element. Hereby, any delay or apodization scheme can be applied, offering maximum control and flexibility in the image processing(Rasmussen, Férin, et al. 2012; Rasmussen, Hansen, et al. 2012; Turnbull and Foster 1991). However, addressing each element individually results in a vast amount of interconnections and offers a great challenge in acquiring and processing the large amount of data. Reducing the number of transducer elements by using sparse arrays has therefore seen a great amount of interest in the last couple of decades (Austeng and Holm 2002; Brunke and Lockwood 1997; Davidsen et al. 1994; Karaman et al. 2009; Yen et al. 2000). One of the drawbacks of sparse arrays is the lower emitted energy from the reduced number of elements. This leads to a lower SNR in the recorded ultrasound image. The sparse arrays also have higher side-lobes and can introduce grating lobes in the field.

2D row-column addressed arrays has recently attracted some attention(Chen et al. 2011; Logan, Wong, Chen, et al. 2011; Logan, Wong, and Yeow 2009; Seo and Yen 2009). In a row-column addressed array, the are elements accessed by their row index in transmit and by their column index in receive, or vice versa. This is illustrated in Fig. D.1. Thus, instead of addressing a single element, an entire row or column of elements is addressed. This effectively reduces the number of elements on a $N \times N$ 2D array from N^2 to $2N$. The new line elements, shown in the bottom left and bottom right array in Fig. D.1, are in this work referred to as row and column elements. The individual physical elements, making up the row and column elements, are referred to as sub-elements or physical elements.

The purpose of this paper is to investigate the imaging performance of row-column addressed arrays. This is done by simulating the point spread function (PSF) and measuring the main lobe width and the cystic resolution. It is shown how the focusing can be achieved with a row-column addressed array. The large emulated elements in a row-column addressed array is shown to give rise to ghost echoes. Apodization of the sub-elements is proposed as a solution to reduce the ghost effects. Finally, the imaging performance of a row-column addressed array is inspected and compared with the imaging quality of a fully addressed 2D array.

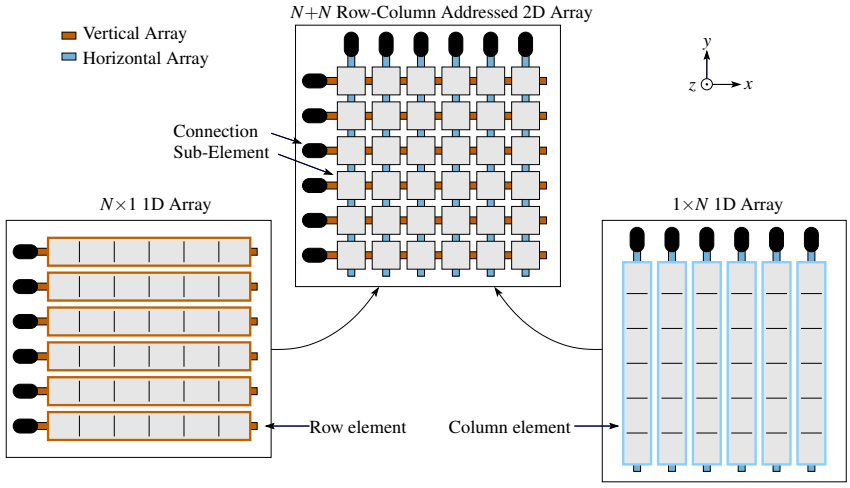

Figure D.1: A row-column addressed 2D array can be interpreted as two orthogonal 1D arrays: One array consisting of row-elements and one array consisting of column elements.

D.2 Methods/Theory

This section describes how 3D focusing can be achieved with a row-column addressed array, what its disadvantages are, and what can be done to minimize them.

D.2.1 Focusing

Each of the emulated 1D arrays can focus in one dimension. When using the vertical array, seen in Fig. D.1, as a transmit array and the horizontal from the same figure as a receive array, the x–dimension can be dynamically focused in receive and the y–dimension focused in transmit. The y–dimension can be dynamically focused in transmit when using synthetic transmit focusing. The emitted wavefront of a single element has the shape of a cylinder surface: it is a plane wave in the z-x plane and a circle arc in z-y plane. This is illustrated in Fig. D.2. The time of flight is given by the shortest distance from the source to the scatterer and back to the receiving element, divided by the speed of sound. Using the notation from Fig. D.2, this can be written as:

$$t_{ToF} = \frac{\|\mathbf{r_e}\| + \|\mathbf{r_r}\|}{c}\,, \tag{D.1}$$

where $\mathbf{r_e}$ is the vector from the emitting element to the focus point, $\mathbf{r_r}$ is the vector from the focus point and back to the receiving element, and c is the speed of sound in the medium. Since the length of each element is large, the usual assumption that the elements are point sources no longer holds. Therefore, $\mathbf{r_e}$ and $\mathbf{r_r}$ connects the focus point to the

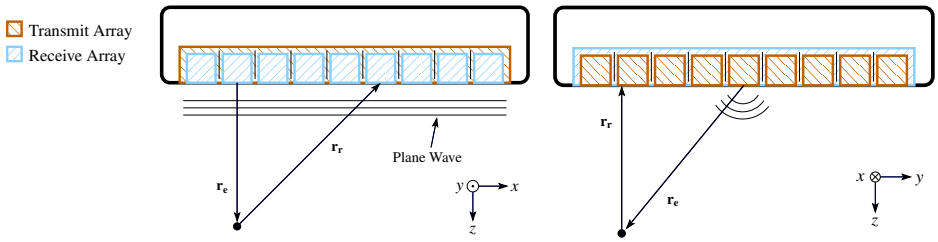

(a) ToF in x–dimension. (b) ToF in y–dimension.

Figure D.2: Time of flight (ToF) illustration of one emission to the focus point and back to one receiving element. $\mathbf{r_e}$ is the vector from the nearest point of the emitting element to the focus point and $\mathbf{r_r}$ is the vector from the focus point to the nearest point on the receive element.

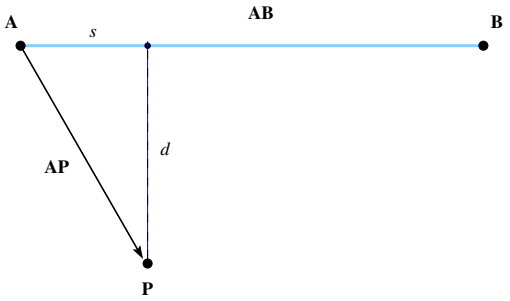

Figure D.3: Projection of the point **P** onto the line segment **AB**. s is the distance from **A** to the projected point and d is the shortest distance from **P** to **AB**.

closest point on respectively the source element and the receiving element. This can also be seen in Fig. D.2.

Determining $\|\mathbf{r_e}\|$ and $\|\mathbf{r_r}\|$ is solved by calculating the distance between an arbitrary point in 3D, the focus point **P**, and a line segment **AB** from point **A** to point **B**. This is illustrated in Fig. D.3. The projection of the point **P** onto the line **AB** is found using the dot product:

$$s = \frac{\mathbf{AP} \cdot \mathbf{AB}}{\|\mathbf{AB}\|}, \tag{D.2}$$

where s is the distance between **A** and the projection of **P** onto **AB**. s is positive if the projected point is located on the same side of **A** as **B**, and negative if it is located on the other side. By normalising s with the length of the line segment it is mapped to lie in the interval $[0,1]$, when the projected point is located on the line segment (between **A** and **B**):

$$\hat{s} = \frac{s}{\|\mathbf{AB}\|} = \frac{\mathbf{AP}\cdot\mathbf{AB}}{\|\mathbf{AB}\|^2} \,. \tag{D.3}$$

When the projection of **P** onto the line lies between **A** and **B**, i.e. when $\hat{s} \in [0,1]$, the standard formula for the distance between a line and a point can be used:

$$d = \frac{\|\mathbf{AB}\times\mathbf{AP}\|}{\|\mathbf{AB}\|}. \tag{D.4}$$

When $\hat{s} \notin [0,1]$, the shortest distance from the line segment to the point is the distance from either one of ends of the line segment (**A** or **B**) to the point (**P**). The following therefore determines the minimum distance between the point **P** and the line segment **AB**:

$$d(\mathbf{AB},\mathbf{P}) = \begin{cases} \dfrac{\|\mathbf{AB}\times\mathbf{AP}\|}{\|\mathbf{AB}\|} & \text{if } 0 \le \hat{s} \le 1, \\ \|\mathbf{AP}\| & \text{if } \hat{s} < 0\,, \\ \|\mathbf{BP}\| & \text{if } \hat{s} > 1\,. \end{cases} \tag{D.5}$$

Using (D.5), the distances $\|\mathbf{r_e}\|$ and $\|\mathbf{r_r}\|$ can now be determined as

$$\|\mathbf{r_e}\| = d(\mathbf{xmt}_m,\mathbf{P}) \quad \text{and} \quad \|\mathbf{r_r}\| = d(\mathbf{rcv}_n,\mathbf{P})\,, \tag{D.6}$$

where $\mathbf{xmt}_m$ is the **A** and **B** coordinates of the m'th transmit element and $\mathbf{rcv}_n$ is the corresponding coordinates for the n'th receive element. By inserting (D.6) into (D.1), we arrive at

$$t_{ToF_{m,n}}(\mathbf{P}) = \frac{d(\mathbf{xmt}_m,\mathbf{P}) + d(\mathbf{rcv}_n,\mathbf{P})}{c} \,. \tag{D.7}$$

The focused signal at point **P** is given by summing all receive signals at the time instances given by (D.7):

$$s(\mathbf{P}) = \sum_{m=1}^{M}\sum_{n=1}^{N} a_n\, y_{m,n}(t_{ToF_{m,n}}(\mathbf{P}))\,, \tag{D.8}$$

where M is the number of transmit elements, N is the number of receive elements, a_n is the receive apodization, $y_{m,n}(t)$ is the received signal from emission m to receive element n at time t.

D.2.2 Area and resolution scaling

The row-column addressed array is similar to the Mills cross array, which has been used and analysed by several authors(Kim and Song 2004; Smith et al. 1991). They both consist of two orthogonal 1D arrays. The difference is that for each channel to the cross array there is one physical element, and for each channel to the row-column array there is an entire row or column of physical elements. The row-column addressed array can therefore emit far more energy than the cross array, or any other of the sparse arrays.

In the following, a comparison of the row-column addressing is made with the sparse 2D Mills cross and the fully sampled 2D array. The Mills cross consists of $2N-1$ elements on a $N \times N$ 2D array. In Fig. D.4(a) the active area of the row-column addressed array, the fully addressed array and the Mill Cross is plotted. The marked points indicate five different array sizes: 32×32, 64×64, 128×128, 256×256 and 512×512 element 2D arrays. As expected, the surface area per channel is much larger for the row-column array than for the two other arrays. The row-column addressed array is seen to have one order of magnitude larger surface area than a cross array for a 32x32 element array. When using 1024 (2^{10}) channels, the surface area of the row-column addressed array is more than two orders of a magnitude larger than the surface area of the two other arrays.

In Fig. D.4(b) a rough estimate of full width at half maximum (FWHM) for each array is plotted. This prediction is only for the main-lobe size and says nothing about the side-lobe levels. The estimate builds on the standard formula for the main-lobe width:

$$\mathrm{FWHM} = \lambda F\# = \frac{\lambda d}{w}\,, \tag{D.9}$$

where d is the depth to the focal point, w is the width of the array and λ is the wavelength.

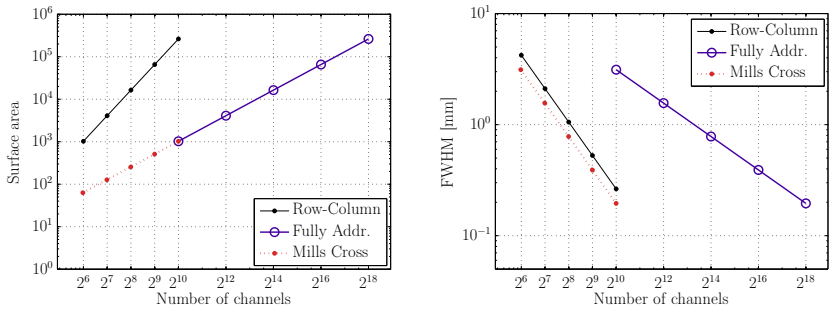

(a) Surface area comparison.

(b) Detail resolution comparison.

Figure D.4: Comparison of three transducer layouts. The marked points indicate 32×32, 64×64, 128×128, 256×256 and 512×512 element 2D arrays.

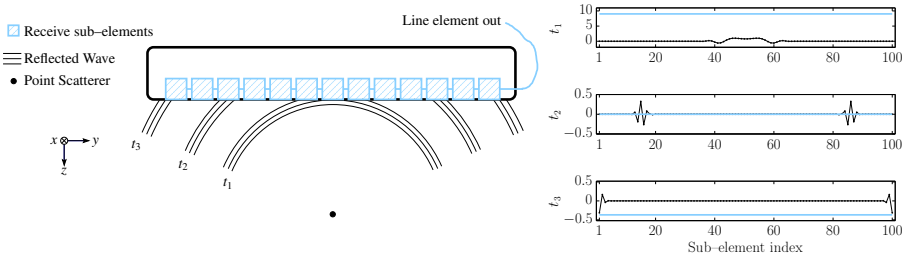

(a) Receiving the reflected wave at the three time instants: t_1, t_2 and t_3.

(b) The measured signal. The response of each sub-element is shown in black and the output of the line element is shown in light blue.

Figure D.5: Edge effect illustration. The three plots in (b) corresponds to the measured signal in (a) at the three time instants t_1, t_2 and t_3. The amplitudes in (b) are normalized to the maximum of the sub-element signals.

The above equation assumes focusing in both transmit and receive. Since the row-column addressed array only focuses one-way in each dimension, a rough estimate is made that its main-lobe size is 35 % wider than predicted by (D.9). The row-column addressed array is seen to perform almost as good as the Mills cross and much better than the fully addressed 2D array for the same amount of elements.

That the row-column addressed array both has a large surface area and promises to achieve a high resolution per active channel is what makes it a very interesting candidate for real-time 3D imaging.

D.2.3 Edge effects

When an emitted waveform is reflected by a point scatterer will the reflected wave have the shape of a sphere. Just as the reflected spherical wave intersects with the receiving line element, will only the first part of the wave interact with the sub-elements. This is illustrated as the wave at t_1 in Fig. D.5(a). The measured signal from the line element is a sum of the sub-element signals. At time t_1 will the signals from the sub-elements be mostly in phase, which is illustrated in the top plot of Fig. D.5(b). The line element therefore outputs a strong signal at t_1. A short time later, the entire reflected wave intersects with the line element at two locations. This is illustrated as the wave at time t_2. The amplitude of the transmit waveform used in medical ultrasound is usually symmetric around zero

Table D.1: Simulation parameters

Parameter name	Notation	Value	Unit
Center frequency	f_0	3.5	MHz
Speed of sound	c	1540	m/s
Wave length	λ	440	µm
Transducer pitch $-x$	d_x	440	µm
Transducer pitch $-y$	d_y	440	µm
Sampling frequency	f_s	100	MHz
Emission pulse	–	2-cycles, Hann-weighted	–

and the integration of the waveform is therefore close to zero. As seen in the center plot in Fig. D.5(b), the output from the line element at t_2 is very close to zero. The output of the line element is zero as long as the entire waveform intersects with it. The first part of the waveform does at the time t_3 not intersect with the line element anymore. The line element therefore has a small output at t_3, which is shown in the bottom plot in Fig. D.5(b).

To minimize this effect, the edge sub-elements should have a lower weighting. This can be achieved by applying an apodization window on the physical sub-elements within the line elements. This apodization is in this work referred to as hardware or sub-element apodization. The hardware apodization is applied in the horizontal direction when using the vertical array in Fig. D.1, and vice versa.

D.3 Simulation setup

All simulations are carried out using Field II(Jensen 1996; Jensen and Svendsen 1992) and beamformed using BFT3(Hansen et al. 2011). The transducer used in the simulations is a row-column addressed $128+128$ element 2D array. The exception is the fully addressed 2D array, used for comparison in Fig. D.8, which is a 16×16 2D array. The simulation parameters can be seen in Table D.1.

The point spread function is simulated by imaging a volume containing a single point scatter. The point scatterer is in all simulations placed in front of the transducer at $(x,y,z) = (0,0,50)$ mm. With both transducers a single element is used per emission. This leads to 128 emissions for the row-column addressed array and to 256 emissions for the fully addressed array. All apodizations applied are implemented using a Hann window.

The row-column array is emulated by simulating a fully addressed 128×128 array and then summing the responses of all elements of each column. This results in one signal per column. In transmit, the same waveform is applied to all elements within the same row. Hence, one waveform is used per row.

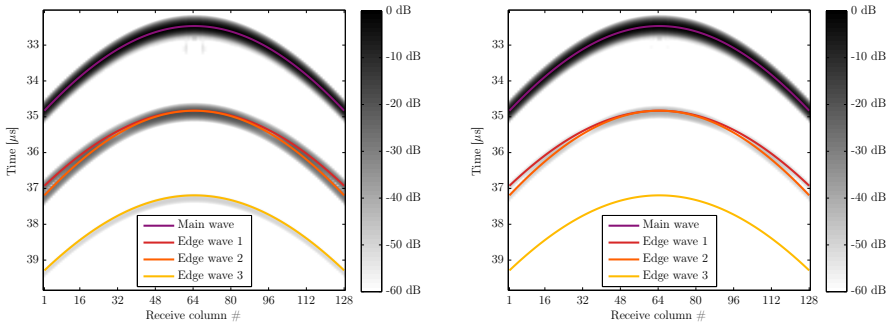

(a) Without apodization.

(b) With apodization.

Figure D.6: Time of flight for a scattere located at $(x,y,z) = (0,0,50)$ mm. The gray scale image is the log-compressed envelope of the simulated received signal of each column. The overlaid colored lines are the prediction of arrival time of each wave.

D.4 Results

In this section, the results of predicting the time of flight and the effect of using apodization is presented.

D.4.1 Time of flight prediction

The gray scale images in Fig. D.6 represent the envelope of the simulated received signal after column element 64 has emitted the transmit waveform. The earliest arrival is the main wavefront, and the following wavefronts appear because of the edge effect. Because of symmetry with the scatterer located at $(x,y) = (0,0)$, only two dominating edge waves appear. The overlaid lines are the calculated arrival times of each wavefront. The lines are seen to be right on top of the wavefront envelopes and they thereby predict their arrival time.

In Fig. D.6(a), no hardware apodization is used and two ghost echoes are clearly visible. The maximum amplitude of the two ghost echoes are −18.7 dB and −42.1 dB relative to the main wavefront. After applying hardware apodization, the two ghost echoes are suppressed to −40.5 dB and −93.0 dB, which is seen in Fig. D.6(b).

D.4.2 Apodization effects

The effect on the PSF of applying apodization is shown in Fig. D.7. In Fig. D.7(c), traditional apodization is applied during the beamforming. In Fig. D.7(b), hardware

apodization, described in section D.2.3, is applied directly on the sub-elements of each transmit and receive row/column element. No apodization is applied in Fig. D.7(a) and in Fig. D.7(d) are both apodization types are applied.

The conventional beamforming apodization is seen to greatly reduce the side lobes of both the main response and the ghosts. The cost is a slightly larger main-lobe. The hardware apodization suppresses the ghosts, but has no influence on the main response. The maximum ghost intensity is reduced by the hardware apodization with 22.2 dB from −22.3 dB to −44.5 dB.

A comparison between the row-column addressed array and a fully addressed array with the same amount of channels is shown in Fig. D.8. The PSF of the fully addressed array is seen to have both a wider main-lobe and larger side-lobes than the row-column addressed array. The FWHM in the lateral direction (x–dimension) of the row-column addressed array is 1.01 mm, while it is 2.81 mm for the fully addressed array. This shows, that when using the same amount of channels in the ultrasound imaging system, but changing the transducer array from a fully addressed array to a row-column addressed array, the resolution can be increased by more than a factor of two. As seen from Fig. D.4(b), this factor increases with larger arrays.

The cystic resolution describes the ability to detect an anechoic cyst in a uniform scattering medium. Specifically, the cystic resolution gives the intensity at the center of an anechoic cyst of a given size relative to its surrounding uniformly back-scattering medium(Vilkomerson et al. 1995). The lower the intensity at the center of the cyst, i.e. the darker it appears in the image for a given cyst size, the better imaging performance of the system. The relative intensity (RI) of the anechoic cyst was shown by Ranganathan and Walker(Ranganathan and Walker 2007), to be quantized as the clutter energy to total energy ratio,

$$\mathrm{RI}(R) = \sqrt{\frac{E_{out}(R)}{E_{tot}}} = \sqrt{1 - \frac{E_{in}(R)}{E_{tot}}}, \tag{D.10}$$

where E_{in} is the signal energy inside a circular region with radius, R, centered on the peak of the point spread function. E_{tot} is the total point spread function energy and E_{out} is the point spread function energy outside the circular region. To achieve a single number from the $\mathrm{RI}(R)$-curve, the required radius to achieve a 20 dB relative intensity between the center of the cyst and its surroundings is determined. This is written as $R_{20\mathrm{dB}}$.

The −20 dB cystic resolution is in the z-x plane 0.76 mm for the row column-addressed array and 3.16 mm for the fully addressed array. This indicates that the achievable contrast will be much higher with the row-column addressed array.

D.5 Conclusion and perspectives

The imaging quality of a row-column addressed array, that promises to greatly reduce the amount active channels used in 3D and 4D ultrasound imaging, was presented. It was

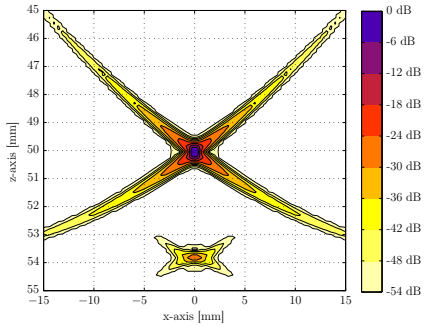

(a) Without apodization.

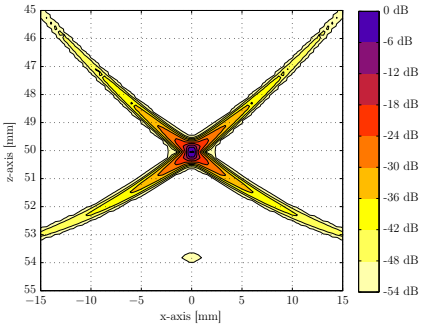

(b) With hardware apodization.

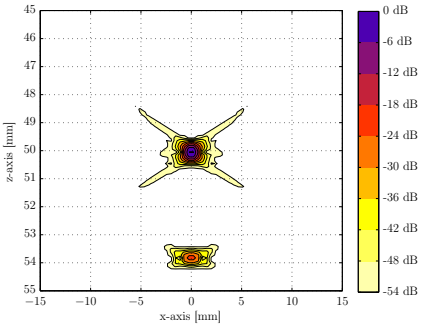

(c) With beamforming apodization.

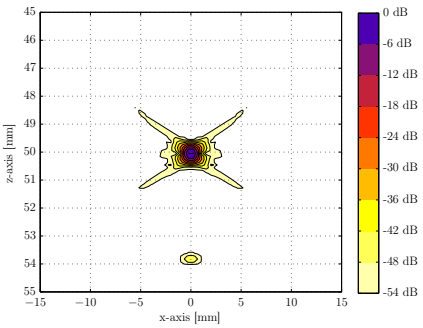

(d) With both beamforming and hardware apodization.

Figure D.7: Effect on PSF of using different apodizations. The scatterer is located at $(x,y,z) = (0,0,50)$ mm. The hardware apodization is seen to not affect the main response, but to suppress ghosts.

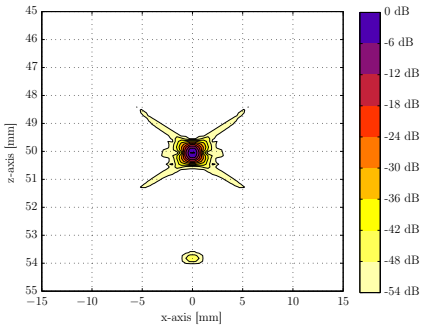

(a) PSF in z-x plane of the row-column addressed array.

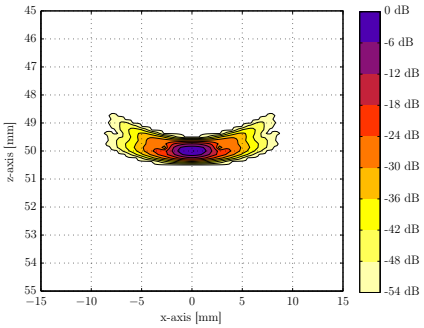

(b) PSF in z-x plane of the fully addressed array.

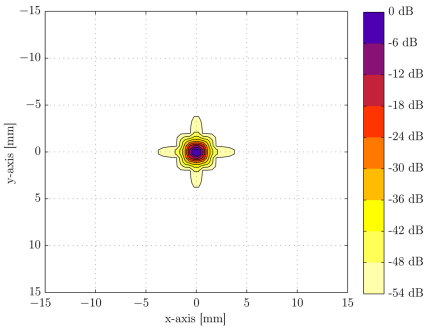

(c) PSF in C-scan at 50 mm depth of the row-column addressed array.

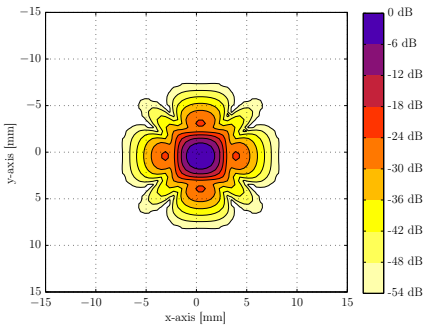

(d) PSF in C-scan at 50 mm depth of the fully addressed array.

Figure D.8: Comparison of the achievable PSF from a row-column addressed array and a fully addressed array, with the same number of active elements. As a result of both the x–dimension (in receive) and the y–dimension (in transmit) being dynamically focused is the performance in the two dimensions completely identical.

demonstrated how focusing can be achieved with a row-column addressed array. The PSF was shown to contain ghosts, originating from edge effects of the long row and column elements. When using synthetic transmit focusing and applying both beamforming and hardware apodization, the imaging quality of the row-column addressed array was shown to be superior to the imaging quality of a fully addressed array using the same amount of channels. The array simulated uses only 128 channels in transmit and 128 channels in receive to achieve 3D imaging. The array also has a large footprint, which gives it the potential to achieve a high penetration depth and signal-to-noise ratio. The array thereby seems very promising for 3D and 4D imaging. Even for 2D imaging, the array could be used. In 2D imaging, it could do plane wave imaging with the out-of-plane dimension dynamically one-way focused.

ACKNOWLEDGMENTS

This work was financially supported by grant 024-2008-3 from the Danish Advanced Technology Foundation and from BK Medical, Herlev, Denmark.

References

Austeng, A. and S. Holm (2002). "Sparse 2-D arrays for 3-D phased array imaging - design methods". In: *IEEE Trans. Ultrason., Ferroelec., Freq. Contr.* 49.8, pp. 1073–1086 (cit. on p. 112).

Brunke, S. S. and G. R. Lockwood (1997). "Broad-bandwidth radiation patterns of sparse two-dimensional vernier arrays". In: *IEEE Trans. Ultrason., Ferroelec., Freq. Contr.* 44.5, pp. 1101–1109 (cit. on p. 112).

Chen, A. I. H., L. L. Wong, A. S. Logan, and J. T. W. Yeow (2011). "A CMUT-based real-time volumetric ultrasound imaging system with row-column addressing". In: *Proc. IEEE Ultrason. Symp.* Pp. 1755–1758 (cit. on p. 112).

Davidsen, R. E., J. A. Jensen, and S. W. Smith (1994). "Two-Dimensional Random Arrays for Real Time Volumetric Imaging". In: *Ultrasonic Imaging* 16.3, pp. 143–163 (cit. on p. 112).

Hansen, J. M., M. C. Hemmsen, and J. A. Jensen (2011). "An object-oriented multi-threaded software beamformation toolbox". In: *Proc. SPIE Med. Imag.* Vol. 7968, pages. URL: http://dx.doi.org/10.1117/12.878178 (cit. on p. 118).

Jensen, J. A. (1996). "Field: A Program for Simulating Ultrasound Systems". In: *Med. Biol. Eng. Comp.* 10th Nordic-Baltic Conference on Biomedical Imaging, Vol. 4, Supplement 1, Part 1, pp. 351–353 (cit. on p. 118).

Jensen, J. A. and N. B. Svendsen (1992). "Calculation of Pressure Fields from Arbitrarily Shaped, Apodized, and Excited Ultrasound Transducers". In: *IEEE Trans. Ultrason., Ferroelec., Freq. Contr.* 39, pp. 262–267 (cit. on p. 118).

Karaman, M., I. O. Wygant, O. Oralkan, and B. T. Khuri-Yakub (2009). "Minimally Redundant 2-D Array Designs for 3-D Medical Ultrasound Imaging". In: *IEEE Trans. Med. Imag.* 7, pp. 1051–1061 (cit. on p. 112).

Kim, K. S. and T. K. Song (2004). "High volume rate 3-D ultrasound imaging using cross array based on synthetic transmit focusing". In: *Proc. IEEE Ultrason. Symp.* Vol. 2, pp. 1409–1412 (cit. on p. 116).

Logan, A. S., L. L. P. Wong, A. I. H. Chen, and J. T. W. Yeow (2011). "A 32 x 32 element row-column addressed capacitive micromachined ultrasonic transducer". In: *IEEE Trans. Ultrason., Ferroelec., Freq. Contr.* 58.6, pp. 1266–1271 (cit. on p. 112).

Logan, A. S., L. L. P. Wong, and J. T. W. Yeow (2009). "2-D CMUT wafer bonded imaging arrays with a row-column addressing scheme". In: *Proc. IEEE Ultrason. Symp.* Pp. 984–987 (cit. on p. 112).

Ramm, O. T. von, S. W. Smith, and H. G. Pavy (1991). "High speed ultrasound volumetric imaging system – Part II: Parallel processing and image display". In: *IEEE Trans. Ultrason., Ferroelec., Freq. Contr.* 38, pp. 109–115 (cit. on p. 112).

Ranganathan, K. and W. F. Walker (2007). "Cystic Resolution: A Performance Metric for Ultrasound Imaging Systems". In: *IEEE Trans. Ultrason., Ferroelec., Freq. Contr.* 54.4, pp. 782–792 (cit. on p. 120).

Rasmussen, M. F., G. Férin, R. Dufait, and J. A. Jensen (2012). "Comparison of 3D Synthetic Aperture Imaging and Explososcan using Phantom Measurements". In: *Proc. IEEE Ultrason. Symp.* Pp. 113–116. DOI: 10.1109/ULTSYM.2012.0028 (cit. on p. 112).

Rasmussen, M. F., J. M. Hansen, G. Férin, R. Dufait, and J. A. Jensen (2012). "Preliminary comparison of 3D synthetic aperture imaging with Explososcan". In: *Proc. SPIE Med. Imag.* Ed. by J. G. Bosch and M. M. Doyley. Vol. 8320. 83200F. SPIE, pp. 1–9 (cit. on p. 112).

Seo, C. H. and J. T. Yen (2009). "A 256 x 256 2-D array transducer with row-column addressing for 3-D rectilinear imaging". In: *IEEE Trans. Ultrason., Ferroelec., Freq. Contr.* 56.4, pp. 837–847 (cit. on p. 112).

Smith, S. W., H. G. Pavy, and O. T. von Ramm (1991). "High speed ultrasound volumetric imaging system – Part I: Transducer design and beam steering". In: *IEEE Trans. Ultrason., Ferroelec., Freq. Contr.* 38, pp. 100–108 (cit. on p. 116).

Turnbull, D. H. and F. S. Foster (1991). "Beam steering with pulsed two-dimensional transducer arrays". In: *IEEE Trans. Ultrason., Ferroelec., Freq. Contr.* 38.4, pp. 320–333 (cit. on p. 112).

Vilkomerson, D., J. Greenleaf, and V. Dutt (1995). "Towards a Resolution Metric for Medical Ultrasound Imaging". In: *Proc. IEEE Ultrason. Symp.* Pp. 1405–1410 (cit. on p. 120).

Yen, J. T., J. P. Steinberg, and S. W. Smith (2000). "Sparse 2-D array design for real time rectilinear volumetric imaging". In: *IEEE Trans. Ultrason., Ferroelec., Freq. Contr.* 47.1, pp. 93–110 (cit. on p. 112).

PAPER E

3-D Ultrasound Imaging Performance of a Row-Column Addressed 2-D Array Transducer: A Measurement Study

Authors: Morten Fischer Rasmussen and Jørgen Arendt Jensen.

Published in: *Proceedings of IEEE Ultrasonic Symposium* pp. 1460-1463, (2013).

Abstract

A real-time 3-D ultrasound measurement using only 32 elements and 32 emissions is presented. The imaging quality is compared to a conventionally fully addressed array using 1024 elements and 256 emissions. The main-lobe of the measured line spread function is almost identical, but the side-lobe levels are higher for the row-column addressed array. The cystic resolution sampled at a relative intensity difference of 20 dB shows a cyst size of 5.00 mm for the row-column addressed array and 2.39 mm for the fully sampled array. A simulation study is carried out which compares how the imaging quality of the two addressing methods scales with the number of beamforming channels used. It is shown that for any fixed number of active elements, a row-column addressed array achieves a better image quality than fully addressing thet array. When using 128 channels, the main-lobe when fully addressing the array is 510 % larger than when row-column addressing the array. The cyst radius needed to achieve -20 dB intensity in the cyst is 396 % larger for the fully addressed array compared to the row-column addressed array. The measurements were made using the experimental ultrasound scanner SARUS and a 32x32 element ultrasound probe made by Vermon S.A.

Center for Fast Ultrasound Imaging, Department of Electrical Engineering, Technical University of Denmark, 2800 Kgs. Lyngby, Denmark

E.1 Introduction

For ultrasonic 3-D imaging, 2-D array transducers are required to achieve real–time scanning of a volume (Ramm et al. 1991; Turnbull and Foster 1991). The number of elements in a fully addressed 2-D array scales with the square of the number of elements in each dimension. To control all elements in the array, a connection to each element is necessary. However, addressing each element individually results in a vast amount of interconnections and a large amount of data to be recorded. This posses both a great practical challenge in producing the internections and in sampling and real-time processing the large amount of data. An $N \times N$ element array can be operated using just $2N$ connections when row-column addressing is used (Daher and Yen 2004; Démoré et al. 2009; Morton and Lockwood 2003; Rasmussen and Jensen 2013; Seo and Yen 2009). This is opposed to the N^2 connections needed when conventionally addressing the elements. An earlier publication by the authors investigated the 3-D imaging performance of row-column addressed arrays via simulations (Rasmussen and Jensen 2013). The simulations indicated that a good imaging performance is achievable when apodizing the sub-elements within each row and column element, thereby suppressing the otherwise distinct ghost echoes. In this paper, the imaging performance of a 32+32 element row-column addressed array is investigated. The investigation is made through measurements carried out using the 1024 channel research ultrasound scanner SARUS and a 32×32 element ultrasound probe. The measurements are compared to a fully addressed array using the 'gold standard' for real-time 3-D ultrasound imaging: Explososcan. It is also investigated through Field II simulations how the imaging performance scales with the number of active elements used for both the fully addressed array and the row-column addressed array.

E.2 Methods

E.2.1 Row-column Addressed Array

The principle of row-column addressing a 2-D array is to address the elements by their row- or column index, thus addressing an entire row or column of elements instead of a single element. This effectively turns the 2-D array into two orthogonal 1-D arrays, which is illustrated in Fig. E.1. The first 1-D array consists of row-elements and the second 1-D array of column elements. Each element in the 2-D array is now a line element, either a row element or a column element, and each line element consists of N sub-elements.

As is shown in (Démoré et al. 2009) and (Rasmussen and Jensen 2013) the creation of large row and column elements leads to edge effects. The more sub-elements a line element consists of, the more apparent the edge effects becomes. To decrease the edge effects, the sub-elements are apodized with a window function that tends to zero towards the edges of the line elements. In this paper the sub-elements are apodized with a Hann-window.

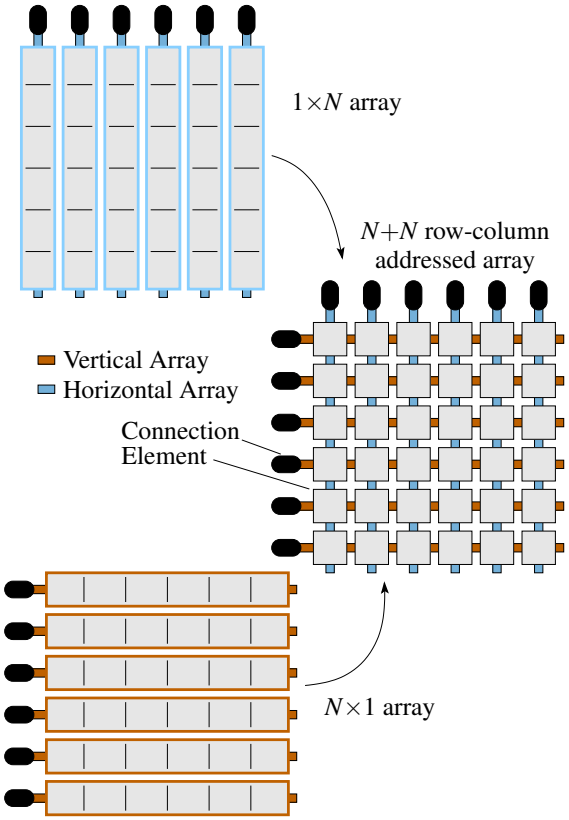

Figure E.1: A row-column addressed 2-D array can be interpreted as two orthogonal 1-D arrays.

For the measurements a 2-D row-column addressed array with 32+32 elements is emulated using a 32×32 fully addressed array. For the Field II simulations a N+N element array is emulated by using a N×N element array. In transmit all elements in the same row are used as one element; they emit the same signal with the same time delay. The focus zone therefore has the shape of a line segment. Synthetic transmit focusing (STF) is used to focus the image in the elevation direction (y–dimension). In receive, the signals measured from elements in the same column are summed to one signal before being dynamically focused in the lateral dimension (x–dimension). The elevation direction can thereby be focused in transmit and the lateral direction in receive. Because of limitations in the beamforming software the emissions are focused using a single line element at a time. The entire 3-D volume is therefore acquired using N emissions for an

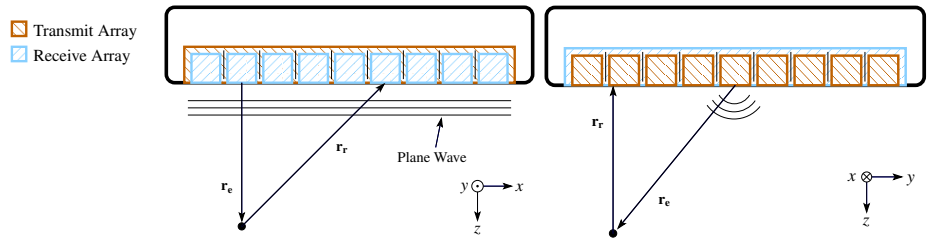

(a) ToF in the x–dimension. (b) ToF in the y–dimension.

Figure E.2: Time of flight (ToF) illustration of one emission to the focus point and back to one receiving element. $\mathbf{r_e}$ is the vector from the nearest point of the emitting element to the focus point and $\mathbf{r_r}$ is the vector from the focus point to the nearest point on the receive element.

N+N element array.

The emitted wavefront of a single element has the shape of a cylinder surface: it is a plane wave in the z-x plane and a circle arc in z-y plane. This is illustrated in Fig. E.2. The time of flight is given by the shortest distance from the source to the scatterer and back to the receiving element, divided by the speed of sound. Using the notation from Fig. E.2, this can be written as:

$$t_{ToF} = \frac{\|\mathbf{r_e}\| + \|\mathbf{r_r}\|}{c}\,, \tag{E.1}$$

where $\mathbf{r_e}$ is the vector from the emitting element to the focus point, $\mathbf{r_r}$ is the vector from the focus point and back to the receiving element, and c is the speed of sound in the medium. Since the length of each element is large, the usual assumption that the elements are point sources no longer holds. Therefore, $\mathbf{r_e}$ and $\mathbf{r_r}$ connects the focus point to the closest point on the source element and the receiving element respectively.

Determining $\|\mathbf{r_e}\|$ and $\|\mathbf{r_r}\|$ is solved by calculating the distance between an arbitrary point in 3-D, the focus point $\mathbf{P}$, and a line segment $\mathbf{AB}$ from point $\mathbf{A}$ to point $\mathbf{B}$. The minimum distance between the point $\mathbf{P}$ and the line segment $\mathbf{AB}$ is in (Rasmussen and Jensen 2013) shown to be:

$$d(\mathbf{AB},\mathbf{P}) = \begin{cases} \dfrac{\|\mathbf{AB}\times\mathbf{AP}\|}{\|\mathbf{AB}\|} & \text{if } 0 \le \hat{s} \le 1, \\ \|\mathbf{AP}\| & \text{if } \hat{s} < 0\,, \\ \|\mathbf{BP}\| & \text{if } \hat{s} > 1\,, \end{cases} \tag{E.2}$$

where $\hat{s}$ is determined by:

$$\hat{s} = \frac{\mathbf{AP} \cdot \mathbf{AB}}{\|\mathbf{AB}\|^2} \ . \tag{E.3}$$

Using (E.2), the distances $\|\mathbf{r_e}\|$ and $\|\mathbf{r_r}\|$ can now be determined as

$$\|\mathbf{r_e}\| = d(\mathbf{xmt}_m, \mathbf{P}) \quad \text{and} \quad \|\mathbf{r_r}\| = d(\mathbf{rcv}_n, \mathbf{P}) \ , \tag{E.4}$$

where $\mathbf{xmt}_m$ is the **A** and **B** coordinates of the m'th transmit element and $\mathbf{rcv}_n$ is the corresponding coordinates for the n'th receive element.

E.2.2 Fully Addressed Array

Explososcan is used as the imaging technique for the fully addressed array. Explososcan is a parallel processing technique developed by Smith, von Ramm and colleagues in the 1980s (Ramm et al. 1991; Shattuck et al. 1984) which increases the acquisition rate compared to standard sequential acquisition. A broad transmit beam is emitted and multiple receive beams are focused in parallel during receive. If for instance 5×5 lines are beamformed per emission instead of just one, the frame rate increases by a factor of 25. This paper beamforms 4×4 lines in receive for each emission. The focus point is placed at a depth of 60 mm and the N closest elements to the center of the aperture are used in both transmission and in receive. The active aperture therefore has the shape of a circle, except when using 1024 active elements which corresponds to all elements in the 32×32 element array. 16 emissions are used per dimension, giving 256 emissions per imaged volume.

E.2.3 Image Quality

The imaging quality is investigated by acquiring the point spread function (PSF) of the simulations and the line spread function (LSF) of the measurements. The LSF is measured on a wire phantom using both with a row-column addressed array and a fully addressed array. The 3-D volume is sliced across the direction of the wire, into a 2-D B-mode image, to emulate the point-spread-function (PSF).

The PSFs are evaluated using both the full-width-at-half-maximum (FWHM) and the cystic resolution. The cystic resolution describes the ability to detect an anechoic cyst in a uniform scattering medium (Vilkomerson et al. 1995). The lower the intensity is at the center of the cyst, i.e. the darker it appears, the better imaging performance. The relative intensity (RI) of the anechoic cyst was shown by Ranganathan and Walker (Ranganathan and Walker 2007), to be quantized as the clutter energy to total energy ratio,

$$\mathrm{RI}(R) = \sqrt{\frac{E_{out}(R)}{E_{tot}}} = \sqrt{1 - \frac{E_{in}(R)}{E_{tot}}} \, , \tag{E.5}$$

Table E.1: Ultrasound probe parameters.

Parameter name	Notation	Value
Emission center frequency	f_0	2.6 MHz
Transducer fundamental resonance freq.	f_T	3.5 MHz
Number of transmitted cycles	N_{cycles}	2
Probe pitch –x	d_x	300 µm
Probe pitch –y	d_y	300 µm
Total number of elements –x	N_{tot_x}	32
Total number of elements –y	N_{tot_y}	35
Inactive rows	–	9,18,27

where E_{in} is the signal energy inside a circular region with radius, R, centered on the peak of the point spread function, E_{tot} is the total point spread function energy, and E_{out} is the point spread function energy outside the circular region. The RI(R)–curve can be compressed to a single number by sampling the curve at 20 dB. The result is the required cyst radius at which the intensity at the cyst center is 20 dB lower than its surroundings, written as $R_{20\text{dB}}$.

E.2.4 Comparison

As is seen from Table E.1 the ultrasound probe contains three inactive rows of elements. This discontinuity in the aperture gives rise to higher side-lobes. When using few active elements in the aperture, fewer of the inactive rows become part of the active aperture. A smaller aperture therefore performs relatively better than a aperture using all available transducer elements. A direct comparison is therefore not feasible between for instance a 16+16 and a 32×32 element array.

The image quality comparison for the measurements is made only between a 32+32 row-column addressed array and a 32×32 element fully addressed array.

To compare how the image quality scales with the number of elements used, a dense aperture is simulated using Field II.

A Field II simulation study is carried out to compare how the image quality scales with the number of active element used. The row-column addressed array is simulated using 16, 32, 64 and 128 active elements and Explososcan is simulated using 32, 64, 128, 256, 512 and 1024 active elements. The simulated apertures have the same element size, pitch and frequency response as the 32×32 element ultrasound probe used for the measurements. The difference between the real and the simulated array being that the simulated array contains no discontinuities and an array size up to 128×128 element array is used.

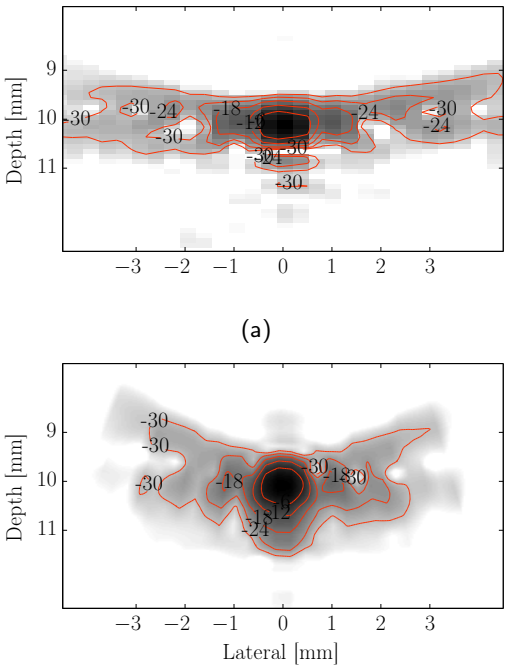

Figure E.3: Line Spread Function of (a) Row-column addressed array 32 channels and 32 emissions and (b) Conventional fully addressed array with 1024 channels and 256 emissions.

E.3 Experimental Setup

The measurements are performed using a 2-D phased array ultrasound probe, made by Vermon S.A., Tours, France, used. The 2-D probe has 35×32 elements, of which row 9,18 and 27 are inactive, effectively giving 32×32 individually controllable elements. The ultrasound probe parameters are listed in Table E.1. The fundamental resonance frequency of the probe is 3.5 MHz, but in order for the element pitch to equal half a wavelength the center frequency of the emission is 2.6 MHz.

All measurements are carried out using the 1024 channel experimental ultrasound scanner SARUS (*synthetic aperture real-time ultrasound system*) (Jensen, Holten-Lund, et al. 2013). The measured data are beamformed using the toolbox BFT3 (Hansen et al. 2011).

When acquirering the LSF a 0.07 mm thick and 10 cm long cobber wire is placed

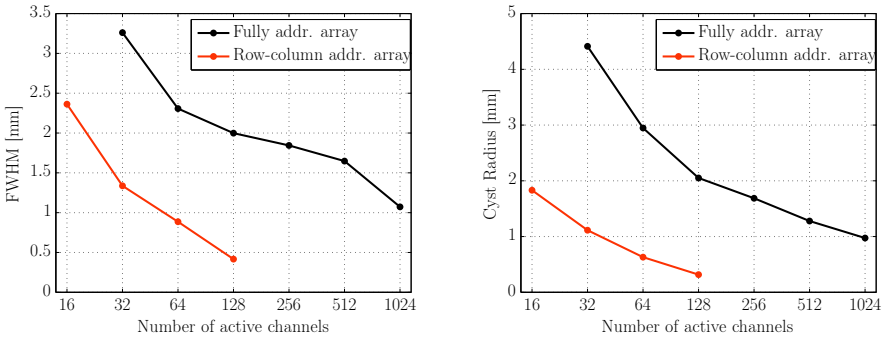

(a) (b)

Figure E.4: Resolution scaling with number og active channels.

in water 10 mm under the ultrasound probe surface. The wire is oriented parallel to the y-axis of the ultrasound probe. The wire is positioned using the positioner of the intensity measurement system "AIMS 3" made by Onda Corporation, Sunnyvale, CA, USA.

The simulation study of the image quality scaling is carried out using Field II (Jensen 1996; Jensen and Svendsen 1992) and MATLAB (The MathWorks, Inc., Natick, Massachusetts, USA).

E.4 Results

The measured LSF is seen in Fig. E.3. The main-lobe size of the LSF is almost identical for the two measurements. The FWHM is 0.89 mm when row-column addressing the array and when fully addressing the array it is 0.86 mm. A larger difference is apparent on the size of the side-lobes. When fully addressing the array a cystic resolution at 20 dB relative intensity difference, the $R_{20\text{dB}}$, of 2.39 mm is achieved, whereas the $R_{20\text{dB}}$ when row-column addressing the array is 5.00 mm. The row-column addressed array thereby has a 3.4 % larger main-lobe and a 109 % larger $R_{20\text{dB}}$. The better image quality of the fully addressed array comes with the cost of using 32 times as many elements and 8 times as many emissions than when row-column addressing the array.

In Fig. E.4 the result of the simulation study is shown. For any given number of active channels row-column addressing an array is seen to give a better imaging quality than fully addressing the array. When using 128 channels the main-lobe is 510 % larger fully addressing the array than when row-column addressing the array. The $R_{20\text{dB}}$ increases 396 % when fully addressing the array.

E.5 Conclusion

A wire phantom measurement made with an array that was both conventionally fully addressed and row-column addressed was presented. It was thereby demonstrated that full 3-D ultrasound imaging can be achieved using only 32 channels and 32 emissions. The measurement showed an almost identical main-lobe size, but larger side-lobes for the row-column addressed array compared to the fully addressed array. The main-lobe was 3.4 % larger and the $R_{20\text{dB}}$ 109 % larger for the row-column addressed array compared to the fully addressed array. This has to be kept in relation to that the fully addressed array used 3200 % more elements and 800 % as many emissions than when row-column addressing the array.

The simulation study showed that for any fixed number of active elements a row-column addressed array achieves better imaging quality than fully addressing the array.

References

Daher, N. M. and J. T. Yen (2004). "Rectilinear 3-D ultrasound imaging using synthetic aperture techniques". In: *Proc. IEEE Ultrason. Symp.* Vol. 2, pp. 1270–1273 (cit. on p. 126).

Démoré, C. E. M., A. Joyce, K. Wall, and G. Lockwood (2009). "Real-time volume imaging using a crossed electrode array". In: *IEEE Trans. Ultrason., Ferroelec., Freq. Contr.* 56.6, pp. 1252–1261 (cit. on p. 126).

Hansen, J. M., M. C. Hemmsen, and J. A. Jensen (2011). "An object-oriented multi-threaded software beamformation toolbox". In: *Proc. SPIE Med. Imag.* Vol. 7968, pages. URL: `http://dx.doi.org/10.1117/12.878178` (cit. on p. 131).

Jensen, J. A. (1996). "Field: A Program for Simulating Ultrasound Systems". In: *Med. Biol. Eng. Comp.* 10th Nordic-Baltic Conference on Biomedical Imaging, Vol. 4, Supplement 1, Part 1, pp. 351–353 (cit. on p. 132).

Jensen, J. A., H. Holten-Lund, R. T. Nilsson, M. Hansen, U. D. Larsen, R. P. Domsten, B. G. Tomov, M. B. Stuart, S. I. Nikolov, M. J. Pihl, Y. Du, J. H. Rasmussen, and M. F. Rasmussen (2013). "SARUS: A Synthetic Aperture Real-time Ultrasound System". In: *IEEE Trans. Ultrason., Ferroelec., Freq. Contr.* 60.9, pp. 1838–1852 (cit. on p. 131).

Jensen, J. A. and N. B. Svendsen (1992). "Calculation of Pressure Fields from Arbitrarily Shaped, Apodized, and Excited Ultrasound Transducers". In: *IEEE Trans. Ultrason., Ferroelec., Freq. Contr.* 39, pp. 262–267 (cit. on p. 132).

Morton, C. E. and G. R. Lockwood (2003). "Theoretical assessment of a crossed electrode 2-D array for 3-D imaging". In: *Proc. IEEE Ultrason. Symp.* Pp. 968–971 (cit. on p. 126).

Ramm, O. T. von, S. W. Smith, and H. G. Pavy (1991). "High speed ultrasound volumetric imaging system – Part II: Parallel processing and image display". In: *IEEE Trans. Ultrason., Ferroelec., Freq. Contr.* 38, pp. 109–115 (cit. on pp. 126, 129).

Ranganathan, K. and W. F. Walker (2007). “Cystic Resolution: A Performance Metric for Ultrasound Imaging Systems”. In: *IEEE Trans. Ultrason., Ferroelec., Freq. Contr.* 54.4, pp. 782–792 (cit. on p. 129).

Rasmussen, M. F. and J. A. Jensen (2013). “3D ultrasound imaging performance of a row-column addressed 2D array transducer: a simulation study”. In: *Proc. SPIE Med. Imag.* 86750C, pp. 1–11 (cit. on pp. 126, 128).

Seo, C. H. and J. T. Yen (2009). “A 256 x 256 2-D array transducer with row-column addressing for 3-D rectilinear imaging”. In: *IEEE Trans. Ultrason., Ferroelec., Freq. Contr.* 56.4, pp. 837–847 (cit. on p. 126).

Shattuck, D. P., M. D. Weinshenker, S. W. Smith, and O. T. von Ramm (1984). “Explososcan: A parallel processing technique for high speed ultrasound imaging with linear phased arrays”. In: *J. Acoust. Soc. Am.* 75, pp. 1273–1282 (cit. on p. 129).

Turnbull, D. H. and F. S. Foster (1991). “Beam steering with pulsed two-dimensional transducer arrays”. In: *IEEE Trans. Ultrason., Ferroelec., Freq. Contr.* 38.4, pp. 320–333 (cit. on p. 126).

Vilkomerson, D., J. Greenleaf, and V. Dutt (1995). “Towards a Resolution Metric for Medical Ultrasound Imaging”. In: *Proc. IEEE Ultrason. Symp.* Pp. 1405–1410 (cit. on p. 129).

PAPER F

Row-Column Addressed 2-D CMUT Arrays with Integrated Apodization

Authors: Thomas Lehrmann Christiansen[a], Morten Fischer Rasmussen[b], Jørgen Arendt Jensen[b] and Erik Vilain Thomsen[a].

Manuscript for (abstract is accepted): *Proceedings of IEEE Ultrasonic Symposium*, (2014).

Abstract

This paper presents experimental results from row-column addressed capacitive micromachined ultrasonic transducers (CMUTs) with integrated apodization. The apodization is applied by varying the density of CMUT cells in the array with the objective of damping the edge waves originating from the element ends. Two row-column addressed $32+32$ CMUT arrays are produced, one with and one without integrated apodization. Measurements of the emitted pressure field from the array with integrated apodization show a reduction in edge wave energy of 8.4 dB (85 %) compared to the array without integrated apodization. Simulations in Field II yield a corresponding reduction of 13.0 dB (95 %). The simulations are able to replicate the measured pressure field, proving the predictability of the technique.

F.1 Introduction

Row-column addressed arrays for ultrasonic imaging have recently attracted some attention, as they offer volumetric imaging with a greatly reduced number of connections to the array compared to fully wired 2-D matrix probes (Démoré et al. 2009; Logan et al. 2011; Sampaleanu et al. 2014; Seo and Yen 2009). Despite this advantage, such arrays have an inherent draw-back: the long elements produce edge waves originating from the

[a]Department of Micro- and Nanotechnology, Technical University of Denmark, 2800 Kgs. Lyngby, Denmark

[b]Center for Fast Ultrasound Imaging, Department of Electrical Engineering, Technical University of Denmark, 2800 Kgs. Lyngby, Denmark

abrupt truncation at the element ends. These edge waves generate artefacts in the image in the form of ghost echoes (Démoré et al. 2009; Rasmussen and Jensen 2013). Due to the row-column addressing scheme, no electronic control is available along the length of the elements. As a consequence, this rules out the option of applying electronic apodization to remove the effect of the truncation. The solution to the problem is therefore to integrate the apodization in the transducer array itself, as suggested in recent studies (Démoré et al. 2009; Rasmussen and Jensen 2013). Several embodiments of the integrated apodization have been suggested, such as attenuating layers (Démoré et al. 2009), variation in the active element area and bias control of capacitive micromachined ultrasonic transducers (CMUTs) (Rasmussen, Christiansen, et al. n.d.).

The objective of this paper is to experimentally demonstrate the effect of an integrated apodization based on variation of the effective area through measurements of the emitted pressure field. Experimental results are presented from two versions of a $32+32$ row-column addressed CMUT array; one without integrated apodization and one with integrated apodization. Simulations in Field II (Jensen 1996; Jensen and Svendsen 1992) are carried out to compare the measured pressure field with the expected, thereby demonstrating the predictability of the technique.

F.2 Transducer Design

In this study, two $32+32$ row-column addressed CMUT arrays are produced; one without integrated apodization and one with integrated apodization. The mask layout of the two transducer arrays are depicted in Fig. F.1. The two transducers both have a total size of $12\,\text{mm}\times12\,\text{mm}$, a pitch of $300\,\mu\text{m}$, an element kerf of $12\,\mu\text{m}$, and a total of 32 row elements and 32 column elements. The aperture size is consequently $9.6\,\text{mm}\times9.6\,\text{mm}$. In the array with no integrated apodization (Fig. F.1a), circular CMUT cells are densely distributed over the array, with 3 cells along the width of the elements and 96 cells along their length. The individual cells have a diameter of $72\,\mu\text{m}$, a plate thickness of $2\,\mu\text{m}$, and a vacuum gap height and insulation oxide thickness of each 195 nm. Each section of the array, where a row and a column intersects, can accommodate a maximum of 9 CMUT cells. For the array with integrated apodization (Fig. F.1b), the number of cells in this square section is varied according to a circularly symmetric Hann function. This effectively alters the active area and consequently the intensity of the emitted/received signal. In this way, the emitted/received signal is gradually decreased towards the edges of the array. The purpose is thereby to suppress the edge waves, which otherwise lead to ghost echoes in images produced by row-column addressed arrays (Rasmussen and Jensen 2013).

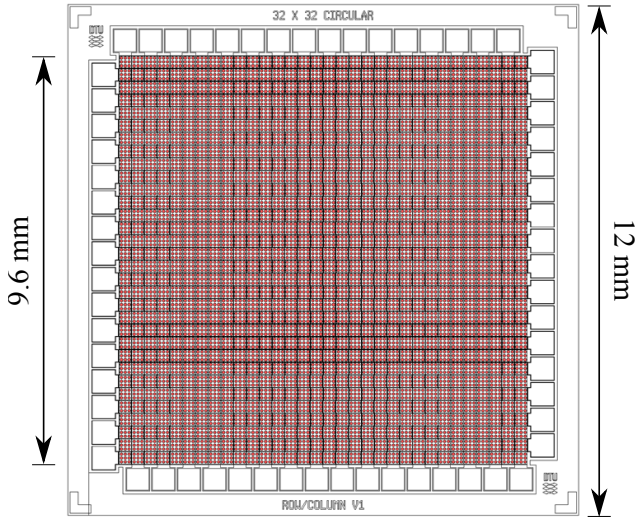

(a)

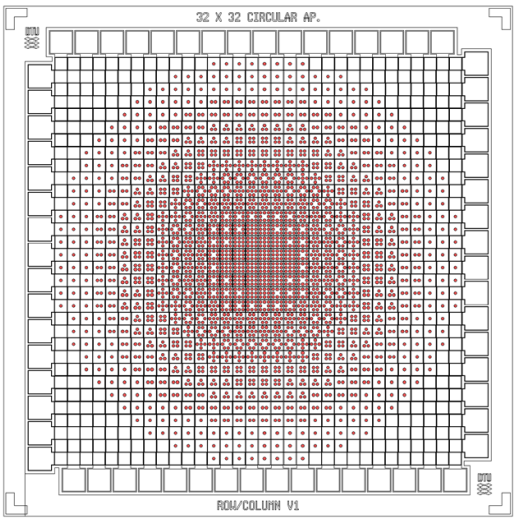

(b)

Figure F.1: Mask layout of the row-column addressed $32+32$ CMUT transducers without integrated apodization (a) and with integrated apodization (b). The red circles indicate the individual CMUT cells, which are densely packed in the non-apodized configuration, while the number of cells follows a circular symmetric Hann function in the apodized layout.

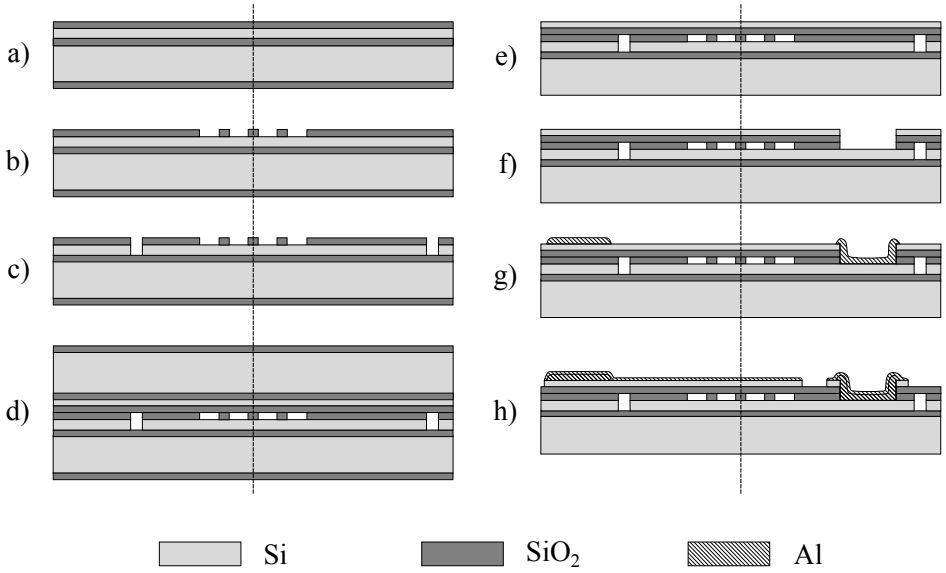

Figure F.2: Process flow of the cleanroom fabrication. The dashed line separates the layer composition comprising the top electrodes (to the left of the line) and the bottom electrodes (to the right of the line). The steps are: a) oxidation, b) cavity etch, c) bottom electrode etch, d) wafer bonding, e) handle etch, f) etch access to bottom electrodes, g) deposit and etch wire-bonding pads, and h) deposit and etch top electrodes. A total of five lithography masks are used (in steps b, c, f, g, and h).

F.3 Transducer Fabrication

The arrays were fabricated using cleanroom processing techniques, partly based on previous works described in the literature (Huang et al. 2003; Zhang et al. 2012). The individual process steps are shown in Fig. F.2.

The fabrication process utilized two silicon-on-insulator (SOI) wafers, both having a 525 µm thick handle layer with high resistivity (1-10 Ω cm), a 1 µm thick buried oxide layer, and a low resistivity (0.01-0.001 Ω cm) device layer. The device layer on the first SOI wafer was 20 µm thick and was used to create the bottom electrodes (rows). The second SOI wafer had a 1.9 µm thick device layer, which was used for the top electrodes (rows) of the array. These top electrodes also constituted the flexible plate of the CMUTs.

Both SOI wafers were dry oxidized at 1100 °C for 2 hours and 30 minutes to grow a 195 nm thick layer of oxide (Fig. F.2a). The CMUT cavities were then defined in the 20 µm SOI wafer using conventional UV lithography and etched using reactive ion etching (RIE) as shown in Fig. F.2b. After stripping the photoresist, a second lithography step was used to define the bottom electrodes as shown in Fig. F.2c. Two consecutive RIE etches

were used to selectively etch first the oxide layer and subsequently the underlying silicon device layer. After stripping the photoresist, the fabrication of the bottom electrodes and the substrate supporting the array was complete.

Both SOI wafers were then cleaned using a standard RCA cleaning procedure (Kern 1990) and bonded together in vacuum (0.01 mbar) using fusion bonding and a subsequent annealing step (70 min at 1100 °C), see Fig. F.2d. The oxide layer covering the back side of both wafers was removed in buffered hydrofluoric acid (BHF), after which the handle layer and buried oxide layer of the top SOI wafer was etched using both RIE and BHF, respectively, as shown in Fig. F.2e.

A third lithography step followed by selective RIE in first the silicon layer and subsequently the oxide layer was used to define openings to the bottom electrodes, see Fig. F.2f. The thin device layer is partly transparent in the visible spectrum, and alignment to the bottom wafer alignment marks could therefore be performed, thereby omitting the need for alignment during the wafer bonding step.

Fig. F.2g shows the wire-bonding pads, which were made by depositing a 800 nm aluminium layer on the entire wafer using electron beam evaporation and structured by performing a lithography step followed by a selective aluminium etch in $H_2O : H_3PO_4$ (1 : 2) at 50 °C. The top electrodes, or columns, were then finally defined by a step similar to the previous, but this time with a 200 nm aluminium deposition. Before removing the photoresist, the exposed silicon layer was etched using RIE to isolate the individual top electrodes, thereby concluding the fabrication process.

F.4 Measurement and Simulation Setup

The acoustic field of the two CMUT arrays were measured with a MH28-5 needle hydrophone (Force Technology, Denmark) and a DSO5012A oscilloscope (Agilent Technologies, CA, USA). The measurement setup is shown in Fig. F.3. For spatial mapping of the transmit fields, the hydrophone was mounted on the positioner of the intensity measurement system AIMS-3 (Onda Corporation, CA, USA). The hydrophone was positioned 5.3 mm from the array and scanned over the center of each array in lateral steps of 0.1 mm. The transducers were actuated using a 8116A pulse/function generator (Hewlett-Packard Company, CA, USA) through a custom made class B amplifier with a bandwidth of 8 MHz. All row elements, respectively column elements, were electrically short circuited to allow simultaneous actuation of the whole array. All measurements were carried out in rapeseed oil (speed of sound: 1476 m/s) to ensure electrical insulation of the prototype transducers.

In this work, Field II (Jensen 1996; Jensen and Svendsen 1992) was used for all simulations. Field II was set up to use lines to describe the apertures with each element of the array being divided into square mathematical elements with a side length of $\lambda/4$. In the simulation, the square intersection of each row- and column element, each consisting of four mathematical elements, were given an apodization value of $\{0, \frac{1}{9}, \frac{2}{9}, \frac{1}{3}, \frac{4}{9}, \frac{5}{9}, \frac{2}{3}, \frac{7}{9}, \frac{8}{9}, 1\}$

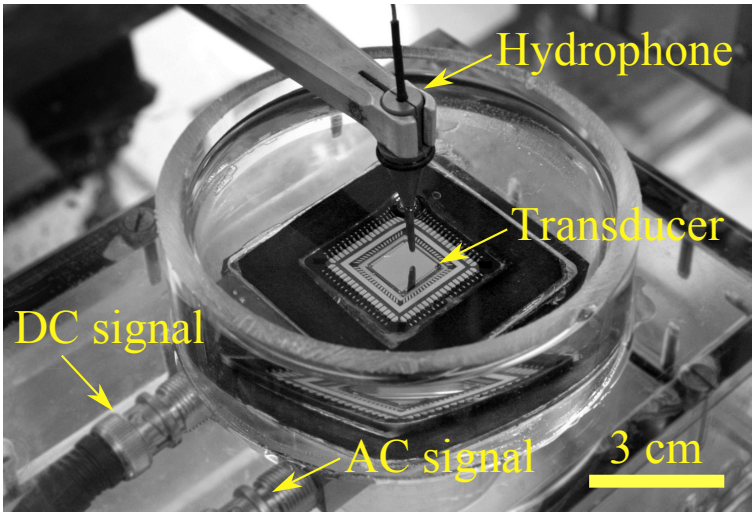

Figure F.3: Picture of the experimental setup used to measure the emitted pressure field. The transducer is mounted and wire-bonded on a chip carrier, which is inserted into a chip socket. The transducer array is submerged in rapeseed oil, and a single AC+DC signal is supplied to all the row channels of the array, while the columns are grounded.

dependent on whether there were 0, 1, 2, 3, 4, 5, 6, 7, 8, or 9 CMUT cells in the real array within this region.

F.5 Results

The measured and simulated emitted fields from the two arrays are shown in Fig. F.4. The result for the array without integrated apodization is shown in Fig. F.4a and Fig. F.4c (simulation and measurement, respectively), while the result for the array with integrated apodization is shown in Fig. F.4b and Fig. F.4d. The main wave arrives after 3.6 s, corresponding to a distance of 5.3 mm. In addition to this, a spherical wave is emitted from the edges of the array. The arrival time of the wave front is the distance travelled divided by the speed of sound. The arrival time of the edge wave at the position of the hydrophone is then

$$t_{\text{edge}} = \frac{\sqrt{d^2 + x^2}}{c}\,, \tag{F.1}$$

where d is the perpendicular distance from the point being measured and the transducer surface, x is the lateral distance of the point being measured from the edge of the array, and c is the speed of sound. The predicted arrival time of an edge wave originating from the array aperture edge at −4.8 mm has been plotted with a dashed line in both the

simulated and measured fields for the array without integrated apodization in Fig. F.4a and Fig. F.4b, respectively. It is seen that the edge wave is accurately predicted, thereby confirming its origin.

For the array with integrated apodization (Fig. F.4b and Fig. F.4d), the two edge waves are seen to be significantly damped. The damping in terms of edge wave energy can be quantified by summing the squared pressure values along the curve given by (F.1) for both arrays. This yields a reduction of edge wave energy of 13.0 dB (95 %) for the simulation and 8.4 dB (85 %) for the measurement. The deviance between the simulation and measurement may be contributed to the significant transducer ringing present in the measurements due to the lack of a backing material. This will add to the calculated edge wave energy in both cases and thereby reduce the energy ratio.

In Fig. F.5a and Fig. F.5b, the amplitude of the measured and simulated pressure field is shown for the two arrays. The amplitude is extracted at the arrival of the main wave at time 3.6 s, and it thereby corresponds to a horizontal cross-section of the plots in Fig. F.4. The profiles of the simulated and measured amplitudes are seen to be comparable for both of the arrays, demonstrating that the field emitted from the arrays are predictable. The correspondence is especially relevant for the array with integrated apodization, since it demonstrates that the emitted field indeed scales directly with the density of CMUT cells.

F.6 Conclusions

This paper demonstrated the effect of an integrated apodization in row-column addressed CMUTs. The apodization was applied by varying the density of CMUT cells in the array with the objective of damping the edge waves originating from the element ends, thereby mitigating the problem of ghost echoes in images produced by such arrays. Two row-column addressed $32 + 32$ CMUT arrays were fabricated, one with and one without integrated apodization. Measurements of the emitted pressure field from the array with integrated apodization showed a reduction in edge wave energy of 8.4 dB (85 %) compared to the array without integrated apodization. Simulations in Field II yielded a corresponding reduction of 13.0 dB (95 %). The simulations were able to replicate the measured pressure field, proving the predictability of the technique.

Acknowledgment

This work was financially supported by the Danish National Advanced Technology Foundation (024-2008-3 and 82-2012-4). The authors would like to thank Jens Christian Jensen for producing the mechanical fixtures and boxes used in the experimental setup, and René Gadkjær for assistance with the electronics.

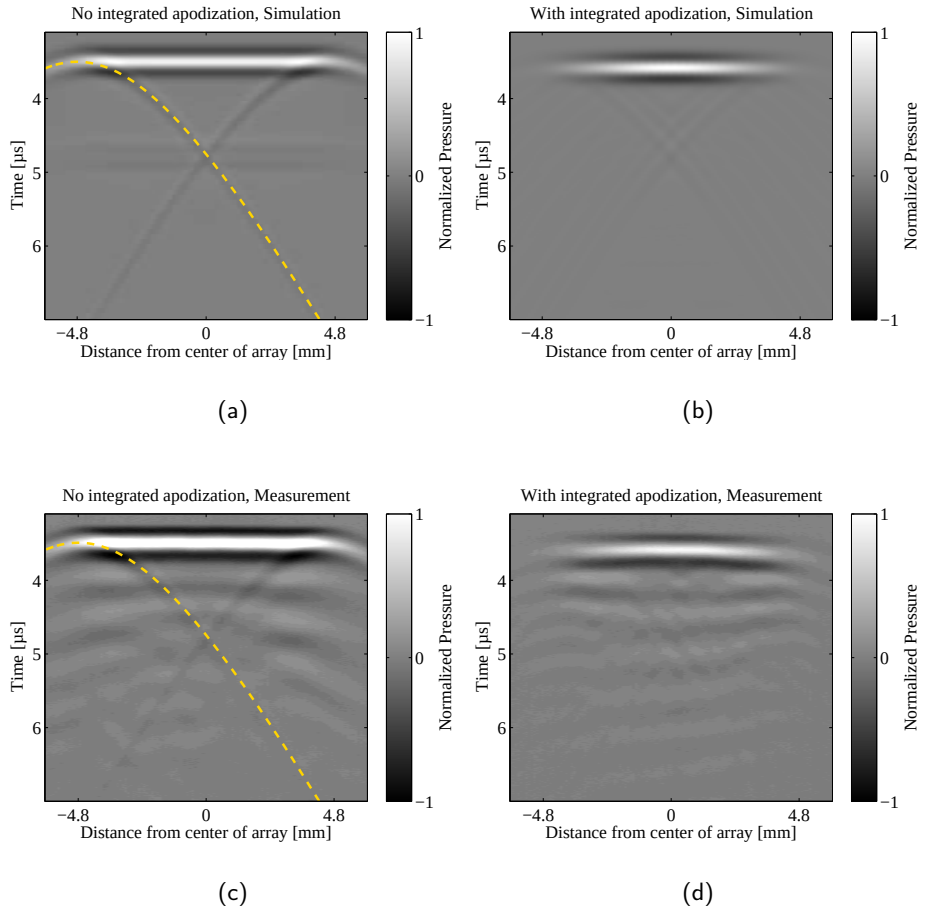

Figure F.4: Simulated (a and b) and measured (c and d) pressure field along a line through the center of the array at a depth of 5.3 mm. a and c show the result for the array without integrated apodization, and b and d show the result with integrated Hann apodization. The pressure has been normalized to the maximum pressure of the measurement with no integrated apodization. The extend of the array aperture (from −4.8 mm to 4.8 mm) is marked. Two edge waves are clearly visible for the non-apodized array, and the dashed line show the analytically calculated expected arrival time of the edge wave originating at −4.8 mm. The ripples in the experimental results are due to transducer ringing, and these are therefore not reproduced in the simulations.

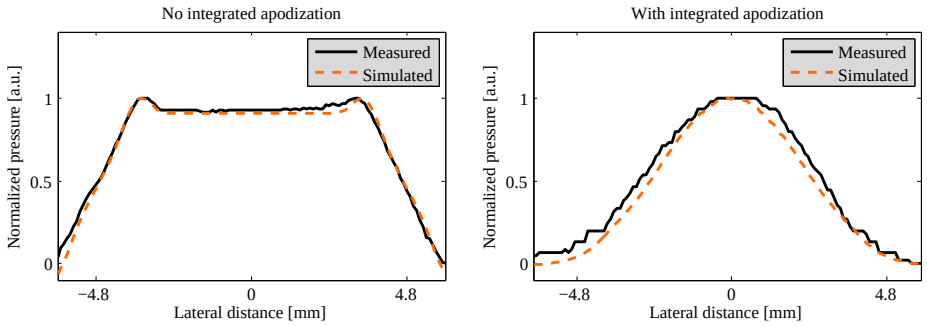

(a) (b)

Figure F.5: Measured and simulated pressure at a distance of 5.3 mm from the transducer surface. The pressure is measured along a line through the center of the array. The extend of the array aperture (from −4.8 mm to 4.8 mm) is marked. The pressure has been normalized to the maximum pressure to allow comparison of the profile of the emitted field over the array.

References

Démoré, C. E. M., A. Joyce, K. Wall, and G. Lockwood (2009). "Real-time volume imaging using a crossed electrode array". In: *IEEE Trans. Ultrason., Ferroelec., Freq. Contr.* 56.6, pp. 1252–1261 (cit. on pp. 135, 136).

Huang, Y., A. S. Ergun, E. Hæggström, M. H. Badi, and B. T. Khuri-Yakub (2003). "Fabricating capacitive micromachined ultrasonic transducers with wafer-bonding technology". In: *J. Microelectromech. Syst* 12.2, pp. 128–137 (cit. on p. 138).

Jensen, J. A. (1996). "Field: A Program for Simulating Ultrasound Systems". In: *Med. Biol. Eng. Comp.* 10th Nordic-Baltic Conference on Biomedical Imaging, Vol. 4, Supplement 1, Part 1, pp. 351–353 (cit. on pp. 136, 139).

Jensen, J. A. and N. B. Svendsen (1992). "Calculation of Pressure Fields from Arbitrarily Shaped, Apodized, and Excited Ultrasound Transducers". In: *IEEE Trans. Ultrason., Ferroelec., Freq. Contr.* 39, pp. 262–267 (cit. on pp. 136, 139).

Kern, W. (1990). "The Evolution of Silicon Wafer Cleaning Technology". In: *J. Electrochem. Soc.* 137.6, pp. 1887–1892 (cit. on p. 139).

Logan, A. S., L. L. P. Wong, A. I. H. Chen, and J. T. W. Yeow (2011). "A 32 x 32 element row-column addressed capacitive micromachined ultrasonic transducer". In: *IEEE Trans. Ultrason., Ferroelec., Freq. Contr.* 58.6, pp. 1266–1271 (cit. on p. 135).

Rasmussen, M. F., T. L. Christiansen, E. V. Thomsen, and J. A. Jensen. "Ultrasound Imaging Transducer Array with Integrated Apodization". PCT/IB2013/002838 (cit. on p. 136).

Rasmussen, M. F. and J. A. Jensen (2013). "3-D Ultrasound Imaging Performance of a Row-Column Addressed 2-D Array Transducer: A Measurement Study". In: *Proc. IEEE Ultrason. Symp.* Pp. 1460–1463 (cit. on p. 136).

Sampaleanu, A., P. Zhang, A. Kshirsagar, W. Moussa, and R. Zemp (2014). "Top-orthogonal-to-bottom-electrode (TOBE) CMUT arrays for 3-D ultrasound imaging." In: *IEEE Trans. Ultrason., Ferroelec., Freq. Contr.* 61.2, pp. 266–276. DOI: 10.1109/TUFFC.2014.6722612 (cit. on p. 135).

Seo, C. H. and J. T. Yen (2009). "A 256 x 256 2-D array transducer with row-column addressing for 3-D rectilinear imaging". In: *IEEE Trans. Ultrason., Ferroelec., Freq. Contr.* 56.4, pp. 837–847 (cit. on p. 135).

Zhang, P., G. Fitzpatrick, T. Harrison, W. A. Moussa, and R. J. Zemp (2012). "Double-SOI Wafer-Bonded CMUTs With Improved Electrical Safety and Minimal Roughness of Dielectric and Electrode Surfaces". In: *J. Microelectromech. Syst.* 21.3, pp. 668–680 (cit. on p. 138).

PAPER G

3-D Imaging with Row-Column Addressed Arrays: Transducer-Integrated Apodization and Line-element Beamforming

Authors: Morten Fischer Rasmussen, Thomas Lehrmann Christiansen, Erik Vilain Thomsen and Jørgen Arendt Jensen.

Submitted to: *IEEE Transaction on Ultrasonics, Ferroelectrics, and Frequency Control*, May 22 2014.

Abstract

The purpose of this paper is to demonstrate the benefits of transducer-integrated apodization in row-column addressed arrays using both simulations and measurements on in-house produced row-column addressed 2-D CMUT arrays. Row-column addressing of 2-D arrays reduces the number of active channels needed to acquire a 3-D volume. A disadvantage of row-column addressing 2-D arrays is an apparent ghost effect in the point spread function due to edge effects. It is demonstrated that using integrated apodization reduces the edge effects. Measurements showed that transducer-integrated apodization reduced the non-main-wave energy by 34 %. In simulations the reduction was 94 %. The performance difference is due to a lack of transducer backing in the measurements. A Hann apodization is shown to be efficient at attenuating the ghost echoes but implies a decrease in SNR at points located off the

Manuscript received May 22, 2014; accepted <month> <day>, <year>. This research was financially supported by grant 024-2008-3 and 82-2012-4 from the Danish Advanced Technology Foundation and from BK Medical ApS (Herlev, Denmark).

M.F. Rasmussen* and J.A. Jensen are with the Center for Fast Ultrasound Imaging, Department of Electrical Engineering, Technical University of Denmark, Kgs. Lyngby, Denmark.

T.L. Christiansen and E.V. Thomsen are with the Department of Micro- and Nanotechnology, Technical University of Denmark, Kgs. Lyngby, Denmark.

*e-mail of corresponding author is: research@mofi.dk

transducer center axis. Instead, a static roll-off apodization region on the sides of the line-elements is proposed to preserve the SNR while attenuating the ghost echo. The peak ghost echo intensity of a scatterer at (**x**,**y**,**z**) = (8,3,30) mm was in simulations decreased by 43 dB by integrating roll-off apodization into the array. Simulations of a 3 mm diameter anechoic blood vessel at 30 mm depth showed that applying the transducer-integrated apodization increased the apparent diameter of the vessel from 2.0 mm to 2.4 mm. This was achieved without affecting the main echo response, altering the number of channels or changing the front-end electronics requirements. A beamformer specific for row-column addressed arrays was presented and made available on-line.

G.1 Introduction

For real-time 3-D ultrasonic imaging, 2-D array transducers are needed to achieve real-time scanning of a volume (Ramm et al. 1991; Turnbull and Foster 1991). The number of elements in a fully addressed $N \times N$ 2-D array scales with N^2. In 2-D imaging, a 1-D array using more than 100 elements is commonly used. Using a fully addressed 2-D array, this would correspond to an array with more than 10 000 elements. To control the individual elements in the array, a connection has to be made to each element. Hereby, any delay or apodization scheme can be applied, offering maximum control and flexibility in the image processing (Karaman, Li, et al. 1995; Thomenius 1996; Turnbull and Foster 1991). However, addressing each element individually results in a vast amount of interconnections and offers a great challenge in acquiring and processing the large amount of data. Reducing the number of transducer elements by using sparse arrays has therefore seen a great amount of interest in the last couple of decades (Austeng and Holm 2002; Brunke and Lockwood 1997; Davidsen et al. 1994; Karaman, Wygant, et al. 2009; Yen et al. 2000). One of the drawbacks of sparse arrays, however, is the lower emitted energy from the reduced number of elements leading to a lower SNR in the recorded ultrasound image. The sparse arrays also have higher side-lobes and can introduce grating lobes in the field.

2-D row-column addressed arrays have recently attracted some attention (Awad and Yen 2009; Chen et al. 2011; Daher and Yen 2004, 2006; Démoré et al. 2009; Logan, Wong, Chen, et al. 2011; Logan, Wong, and Yeow 2009; Morton and Lockwood 2003; Rasmussen and Jensen 2013a,b; Sampaleanu et al. 2014; Seo and Yen 2006, 2007, 2008, 2009; Yen 2013). In a row-column addressed array, the elements are accessed by their row or column index. Each row and column in the array thereby acts as one large element. This effectively transforms the dense 2-D array into two orthogonal 1-D arrays, which is illustrated in Fig. G.1. This effectively reduces the number of elements in an $N \times N$ 2-D array from N^2 to $2N$. The long elements are in this work referred to as row- and column elements, or simply as line-elements.

Considering a fully populated array with $N \times N$ elements, a row-column addressed array of the same size would contain $N + N$ line elements. The size of one line-element

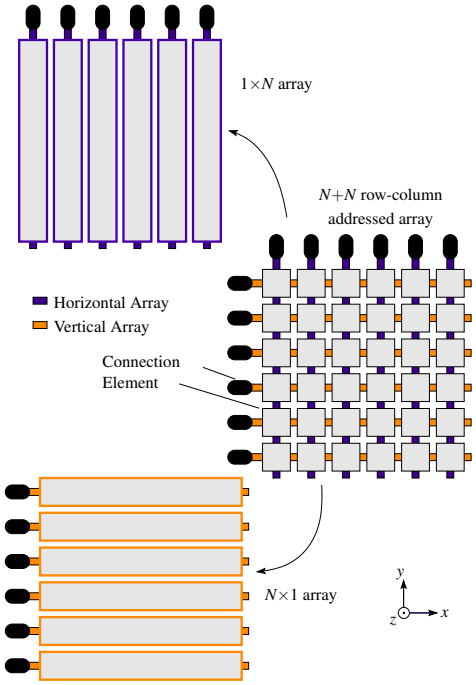

Figure G.1: A row-column addressed 2-D transducer array can be interpreted as two orthogonal 1-D arrays. To the right is shown a 2-D transducer array, where each transducer element is addressed by its row or column index, effectively creating the two arrays shown to the left.

is then $1 \times N$, in units of the fully populated array elements. The vibrating surface area, when exciting a single row-column addressed transducer array channel, is therefore N times as large as the excited area of the fully populated area. A row-column addressed array therefore emits far more energy than a fully populated array per transducer channel. In (Rasmussen and Jensen 2013b), the resolution and contrast of row-column addressed arrays is shown to be better than for fully addressed arrays, when they use the same number of active channels. That the row-column addressed array both has a large surface area, and promises to achieve a high resolution per active channel, makes it a very interesting candidate for real-time 3-D imaging. While the row-column addressing scheme greatly reduces the number of elements and beamformer channels needed to perform real-time 3-D imaging, it has one major disadvantage compared to the fully addressed 2-D arrays: the long row- and column-elements have considerably increased edge effects. As was shown in (Rasmussen and Jensen 2013b), the edge effect limits the image quality obtainable with 2-D row-column addressed arrays. This paper demonstrates how these edge effects can be effectively reduced, making row-column addressed arrays capable of providing a high

Table G.1: Simulation parameters.

Parameter name	Notation	Value	Unit
Center frequency	f_0	5.0	MHz
Speed of sound	c	1480	m/s
Wave length	λ	296	µm
Array pitch -x	d_x	$\lambda/2 = 148$	µm
Array pitch -y	d_y	$\lambda/2 = 148$	µm
Sampling frequency	f_s	120	MHz
Emission pulse	–	2-cycles, Hann-weighted	–

image quality for real-time 3-D imaging with a low channel count.

The paper is divided into three main sections. The first section describes the edge effects of long, thin line-elements, and demonstrates the importance of apodizing the line-elements along their length to reduce the edge effects. Subsequently, a transducer integrated apodization is designed. It is shown that the previously proposed apodization in the literature (Démoré et al. 2009; Rasmussen and Jensen 2013b) is not generally applicable for 3-D imaging. Instead, a new apodization scheme is proposed and simulated. The feasibility of a transducer-integrated apodization is demonstrated on two in-house produced capacitive micromachined ultrasonic transducer (CMUT) arrays. Hydrophone measurements of the pressure field generated by the CMUTs verifies the transducer-integrated apodization to function as expected. Then, it is demonstrated how beamforming can be carried out when both the transmit line-elements, the receive line-elements, and the focal zone are line-segments instead of points. Finally, the effectiveness of the proposed apodization is demonstrated via simulated point spread functions (PSF) and a simulated anechoic blood vessel surrounded by tissue.

G.2 Edge effects

Row column addressed arrays are quite different acoustically from fully addressed arrays. Due to the row-column addressing, each line-element may have a length that is hundreds of times longer than the lengths of the square elements used in a fully addressed array. The long length of the line-elements results in prominent edge effects. This section investigates how the line-elements of a row-column addressed array behave and what can be done to decrease the edge effects. The behavior of the line-elements is first investigated by analyzing their spatial impulse response.

In the following, the importance of apodizing the line-elements along their length is demonstrated. For this purpose, an approximation to spatial impulse response is derived. The purpose of the derivation is thereby not to introduce a new equation suitable for calculating the impulse response, but to motivate how the edge effects can be minimized.

The origin of the edge waves can be analyzed by the linear theory of wave propagation. The pressure at a given point $\mathbf{p}$ at the time t has in the literature (Pierce 1989) been shown to be

$$p(\mathbf{p},t) = \rho_0 \frac{\partial}{\partial t} v(t) * h(\mathbf{p},t) \tag{G.1a}$$

$$= \rho_0 \, v(t) * \frac{\partial}{\partial t} h(\mathbf{p},t) \ , \tag{G.1b}$$

where $*$ denotes convolution, ρ_0 is the density of the medium, v is the velocity normal to the transducer surface, and h is the spatial impulse response. It is noted that v is the convolution of the aperture excitation signal and the electro-mechanical impulse response of the aperture. The spatial impulse response $h(\mathbf{p},t)$ is the observed sound field at the point $\mathbf{p}$ when the aperture is excited by a Dirac delta function. The Huygen-Fresnel principle states that the field originating from a sound radiating surface can be calculated by considering all points on the surface as the source of an outgoing spherical wave. The field at any point in space is then constructed by superposition of these spherical waves. The acoustic reciprocity theorem states that if the sound source and the sound receiver are interchanged, the received signal remains unchanged. In other words, the spatial impulse response can be determined by letting the point $\mathbf{p}$ be the source of a spherical wavefront and then integrate the wave's intersection with the aperture. This integral is termed the Rayleigh integral (Harris 1981a; Stepanishen 1971).

The intersection of the spherical wave and the plane of the aperture makes a circle arc. The spatial impulse response at a certain time t is thereby determined by the length of the arc that intersects the aperture. The radius of the expanding sphere is $R = ct$, where t is time and c is the speed of sound. Determining the arc intersection is reduced to a two-dimensional problem by projecting the point $\mathbf{p}$ on to the transducer plane. Without loss of generality, the aperture is assumed flat. In the following, a normal right-handed coordinate system consisting of l, m, and n coordinates is used. The aperture plane is spanned by the l- and m-axes and the n-axis is orthogonal to the aperture plane. If the coordinate of $\mathbf{p}$ is (p_l, p_m, p_n), then the projection of $\mathbf{p}$ onto the $l\,m$-plane is (p_l, p_m, 0). The radius of the circle created by the intersection between the aperture and the expanding spherical wave is $r(t) = \sqrt{(ct)^2 - p_n^2}$ and the center of the circle is located at (p_l, p_m). The line integral along this expanding arc is the Rayleigh integral in polar coordinates. This is the case shown in the aperture at the top of Fig. G.2. The integration is performed along the gray dashed lines. Several authors (Harris 1981b; Stepanishen 1981; J. N. Tjøtta and S. Tjøtta 1982) have determined the solution to the Rayleigh integral in polar coordinates of an apodized aperture to be:

$$h(\mathbf{p},t) = \begin{cases} \dfrac{c}{2\pi} \displaystyle\int_{\theta_1(t)}^{\theta_2(t)} a(r(t),\theta)\,\mathrm{d}\theta \ , & \text{if } t \geq \dfrac{p_n}{c} \\ 0 \ , & \text{else} \ , \end{cases} \tag{G.2}$$

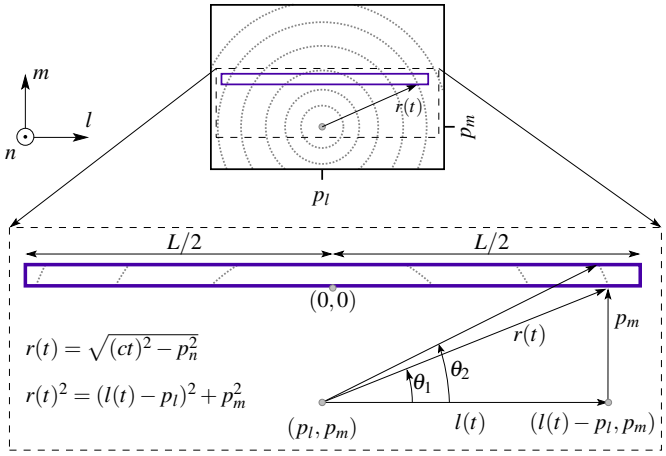

Figure G.2: Spatial impulse response of long thin line-elements. At the top a large aperture is shown with the integration paths used in (G.2) to determine its spatial impulse response. Within the large aperture a thin line-element is illustrated. At the bottom a zoom on the line-element is shown. The expression in (G.5) approximates the integration paths with vertical lines. The thinner the line-element is, the better the approximation.

where a is the apodization function of the aperture in polar coordinates with origin at the projection of $\mathbf{p}$ onto the aperture plane. a is equal to 0 when evaluated outside of the aperture surface. If the apodization function is constant along the integration paths, (G.2) becomes

$$h(\mathbf{p},t) = \begin{cases} \frac{c}{2\pi}(\theta_2(t) - \theta_1(t))\, a_r(r(t)) \,, & \text{if } t \geq \frac{p_n}{c} \\ 0 \,, & \text{else .} \end{cases} \tag{G.3}$$

In the following, the aperture is assumed to be a long, thin, and rectangular line-element. The l, m -coordinates are chosen such that the l-axis is oriented along the length of the line-element and the origin is placed at the center of the line-element length. This is illustrated in Fig. G.2.

At the top of Fig. G.2, a large aperture is shown where the full integral along the dashed lines must be carried out to find the spatial impulse response. Within the large aperture, a line-element is shown. A zoom on the line-element is shown at the bottom of the figure. By approximating the integration paths on the line-element by a vertical line, the apodization function $a_r(r)$ from (G.3) changes dependent variable from the radius r to the position l, representing the position along the line-element: $a_l(l(t))$. The thinner the line-element is, the better is the approximation. From the triangle at the bottom right in

Fig. G.2, the l-variable as a function of time is determined to:

$$l(t) = p_l \pm \sqrt{r(t)^2 - p_m^2} \tag{G.4a}$$

$$= p_l \pm \sqrt{(ct)^2 - p_n^2 - p_m^2}\,. \tag{G.4b}$$

The spatial impulse response then approximately becomes:

$$h(\mathbf{p},t) \approx \begin{cases} \dfrac{c}{2\pi}(\theta_2(t) - \theta_1(t))\, a_l(l(t))\,, & \text{if } t \geq t_1 \\ 0\,, & \text{else}\,, \end{cases} \tag{G.5}$$

where $t_1 = \sqrt{p_m^2 + p_n^2}/c$ is the earliest time at which the spherical wave arrives at the aperture. For a long thin line-element, the angular element width $(\theta_2(t) - \theta_1(t))$ changes much slower than the apodization function at the edges of the line-element:

$$\frac{\frac{\mathrm{d}}{\mathrm{d}t}(\theta_2(t) - \theta_1(t))}{2\pi} \ll \frac{\mathrm{d}}{\mathrm{d}t} a_l(l(t))\,. \tag{G.6}$$

By inserting (G.5) into (G.1b), and using (G.6), the pressure field is seen to be proportional to

$$p(\mathbf{p},t) \propto \begin{cases} v(t) * \frac{\mathrm{d}}{\mathrm{d}t} a_l(l(t))\,, & \text{if } t \geq t_1 \\ 0\,, & \text{else}\,. \end{cases} \tag{G.7}$$

If the line-element emits a short pulse, then no pressure difference is measured at the point $\mathbf{p}$ until the wave reaches $\mathbf{p}$ at $t = t_1$. In the following it is shown that 7 cases of the derivative of $a_l(l(t))$ exists as the emitted wave passes the point $\mathbf{p}$. Using again the acoustic reciprocity, $\mathbf{p}$ emits a spherical wavefront that is received by the line-element. The wavefront reaches the line-element at $t = t_1$. At $t = t_2$ the wavefront first reaches the closest edge, and at $t = t_3$ the wavefront reaches the furthest edge of the line-element. The apodization of a single line-element is usually constant or only slowly varying over the entire element surface. Since the apodization function evaluates to zero outside of the element area, there is a discontinuity at the element edge. The derivative of the aperture function is therefore approximately zero everywhere except at the discontinuities, where it is the Dirac delta function, δ:

$$\frac{\mathrm{d}}{\mathrm{d}t} a_l(l(t)) \approx \delta(t - t_1) - \delta(t - t_2) - \delta(t - t_3) \tag{G.8}$$

By inserting (G.8) into (G.7), it is seen that the spatial transmit impulse response contains three individual responses. As a result, a single transmit pulse develops three wavefronts that passes the point $\mathbf{p}$. When a scatterer is located at $\mathbf{p}$, there are therefore three reflected waves returning to the line-element. Using the same argumentation, the

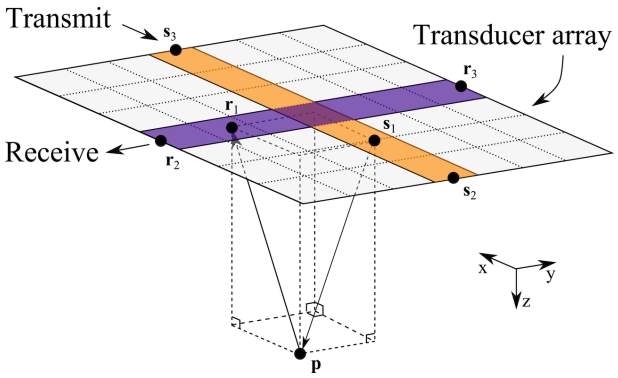

Figure G.3: Illustration of a pulse-echo simulation setup with one line-element transmitting and one line-element receiving. A scatterer is located at the point $\mathbf{p}$, $\mathbf{s}_1$ is the closest point on the transmit element to $\mathbf{p}$, and $\mathbf{r}_1$ is the closest point on the receive element to $\mathbf{p}$. $\mathbf{s}_2$, $\mathbf{s}_3$ and $\mathbf{r}_2$, $\mathbf{r}_3$ are the edges of the transmit and receive line-elements, respectively.

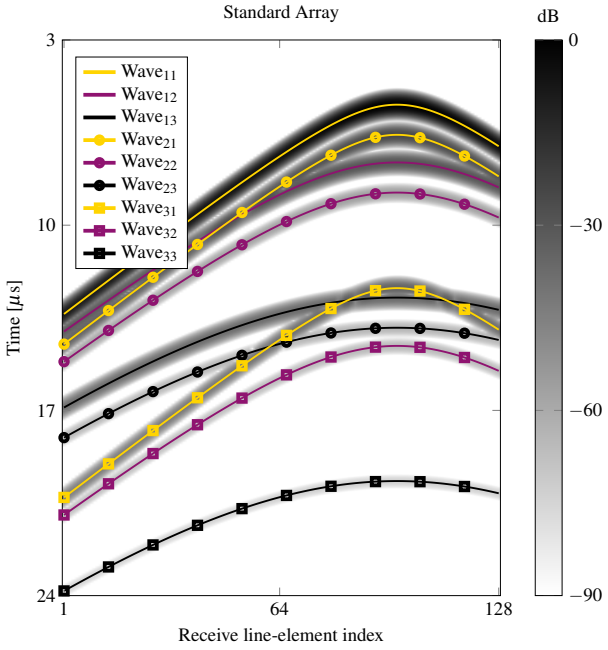

Figure G.4: Nine echoes are received from a single line-element emission reflected by a scatter located at $(x,y,z) = (5,4,3)$ mm. The gray-scale image is the envelope of the received signals and the overlaid lines are predicted time-of-flights.

spatial receive impulse response contains also three responses, meaning each wavefront is measured three times. The pulse-echo spatial impulse response is the convolution of the transmit and receive impulse responses and therefore contains up to nine responses (Jensen 1991). In Fig. G.3, a row-column addressed array is seen with a scatterer at the point $\mathbf{p}$ in front of it. When observing the pressure at point $\mathbf{p}$, the three wavefronts appears to originate from $\mathbf{s}_1$, $\mathbf{s}_2$ and $\mathbf{s}_3$. The receive line-element behaves as if it measures at the three discrete points $\mathbf{r}_1$, $\mathbf{r}_2$ and $\mathbf{r}_3$.

That nine echoes are measured from a single scatterer can be tested by a single line-element pulse-echo simulation. Fig. G.4 shows the signals received by a 128+128 element row-column addressed array from a single scatter located at the point $\mathbf{p} = (5,4,3)$ mm, when exciting the center line-element with a two-cycle sinusoidal 5 MHz pulse. As expected, nine echoes are received. Overlaid on the gray level receive echoes are the expected echo arrival time combinations of the three sources and the three receive points of Fig. G.3. The echo arrival time, also termed the time-of-flight (ToF), is calculated as

$$\mathrm{ToF}(\mathbf{p},n,i) = \frac{\|\mathbf{p}-\mathbf{s}_n\| + \|\mathbf{r}_i - \mathbf{p}\|}{c}\,, \tag{G.9}$$

where both n and i are indices between 1 and 3. The wavefronts are named wave_{ni}, where n indicates the $\mathbf{s}$-index and i indicates the $\mathbf{r}$-index. It is seen that the arrival time at each receive line-element of all received echoes are perfectly predicted, and the location assumption of the transmitter and receiver of each wavefront, shown in Fig. G.3, must therefore be correct.

It is only the first echo, wave_{11} that can be used for imaging, as the amplitudes of the other ghost echoes are too weak. Even though the ghost echoes cannot be used for imaging, they still degrade the image quality. It is seen from (G.7) that to reduce the edge waves, and thereby the ghost echoes, the derivative of the apodization function must be kept as small as possible. The apodization function therefore has to converge to zero when approaching the line-element edges. This cannot be achieved by the usual electronic apodization, since this does not change the line-element apodization value along the length of it. Instead, the apodization must be integrated into the transducer array itself, which is the subject of the Section G.4.

G.3 Simulation and Measurement Setup

In this work, Field II (Jensen 1996; Jensen and Svendsen 1992) is used for all simulations. The simulated receive signals are beamformed using a MATLAB (MathWorks Inc., Massachusetts, USA) implemented beamformer for row-column addressed arrays, made by the authors for this article and made available on-line (Rasmussen 2014). The transducer arrays used in the simulations are row-column addressed 128+128 element 2-D arrays using the parameters shown in Table G.1. Field II is set up to use lines to describe the apertures and each line-element is divided into square mathematical sub-elements with a side length of $\lambda/4$.

Measurements are made with two in-house produced 32+32 element row-column addressed CMUT arrays. The acoustic field of the two CMUT arrays were measured with a MH28-5 needle hydrophone (Force Technology, Denmark) and a DSO5012A oscilloscope (Agilent Technologies, CA, USA). For spatial mapping of the transmit fields, the hydrophone was mounted on the positioner of the intensity measurement system AIMS-3 (Onda Corporation, CA, USA). The transducers were actuated using a 8116A pulse/function generator (Hewlett-Packard Company, CA, USA) through a custom made class B amplifier with a bandwidth of 8 MHz. All measurements were carried out in rapeseed oil to ensure electrical insulation of the prototype transducers.

G.4 Transducer-Integrated Apodization

Apodizing both the row and column line-elements with a Hann function in the entire length of the line-elements is very effective at suppressing the ghost echoes (Démoré et al. 2009; Rasmussen and Jensen 2013b). A Hann apodized row-column addressed array is shown in Fig. G.5, where the top graph shows the apodization of a single line-element. Since the row and column line-elements are overlapping, so are their apodization functions. At each position on the transducer surface, two apodization functions are overlapping, one from a row element and one from a column element. The effective apodization is the multiplication of the two apodization functions. The vertical line-elements close to the edges are multiplied by values close to zero by the horizontal apodization function. Similarly, the horizontal line-elements at the edges are multiplied by values close to zero by the vertical apodization function. The sensitivity of the edge line-elements are therefore highly limited. The only location where this apodization function allows the row-column addressed array to perform well, is straight down at the center of the array. Even if the array angles the transmit beam to the sides, like a phased array transducer, the echoes returning to the transducer surface will be significantly attenuated.

An alternative to the overlapping apodizations is to not apodize the central part of the transducer surface, but instead adding a roll-off region on both sides of all line-elements as shown in Fig. G.6. This roll-off region is used for the apodization function to converge smoothly to zero. This way, the central region of the aperture surface has a uniform apodization value of 1, and there is no overlapping of the apodization functions where $a_l(l) < 1$. At the same time, the discontinuities at the edges have been removed. If the added roll-off region is short, then the derivative of the aperture function will be high, and if the roll-off region is wide, the derivative will be low. From (G.7), it then follows that a wider roll-off region is better at suppressing the edge waves. Each line-element thereby becomes longer, but there are the same number of row- and column-elements in the array. This apodization thereby does not affect the electronics, interconnections, or the data processing.

In Fig. G.7, the simulated maximum received main echo as a function of scatterer position is shown. This expresses the array sensitivity as a function of position. The

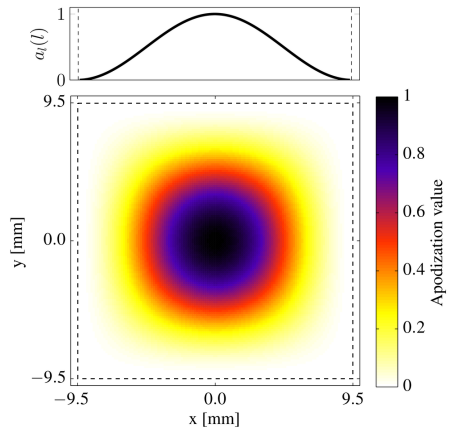

Figure G.5: The row-column addressed array with a transducer-integrated Hann apodization. The graph at the top shows the Hann apodization of a single line-element as a function of the position along the line-element, l. The bottom figure shows the Hann apodization of the full transducer array. The dashed lines mark the edge of the line-elements and the row-column addressed array. The size of the area within the dashed lines is identical to that of the area within the dashed lines in Fig. G.6.

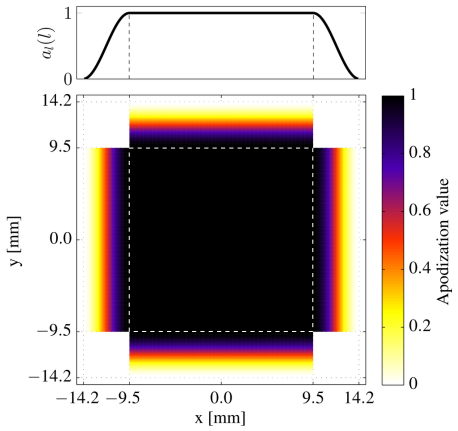

Figure G.6: New integrated-apodization layout where a roll-off region is added to the ends of the line-elements. The central region, marked with dashed lines, has an apodization value of one. The size of the area within the dashed lines is identical to that of the area within the dashed lines in Fig. G.5.

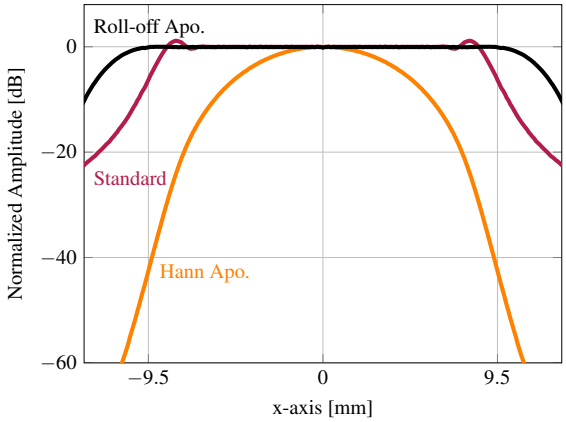

Figure G.7: Maximum received echo intensity from a single scatter at a depth of 10 mm and with its x-coordinate varying from −13 mm to 13 mm. The center line-element is sending and all 128 receive elements are receiving. The maximum of all envelope-detected signals is plotted for each scatterer location. The three curves were simulated with three different apertures. The received signal acquired with an integrated Hann apodized array is seen to decrease fast already from the center of the array. The signal received with the standard array without any apodization decreases just before the edge of the array, and the roll-off apodized array maintains the same signal strength until the edge of the array.

scatterer is placed directly in front of the transmitting line-element at a depth of 10 mm. The center line-element of the array emits a two-cycle pulse and the RF-data is measured on all receive line-elements. The received signal is envelope detected and the maximum value is plotted against the scatterer position. The Hann apodized array is seen to loose sensitivity very fast. At the edge of the array, the returned main echo is 40 dB weaker than in the center of the array. On the standard array without the integrated apodization, the Fresnel-diffraction of a sharp edge is evident close to the aperture edges at ± 9.5 mm (Naik 2010, p.145). The edge apodized array has a constant sensitivity over the entire central aperture, spanning from −9.5 mm to 9.5 mm in both dimensions. Adding roll-off regions to row-column addressed arrays is therefore proposed as the standard solution.

In Fig. G.8, the simulated maximum received ghost echo as a function of roll-off region width is shown. The scatterers are located at depths from 10 mm to 80 mm at the center of the aperture, where the ghost echoes reaches their maximum amplitude. As expected, the wider the roll-off region, the more the ghost echoes are suppressed. The deeper the scatter is located, the narrower is the effective width of the edge aperture, and its ghost suppressing effect therefore decreases with depth. There is, however, an upper limit on the edge apodization width. A very large footprint results in difficulties getting a good acoustical contact between the aperture and the human body. For the rest of this

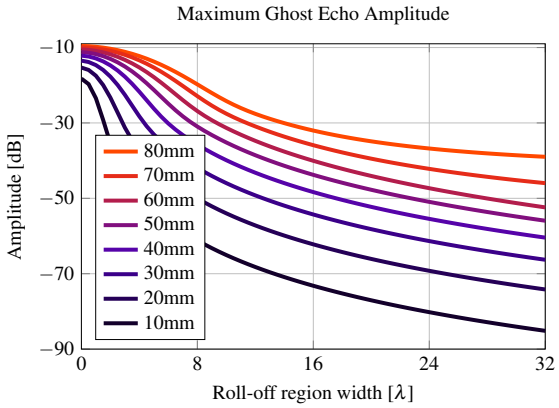

Figure G.8: Maximum ghost-echo intensity of a single scatterer as a function of edge apodization width. The wider the edge, the more the ghost echoes are suppressed. Each curve in the figure corresponds to a given scatterer depth, shown in the legend.

paper, an edge width of 16 λ is chosen as a compromise. 16 λ is 1/4 of the original side length of 64 λ, yielding a total aperture side length 28.4 mm. As seen in Fig. G.8, this will for a scatterer located at a depth of 10 mm attenuate the ghost echo from −18 dB to −73 dB and for a scatterer at 80 mm depth from −10 dB to −32 dB. This corresponds to a damping of 55 dB and 22 dB, respectively. Importantly, this is without altering the electronics, interconnections, or data processing.

G.4.1 Implementation of Transducer-Integrated Apodization

As demonstrated in the previous section, apodization along the length of the row- and column elements is needed to suppress edge waves. This apodization must be integrated in the transducer itself as only one beamformer channel is available per element. There exist several options for achieving this (Rasmussen, Christiansen, et al. n.d.). One is to apply an attenuating material with varying thickness or damping coefficient on top of the transducer as suggested by Demoré et al (Démoré et al. 2009). An alternative approach is to vary the active area of the element along its length. For a piezo-transducer, this would essentially correspond to reducing the width of the element towards the element ends according to the desired apodization profile. As the resonance frequency of piezo-elements are given by their height, this can be done without altering the resonance frequency. For the very simplest of apodization profiles, e.g. linear, the elements can be diced into shape, but for more advanced profiles, the elements must be made using either laser cutting or through the use of screen-printing, which allows for maximum flexibility in designing the element shape (Lou-Møller et al. 2007).

The area apodization technique can also be applied to CMUTs, where a single element

Table G.2: Transducer parameters common for both CMUT arrays.

Parameter	Value	Unit
Array		
Number of elements	32+32	–
Element pitch	300	µm
Element kerf	12	µm
Element length	9.6	mm
Center frequency in immersion	3	MHz
CMUT cell		
Cell diameter	72	µm
Min. distance between cells	20	µm
Top plate thickness	2	µm
Al thickness	200	nm
Insulation oxide thickness	200	nm
Vacuum gap height	200	nm
Pull-in voltage	52	V

consists of a large number of small capacitor cells, each having a freely suspended plate as a top electrode, which can generate and receive the ultrasound (Ladabaum et al. 1998; Savoia et al. 2012). In this case, the size of the individual cells defines the resonance frequency, and the active area is therefore varied by changing the number of cells along the length of the element. Introducing such a variation in the number of cells has no influence on the fabrication process, as it is only a matter of changing the layout of the lithographic masks. This results in discrete apodization levels, the number of which depends on the number of cells that can be accommodated in the elements.

G.4.2 Verification of Transducer-Integrated Apodization

To demonstrate the feasibility of an integrated apodization, two 32+32 row-column addressed CMUT arrays have been fabricated using a wafer bonding technique based on previous works in the literature (Huang et al. 2003; Kupnik et al. 2010; Zhang et al. 2012). The transducer parameters common to both arrays are given in Table G.2.

Both transducers consist of 32 bottom electrodes and 32 top electrodes oriented perpendicular to each other, both made from highly doped silicon. Each CMUT cell is circular and has a lithographically defined diameter of 72 µm. The cells are etched out using reactive ion etching (RIE) in a 200 nm thermal oxide grown on a silicon-on-insulator (SOI) wafer. The bottom electrodes are subsequently defined in the 20 µm thick device layer of the SOI wafer using deep RIE. A second SOI wafer with a 200 nm thermal oxide layer is bonded to the first SOI wafer at an ambient pressure of 1 µbar. After removal of the SOI handle and buried oxide layer, only the 2 µm thick device layer of the second

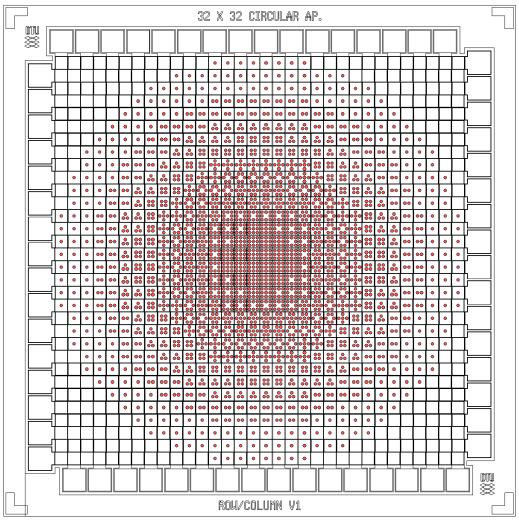

Figure G.9: Mask layout of the $32+32$ prototype CMUT array with integrated apodization. The red circles are the individual capacitor cells, the number of which varies according to a circularly symmetric Hann function.

SOI wafer is left bonded to the first SOI wafer, and defines the suspended top plate of the CMUT cells. A layer of aluminium is subsequently deposited on the top plate using electron beam evaporation, and the top electrodes are etched out using H_2O:H_3PO_4 (1:2) at 50 °C and deep RIE.

The first of the two arrays contains a total of 9216 circular CMUT cells, 3 along the width and 96 along the length of each element. The second array is apodized by varying the number of cells according to a circularly symmetric Hann function with nine discrete levels as seen in Fig. G.9. This apodization is chosen for practical reasons, as it provides the most aggressive apodization for the relatively small prototype arrays, which are kept below 9.6 mm by 9.6 mm to ensure an adequate number of arrays per wafer in the fabrication. All row elements, and all column elements, are electrically shorted on each array to ensure that the entire array can be actuated simultaneously using a single channel, one cycle sinusoidal burst at 3 MHz 15 Vpp AC on top of a 40 V DC bias voltage. Thus, no electronically controlled apodization is applied.

For each array, the transmitted field was measured using the setup seen in Fig. G.10. The speed of sound in the oil was found by measuring a single pulse at different distances between 2 mm and 10 mm from the array and subsequently finding the corresponding time shift of the maximum pressure. A linear regression of this data yielded a speed of sound of 1476 m/s. In the measurements of the transmitted field, the hydrophone was scanned over the center of each array at a depth of 5.3 mm in steps of 0.1 mm, resulting in the

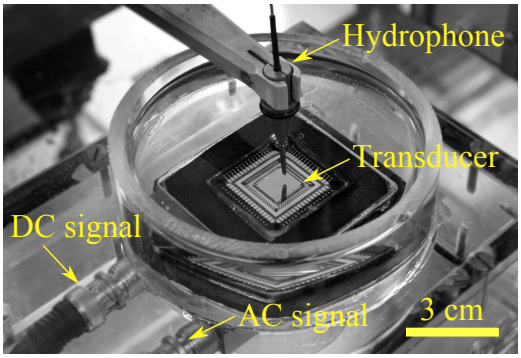

Figure G.10: The measurement setup. The 32+32 element row-column addressed array is submerged in rapeseed oil for electrical insulation and a needle hydrophone from Force Technology is used to measure the pressure. The hydrophone is mounted on the positioner of the *xyz*-intensity measurement system AIMS-3 made by Onda Corporation.

measured sound fields seen in Figs. G.11(a) and G.11(b). The corresponding simulated sound fields are given in Figs. G.11(c) and G.11(d). Note the close correspondence between the simulated and the measured data, showing a pair of distinct edge waves after the main pulse for the non-apodized array. Some ringing from the transducer is seen in the measured data due to the lack of a backing layer in this simple setup. For the apodized array, the edge waves are seen to be significantly attenuated in both simulation and measurement.

The effect of the apodization can be evaluated by integrating the total energy after the main pulse of the apodized array and comparing to the total energy of the non-apodized array. In practice, the –40 dB pulse length was used to define the end of the main pulse, and a measure of the total energy was found by integrating the squared voltage signal in the emitted field after this time instance. Using this approach, the reduction in edge wave energy was measured to be 94 % for the simulation and 34 % for the measurement. The lower relative damping in the measurement compared to the simulation is mainly due to the significant energy contribution from the transducer ringing.

G.5 Beamforming with Line Sources

With a 1-D transducer array, focusing of the ultrasound wavefronts can be accomplished in the lateral direction. In 2-D ultrasound imaging, the 1-D transmit and receive arrays are both used for focusing in the lateral direction. When focusing the ultrasound wavefronts using a row-column addressed array, the transmit and receive arrays are orthogonal. This enables focusing of a 3-D volume, but the azimuth and elevation directions are only

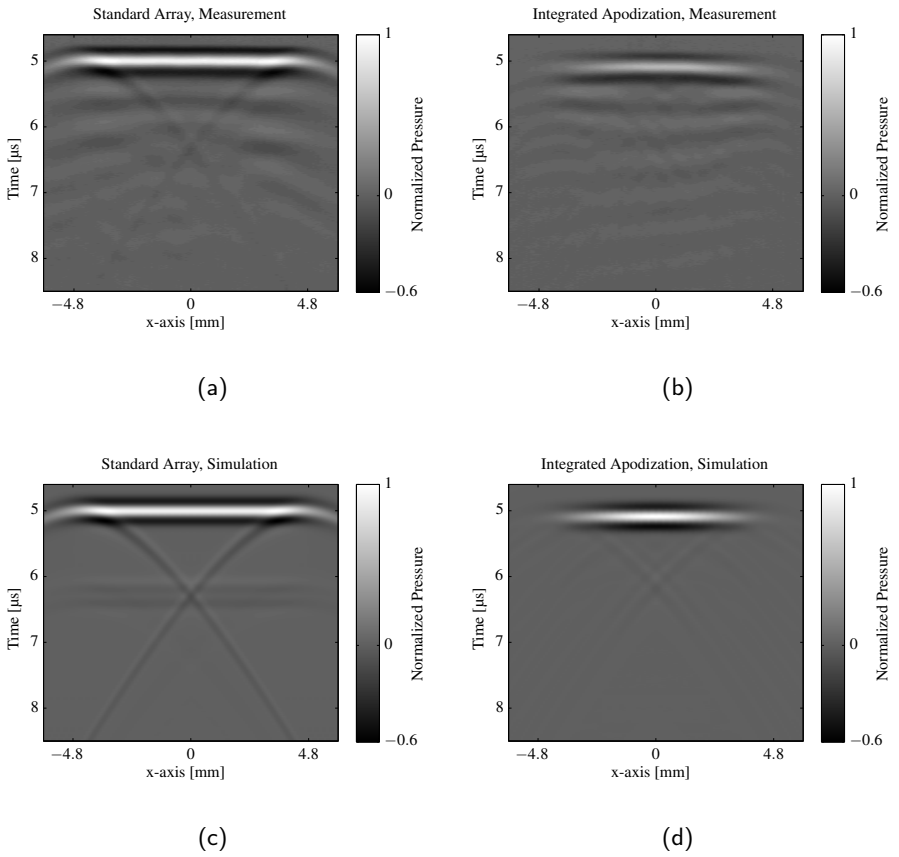

Figure G.11: The measured and simulated sound field pressures at a distance of approximately 5 mm. The left column, (a) and (c), are pressure fields from standard CMUT row-column addressed arrays and the right column, (b) and (d), are pressure fields from arrays with integrated apodization.

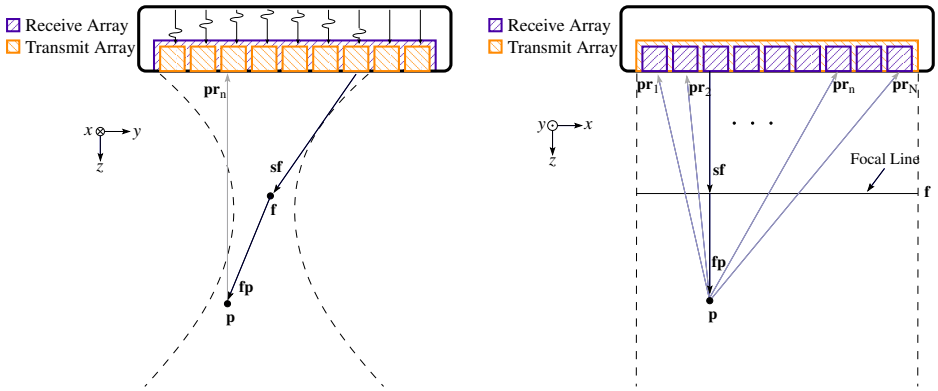

(a) ToF in y–dimension. (b) ToF in x–dimension.

Figure G.12: Time of flight (ToF) illustration of a focused emission. The vector **sf** connects the first source line-element that is excited with the focal line **f**. **fp** is the vector from the nearest point on the focal line to the point being beamformed (**p**), and $\mathbf{pr}_i$ is the vector from **p** to the nearest point on the receive line-element $\mathbf{r}_i$. In (a) the setup is sliced orthogonal to the transmitting line-elements and parallel with the receiving line elements. In (b) the setup is sliced parallel with the transmitting line-elements and orthogonal to the receiving line elements. In (a) the focal zone **f** looks like a focal point, but in (b) it is seen to be a focal line.

focused once (Démoré et al. 2009; Morton and Lockwood 2003; Rasmussen and Jensen 2013b; Seo and Yen 2009; Yen 2013).

Delay-and-sum beamformers usually assumes the geometry the sound sources and receivers to be points. The emitted wavefront of a line-element has the shape of a cylinder surface: it is a plane wave in the plane aligned along the line-element and a circle arc in the plane orthogonal to the line-element. Assuming the geometry of the line-elements to be points is therefore a poor approximation. A better approximation assumes the line-elements to be line segments. When an array of line-elements is focused, the geometry of the focal zone is also a line segment. Calculating the distances between the line-elements and a given point should therefore be calculated as the distance between a line segment and a point.

The vectors **fp** and $\mathbf{pr}_n$, seen in Fig. G.12, connects the point **p** to the closest point on respectively the focal line **f** and the receiving element $\mathbf{r}_n$. **sf** is the vector from the source line-element **s** to the focal line **f**. Since the source elements and the focal line are parallel, determining the distance between them can be solved in the z-y plane.

The time of flight of a wavefront is given by the shortest distance from the source **s**

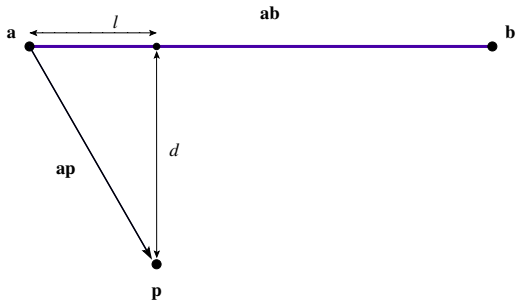

Figure G.13: Projection of the point **p** onto the line segment **ab**. l is the distance from **a** to the projected point and d is the shortest distance from **p** to **ab**.

through the focal line **f** to the point being focused **p** and back to the receiving element $\mathbf{r}_n$, divided by the speed of sound. Using the notation from Fig. G.12, this can be written as:

$$\mathrm{ToF}_m(\mathbf{p},n) = \frac{\|\mathbf{sf}\| \pm \|\mathbf{fp}\| + \left\|\mathbf{pr}_n\right\|}{c} , \tag{G.10}$$

where c is the speed of sound in the medium, n is an index from 1 to the number of receive line-elements N and m is the emission index. Only one value of ToF_m is calculated per emission. If the point being focused is closer to the transducer array than the focal line, then the case of $-\|\mathbf{fp}\|$ is used, otherwise $+\|\mathbf{fp}\|$ is used.

To determine $\|\mathbf{fp}\|$ and $\left\|\mathbf{pr}_n\right\|$, the distance between a point and line must be calculated. The line segment from point **a** to point **b** is termed **ab**. This is illustrated in Fig. G.13. The projection of the point **p** onto the line **ab** is termed l and is determined by the usual equation for projection. l is positive if the projected point is located on the same side of **a** as **b**, and negative if it is located on the other side. By normalizing l with the length of the line segment, $\hat{l}$ takes the values $[0,1]$ when the projected point is located between **a** and **b**:

$$\hat{l} = \frac{l}{\|\mathbf{ab}\|} = \frac{\mathbf{ap}\cdot\mathbf{ab}}{\|\mathbf{ab}\|^2} . \tag{G.11}$$

When the projection of **p** onto the line lies between **a** and **b**, i.e. when $\hat{l} \in [0,1]$, the standard formula for the distance between a line and a point can be used:

$$d = \frac{\|\mathbf{ab}\times\mathbf{ap}\|}{\|\mathbf{ab}\|} . \tag{G.12}$$

When $\hat{l} \notin [0,1]$, the shortest distance from the line segment to the point is the distance from the closest end of the line segment (**a** or **b**) to the point (**p**). The following therefore

determines the minimum distance between the point **p** and the line segment **ab**:

$$d(\mathbf{ab},\mathbf{p}) = \begin{cases} \dfrac{\|\mathbf{ab}\times\mathbf{ap}\|}{\|\mathbf{ab}\|} & \text{if } 0 \le \hat{l} \le 1 \\ \|\mathbf{ap}\| & \text{if } \hat{l} < 0 \\ \|\mathbf{bp}\| & \text{if } \hat{l} > 1\ . \end{cases} \tag{G.13}$$

Using (G.13), the distances $\|\mathbf{fp}\|$ and $\left\|\mathbf{pr}_n\right\|$ can now be determined as

$$\|\mathbf{fp}\| = d(\mathbf{f},\mathbf{p}) \quad \text{and} \quad \left\|\mathbf{pr}_n\right\| = d(\mathbf{r}_n,\mathbf{p})\ . \tag{G.14}$$

By inserting (G.14) into (G.10), we arrive at

$$\mathrm{ToF}_m(\mathbf{p},n) = \frac{\left\|\mathbf{s}_{zy} - \mathbf{f}_{zy}\right\|}{c} + \frac{d(\mathbf{r}_n,\mathbf{p}) \pm d(\mathbf{f},\mathbf{p})}{c}\ , \tag{G.15}$$

where $\mathbf{s}_{yz}$ and $\mathbf{f}_{yz}$ are the coordinates in the z-y plane of **s** and **f**, respectively. The focused signal at point **p** is calculated by summing all receive signals at the time instances given by (G.15):

$$s_m(\mathbf{p}) = \sum_{n=1}^{N} a_{\mathrm{elec}}(n)\, y_{m,n}(\mathrm{ToF}_m(\mathbf{p},n))\ , \tag{G.16}$$

where N is the number of receive elements, $a_{\mathrm{elec}}(n)$ is the electronic receive apodization, and $y_{m,n}(t)$ is the measured signal from emission m on the receive element n at time t.

A MATLAB beamformer that implements (G.16) was programmed in order to beamform data from row-column addressed arrays and produce the point spread functions included in this paper. From (G.15) only the case where $\|\mathbf{fp}\|$ is added is implemented, so that only points further away from the array than the focal line can be beamformed. The beamformer can IQ-beamform 250 000 voxels from a complex data set of 1.5 MiB from 128 receive line-elements in approximately 11.4 s on a PC with a 3.4 GHz Intel Core i7-3770 CPU. The beamformer can therefore not achieve a frame rate useful for real-time applications, but the frame rate is adequate for research purposes.

G.6 Image Quality

3-D rectilinear imaging can be achieved directly under the transducer array, marked with dashed lines in Fig. G.6. The size of this area can be changed by varying number of transducer elements in the array and the pitch of the elements. The emission sequence can be designed exactly as when performing imaging with a 1-D transducer array. In this work, a single element emission sequence is used leading to 128 emissions for acquiring a full volume.

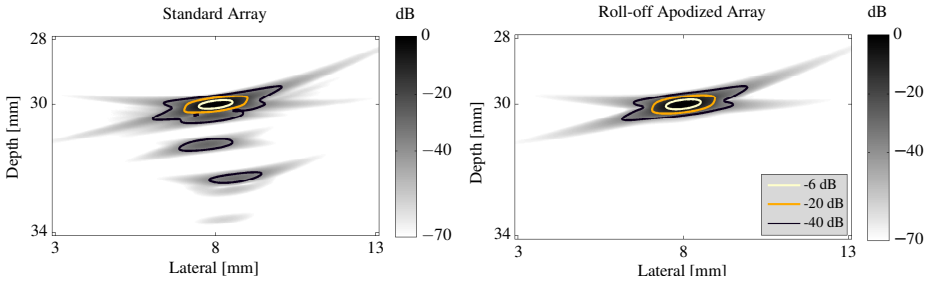

(a) (b)

Figure G.14: PSF at $(x,y,z) = (8,3,30)$ mm. The PSF of a standard non-apodized transducer array is shown in (a) and the PSF of a transducer array with integrated roll-off apodization is shown in (b). The main response of the PSFs are practically identical, but the ghost echoes of the roll-off apodized array are greatly suppressed compared to the non-apodized standard array.

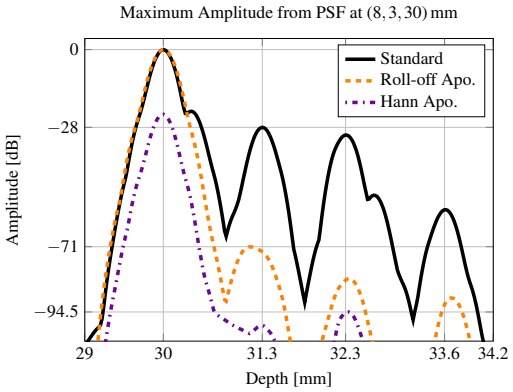

Figure G.15: Maximum intensity of the PSFs at $(x,y,z) = (8,3,30)$ mm as a function of depth. The Hann apodized array is added for comparison. Both the roll-off apodized array and the Hann apodized array greatly suppresses the ghost echoes, but the maximum intensity of the main response of the Hann apodized array is 24 dB lower compared to the two other arrays.

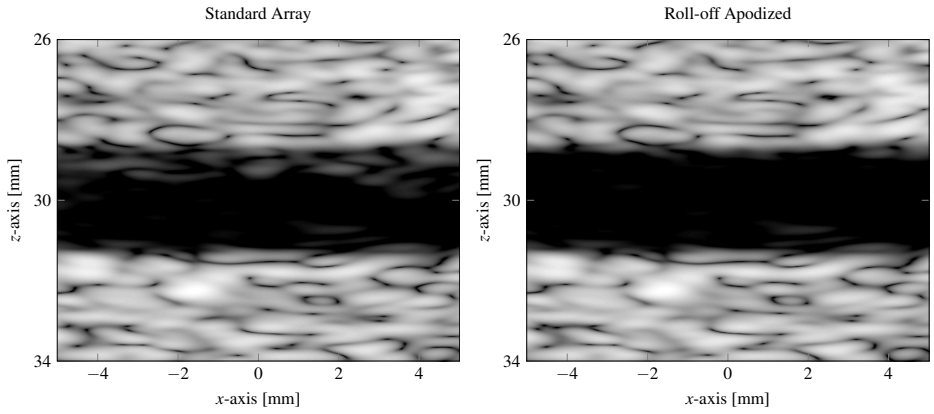

Figure G.16: B-mode images of a slice through the center of an anechoic blood vessel with a diameter of 3 mm located at 30 mm depth. (a) is made with a standard array and (b) with the roll-off apodized array. The dynamic range is 40 dB for both images. Because of ghost echoes in the PSF for the standard array, the blood vessel in (a) appears to be smaller than the blood vessel in (b).

In Fig. G.14, the PSF at $(x,y,z) = (8,3,30)$ mm, where 9 echoes are measured, is shown for both the standard and roll-off apodized array. Because several of the ghost echoes arrive with a very short time interval, only 5 of the 8 ghost responses can be distinguished. The main response of the two arrays are almost identical, but the ghost echoes of the roll-off apodized array are greatly suppressed compared to the non-apodized standard array. The maximum intensity of the PSFs in Fig. G.14 is seen in Fig. G.15 as a function of depth. The corresponding values for the Hann-apodized array has been added for comparison. The ghost responses seen on the PSF from the standard array are greatly attenuated by both the Hann-apodized array and the roll-off apodized array. The maximum ghost echo is attenuated by 43 dB for the roll-off apodized array and by 66.5 dB for the Hann apodized array. On the other hand, the main response of the Hann apodized array is seen to be attenuated by 24 dB, which clearly demonstrates the problem with the Hann apodization. As opposed to this, the roll-off apodized array has preserved the amplitude of the main response. Taking the main response damping into consideration, the maximum ghost echo damping of the Hann apodized array becomes 42.5 dB.

In Fig. G.16, B-mode images of a simulated anechoic blood vessel is shown. The diameter of the blood vessel is 3 mm and both B-mode images were acquired using 128 single line-element emissions with a standard array (a) and with a roll-off apodized array

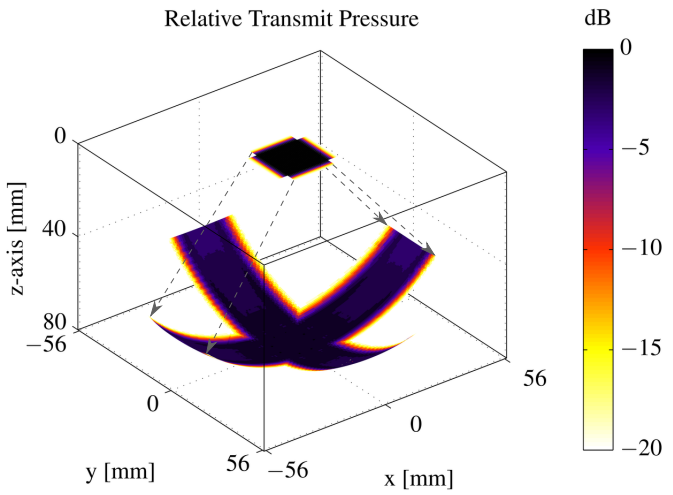

Figure G.17: Peak pressure distribution of a phased row-column addressed array. The transmit array of the row-column addressed array is used as a normal 1-D phased array from 2-D ultrasound imaging. Each voxel representing the pressure is located within the focal line. 200 emissions are used for simulating the figure and all 128 elements are excited during each emission. Each emission focuses at a different focal angle, but the focal distance is kept constant. For the pressure field to attain the cross shape shown in the figure, the transmit and receive arrays are interchanged after 100 emissions. This enables beamforming of cross-planes.

(b). The blood vessel phantoms used in Fig. G.16(a) and Fig. G.16(b) are identical, but the blood vessel in Fig. G.16(a) appears smaller than the blood vessel in Fig. G.16(b). The blood vessel diameter in Fig. G.16(a) is decreased by the ghost echoes apparent when using the standard array. By determining the mean of the B-mode images in Fig. G.16 along the x–dimension, the diameter of the blood vessel can be estimated. Defining the vessel wall as the location where the x–dimension mean crosses -20 dB, the blood vessel diameter is determined to 2.4 mm and 2.0 mm for the apodized array and the standard array, respectively. This corresponds to 80 % and 66.7 % of the true vessel diameter, and shows how applying the transducer-integrated apodization increases the detectability of small anechoic objects. The imaging quality is therefore significantly better when the ghost echoes are removed by integrating roll-off apodization into the transducer array.

The row-column addressed array can also be used for phased array imaging. The vertical and horizontal arrays of the row-column addressed 2-D array can each steer the transmit beam in one direction. In Fig. G.17, the relative peak pressure is shown when steering the transmit beam to the sides. For the phased array transmit beam, all 128 elements were focused at a distance of 80 mm. The transmit beam was varied by $\pm 45°$

and each voxel in the figure is placed on the focal line for a given emission. 200 emissions were used to create Fig. G.17. When the horizontal array is used as a transmit array, it can steer the transmit angle within in the z-x plane, and at the same time the vertical array is receiving. When the sequence has completed, the two arrays switch function, and now the vertical array is used as a transmit array. This leads to the energy being distributed as a cross, as seen in Fig. G.17. Row-column addressed arrays are therefore also well suited for cross-plane imaging.

When the transmit beam is steered to the side, the echoes arrive at the edge of the receive array first. To measure this signal, the roll-off region of the receive line-elements must be disabled in that direction. For CMUTs, this can conveniently be achieved by simply removing the bias from the roll-off region. For piezo-element arrays, the roll-off region could be connected with switches to the line-elements that then open when needed.

G.7 Discussion and Conclusion

The spatial impulse response of thin line-elements was shown to be proportional to the derivative of the line-element's 1-D apodization function. The ghost echoes, apparent with row-column addressed arrays, therefore originate from the discontinuity of the apodization function at the edge of the line-elements. To minimize the ghost echoes, the derivative of the apodization functions must be minimized.

In the literature, it has previously been proposed to use the Hann apodization to minimize the ghost echoes. In this work, it was shown that using the Hann apodization has the large disadvantage of emitting and receiving little energy. Instead, it was proposed to add a transducer-integrated roll-off apodization region to the ends of the line-elements. This way, the apodization functions of the horizontal and vertical line-elements do not overlap when they differ from the apodization value of 1. The entire central region can thereby emit and receive at full strength.

A wider the roll-off region yields a better ghost echo attenuation. A roll-off region width of $16\,\lambda$ was chosen, which led to a ghost echo damping in the PSF at $(x,y,z) = (8,3,30)$ mm of 43 dB. The transducer-integrated apodization was demonstrated to work by use of hydrophone measurements on an in-house produced 32+32 element row-column addressed CMUTs. Attenuation of the edge waves from transducer-integrated apodization was verified by calculating the energy of the received signals after the main wavefront. Using transducer-integrated apodization reduced the energy by 94 % in simulations and 34 % in measurements. The performance difference was mainly due to the significant energy contribution from the transducer ringing. This ringing originated from the lack of a backing layer in the experimental setup.

It was shown how data from a row-column addressed array with a focal line can be delay-and-sum beamformed. The focal line can be located both in front of the array and behind it, and thereby both focused and unfocused emissions can be beamformed.

A beamformer that can IQ-beamform 250 000 voxels from one emission in 11.4 s on a standard PC was presented and made available on-line.

Simulations of a 3 mm diameter anechoic blood vessel at 30 mm depth showed that applying the transducer-integrated apodization increased the apparent diameter of the vessel from 2.0 mm to 2.4 mm. This corresponds to an increase from 67 % to 80 % of the true vessel diameter, and shows how applying the transducer-integrated apodization increases the detectability of small anechoic objects. The imaging quality is therefore improved, when the ghost echoes are removed by integrating roll-off apodization into the transducer array. This is without affecting the front-end electronics, beamforming or number of channels.

References

Austeng, A. and S. Holm (2002). "Sparse 2-D arrays for 3-D phased array imaging - design methods". In: *IEEE Trans. Ultrason., Ferroelec., Freq. Contr.* 49.8, pp. 1073–1086 (cit. on p. 146).

Awad, S. I. and J. T. Yen (2009). "3-D spatial compounding using a row-column array". In: *Ultrason. Imaging* 31.2, pp. 120–130 (cit. on p. 146).

Brunke, S. S. and G. R. Lockwood (1997). "Broad-bandwidth radiation patterns of sparse two-dimensional vernier arrays". In: *IEEE Trans. Ultrason., Ferroelec., Freq. Contr.* 44.5, pp. 1101–1109 (cit. on p. 146).

Chen, A. I. H., L. L. Wong, A. S. Logan, and J. T. W. Yeow (2011). "A CMUT-based real-time volumetric ultrasound imaging system with row-column addressing". In: *Proc. IEEE Ultrason. Symp.* Pp. 1755–1758 (cit. on p. 146).

Daher, N. M. and J. T. Yen (2004). "Rectilinear 3-D ultrasound imaging using synthetic aperture techniques". In: *Proc. IEEE Ultrason. Symp.* Vol. 2, pp. 1270–1273 (cit. on p. 146).

— (2006). "2-D Array for 3-D Ultrasound Imaging Using Synthetic Aperture Techniques". In: *IEEE Trans. Ultrason., Ferroelec., Freq. Contr.* 53.5, pp. 912–924 (cit. on p. 146).

Davidsen, R. E., J. A. Jensen, and S. W. Smith (1994). "Two-Dimensional Random Arrays for Real Time Volumetric Imaging". In: *Ultrasonic Imaging* 16.3, pp. 143–163 (cit. on p. 146).

Démoré, C. E. M., A. Joyce, K. Wall, and G. Lockwood (2009). "Real-time volume imaging using a crossed electrode array". In: *IEEE Trans. Ultrason., Ferroelec., Freq. Contr.* 56.6, pp. 1252–1261 (cit. on pp. 146, 148, 154, 157, 162).

Harris, G. R. (1981a). "Review of transient field theory for a baffled planar piston". In: *J. Acoust. Soc. Am.* 70, pp. 10–20 (cit. on p. 149).

— (1981b). "Transient field of a baffled planar piston having an arbitrary vibration amplitude distribution". In: *J. Acoust. Soc. Am.* 70, pp. 186–204 (cit. on p. 149).

Huang, Y., A. S. Ergun, E. Hæggström, M. H. Badi, and B. T. Khuri-Yakub (2003). "Fabricating capacitive micromachined ultrasonic transducers with wafer-bonding technology". In: *J. Microelectromech. Syst* 12.2, pp. 128–137 (cit. on p. 158).

Jensen, J. A. (1991). "A Model for the Propagation and Scattering of Ultrasound in Tissue". In: *J. Acoust. Soc. Am.* 89, pp. 182–191 (cit. on p. 153).

— (1996). "Field: A Program for Simulating Ultrasound Systems". In: *Med. Biol. Eng. Comp.* 10th Nordic-Baltic Conference on Biomedical Imaging, Vol. 4, Supplement 1, Part 1, pp. 351–353 (cit. on p. 153).

Jensen, J. A. and N. B. Svendsen (1992). "Calculation of Pressure Fields from Arbitrarily Shaped, Apodized, and Excited Ultrasound Transducers". In: *IEEE Trans. Ultrason., Ferroelec., Freq. Contr.* 39, pp. 262–267 (cit. on p. 153).

Karaman, M., P. C. Li, and M. O'Donnell (1995). "Synthetic aperture imaging for small scale systems". In: *IEEE Trans. Ultrason., Ferroelec., Freq. Contr.* 42, pp. 429–442 (cit. on p. 146).

Karaman, M., I. O. Wygant, O. Oralkan, and B. T. Khuri-Yakub (2009). "Minimally Redundant 2-D Array Designs for 3-D Medical Ultrasound Imaging". In: *IEEE Trans. Med. Imag.* 7, pp. 1051–1061 (cit. on p. 146).

Kupnik, M., S. Vaithilingam, K. Torashima, I. Wygant, and B. Khuri-Yakub (2010). "CMUT fabrication based on a thick buried oxide layer". In: *Proc. IEEE Ultrason. Symp.* Pp. 547–550. DOI: 10.1109/ULTSYM.2010.5935935 (cit. on p. 158).

Ladabaum, I., X. Jin, H. T. Soh, A. Atalar, and B. T. Khuri-Yakub (1998). "Surface Micromachined Capacitive Ultrasonic Transducers". In: *IEEE Trans. Ultrason., Ferroelec., Freq. Contr.* 45.3, pp. 1–6 (cit. on p. 158).

Logan, A. S., L. L. P. Wong, A. I. H. Chen, and J. T. W. Yeow (2011). "A 32 x 32 element row-column addressed capacitive micromachined ultrasonic transducer". In: *IEEE Trans. Ultrason., Ferroelec., Freq. Contr.* 58.6, pp. 1266–1271 (cit. on p. 146).

Logan, A. S., L. L. P. Wong, and J. T. W. Yeow (2009). "2-D CMUT wafer bonded imaging arrays with a row-column addressing scheme". In: *Proc. IEEE Ultrason. Symp.* Pp. 984–987 (cit. on p. 146).

Lou-Møller, R., C. C. Hindrichsen, L. H. Thamdrup, T. Bove, E. Ringgaard, A. F. Pedersen, and E. V. Thomsen (2007). "Screen-printed piezoceramic thick films for miniaturised devices". In: *J. Electroceram.* 19.7, pp. 333–338 (cit. on p. 157).

Morton, C. E. and G. R. Lockwood (2003). "Theoretical assessment of a crossed electrode 2-D array for 3-D imaging". In: *Proc. IEEE Ultrason. Symp.* Pp. 968–971 (cit. on pp. 146, 162).

Naik, P. (2010). *Principles of Physics*. 4th ed. PHI (cit. on p. 156).

Pierce, A. D. (1989). *Acoustics, An Introduction to Physical Principles and Applications*. New York: Acoustical Society of America (cit. on p. 149).

Ramm, O. T. von, S. W. Smith, and H. G. Pavy (1991). "High speed ultrasound volumetric imaging system – Part II: Parallel processing and image display". In: *IEEE Trans. Ultrason., Ferroelec., Freq. Contr.* 38, pp. 109–115 (cit. on p. 146).

Rasmussen, M. F. (2014). *A Row-column beamformer*. URL: www.rc-beamformer.mofi.dk (cit. on p. 153).

Rasmussen, M. F., T. L. Christiansen, E. V. Thomsen, and J. A. Jensen. "Ultrasound Imaging Transducer Array with Integrated Apodization". PCT/IB2013/002838 (cit. on p. 157).

Rasmussen, M. F. and J. A. Jensen (2013a). "3-D Ultrasound Imaging Performance of a Row-Column Addressed 2-D Array Transducer: A Measurement Study". In: *Proc. IEEE Ultrason. Symp.* Pp. 1460–1463 (cit. on p. 146).

— (2013b). "3D ultrasound imaging performance of a row-column addressed 2D array transducer: a simulation study". In: *Proc. SPIE Med. Imag.* 86750C, pp. 1–11 (cit. on pp. 146–148, 154, 162).

Sampaleanu, A., P. Zhang, A. Kshirsagar, W. Moussa, and R. Zemp (2014). "Top-orthogonal-to-bottom-electrode (TOBE) CMUT arrays for 3-D ultrasound imaging." In: *IEEE Trans. Ultrason., Ferroelec., Freq. Contr.* 61.2, pp. 266–276. DOI: 10.1109/TUFFC.2014.6722612 (cit. on p. 146).

Savoia, A. S., G. Caliano, and M. Pappalardo (2012). "A CMUT Probe for Medical Ultrasonography: From Microfabrication to System Integration". In: *IEEE Trans. Ultrason., Ferroelec., Freq. Contr.* 59.6, pp. 1127–1138 (cit. on p. 158).

Seo, C. H. and J. T. Yen (2006). "64 x 64 2-D array transducer with row-column addressing". In: *Proc. IEEE Ultrason. Symp.* Vol. 1, pp. 74–77 (cit. on p. 146).

— (2007). "256 x 256 2-D array transducer with row-column addressing for 3-D imaging". In: *Proc. IEEE Ultrason. Symp.* Pp. 2381–2384 (cit. on p. 146).

— (2008). "Recent results using a 256 x 256 2-D array transducer for 3-D Rectilinear Imaging". In: *Proc. IEEE Ultrason. Symp.* Vol. 1-4, pp. 1146–1149 (cit. on p. 146).

— (2009). "A 256 x 256 2-D array transducer with row-column addressing for 3-D rectilinear imaging". In: *IEEE Trans. Ultrason., Ferroelec., Freq. Contr.* 56.4, pp. 837–847 (cit. on pp. 146, 162).

Stepanishen, P. R. (1971). "Transient radiation from pistons in an infinite planar baffle". In: *J. Acoust. Soc. Am.* 49, pp. 1629–1638 (cit. on p. 149).

— (1981). "Acoustic transients from planar axisymmetric vibrators using the impulse response approach". In: *J. Acoust. Soc. Am.* 70, pp. 1176–1181 (cit. on p. 149).

Thomenius, K. E. (1996). "Evolution of ultrasound beamformers". In: *Proc. IEEE Ultrason. Symp.* Vol. 2, pp. 1615–1621 (cit. on p. 146).

Tjøtta, J. N. and S. Tjøtta (1982). "Nearfield and farfield of pulsed acoustic radiators". In: *J. Acoust. Soc. Am.* 71, pp. 824–834 (cit. on p. 149).

Turnbull, D. H. and F. S. Foster (1991). "Beam steering with pulsed two-dimensional transducer arrays". In: *IEEE Trans. Ultrason., Ferroelec., Freq. Contr.* 38.4, pp. 320–333 (cit. on p. 146).

Yen, J. T., J. P. Steinberg, and S. W. Smith (2000). "Sparse 2-D array design for real time rectilinear volumetric imaging". In: *IEEE Trans. Ultrason., Ferroelec., Freq. Contr.* 47.1, pp. 93–110 (cit. on p. 146).

Yen, J. T. (2013). “Beamforming of sound from two-dimensional arrays using spatial matched filters”. In: *J. Acoust. Soc. Am.* 134.5, pp. 3697–704. DOI: 10.1121/1.4821988 (cit. on pp. 146, 162).

Zhang, P., G. Fitzpatrick, T. Harrison, W. A. Moussa, and R. J. Zemp (2012). “Double-SOI Wafer-Bonded CMUTs With Improved Electrical Safety and Minimal Roughness of Dielectric and Electrode Surfaces”. In: *J. Microelectromech. Syst.* 21.3, pp. 668–680 (cit. on p. 158).

PAPER H

3-D Imaging using Row-Column Addressed Arrays with Integrated Apodization: Transducer Fabrication and Experimental Results

Authors: Thomas Lehrmann Christiansen, **Morten Fischer Rasmussen**, Jan Peter Bagge, Lars Nordahl Moesner, Jørgen Arendt Jensen, and Erik Vilain Thomsen

Submitted to: IEEE Transactions on Ultrasonics, Ferroelectrics, and Frequency Control, June 18, 2014.

Abstract

This paper demonstrates the fabrication, characterization, and experimental imaging results of a $62+62$ element $\lambda/2$-pitch row-column addressed capacitive micromachined ultrasonic transducer (CMUT) array with integrated apodization. A new fabrication process was used to manufacture a 26.3 mm by 26.3 mm array using five lithography steps. The array includes an integrated apodization presented in a previous work by the authors, which is designed to reduce the amplitude of the ghost echoes that are otherwise prominent for row-column addressed arrays. Custom front-end electronics was produced with the capability of transmitting and receiving on all elements, and the option of disabling the integrated apodization. The center frequency and -6 dB fractional bandwidth of the array elements were 2.77 ± 0.26 MHz and 102 ± 10 %, respectively. The surface transmit pressure at 2.5 MHz was 590 ± 73 kPa, and the sensitivity was 0.299 ± 0.090 µV/Pa. The nearest neighbour cross-talk level

Manuscript received June 18, 2014; accepted <month> <day>, <year>. This work was financially supported by grant 82-2012-4 from the Danish National Advanced Technology Foundation.

T.L. Christiansen and E.V. Thomsen are with the Department of Micro- and Nanotechnology, Technical University of Denmark, Kgs. Lyngby, Denmark.

M.F. Rasmussen and J.A. Jensen are with the Center for Fast Ultrasound Imaging, Department of Electrical Engineering, Technical University of Denmark, Kgs. Lyngby, Denmark.

J.P. Bagge and L.N. Moesner are with BK Medical, Analogic Ultrasound Group, Herlev, Denmark.

was -22.4 ± 4.5 dB, while the transmit to receive elements cross-talk level was -38.0 ± 3.4 dB. Imaging of a 0.3 mm diameter steel wire using synthetic transmit focusing with 62 single-element emissions demonstrated an axial and lateral FWHM of 0.71 mm and 1.79 mm (F-number: 1.4), respectively, compared to a simulated axial and lateral FWHM of 0.58 mm and 1.56 mm. The dominant ghost echo was reduced by 15.8 dB using the integrated apodization compared to the disabled configuration. The effect was reproduced in simulations showing a ghost echo reduction of 11.5 dB.

H.1 Introduction

Recently, row-column addressed arrays have attracted some attention as they offer real-time volumetric imaging with a greatly reduced number of connections to the array compared to a fully addressed array. Where an $N \times N$ fully addressed array will need N^2 individual connections, a row-column addressed array only needs $2N$ connections. Numerous techniques have been introduced to reduce the complexity of 2-D matrix arrays, such as sparse arrays (Austeng and Holm 2002; Brunke and Lockwood 1997; Davidsen et al. 1994; Karaman et al. 2009; Yen, Steinberg, et al. 2000) and integrated electronics in the probe handle (Blaak et al. 2009; Halvorsrod et al. 2005; Savord and Solomon 2003). Despite these measures, the dense interconnect requirements, high electrical impedance of the elements, and heating of integrated electronics remain significant challenges for 2-D matrix arrays. Therefore, row-column addressed arrays provide an attractive alternative to such arrays for real-time volumetric ultrasound imaging.

The concept of volumetric imaging using row-column addressing, where transmit focusing is performed in one dimension and receive focusing is performed in the orthogonal dimension, was first introduced by Morton and Lockwood in 2003 (Morton and Lockwood 2003), and later expanded by Demoré et al. (Démoré et al. 2009). Different techniques to improve the resolution, sensitivity, or frame rate of row-column addressed arrays were explored theoretically by Daher et al. (Daher and Yen 2004, 2006) and Yen (Yen 2013) using synthetic aperture techniques and spatial matched filters. Recently, Rasmussen and Jensen used a fully addressed 32×32 array in a measurement study to compare the imaging performance of a fully addressed array to that of a row-column addressed array (Rasmussen and Jensen 2013a). For the same number of channels used, the row-column addressed array exhibited superior detail resolution compared to the fully addressed array.

Several groups have presented realizations of row-column addressed arrays. Yen's group have demonstrated imaging with several versions of row-column addressed piezo-arrays, starting in 2006 where Seo and Yen (Seo and Yen 2006) presented the first experimental demonstration of a row-column addressed array. The $64 + 64$ elements used in this array was later surpassed by a $256 + 256$ element array (Seo and Yen 2007, 2008, 2009) by the same authors. More recently, Chen et al. (Y. Chen et al. 2011) and Yen et al. (Yen, Seo, et al. 2009) have introduced arrays manufactured with a dual layer structure to simplify the fabrication process. Zemp et al. (Zemp et al. 2011) and

Sampaleanu et al. (Sampaleanu et al. 2014) have performed feasibility studies using capacitive micromachined ultrasonic transducers (CMUTs). Additionally, the group of Yeow have demonstrated both characterization (Logan, Wong, and Yeow 2009) and imaging using a $16+16$ element (A. I. H. Chen et al. 2011) and a $32+32$ element (Logan, Wong, A. I. H. Chen, et al. 2011) row-column addressed CMUT array.

Despite the promises of row-column addressing, such arrays have an inherent drawback: The long elements produce prominent edge effects leading to ghost echoes in the beamformed image. The row-column addressing scheme does not allow for electronic control along the length of the elements, and the ghost echoes can therefore not be removed using conventional electronic apodization techniques. This issue was first observed by Demoré et al. (Démoré et al. 2009) and later described in further detail by Rasmussen and Jensen (Rasmussen and Jensen 2013b). Both authors concluded that a solution to the problem was to integrate the apodization in the transducer array itself, and several embodiments of a transducer-integrated apodization have been suggested (Rasmussen et al. n.d.). Recently, Rasmussen et al. (Rasmussen et al. 2014) presented an in-depth study of the possibilities of such a transducer-integrated apodization. It was shown how transducer-integrated apodization could be implemented in CMUTs based on simple measurements of the emitted field from CMUT prototypes. Simulation studies were used to develop an optimized transducer-integrated apodization that is able to efficiently damp the ghost echoes from row-column addressed arrays in the entire imaged 3-D volume. Importantly, this was achieved without affecting the main echo regardless of the position of the object being imaged, and without altering the number of channels needed or changing the beamforming in any way.

This paper demonstrates the fabrication and characterization of a $62+62$ element row-column addressed CMUT array with such an integrated apodization based on the layout presented in (Rasmussen et al. 2014). Custom front-end electronics with transmit and receive capability on all channels are made in order to drive the array. The array is used to perform volumetric imaging of a steel wire twice; once with the apodization enabled and once with the apodization disabled. The purpose is thereby to experimentally demonstrate the effect of an integrated apodization when performing 3-D imaging with row-column addressed arrays.

The paper is organized as follows: Section H.2 covers the design and fabrication of the CMUT array as well as a description of the front-end electronics. Section H.3 contains a characterization of the array using impedance measurements and acoustical measurements. In section H.4, the imaging results are presented, and section H.5 concludes the paper.

H.2 Array Design, Fabrication, and Interconnect Electronics

H.2.1 Array Design

The design of the transducer array used in this work can be divided into three main components: Design of the individual CMUT cells to achieve the desired operating

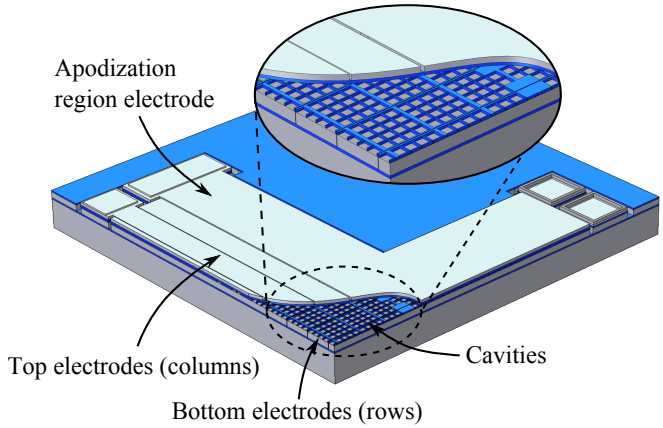

Figure H.1: 3-D illustration of the CMUT row-column addressed transducer array showing a detail of the upper right corner of the array seen in Fig. H.2 (top corner of the mounted array shown in Fig. H.3). A section of the top electrodes have been removed to reveal the underlying CMUT cavities. Oxide is drawn blue, silicon grey and aluminium light grey. Dimensions are not to scale.

frequency and operating voltage, determination of the element size and pitch, and finally design of the layout of the integrated apodization. These three components are addressed in the following.

A single element of the array consists of multiple individual CMUT cells. The operating frequency of the array is determined by the plate thickness and lateral dimension of the CMUT cells (Ventsel and Krauthammer 2001). To obtain a high fill-factor, the geometry of the CMUT cells is designed to be square, and the operating frequency is adjusted such that the cells can be closely fitted in the width of a $\lambda/2$–pitch array element. These considerations resulted in a CMUT cell with a plate thickness of 1.7 µm, and a square side length of 60 µm, designed for a center frequency in immersion of 2.74 MHz. The corresponding element pitch for this frequency was 270 µm. The distance between the individual cells as well as the kerf was set to 5 µm to provide adequate bonding area during the fabrication as covered in section H.2.2. All dimensions can be seen in Table H.1.

The operating voltage of the array is, for fixed CMUT plate dimensions, determined by the gap between the top- and bottom electrodes. The gap consists of a vacuum region and an oxide layer; the latter is used to provide insulation in case of pull-in. The pull-in voltage is here defined as the voltage where the top plate collapses down to the bottom electrode due to the electrostatic forces being larger than the mechanical forces. The thickness of the vacuum gap is aimed for 400 nm, while the insulation oxide is designed to be 200 nm, which is designed to give a pull-in voltage of approximately 100 V. The

Table H.1: Transducer dimensional parameters

Parameter	Value	Unit
Array		
Number of elements	62+62	–
Number of apodization region electrodes	4	–
Element pitch	270	µm
Element width	265	µm
Element length	24.84	mm
Length of apodization regions	4.05	mm
Array outer dimensions (square)	26.3	mm
CMUT cell		
Cell side length (square)	60	µm
Distance between cells	5	µm
Plate thickness	1.7	µm
Al electrode thickness	200	nm
Insulation oxide thickness	296	nm
Vacuum gap height	413	nm

actual gap dimensions, dictated by the fabrication accuracy, is seen in Table H.1.

The layout of the array is seen in Fig. H.2, and is based on the previous work by the authors (Rasmussen et al. 2014). A 3-D drawing of the corner portion of the array is given in Fig. H.1. It consists of 62 row elements, 62 column elements, and four apodization region electrodes. The apodization region electrodes provide DC bias to the integrated apodization, which is located at both ends of the elements. To the right in Fig. H.2, a zoom-in on one apodized element end is shown. As seen, it consists of a collection of CMUT cells (red squares), the number of which is reduced towards the outer edge. As demonstrated in (Rasmussen et al. 2014), such a reduction in the number of CMUT cells will provide a fixed integrated apodization, since the energy transmitted and received by the array scales with the density of the cells. As in (Rasmussen et al. 2014), the number of cells follows a Hann function, which in this case is discrete.

The central part of the array, i.e. excluding the apodized element ends, is densely populated with CMUT cells and is thus not apodized in any way. In other words, the part of the array seen within the dashed line in Fig. H.2 may be considered a ”conventional” row-column addressed CMUT transducer array. The apodized regions located outside this central part is responsible for removing the otherwise abrupt truncation of the elements, which is the origin of the ghost echoes produced by row-column addressed arrays (Rasmussen et al. 2014). This configuration allows the array to perform as a conventional row-column addressed array, regardless of the position of the object being imaged, but with a significant damping of the ghost echoes as demonstrated in (Rasmussen et al.

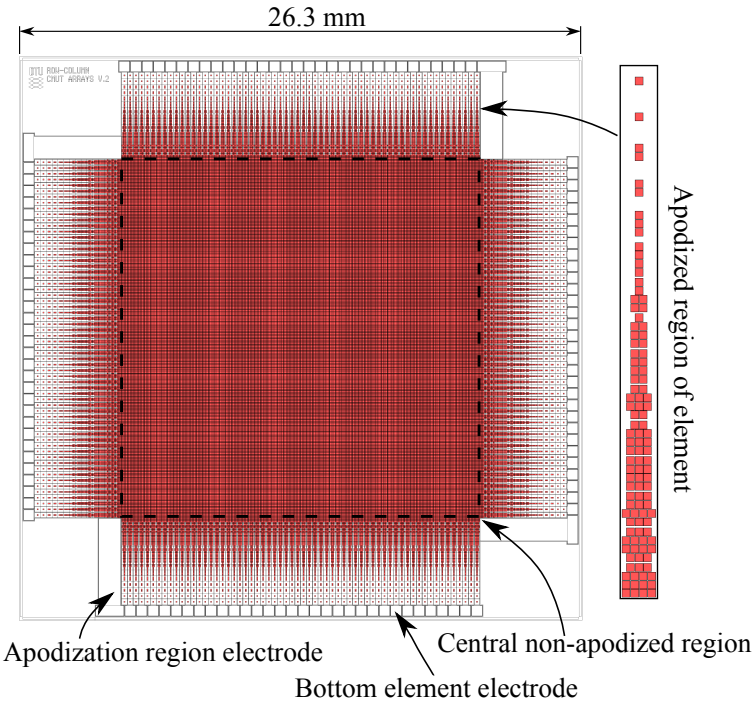

Figure H.2: Array mask layout. The red squares are the individual CMUT cells, which are densely populated in the central region of the array shown within the dashed line. A zoom on the apodized region of one element is seen in the right part of the figure. The four large contact pads provides electrical access to the apodization region electrodes.

2014).

H.2.2 Array Fabrication

The array was fabricated using cleanroom processing techniques, partly based on previous works described in the literature (Y. Huang et al. 2003; Zhang et al. 2012). The individual process steps are shown in Fig. H.4.

The fabrication process utilized two silicon-on-insulator (SOI) wafers, both having a 525 µm thick handle layer with high resistivity (1-10 Ωcm), a 1 µm thick buried oxide layer, and a low resistivity (0.01-0.001 Ωcm) device layer. The device layer on the first SOI wafer was 20 µm thick and was used to create the bottom electrodes, from here on defined as the rows. The second SOI wafer had a 1.9 µm thick device layer, which was used for the top electrode (plate) of the CMUT. These top electrodes are defined as the columns of the row-column addressed array.

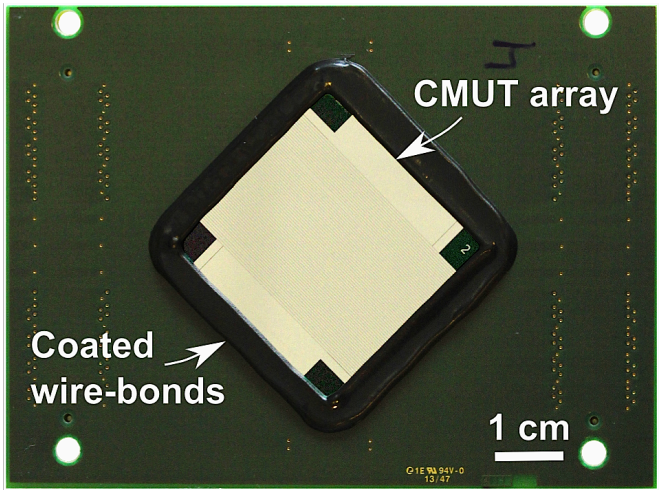

Figure H.3: The row-column addressed CMUT array mounted and wire-bonded on the carrier board. Two connectors are located on the back-side of the carrier board (the vias to the connectors can be seen to the left and right in the picture). The CMUT array is rotated 45° clockwise to ensure that the length of each lead to the connector pins are equal. The top electrodes (columns) can be seen going from the top left to the bottom right of the array.

The SOI wafer with 20 µm device layer was dry oxidized at 1050 °C for 8 hours and 35 minutes to grow a 296 nm thick layer of oxide (Fig. H.4a). The CMUT cavities were then defined using conventional UV lithography and etched using reactive ion etching (RIE) as shown in Fig. H.4b. After stripping the photoresist, a second lithography step was used to define the bottom electrodes, or rows, as shown in Fig. H.4c. Two consecutive RIE etches were used to selectively etch first the oxide layer and subsequently the underlying silicon device layer. After stripping the photoresist, the fabrication of the bottom electrodes and the substrate supporting the array was complete.

The second SOI wafer was dry oxidized at 1100 °C for 8 hours and 55 minutes to grow a 413 nm thick layer of oxide, reducing the silicon device layer thickness from 1.9 µm to 1.7 µm. Both SOI wafers were then cleaned using a standard RCA cleaning procedure (Kern 1990) and bonded together in vacuum (0.01 mbar) using fusion bonding and a subsequent annealing step (70 min at 1100 °C), see Fig. H.4d. The oxide layer covering both wafers was removed in buffered hydrofluoric acid (BHF), after which the handle layer and buried oxide layer of the top SOI wafer was etched using both RIE and BHF, respectively, as shown in Fig. H.4e.

A third lithography step followed by selective RIE in first the silicon layer and subsequently the oxide layer was used to define openings to the bottom electrodes, see Fig. H.4f. The thin device layer is partly transparent in the visible spectrum, and alignment

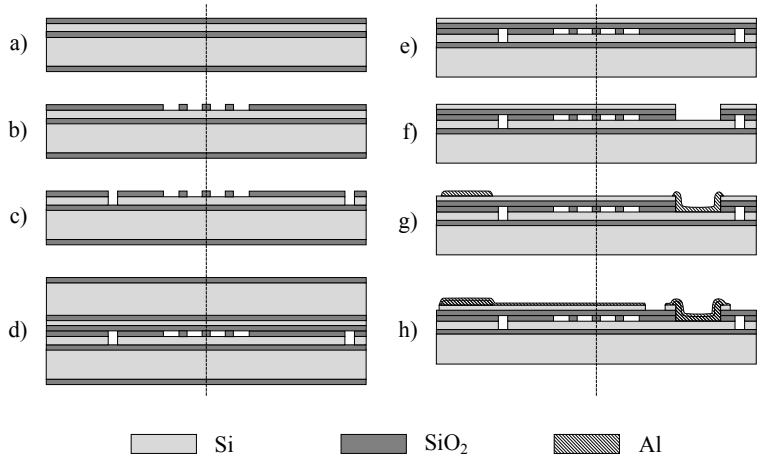

Figure H.4: Process flow of the cleanroom fabrication. The dashed line separates the layer composition comprising the top electrodes (to the right of the line) and the bottom electrodes (to the left of the line), corresponding to a cross-section from left to right in Fig. H.1. The steps are: a) oxidation, b) cavity etch, c) bottom electrode etch, d) wafer bonding, e) handle etch, f) etch access to bottom electrodes, g) deposit and etch wire-bonding pads, and h) deposit and etch top electrodes. A total of five lithography masks are used (in steps b, c, f, g, and h).

to the bottom wafer alignment marks could therefore be performed, thereby omitting the need for alignment during the wafer bonding step.

Fig. H.4g shows the wire-bonding pads, which were made by depositing a 800 nm aluminium layer on the entire wafer using electron beam evaporation and structured by performing a lithography step followed by a selective aluminium etch in H_2O: H_3PO_4 (1: 2) at 50 °C. The top electrodes, or columns, were then finally defined by a step similar to the previous, but this time with a 200 nm aluminium deposition. Before removing the photoresist, the exposed silicon layer was etched using RIE to isolate the individual top electrodes, thereby concluding the fabrication process.

It should be noted that this process only uses five lithography steps, and, wherever possible, the same lithography step is used for multiple etches. Any front-to-back or wafer-to-wafer alignment is omitted to improve the robustness of the process. Also, the oxide-oxide bonding previously presented in (Christiansen et al. 2013) was chosen, as it allows for protrusion-free surfaces and thereby very low void density, which is essential for such large arrays.

H.2.3 Interconnect Electronics

The fabricated array was mounted on a printed circuit board acting as a carrier board as shown in Fig. H.3. This carrier board contained one lead per channel in the array, having wire-bonding pads in one end and terminating in one of two connectors in the other end (located on the back side of the carrier board shown in Fig. H.3). All leads were designed to have equal length to ensure uniformity of the channels. To facilitate this, the orientation of the array was set to 45° relative to the sides of the carrier board. The array was mounted on the carrier board using Namics XS8481-8 epoxy glue (Namics Corporation, Niigata, Japan) with no further backing applied. The electrical connection between array and carrier board was made using wire-bonding, and glob-top (dam and fill, Namics G8245-D and G8345-6, Namics Corporation, Niigata, Japan) was applied afterwards to protect and insulate the bonds.

The carrier board was designed to easily connect with a second printed circuit board via the connectors, which acts as an interconnect board (ICB) between the mounted array and the scanner used to send and acquire the data. In this work, the experimental Synthetic Aperture Real-time Ultrasound System (SARUS) (Jensen, Holten-Lund, et al. 2013) was used. A total of 192 transmit/receive channels could be interfaced using this ICB, and connection to the scanner was made via a 192 channel coaxial cable (BK Medical, Herlev, Denmark). Every channel was connected to a MAX4805A pre-amplifier (Maxim Integrated, San Jose, CA, USA), providing a nominal 8.7 dB voltage gain of the receive signals in order to drive the cable. The MAX4805A contains a built-in switching circuit that can protect the pre-amplifier during transmit, so that all channels on the ICB could be used for both transmission and reception.

A DC biasing circuit with two DC bias supplies was made. A sketch of the electronics can be seen in Fig. H.5, where the variable capacitor denotes the CMUT element. This particular sketch illustrates the case for a column element, but the setup is identical for the row elements. The column element has contact to a single channel on the ICB, here dubbed column channel m, which is held at the voltage potential defined by DC bias 1. DC bias 1 also supplies all the remaining column channels. The row elements passing perpendicularly below it are all held at the voltage potential defined by DC bias 2. The total DC bias seen by the CMUT element thereby becomes the difference between the two DC supplies. The DC bias supply to each element is provided through a 1 MΩ resistor (R), partly acting as a low-pass filter, and partly ensuring that the DC voltage can be maintained in the event of a short circuit of a top- and bottom electrode within the CMUT array, or any other DC short of the row- or column signals. A 10 nF capacitor (C) is placed in front of the input of the MAX4805A to separate the DC bias from the ground reference of the transmitters and the receive circuit.

If a transmit pulse is sent on column channel m, all the row channels will provide a ground path for the AC signal. This will be established through the rows' 10 nF capacitor (C), then through the transmit-path diodes (D) inside the MAX4805A (see inset in Fig. H.5) and finally to the transmit amplifier output of the row channels. It is therefore

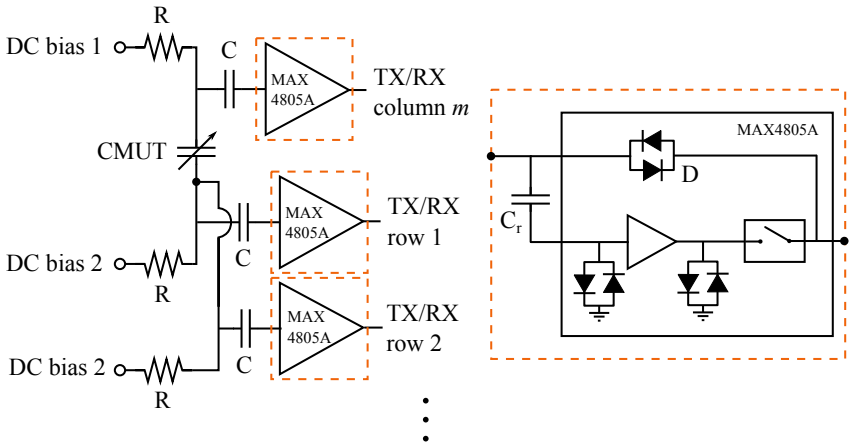

Figure H.5: Sketch of the front end electronics as seen by a column element. The element has contact to all row channels as illustrated with the three dots in the bottom right. The DC biases are low pass filtered through a 1 MΩ resistor (R) in conjunction with the CMUT, while the AC signal to and from the CMUT via the MAX4805A pre-amplifier is high-pass filtered using a 10 nF capacitor (C) together with the resistor R. The inset shows a detail of the MAX4805A circuit (Savoia et al. 2012).

mandatory that the row channels are in the low impedance transmit mode to establish this ground-reference. No ground is accessible through the receive path due to the high impedance of the 47 pF capacitor, C_r. During reception, the AC voltage generated by the CMUT element is low enough, so that the diode pair (D) in the transmit path does not provide a path to ground. Therefore, all row channels and column channel *m* will receive and amplify the received signal. This is true for all elements, so all rows and columns in the array are able to receive simultaneously using this circuit design.

Note that although all 128 channels of the array are able to both transmit and receive, four of the channels are not used for imaging, since they are only providing DC bias for the apodized regions of the elements. In this setup, however, these four apodization region electrodes are connected like all of the remaining elements, since this provides a convenient DC bias source for the apodization region electrodes.

H.3 Transducer Characterization

The transducer presented in the previous section was characterized both electrically using impedance measurements and acoustically in vegetable oil through hydrophone and pulse-echo measurements. This section describes these measurements, thereby providing an evaluation of the performance of the array.

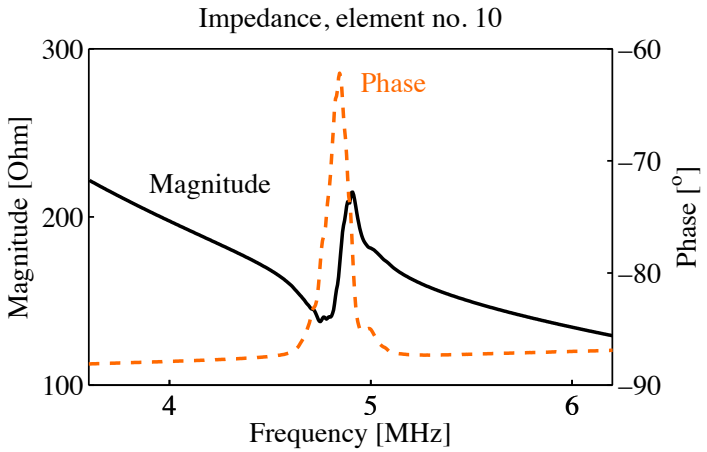

Figure H.6: Impedance magnitude (solid line) and phase (dashed line) for element no. 10 acquired at a DC bias of 40 V in the vicinity of the mechanical resonance of the element.

H.3.1 Impedance measurements

The electrical characterization of the transducer array was carried out using an Agilent 4294A impedance analyzer (Hewlett-Packard, Palo Alto, CA, USA). The measurements were performed after mounting the array on the carrier board shown in Fig. H.3. Each element of the array was accessed via the pins of the connectors on the carrier board using an Agilent 42941A probe (Hewlett-Packard, Palo Alto, CA, USA). When measuring on individual columns, all rows were electrically shorted using a custom-built connector to enable measurement of a whole column at the time. The reverse was true when measuring on individual rows. In all measurements, a 500 mV excitation voltage was used on top of a DC bias of 40 V, which was applied to the array using the built-in DC bias of the impedance analyzer. These values were chosen to acquire adequate signal from the array to locate the resonance peak, whilst at the same time ensuring negligible frequency shift of the resonance peak due to the spring softening effect.

For every element, a set of three impedance sweeps were performed: one spanning the whole range of the impedance analyzer from 40 Hz to 110 MHz, a second from 1 MHz to 20 MHz, and a final in an interval of ± 1 MHz from the detected resonance frequency of the element. From this, the capacitance and resonance frequency in air of each individual element were found. The capacitance was determined at the lowest measured frequency (40 Hz), and the resonance frequency was found as the local minimum in impedance magnitude in the vicinity of the resonance. An example of an impedance sweep showing the resonance of element no. 10 is seen in Fig. H.6.

The resonance frequency in air and capacitance of each element are shown in Figs. H.7a and H.7b. Mean and standard deviation over the whole array is given in Table H.2. The capacitance is seen to be very homogeneous for both the rows and columns with a standard deviation of 1.2 % and 0.5 %, respectively. This is a consequence of the lateral accuracy of the cleanroom processing, which uses UV photolithography for defining the lateral dimensions of the array. The rows (bottom electrodes) have a higher capacitance than the columns (top electrodes) as they can couple capacitively to the substrate of the bottom SOI wafer. At higher frequencies, the capacitances of the rows and columns will approach each other, since the low conductivity of the substrate effectively produces a low-pass filter. The apodization region electrodes have a much higher capacitance than the elements, and their capacitance has therefore only been listed in Table H.2 to better visualize the capacitance of the elements in H.7b. This higher capacitance is a consequence of the large area of the apodization region electrodes as can be seen in Fig. H.1. Note also that the column elements 4-5, 11-12, and 21-22 are pair-wise shorted. This is due to fabrication errors in the final aluminium and silicon etch shown in Fig. H.4h. Any particle covering the element kerf on the mask during the lithography step prior to these etches will result in contact between two top electrodes (columns). This is especially critical for row-column addressed arrays, where the size of the elements results in a extensive total kerf length. The kerf is only 5 µm, so any particle larger than this will result in a short circuit, which was seen to affect these three different locations of the array.

The resonance frequency in air given in Fig. H.7a is seen to vary slightly more than the capacitance, the standard deviation being 4 %. This is a consequence of the thickness variation of the device layer of the SOI wafer, which is used to define the top electrode that acts as the top vibrating plate of the individual CMUT cells. This thickness is harder to control precisely, as the SOI wafer was ordered from external wafer suppliers, who promised a thickness tolerance of 300 nm. Since the resonance frequency in air scales linearly with the thickness (Ventsel and Krauthammer 2001), the observed frequency variation is well within this tolerance limit. Note that the resonance frequency in air is far from the intended center frequency of the array of 2.74 MHz. This is a predictable and well-known effect, as the acoustical loading of air is much lower than the loading from a liquid medium. The resonances reported here therefore only serves as a measure of the functionality and homogeneity of the array.

Finally, the pull-in voltage was measured to determine the operating voltage of the array. To avoid charging of the array elements during pull-in (Y. L. Huang et al. 2005), the pull-in voltage was measured on test-elements made on the same wafer as the array. The pull-in voltage was found by performing impedance sweeps whilst increasing the DC bias voltage sequentially using a Keithley 2400 sourcemeter (Keithley Instruments Inc., Cleveland, OH, USA). The pull-in voltage was then identified as the point where the resonance peak seen in Fig. H.6 was abruptly shifted to a higher frequency due to the collapse of the plates. This was done on a total of five test elements, yielding a pull-in voltage of 100 ± 3 V as reported in Table H.2. It was chosen to operate the array with a

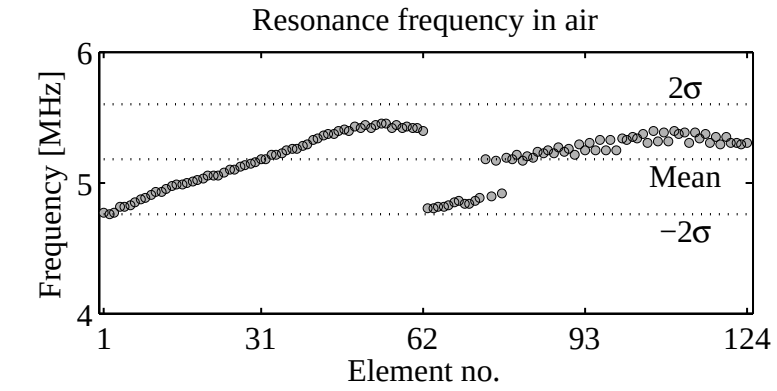

(a)

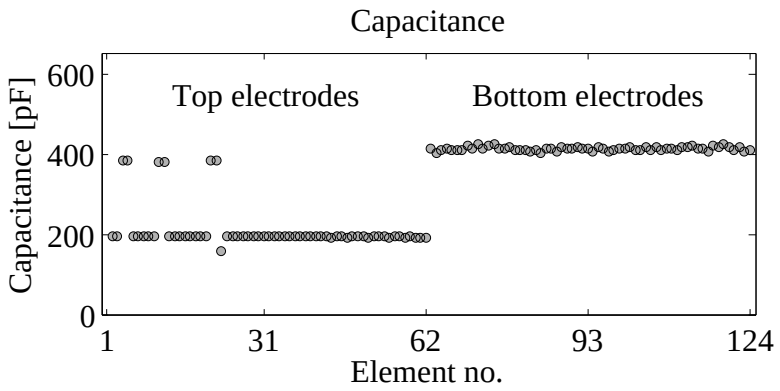

(b)

Figure H.7: Resonance frequency in air (a) and capacitance evaluated at 40 Hz (b) vs. element number. The resonance frequency is shown with mean and two standard deviations (2σ). Element 1-62 are top electrode elements and element 63-124 are bottom electrode elements. The elements 4-5, 11-12, and 21-22 are pair-wise shorted due to fabrication errors, hence the altered capacitance.

Table H.2: Transducer impedance characterization parameters

Parameter	Mean value	Std.	Unit
Resonance frequency in air	5.18	0.21	MHz
Element capacitance (top)	194	1	pF
Element capacitance (bottom)	413	5	pF
Apo. reg. electrode capacitance (top)	2677	105	pF
Apo. reg. electrode capacitance (bottom)	4308	14	pF
Pull-in voltage	100	3	V

Table H.3: Transducer acoustical characterization parameters

Parameter	Mean	Std.	Unit
Center frequency in immersion	2.77	0.26	MHz
-6 dB fractional bandwidth	102	10	%
Transmit pressure peak-to-peak	590	73	kPa
Sensitivity at 2.5 MHz	0.299	0.090	µV/Pa
Nearest neighbour crosstalk level	-22.4	4.5	dB
Transmit to receive elements crosstalk level	-38.0	3.4	dB

DC bias voltage of 80 % of the pull-in voltage and an AC amplitude of 50 % of the pull-in voltage. Thus, for all subsequently described measurements, the DC bias voltage was set to 80 V ($\pm$40 V on the two bias supplies), and the AC amplitude to 50 V.

H.3.2 Acoustical measurements

The acoustical characterization of the array was performed with the carrier board mounted on the ICB described in section H.2.3. The electronics and the array was then mounted in a plexiglass box closed using an aluminium lid with a hole, through which there was access to the array. All measurements were performed in rapeseed oil to provide electrical insulation of the exposed electrodes on the array. The speed of sound in the oil was measured to be 1480 m/s, and the damping 0.3 dB/MHz cm (Rasmussen et al. 2014), which is in agreement with previously reported values for vegetable oil (Oralkan et al. 2002). As mentioned in the previous section, the DC bias voltage was in all measurements set to 80 V, while the amplitude of the AC signal was set to 50 V. The DC bias was provided through a TOE8842 dual DC power supply (Toellner Electronic Instrumente GmbH, Herdecke, Germany) set to $\pm$40 V, and the AC signals were generated using the experimental ultrasound system SARUS (Jensen, Holten-Lund, et al. 2013), which was also used to record all received signals. The system was set to sample at 70 MHz and to record signals down to a depth of 4 cm. Note that the four apodization region

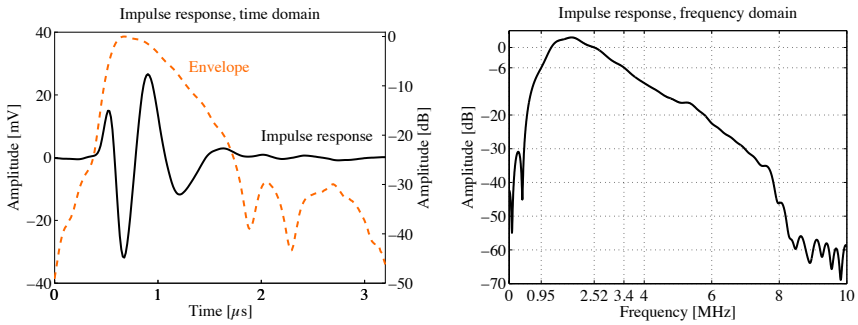

(a) (b)

Figure H.8: (a) Pulse-echo impulse response from the center bottom electrode element (no. 96). The solid line (left axis) shows the measured voltage signal and the dashed line (right axis) shows the envelope of the measured signal given in dB. (b) Frequency domain of the impulse response. The center frequency (2.54 MHz) and the -6 dB bandwidth relative to the center frequency (0.95 MHz to 3.4 MHz) have been indicated.

electrodes are not included in the results presented below, as they were not used as actual transmitting/receiving elements during imaging.

First, a reference measurement was made using a 2.5 MHz sinusoidal excitation with 2 and 4 cycles, respectively. Here, each individual element was excited one at a time in a tank of oil with no immediate reflecting structures. For each excitation, the signals received by all elements were recorded. This served the dual purpose of determining the cross-talk of the array and providing a noise frame reference, that has been subtracted from all subsequent measurements. As listed in Table H.3, the nearest neighbour cross-talk level was -22.4 ± 4.5 dB. This is in agreement with previously reported values from 1-D CMUT arrays (Bayram et al. 2007). During imaging, either the rows or columns may be used as transmitters and the other part as receivers. To illustrate the cross-talk between a transmit and a receive event, the average signal on all rows when transmitting with one column at a time was determined. The same was done with the columns when one row at a time was used for transmitting. The resulting transmit-to-receive crosstalk was here -38 ± 3.4 dB as given in Table H.3.

A second setup was established to determine the pulse-echo impulse response of each element. A plane reflector (a 4.1 cm thick PVC plastic material) was positioned 2.5 cm away from and parallel to the transducer surface. Then, 20 realizations of random Gaussian noise was transmitted on one element at a time and received on the transmitting element. The recorded signal was cross-correlated with the excitation signal for each of the

20 realizations, and the 20 results were averaged to yield the pulse-echo impulse response of the respective element (Schroeder 1979). The higher the number of realizations, the closer one gets to a true white signal, so the number of realizations is a compromise between acquisition/processing time and accuracy. In Fig. H.8(a), the impulse response of element no. 96 (the center row element) is shown, in this case using 600 realizations of the Gaussian noise, and the corresponding spectrum is shown in Fig. H.8(b). Note that the deduced impulse response describes the impulse response of the whole system consisting of transducer, front-end electronics, as well as receivers and transmit amplifiers in the SARUS system. It thereby characterizes the impulse response of the actual imaging setup, which may explain the drop in the spectrum amplitude for higher frequencies.

From the spectrum of the impulse response, the center frequency and bandwidth for each element can be found. The center frequency, f_c, was determined by summing all frequencies from 0 to the half the sampling frequency, f_s, weighted by the spectrum amplitude for each frequency, S, and dividing by the sum of the spectrum amplitudes:

$$f_c = \sum_{i=0}^{N/2} \left[S(if_s/N) \cdot if_s/N \right] \Big/ \sum_{i=0}^{N/2} S(if_s/N) \, . \tag{H.1}$$

This yielded a center frequency in immersion of 2.77 ± 0.26 MHz. Since the pitch of the array was 270 µm, see Table H.1, the pitch in units of the wavelength is thereby 0.51, which is very close to the desired pitch of $\lambda/2$. The relative -6 dB bandwidth was determined as the distance in frequency between the -6 dB points in the spectrum relative to the center frequency of the element, yielding a relative bandwidth of 102 ± 10 %. The -6 dB bandwidth is illustrated for element no. 96 in Fig. H.8(b). Fig. H.8(a) also shows the envelope of the impulse response in decibels, computed as the log-compressed absolute values of the analytic signal. The -20 dB and -40 dB pulse duration for this element is seen to be 1.23 µs and 3.06 µs, respectively, corresponding to 3.1 and 7.7 periods at its center frequency of 2.52 MHz.

A third setup was established to determine the transmit pressure of the elements. A HGL-0400 hydrophone connected to a AC-2010 pre-amplifier (Onda Corporation, CA, USA) was placed 7 mm from the transducer surface and scanned over each element using the positioner of the intensity measurement system AIMS-3 (Onda Corporation, CA, USA), while transmitting a 2.5 MHz, 4-cycle sinusoidal signal on the element being measured. The recorded pressure at 7 mm was then compensated to find the pressure at the transducer surface. The compensation was found by a simulation in COMSOL Multiphysics 4.4 (COMSOL AB, Stockholm, Sweden). Here, an element with the same dimensions as the physical elements in the array was set to emit a continuous 2.5 MHz pressure wave, and the pressure magnitude at a distance of 7 mm from the element relative to the pressure magnitude at the element surface was found and used as the compensation factor (9.6). The resulting surface pressure emitted by the elements is seen in Table H.3 to be 590 ± 73 kPa.

Subsequently, the pulse-echo signal from each element against a plane reflector (a 4.1 cm thick PVC plastic material) set at a distance of 7 mm from and parallel to the transducer surface was measured. Once again, a 2.5 MHz 4-cycle sinusoidal excitation pulse was used. The pressure received by the element was deduced by using the pressure measured with the hydrophone setup at a distance of 7 mm from the transducer surface and compensating for the pressure drop from 7 mm to 14 mm (the return trip to the transducer surface) by using the COMSOL Multiphysics simulation described above. This yielded a factor of 0.7, which was used to compensate for the pressure drop. Thereby, the sensitivity of each element could be found by dividing the received voltage signal with the incident pressure (0.7 times the measured pressure). The value of 0.299 ± 0.090 µV/Pa listed in Table H.3 is the signal generated by the transducer itself, i.e. the signal has been reduced to account for the nominal 8.7 dB voltage gain supplied by the pre-amplifiers.

H.4 Imaging

For the imaging experiments, a wire phantom consisting of a steel wire with a diameter of 0.3 mm was used. It was positioned 23 mm away from the transducer array surface and oriented approximately parallel to the rows of the array, but with a 5°–10° angle with respect to the transducer array surface due to alignment inaccuracies. Both the transducer array and the wire phantom was positioned in electrically insulating rapeseed oil as with the measurements described in the previous section. In the following, the azimuth direction is defined as being parallel to the column elements, while the elevation direction is parallel to the row elements.

To image the 3-D volume, synthetic transmit focusing with single element emissions was used. The rows were used as transmitters and the columns as receivers. Each row element was excited with a 2-cycle sinusoidal signal, one row element at a time. The acoustical pressure was for each emission recorded on all 62 receive elements. From each measured data set, the entire 3-D volume was beamformed, creating one low resolution image. Due to the very long elements, a standard delay-and-sum beamformer cannot easily be used to beamform data measured with a row-column addressed array. Instead, beamforming was performed using a custom-made beamformer developed for the predecessor to this paper (Rasmussen et al. 2014), which has been made publicly available (Rasmussen 2014). By summation of each beamformed low resolution image, the final 3-D volume was created. A Hann apodization function was used both in transmit and in receive. The pulse repetition frequency was 20 Hz, the sampling rate was 70 MHz, and data were recorded until a depth of 4 cm was reached. The imaging sequence was identical for the transducer array with both the integrated apodization regions enabled and disabled. As with the previous measurements, a 50 V excitation amplitude and a 80 V DC bias was used.

Two imaging sequences were run: One with the apodization enabled, and one with the apodization disabled. In practice, the disabling of the apodization was achieved

Table H.4: Imaging results

Parameter	Measurement	Simulation	Unit
Lateral FWHM, no apodization	1.79	1.55	mm
Lateral FWHM, with apodization	1.91	1.56	mm
Axial FWHM, no apodization	0.71	0.58	mm
Axial FWHM, with apodization	0.71	0.58	mm
Ghost echo damping	15.8	11.5	dB

by modifying the DC bias supply on the front-end electronics, such that the DC bias voltage seen by the apodized regions of the array became zero. The electro-mechanical coupling efficiency of CMUTs is highly dependent on the DC bias (Yaralioglu et al. 2003), and removing the DC bias should therefore make the contribution from the apodized regions of the array negligible. To evaluate this, the pulse-echo sensitivity of the apodized regions before and after removal of the effective DC bias was measured by performing a pulse-echo measurement with each of the four apodization region electrodes against a plane reflector positioned 7 mm from the transducer surface. The recorded signal with 0 V across the apodization regions was 18 dB lower than the signal with 80 V DC bias, showing that the apodization was considerably suppressed in the 0 V configuration.

The result of the two measurements is seen in Fig. H.9a (apodization disabled) and Fig. H.9b (apodization enabled). Both figures show a cross-section of the wire beamformed with 800×800 points and displayed with a dynamic range of 40 dB. This thereby is a measure of the line spread function (LSF) of the array, i.e. the array's ability to resolve a line source. In Fig. H.9a, where the integrated apodization is disabled, a ghost echo is clearly visible below the main echo. The maximum amplitude of this ghost echo is -22.6 dB relative to the maximum amplitude of the main echo. The lateral and axial full-with-at-half-maximum (FWHM), i.e. the -6 dB resolution, are 1.79 mm and 0.71 mm, respectively. Fig. H.9b shows the result with the integrated apodization enabled, and here the ghost echo is not visible within the 40 dB dynamic range. The amplitude of the signal the same distance from the main echo as the ghost echo in Fig. H.9a is -38 dB relative to the maximum amplitude of the main echo. Thus, the apodization has reduced the amplitude of the ghost echo by 15.8 dB. The lateral and axial FWHM are here 1.91 mm and 0.71 mm, respectively. The axial FWHM is therefore unchanged, while the lateral FWHM is 12 % larger for the apodized measurement. However, this can be attributed to the wire being placed 1 mm further from the center of the array in the apodized measurement due to alignment imperfections.

For comparison, the LSF was simulated in Field II (Jensen 1996; Jensen and Svendsen 1992) using a row-column addressed transducer array closely emulating the real transducer array used for the measurements. The exact same imaging sequence and beamforming technique as in the measurements were used in the simulation. The impulse response

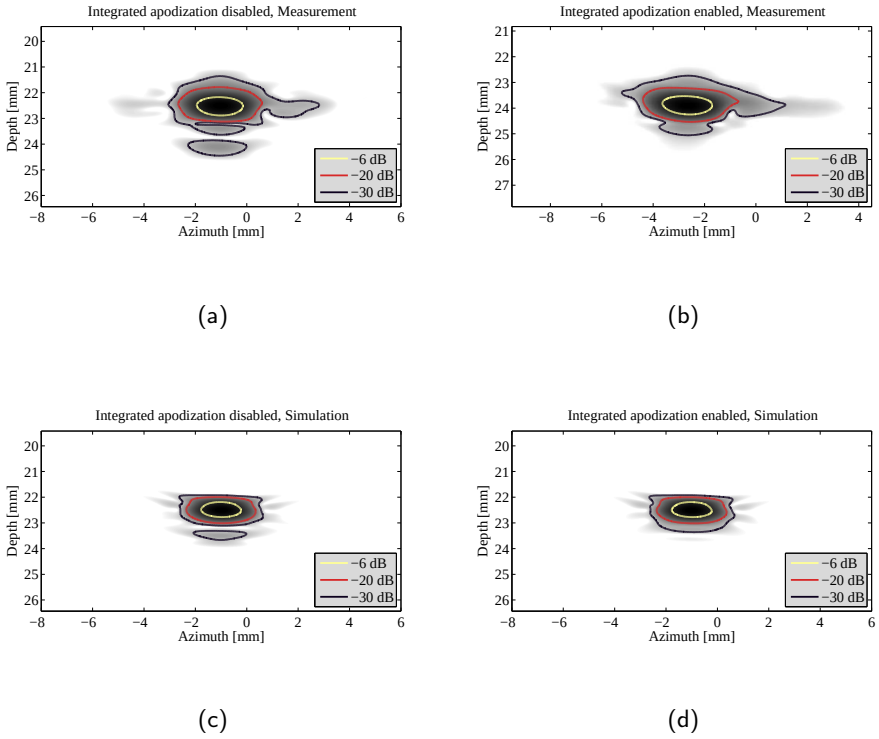

Figure H.9: Measured (a and b) and simulated (c and d) line spread function at a depth of 2.3 cm using dynamic range of 40 dB. a and c show the result with the integrated apodization disabled, while b and d show the result with the integrated apodization enabled. The line spread function was acquired using a line of point scatterers in the simulation, while a 0.3 mm diameter steel wire was used for the measurements. The image was beamformed using full synthetic aperture imaging with 62 single element emissions and data received by 62 receive elements for each emission. The azimuth zero-point is positioned at the center of the array.

estimated for element number 96, shown in Fig. H.8(a), was used in the simulations. The side length of the square CMUT cells in the physical array are approximately $\lambda/8$. Each element in the simulated transducer array was therefore divided into mathematical elements with a side length of $\lambda/2$ across the element width (i.e. the entire element width) and $\lambda/8$ along the length of the element. Each mathematical element was given an apodization value of $\{0, \frac{1}{4}, \frac{1}{2}, \frac{3}{4}, 1\}$ dependent on whether there are 0, 1, 2, 3, or 4 CMUT cells in the real array within the region of each respective mathematical element.

To emulate a wire, 1000 point scatterers were distributed on a line from $(x,y,z) = (-3.3,-1,22.5)$ mm to $(1.3,-1,22.5)$ mm. The point scatterers' amplitude were weighted by a Hann window along the length of the line. This was done to emulate the effect of a real wire object, which reflects less energy back to the array as the angle to the array is increased. Note that the wire used in the simulation (consisting of point scatterers) does not have the same thickness as the wire used in the measurements (having a diameter of 0.3 mm). Thus, the simulation is intended to give a measure of the true LSF, rather than an exact replica of the experimental result.

The result of the simulation is seen in Fig. H.9c (without integrated apodization) and Fig. H.9d (with integrated apodization). The lateral and axial FWHM of the LSF for the simulated array without integrated apodization are 1.55 mm and 0.58 mm, respectively. The corresponding metrics for the LSF of the simulated array with integrated apodization are 1.56 mm and 0.58 mm. Note that, as opposed to the measurements, the wire phantom is placed in exactly the same position in the two simulations (corresponding to the position of the wire during the measurement with the integrated apodization disabled). Therefore, both the axial and lateral FWHM are practically unchanged between the two. The ghost echo is clearly visible in the simulation of the array without integrated apodization (Fig. H.9c), while the integrated apodization is seen to reduce it significantly (Fig. H.9d). The damping of the ghost echo in the simulations is 11.5 dB; a comparison between the experimental and simulated results is seen in Table H.4.

In Fig. H.10, a 3-D rendered image of the wire is shown. Note that the signal from the wire dies out as it crosses the borders of the array. This is partly because the transmitting elements are oriented parallel to the wire, partly because the regions of the wire located outside the array is reflecting the received sound away from the array. The first issue could be addressed by using a phased array technique as proposed in (Rasmussen et al. 2014), while the second issue is related to the nature of the wire used, and will not be seen for a structure behaving like a collection of point scatterers. The latter effect also implies that the front of the emitted single-element plane wave is parallel to the element surface once emitted, but the smooth wire reflects the wave as a mirror in the direction along the wire. Since the wire is not parallel to the transducer array surface, more energy is received at one end of the transducer array than the other. This is seen in Fig. H.10, where the beamformed wire is not symmetric around zero in the elevation direction.

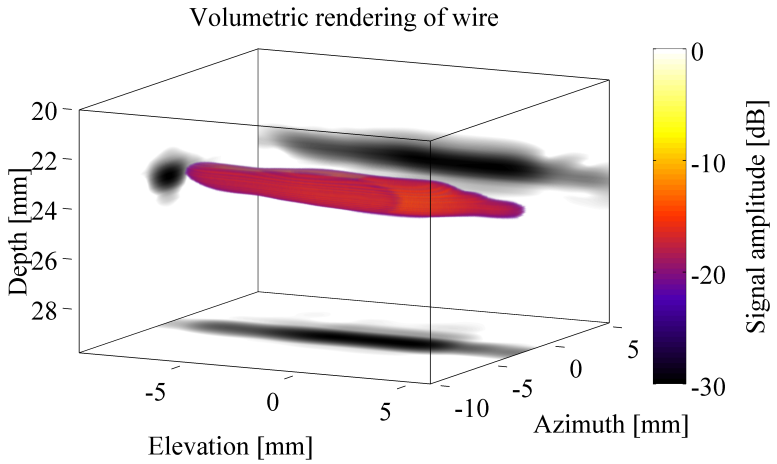

Figure H.10: 3-D beamformed image of the wire shown at a dynamic range of 30 dB. The beamformed image has been projected to the side-walls of the plot in all three dimensions using the same dynamic range. The azimuth and elevation zero-point is positioned at the center of the array.

H.5 Conclusions

In this paper, the first experimental results of a row-column addressed transducer array with integrated apodization was presented. A 23.6 mm by 23.6 mm $62+62$ element capacitive micromachined ultrasonic transducer array with a center frequency in immersion of 2.77 MHz and a $\lambda/2$ element pitch was produced using cleanroom techniques in a five-mask fabrication process. The array incorporated an integrated apodization layout developed by the authors in a previous work. The purpose of the integrated apodization was to reduce the ghost echoes that are otherwise prominent for row-column addressed arrays. Custom front-end electronics were developed to enable transmission and reception on all elements, and the array was characterized using both electrical impedance measurements and acoustical measurements. Thereby, the resonance frequency in air, capacitance, pull-in voltage, impulse response, center frequency, bandwidth, transmit pressure, sensitivity, and cross-talk were determined for all elements. The array was used for volumetric imaging of a 0.3 mm diameter steel wire placed at a depth of 23 mm, both with the integrated apodization enabled and disabled, the latter by removing the effective DC voltage over the apodized regions of the array. The integrated apodization was seen to reduce the ghost echo by 15.8 dB relative to the measurement with the integrated apodization disabled. Simulations in Field II were performed to mimic the experimental setup. The simulations reproduced the effect seen in the measurements with a ghost echo

damping of 11.5 dB.

Acknowledgments

The authors would like to thank Daniel Bøjle (DELTA Dansk Elektronik, Lys & Akustik, Hørsholm, Denmark) for wire-bonding and glob-topping of the array, Jens Christian Jensen for producing the mechanical fixtures and boxes used in the experimental setup, and René Gadkjær for providing help with soldering during modifications of the electronics.

References

Austeng, A. and S. Holm (2002). "Sparse 2-D arrays for 3-D phased array imaging - design methods". In: *IEEE Trans. Ultrason., Ferroelec., Freq. Contr.* 49.8, pp. 1073–1086 (cit. on p. 174).

Bayram, B., M. Kupnik, C. G. Yaralioglu, Ö. Oralkan, A. S. Ergun, D.-S. Lin, S. H. Wong, and B. T. Khuri-Yakub (2007). "Finite element modeling and experimental characterization of crosstalk in 1-D CMUT arrays". In: *IEEE Trans. Ultrason., Ferroelec., Freq. Contr.* 54.2, pp. 418–430. DOI: 10.1109/TUFFC.2007.256 (cit. on p. 187).

Blaak, S., Z. Yu, G. Meijer, C. Prins, C. Lancee, J. Bosch, and N. de Jong (2009). "Design of a micro-beamformer for a 2D piezoelectric ultrasound transducer". In: *Proc. IEEE Ultrason. Symp.* Pp. 1338–1341. DOI: 10.1109/ULTSYM.2009.5441534 (cit. on p. 174).

Brunke, S. S. and G. R. Lockwood (1997). "Broad-bandwidth radiation patterns of sparse two-dimensional vernier arrays". In: *IEEE Trans. Ultrason., Ferroelec., Freq. Contr.* 44.5, pp. 1101–1109 (cit. on p. 174).

Chen, A. I. H., L. L. Wong, A. S. Logan, and J. T. W. Yeow (2011). "A CMUT-based real-time volumetric ultrasound imaging system with row-column addressing". In: *Proc. IEEE Ultrason. Symp.* Pp. 1755–1758 (cit. on p. 175).

Chen, Y., M. Nguyen, and J. T. Yen (2011). "Real-time rectilinear volumetric acquisition with a 7.5 MHz dual-layer array transducer - Data acquisition and signal processing". In: *Proc. IEEE Ultrason. Symp.* Pp. 1759–1761 (cit. on p. 174).

Christiansen, T. L., O. Hansen, M. D. Johnsen, J. N. Lohse, J. A. Jensen, and E. V. Thomsen (2013). "Void-free direct bonding of CMUT arrays with single crystalline plates and pull-in insulation". In: *Proc. IEEE Ultrason. Symp.* Pp. 1737–1740. DOI: 10.1109/ULTSYM.2013.0443 (cit. on p. 180).

Daher, N. M. and J. T. Yen (2004). "Rectilinear 3-D ultrasound imaging using synthetic aperture techniques". In: *Proc. IEEE Ultrason. Symp.* Vol. 2, pp. 1270–1273 (cit. on p. 174).

— (2006). "2-D Array for 3-D Ultrasound Imaging Using Synthetic Aperture Techniques". In: *IEEE Trans. Ultrason., Ferroelec., Freq. Contr.* 53.5, pp. 912–924 (cit. on p. 174).

Davidsen, R. E., J. A. Jensen, and S. W. Smith (1994). "Two-Dimensional Random Arrays for Real Time Volumetric Imaging". In: *Ultrasonic Imaging* 16.3, pp. 143–163 (cit. on p. 174).

Démoré, C. E. M., A. Joyce, K. Wall, and G. Lockwood (2009). "Real-time volume imaging using a crossed electrode array". In: *IEEE Trans. Ultrason., Ferroelec., Freq. Contr.* 56.6, pp. 1252–1261 (cit. on pp. 174, 175).

Halvorsrod, T., W. Luzi, and T. Lande (2005). "A log-domain µbeamformer for medical ultrasound imaging systems". In: *IEEE Trans. Circuits Syst. I, Reg. Papers* 52.12, pp. 2563–2575. DOI: 10.1109/TCSI.2005.857544 (cit. on p. 174).

Huang, Y. L., E. O. Hæggström, X. F. Zhuang, A. S. Ergun, and B. T. Khuri-Yakub (2005). "A solution to the charging problems in capacitive micromachined ultrasonic transducers". In: *IEEE Trans. Ultrason., Ferroelec., Freq. Contr.* 52.4, pp. 578–580. DOI: 10.1109/TUFFC.2005.1428039 (cit. on p. 184).

Huang, Y., A. S. Ergun, E. Hæggström, M. H. Badi, and B. T. Khuri-Yakub (2003). "Fabricating capacitive micromachined ultrasonic transducers with wafer-bonding technology". In: *J. Microelectromech. Syst* 12.2, pp. 128–137 (cit. on p. 178).

Jensen, J. A. (1996). "Field: A Program for Simulating Ultrasound Systems". In: *Med. Biol. Eng. Comp.* 10th Nordic-Baltic Conference on Biomedical Imaging, Vol. 4, Supplement 1, Part 1, pp. 351–353 (cit. on p. 190).

Jensen, J. A., H. Holten-Lund, R. T. Nilsson, M. Hansen, U. D. Larsen, R. P. Domsten, B. G. Tomov, M. B. Stuart, S. I. Nikolov, M. J. Pihl, Y. Du, J. H. Rasmussen, and M. F. Rasmussen (2013). "SARUS: A Synthetic Aperture Real-time Ultrasound System". In: *IEEE Trans. Ultrason., Ferroelec., Freq. Contr.* 60.9, pp. 1838–1852 (cit. on pp. 181, 186).

Jensen, J. A. and N. B. Svendsen (1992). "Calculation of Pressure Fields from Arbitrarily Shaped, Apodized, and Excited Ultrasound Transducers". In: *IEEE Trans. Ultrason., Ferroelec., Freq. Contr.* 39, pp. 262–267 (cit. on p. 190).

Karaman, M., I. O. Wygant, O. Oralkan, and B. T. Khuri-Yakub (2009). "Minimally Redundant 2-D Array Designs for 3-D Medical Ultrasound Imaging". In: *IEEE Trans. Med. Imag.* 7, pp. 1051–1061 (cit. on p. 174).

Kern, W. (1990). "The Evolution of Silicon Wafer Cleaning Technology". In: *J. Electrochem. Soc.* 137.6, pp. 1887–1892 (cit. on p. 179).

Logan, A. S., L. L. P. Wong, A. I. H. Chen, and J. T. W. Yeow (2011). "A 32 x 32 element row-column addressed capacitive micromachined ultrasonic transducer". In: *IEEE Trans. Ultrason., Ferroelec., Freq. Contr.* 58.6, pp. 1266–1271 (cit. on p. 175).

Logan, A. S., L. L. P. Wong, and J. T. W. Yeow (2009). "2-D CMUT wafer bonded imaging arrays with a row-column addressing scheme". In: *Proc. IEEE Ultrason. Symp.* Pp. 984–987 (cit. on p. 175).

Morton, C. E. and G. R. Lockwood (2003). "Theoretical assessment of a crossed electrode 2-D array for 3-D imaging". In: *Proc. IEEE Ultrason. Symp.* Pp. 968–971 (cit. on p. 174).

Oralkan, Ö., A. S. Ergun, J. A. Johnson, M. Karaman, U. Demirci, K. Kaviani, T. H. Lee, and B. T. Kuri-Yakub (2002). "Capacitive micromachined ultrasonic transducers: Next-generation arrays for acoustic imaging?" In: *IEEE Trans. Ultrason., Ferroelec., Freq. Contr.* 49, pp. 1596–1610 (cit. on p. 186).

Rasmussen, M. F. (2014). *A Row-column beamformer*. URL: `www.rc-beamformer.mofi.dk` (cit. on p. 189).

Rasmussen, M. F., T. L. Christiansen, E. V. Thomsen, and J. A. Jensen. "Ultrasound Imaging Transducer Array with Integrated Apodization". PCT/IB2013/002838 (cit. on p. 175).

— (2014). "3-D Imaging with Row-Column Addressed Arrays: Transducer-Integrated Apodization and Line-element Beamforming". In: *IEEE Trans. Ultrason., Ferroelec., Freq. Contr.* Submitted (cit. on pp. 175, 177, 186, 189, 192).

Rasmussen, M. F. and J. A. Jensen (2013a). "3-D Ultrasound Imaging Performance of a Row-Column Addressed 2-D Array Transducer: A Measurement Study". In: *Proc. IEEE Ultrason. Symp.* Pp. 1460–1463 (cit. on p. 174).

— (2013b). "3D ultrasound imaging performance of a row-column addressed 2D array transducer: a simulation study". In: *Proc. SPIE Med. Imag.* 86750C, pp. 1–11 (cit. on p. 175).

Sampaleanu, A., P. Zhang, A. Kshirsagar, W. Moussa, and R. Zemp (2014). "Top-orthogonal-to-bottom-electrode (TOBE) CMUT arrays for 3-D ultrasound imaging." In: *IEEE Trans. Ultrason., Ferroelec., Freq. Contr.* 61.2, pp. 266–276. DOI: `10.1109/TUFFC.2014.6722612` (cit. on p. 175).

Savoia, A. S., G. Caliano, and M. Pappalardo (2012). "A CMUT Probe for Medical Ultrasonography: From Microfabrication to System Integration". In: *IEEE Trans. Ultrason., Ferroelec., Freq. Contr.* 59.6, pp. 1127–1138 (cit. on p. 182).

Savord, B. and R. Solomon (2003). "Fully sampled matrix transducer for real time 3D ultrasonic imaging". In: *Proc. IEEE Ultrason. Symp.* Vol. 1, pp. 945–953 (cit. on p. 174).

Schroeder, M. R. (1979). "Integrated-impulse method measuring sound decay without using impulses". In: *J. Acoust. Soc. Am.* 66.2, pp. 497–500 (cit. on p. 188).

Seo, C. H. and J. T. Yen (2006). "64 x 64 2-D array transducer with row-column addressing". In: *Proc. IEEE Ultrason. Symp.* Vol. 1, pp. 74–77 (cit. on p. 174).

— (2007). "256 x 256 2-D array transducer with row-column addressing for 3-D imaging". In: *Proc. IEEE Ultrason. Symp.* Pp. 2381–2384 (cit. on p. 174).

— (2008). "Recent results using a 256 x 256 2-D array transducer for 3-D Rectilinear Imaging". In: *Proc. IEEE Ultrason. Symp.* Vol. 1-4, pp. 1146–1149 (cit. on p. 174).

— (2009). "A 256 x 256 2-D array transducer with row-column addressing for 3-D rectilinear imaging". In: *IEEE Trans. Ultrason., Ferroelec., Freq. Contr.* 56.4, pp. 837–847 (cit. on p. 174).

Ventsel, E. and T. Krauthammer (2001). *Thin plates and shells: theory, analysis, and applications*. Dekker (cit. on pp. 176, 184).

Yaralioglu, G. G., A. S. Ergun, B. Bayram, E. Hæggström, and B. T. Khuri-Yakub (2003). "Calculation and measurement of electromechanical coupling coefficient of capacitive micromachined ultrasonic transducers". In: *IEEE Trans. Ultrason., Ferroelec., Freq. Contr.* 50.4, pp. 449–456. DOI: 10.1109/TUFFC.2003.1197968 (cit. on p. 190).

Yen, J. T., C. H. Seo, S. I. Awad, and J. S. Jeong (2009). "A dual-layer transducer array for 3-D rectilinear imaging". In: *IEEE Trans. Ultrason., Ferroelec., Freq. Contr.* 56.1, pp. 204–212 (cit. on p. 174).

Yen, J. T., J. P. Steinberg, and S. W. Smith (2000). "Sparse 2-D array design for real time rectilinear volumetric imaging". In: *IEEE Trans. Ultrason., Ferroelec., Freq. Contr.* 47.1, pp. 93–110 (cit. on p. 174).

Yen, J. T. (2013). "Beamforming of sound from two-dimensional arrays using spatial matched filters". In: *J. Acoust. Soc. Am.* 134.5, pp. 3697–704. DOI: 10.1121/1.4821988 (cit. on p. 174).

Zemp, R. J., W. Zheng, and P. Zhang (2011). "Feasibility of Top-Orthogonal-to-Bottom Electrode (TOBE) 2D CMUT arrays for low-channel-count 3D imaging". In: *Proc. IEEE Ultrason. Symp.* Pp. 498–502 (cit. on p. 174).

Zhang, P., G. Fitzpatrick, T. Harrison, W. A. Moussa, and R. J. Zemp (2012). "Double-SOI Wafer-Bonded CMUTs With Improved Electrical Safety and Minimal Roughness of Dielectric and Electrode Surfaces". In: *J. Microelectromech. Syst.* 21.3, pp. 668–680 (cit. on p. 178).

Patent Application

PATENT APPLICATION A

Ultrsound Imaging Transducer Array with Integrated Apodization

Authors Morten Fischer Rasmussen, Thomas Lehrmann Christiansen, Erik Villain Thomsen, and Jørgen Arendt Jensen.

File date December 19, 2013

Number PCT/IB2013/002838

A.1 Technical Field

The following generally relates to a transducer array and more particularly to an ultrasound imaging transducer array with integrated apodization.

A.2 Background

Ultrasound imaging has been used to determine information about the interior characteristics of an object or a subject. Generally, an ultrasound imaging system includes a transducer array and components for at least generating and transmitting ultrasound waves, receiving echoes or reflected waves, processing the received signal, generating images, and displaying the images. The transducer array may include a one-dimensional (1D) array of elements or a two-dimensional (2D) transducer array of elements.

For three dimensional (3D) imaging with a 2D transducer array, the elements can be addressed element-wise where each element is individually addressed. Alternatively, the elements can be addressed group-wise, e.g., using row-column addressing. In a configuration in which each element is individually addressed, an NxN array of elements would require NxN (or N2) electrical connections and channels to fully address the array. With row-column addressing, an NxN array of elements can be operated using 2N electrical connections and channels to fully address the array. As such, the row-column addressing approach can simplify fabrication of the transducer array, for example, due to the reduced number of electrical interconnects to the transducer array (e.g., from NxN to 2N). Furthermore, the data bandwidth requirements are also reduced. Unfortunately, the row-column addressing approach may introduce ghost artifact in the images, for example,

because of the significant element height, the lack of an acoustic lens, and the lack of electronic control along the length of the row/column elements.

A non-limiting example of row-column addressing of a 2D transducer array 100 is shown in Figures 1 and 2. In Figure 1, each 1D array 102, 104, and 106 of elements (three elements in the illustrated embodiment) in a first direction (y in the illustrated embodiment) respectively is excited with a single pulse 108, 110, and 112 in transmit. In Figure 2, a single signal 202, 204, and 206 respectively is produced for each 1D array 208, 210, and 212 of elements (three elements in the illustrated embodiment) in a second different direction (x in the illustrated embodiment, where x is transverse to y) in receive.

Figures 3, 4, 5, 6, and 7 provide an example of ghost artifact originating during both receive and transmit in connection with the 1D arrays 208-212 of Figure 2. For sake of brevity, this example is described with respect to the array 208 in receive. However, the same edge effect arises in transmit due to the receive/transmit reciprocity of the sound field. In Figure 3, when an emitted waveform is reflected by a point scatterer 304, the reflected wave will have the shape of a sphere 300. At a first time 306 thereafter, the reflected spherical wave 300 intersects only a first subset 308 of elements of the array 208 of the 1D array. Figure 4 shows the response 402 of the 1D array and the corresponding output signal 404, which is a sum of the measured signals, which are approximately in phase, producing a strong output signal.

Returning to Figure 3, subsequently, at time 310, the reflected wave 300 intersects with a second subset 312 of elements of the array 208. Where the amplitude of the transmit waveform is symmetric around zero, which it typically is in at least medical ultrasound, the integration of the output is close to zero. Figure 5 shows the response 502 of the array 208 and the corresponding output signal 504 at time 310. Returning to Figure 3, subsequently, at time 314, the reflected wave crosses edges 316. Figure 6 shows the response 602 of the array 208 and the corresponding output signal 604 at time 314.

From the above, during receive, a point scatterer will receive three pressure waves: one main wave and one from each edge of the 1D array. Each of these three waves is reflected and each generates three signals during receive: One main, and one at each edge of the 1D array. Thus, a total of nine signals are generated from one point scatterer. However, only one of these is of interest (the main echo, i.e. the shortest distance from the array to the point scatterer). The remaining eight echoes are artifacts that, in general, are seen as ghosts (three pairs and two single). Where the point scatterer is located directly above the center of the 1D array (the scenario shown in FIGURE 3), the number of ghosts collapses to two (each containing four of the eight artifacts). This is shown in Figure 7, which shows a main wave 702, and two ghost waves 704 and 706. In the example shown in Figure 3-7, row-column addressing results in a main lobe at the center at 0 dB, and, beneath it, two ghosts as a result of edge effects on the long row and column elements. Unfortunately, the ghosts introduce artifact, degrading image quality.

A.3 Summay

Aspects of the application address the above matters, and others. In one aspect, a transducer array includes at least one 1D array of transducing elements. The at least one 1D array of transducing elements includes a plurality of transducing elements. A first of the plurality of transducing elements has a first apodization and a second of the plurality of transducing elements has a second apodization. The first apodization and the second apodization are different. The transducer array further includes at least one electrically conductive element in electrical communication with each of the plurality of transducing elements. The transducer array further includes at least one electrical contact in electrical communication with the at least one electrically conductive element. The at least one electrical contact concurrently addresses the plurality of transducing elements through the at least one electrically conductive element. In another aspect, a method includes transmitting an ultrasound waveform with a transducer array that includes apodization that is integrated into physical elements of the transducer array. The method further includes receiving a reflected wave with the transducer array. The method further includes processing the received reflected wave to generate at least one image. In another aspect, an ultrasound imaging system includes a transducer array with an array-wise addressable array of elements that includes at least two elements with a different apodization. The apodization is one of a fixed area controlled apodization, a dynamic area controlled apodization, a fixed bias controlled apodization, or a dynamic bias controlled apodization. The ultrasound imaging system further includes transmit circuitry that conveys an excitation pulse to the transducer array. The ultrasound imaging system further includes receive circuitry that receives a signal indicative of an ultrasound echo from the transducer array. The ultrasound imaging system further includes a beamformer that processes the received signal, generating ultrasound image data. Those skilled in the art will recognize still other aspects of the present application upon reading and understanding the attached description.

A.4 Brief Description of the Drawings

The application is illustrated by way of example and not limited by the figures of the accompanying drawings, in which like references indicate similar elements and in which:

Figure 1 schematically illustrates prior art row or column addressing for transmit or receive in connection with a 2D transducer array;

Figure 2 schematically illustrates prior art column or row addressing for receive or transmit in connection with a 2D transducer array;

Figure 3 schematically illustrates prior art interaction of a wave reflected by a point scatterer with a 1D array of a 2D transducer array at three different points in time;

Figure 4 graphically illustrates a prior art response and output of the 1D array of Figure 3 at a first of the three points in time;

Figure 5 graphically illustrates a prior art response and output of the 1D array of Figure 3 at a second of the three points in time;

Figure 6 graphically illustrates a prior art response and output of the 1D array of Figure 3 at a third of the three points in time;

Figure 7 graphically illustrates a main lobe and ghost lobes in connection with the prior art row-column addressing of Figures 1-6;

Figure 8 schematically illustrates an example ultrasound imaging system with a transducer array with integrated apodization;

Figure 9 schematically illustrates an example of fixed area controlled apodization in connection with rectangular piezoelectric elements;

Figure 10 schematically illustrates an example of fixed area controlled apodization in connection with rectangular and triangular piezoelectric elements;

Figure 11 schematically illustrates an example of dynamic area controlled apodization in connection with a piezoelectric 2D transducer array;

Figure 12 schematically illustrates an example of a CMUT 2D transducer array.

Figure 13 schematically illustrates an example of fixed area controlled apodization in connection with a CMUT 2D transducer array;

Figure 14 schematically illustrates an example of dynamic area controlled apodization in connection with a CMUT 2D transducer array;

Figure 15 schematically illustrates an example of bias controlled apodization in connection with a CMUT 2D transducer array;

Figure 16 schematically illustrates an example of area apodization with nine apodization levels that are set as a rotationally symmetric 2D Hann window;

Figure 17 schematically illustrates an example mask layout for the apodization of Figure 16;

Figure 18 illustrates an example of integrated fixed area apodization enabling homogeneous rectilinear imaging with optional beam steering;

Figure 19 graphically illustrates a main lobe in connection with the row-column addressing of Figures 8 and 17;

Figure 20 illustrates a method in accordance with the embodiments discussed herein; and

Figure 21 illustrates an example mask layout for a CMUT using the apodization described in connection with Figure 18.

A.5 Detailed Description

Figure 8 schematically illustrates an example ultrasound imaging system 800. The ultrasound imaging system 800 includes a transducer array 802 that includes at least one 1D array of transducing elements 804. The at least one 1D array of transducing elements 804 is configured to transmit ultrasound signals when in transmit mode and receive echoes, reflected waveforms, etc. when in receive mode. In one non-limiting

instance, the at least one 1D array of transducing elements 804 includes a 2D array of two or more 1D arrays. An example 2D array includes a 16x16 array, a 32x32 array, a 64x64 array, a larger array, or a smaller array. In another embodiment, the at least one 1D array of transducer elements 804 includes a non-square array such as rectangular, circular array, and/or other shaped arrays. In yet another instance, the array of transducing elements 804 includes only a single 1D array of transducing elements.

As described in greater detail below, the at least one 1D array of transducer elements 804 includes integrated apodization, or apodization that is integrated in and part of the physical transducing elements themselves. In one instance, the integrated apodization, e.g., weights end or peripheral regions of each 1D array of transducing elements lower than other regions (e.g., more central regions) of the at least one 1D array of transducer elements 804. This may reduce or mitigate the artifacts such as the ghost artifacts such as from the edges of a transducer array as discussed in connection with Figures 3-7 and/or other artifacts. Examples of such apodization include, but are not limited to, area (fixed and dynamic) and/or voltage bias (fixed and dynamic) controlled apodization. These approaches can be used with different types of transducing elements such as piezoelectric, capacitive micro machined ultrasonic transducer (CMUT), and/or other transducing elements.

Transmit circuitry 806 generates pulses that excite a predetermined set of addressed 1D arrays of the at least one 1D array of transducer elements 804 to emit one or more ultrasound beams or waves into a scan field of view. Receive circuitry 808 receives echoes or reflected waves, which are generated in response to the transmitted ultrasound beam or wave interacting with (stationary and/or flowing) structure in the scan field of view, from a predetermined set of addressed arrays of the at least one 1D array of transducer elements 804. A switch 810 switches between the transmit circuitry 806 and the receive circuitry 808, depending on whether the transducer array 802 is being operated in transmit or receive mode. In transmit mode, the switch 810 electrically connects the transmit circuitry 806 to the at least one 1D array of transducer elements 804. In receive mode, the switch 810 electrically connects the receive circuitry 808 to the at least one 1D array of transducer elements 804.

A beamformer 812 processes the received echoes, for example, by applying time delays and weights, summing, and/or otherwise processing the received echoes. In one non-limiting instance, the beamformer 812 includes a single sub-beamformer for each of the at least one 1D array of transducer elements 804. In another instance, more than a single sub-beamformer can be used with a 1D array and/or a single sub-beamformer can be used two more of the 1D arrays. A scan converter 814 scan converts the beamformed data, converting the beamformed data (e.g., images) into the coordinate system of a display 816, which visually displays the data. In one instance, the data is visually displayed in an interactive graphical user interface (GUI), which allows the user to selectively rotate, scale, and/or manipulate the displayed data through a mouse, a keyboard, touch-screen controls, etc.

A controller 818 controls one or more of the components of the system 800 such as at

least one of the transmit circuitry 806 or receive circuitry 806, the switch 810 based on whether the at least one 1D array of transducer elements 804 is transmitting or receiving, etc. Such control can be based on available modes of operation (e.g., B-mode, C-mode, Doppler, etc.) of the system 800. A user interface 820 includes include one or more input devices (e.g., a button, a knob, a slider, a touch pad, etc.) and/or one or more output devices (e.g., a display screen, lights, a speaker, etc.). A particular mode, scanning, and/or other function can be activated by one or more signals indicative of input from the user interface 820. The user interface 820 can also be used to set and/or change parameters such as imaging parameters, processing parameters, display parameters, etc.

In one instance, the transducer array 802 is part of a probe and the transmit circuitry 806, the receive circuitry 808, the switch 810, the beamformer 812, the scan converter 814, the controller 818, the user interface 820, and the display 816 are part of a console. Communication there between can be through a wired (e.g., a cable and electro-mechanical interfaces) and/or wireless communication channel. In this instance, console can be similar to a portable computer such as a laptop, a notebook, etc., with additional hardware and/or software for ultrasound imaging. The console can be docked to a docketing station and used.

Alternatively, the console can be part (fixed or removable) of a mobile or portable cart system with wheels, casters, rollers, or the like, which can be moved around. In this instance, the display 816 may be separate from the console and connected thereto through a wired and/or wireless communication channel. Where the cart includes a docking interface, the laptop or notebook computer type console can be interfaced with the cart and used. An example of a cart system where the console can be selectively installed and removed is described in US publication 2011/0118562 A1, entitled "Portable ultrasound scanner," and filed on November 17, 2009, which is incorporated herein in its entirety by reference.

Alternatively, the transducer 802, the transmit circuitry 806, the receive circuitry 808, the switch 810, the beamformer 812, the scan converter 814, the controller 818, the user interface 820, and the display 816 are all housed and enclosed within a hand-held ultrasound apparatus, with a housing that mechanically supports and/or shields the components within. In this instance, the transducer 802 and/or display 816 are also part of the housing, being structurally integrated or part of a surface or end of the hand-held ultrasound apparatus. An example of a hand-held device is described in US patent 7,699,776, entitled "Intuitive Ultrasonic Imaging System and Related Method Thereof," and filed on March 6, 2003, which is incorporated herein in its entirety by reference.

As briefly discussed above, the at least one 1D array of transducer elements 804 includes integrated apodization, including, but not limited to, fixed area controlled apodization, dynamic area controlled apodization, fixed bias controlled apodization, and dynamic bias controlled apodization. Non-limiting examples of each of these are discussed below.

Figures 9, 10, and 11 show examples of area controlled apodization where the transducer array 802 includes a piezoelectric transducer array. Figure 9 illustrates fixed area controlled apodization where the elements include rectangular elements. Figure 10 il-

lustrates fixed area controlled apodization where the elements include rectangular and non-rectangular elements. Figure 11 illustrates dynamic area controlled apodization. Generally, area-controlled apodization refers to apodization that is based on a physical area of a transducing surface of each element of each of the at least one 1D array of transducer elements 804. With area controller apodization, the transmit pressure and the signal generated during receive for each transducing element scale with the physical surface area of the transducing element.

For sake of clarity and explanatory purposes, a first direction 900 of the array 802 is referred to herein as a row, and a second direction 902 of the array 802 is referred to herein as a column, and the first direction is considered the transmit direction, and the second direction is considered the receive direction. However, the directions 900 and 902 respectively can alternatively refer to the column and the row and/or receive and transmit. In general, the first direction 900 and the second direction 902 are different directions, approximately perpendicular, as shown in Figure 9, or otherwise angularly offset. Furthermore, transmit and/or receive can be performed in more than one direction.

Initially referring to Figure 9, the transducer array 802 includes NxM transducing elements 904 (or elements $904_{1,1}$, ..., $904_{N,M}$, where N and M are positive integers). In one instance, N = M. In another instance, N $\neq$ M. The transducer array 802 further includes N electrical contacts 906_1, ..., 906_N, and M electrical contacts 908_1, ..., 908_M.

The array 902 further includes an electrically conductive element 910_1 that electrically connects the electrical contact 906_1 to each of the elements $904_{1,1}$, ..., $904_{1,M}$, forming a row line element 912_1. Likewise, electrically conductive elements 910_2, 910_3, 910_4, ...910_N, respectively electrically connect the electrical contacts 906_2, 906_3, 906_4, ...906_N to the elements $904_{2,1}$, ..., $904_{2,M}$, $904_{3,1}$, ..., $904_{3,M}$, $904_{4,1}$, ..., $904_{4,M}$, ...$904_{N,1}$, ..., $904_{N,M}$, forming row line elements 912_2, 912_3, 912_4, ..., 912_N.

Each of the row line element 912_1, 912_2, 912_3, 912_4, ..., 912_N is addressed via the corresponding electrically conductive element 906_1, 906_2, 906_3, 906_4, ...906_N. For example, an excitation signal at the electrically conductive element 906_1 excites the entire row line element 912_1, or the elements $904_{1,1}$, ..., $904_{1,M}$, ..., an excitation signal at the electrically conductive element 906_N excites the entire row line element 912_N, or the elements $904_{N,1}$, ..., $904_{N,M}$. In another example, receiving a signal from the electrically conductive element 906_1 receives signals from the entire row line element 912_1, or the elements $904_{1,1}$, ..., $904_{1,M}$, ..., receiving a signal from the electrically conductive element 906N receives signals from the entire row line element 912_N, or the elements $904_{N,1}$, ..., $904_{N,M}$.

The array 902 further includes an electrically conductive element 914_1 that electrically connects the electrical contact 908_1 to each of the elements $904_{1,1}$, ..., $904_{N,1}$, forming a column line element 916_1. Likewise, electrically conductive elements 914_2, 914_3, 914_4, ...914_M, respectively electrically connect the electrical contacts 908_2, 908_3, 908_4, ...908_N to the elements $904_{2,1}$, ..., $904_{2,M}$, $904_{3,1}$, ..., $904_{3,M}$, $904_{4,1}$, ..., $904_{4,M}$, ...$904_{N,1}$, ..., $904_{N,M}$, forming column line elements 916_2, 916_3, 916_4, ..., 916_N.

Each of the column line element 916_1, 916_2, 916_3, 916_4, ..., 916_M is addressed via

the corresponding electrically conductive element 908_1, 908_2, 908_3, 908_4, ...908_M. For example, an excitation signal at the electrically conductive element 908_1 excites the entire column line element 916_1, or the elements $904_{1,1}$, ..., $904_{N,1}$, ..., an excitation signal at the electrically conductive element 908_M excites the entire column line element 916_M, or the elements $904_{1,M}$, ..., $904_{N,M}$. In another example, receiving a signal from the electrically conductive element 908_1 reads signal from the entire column line element 916_1, or the elements $904_{1,1}$, ..., $904_{N,1}$, ..., receiving a signal from the electrically conductive element 908_M reads signals from the entire column line element 916_M, or the elements $904_{1,M}$, ..., $904_{N,M}$.

A first group 918 of elements at a central region of the array 802 each have a first area A1 (W1*L1). A second group 920 of sub-elements (which excludes the first group 918) disposed along a perimeter or periphery of the array 802 each have a second area A2 (W2*L2). A third group of sub-elements 922 disposed at the corners of the array 802 each have a third area A3 (W3*L3). However, this configuration is not limiting. For example, in another embodiment, there may be more or less groups and/or different groups. Furthermore, in Figure 9, the elements for all three of the groups 918, 920 and 922 is rectangular or square, and, in another embodiment, at least one of the sub-elements is otherwise shaped, such as circular, elliptical, triangular, hexagonal, etc.

In the illustrated embodiment, W1 > W2 $\approx$ W3 and L1 $\approx$ L2 > L3, However, this configuration is not limiting. Generally, the width (W) and length (L) of each element is such that A1 > A2 >. A3. The pressure output (the transmitted pressure), transmitted in response to an excitation signal (e.g., a voltage pulse) of an element with an area A (or W*L) is P. As such, the pressure output, due to excitation signal, of the elements of the first group 918, which have an area A1, is P1. The pressure output, due to excitation signal, of the elements of the second group 920, which have an area A2, is P2, where P2 = αP1, where α = A2/A1. The pressure output, due to excitation signal, of the elements of the third group, which have an area A3, is P3, where P3 = βP1, where β = A3/A1.

The signal output, generated by an element in response to an incident acoustical wave impinging thereon, for an element with an area A is S. As such, the signal output, due to an impinging acoustical wave, of the elements of the first group 918, which have an area A1, is S1. The signal output, due to an impinging acoustical wave, of the elements of the second group 920, which have an area A2, is S2, where S2 = αS1, where α = A2/A1. The signal output, due to an impinging acoustical wave, of the elements of the third group 922, which have an area A3, is S3, where S3 = βS1, where β = A3/A1.

With this configuration, the transmit pressure and/or the signal generated during transmit and receive scale with the transducing area of each element. In the illustrated embodiment, the scaling scales down the transmit pressure and the signal generated during receive going from the first group 918, to the second group 920, to the third group 922 of elements. Thus, a particular row line element or column line element includes fixed discrete area controlled apodization. Such apodization effectively down weights the output pressure transmitted by (during transmit) and the electrical signal generated by (during receive) at the ends of each row and/or column line element, mitigating or

reducing ghost artifact introduced by the edge elements.

The configuration shown in Figure 9, can be formed by through dicing, screen-printing (where the layout of each cell is defined by a mask), and/or other approach. Dicing is well suited for creating the rectangular sub-elements shown in Figure 9. As the resonance frequency of piezo-elements is given by the height, the area can be freely adjusted without altering the operating frequency of each sub-element. This configuration allows for varying the transmitted/received signal of a single line element. For transmit, the amplitude of the excitation pulses need not be varied, so a fixed excitation pulse waveform at a single amplitude can be used. Only phase control is required to allow focusing and steering of the beam.

Figure 10 schematically illustrates a variation of the transducer array 802 in Figure 9 in which the geometry of the second group 920 of elements is not rectangular, and the apodization linearly scales (rather than discretely scales) the output pressure transmitted by (during transmit) and the electrical signal generated by (during receive) of the elements of the periphery. This is achieved in this example through a triangular geometry of the second group 920 of elements in which the apodization decreases in a direction towards the periphery. Again, other geometries, such as hexagonal, irregular, circular, etc. are also contemplated herein. Screen-printing is well suited for such shapes. The configuration of Figure 10 also does not include the third group 922, or corner elements 904_1,1, 904N,1, 904_1,M, and 904N,M. In another variation, the apodization can scale in a non-linear manner, for example, where the geometry of the outer sub-elements in a non-linear. Furthermore, the first group 916 can also have non-linear geometries.

Figure 11 shows an example of dynamic area controlled apodization for a single one of the elements 904 of the transducer array 802. In Figure 11, the single element 904 includes a 3x3 arrangement of piezo sub-elements 1102, including a first row 1104_1 of sub-elements 1102, a second row 1104_2 of sub-elements 1102, and a third row 1104_3 of sub-elements 1102, each row including three sub-elements 1102, and a first column 1106_1 of sub-elements 1102, a second column 1106_2 of sub-elements 1102, and a third column 1106_3 of sub-elements 1102, each column including three sub-elements 1102.

A row electrode 1108 is in electrical communication with the sub-elements 1102 of the second row 1104_2. A first plurality of switches 1110 and 1112 respectively selectively electrically connect the sub-elements 1102 of the first row 1104_1 and the sub-elements 1102 of the third row 1104_3 to the row electrode 1108. As such, the area of the illustrated element 904 can be dynamically changed, row-wise, between three different discrete area levels. The levels include: only the second row 1104_2; the second row 1104_2 and either the first row 1104_1 or the third row 1104_3, and all three rows.

A column electrode 1114 is in electrical communication with the sub-elements 1102 of the second column 1106_2. A second plurality of switches 1116 and 1118 respectively selectively electrically connect the sub-elements 1102 of the first column 1106_1 and the sub-elements 1102 of the third column 1106_3 to the column electrode 1114. As such, the area of the illustrated element 904 can be dynamically changed, column-wise, between three different discrete area levels. The levels include: only the second row 1106_2; the

second row 1106_2 and either the first row 1106_1 or the third row 1106_3, and all three rows.

Combining the switching of the rows and columns, the area of the illustrated element 904 can be dynamically changed between nine different discrete area levels. This includes only the central sub-elements 1102 up to all of the sub-elements 1102.

Generally, if the number of enabled switches in row i is denoted ki and the number of enabled switches in column j is denoted kj, the area apodization A of element (i; j) is A(i; j) = ki x kj. Any separable 2-D function can be implemented as an apodization function. The number of switches per row or column for k x k cells per element can in principle be reduced to 2k - 2, as this – together with the possibility of not reading out the signal from a row or column – allows any number of cells in a given element to be active.

Figures 12, 13, and 14 shows examples of area controlled apodization where the transducer array 802 includes a CMUT transducer array. Figure 12 shows a sub-portion of a CMUT transducer array 802. Figure 13 shows an example of fixed area controlled apodization. Figure 14 shows an example of dynamic area controlled apodization.

In Figure 12, the sub-portion of the transducer array 802 includes two line elements 1202 and 1204 in one direction 1206 and four line elements 1208, 1210, 1212 and 1214 in a different direction 1216. An element 904 includes XxY cells 1218, where X and Y are positive integers, and X = Y or X $\neq$ Y. Different elements 904 may have the same or a different number of cells 1218.

In Figure 13, X = Y = 5, arranged as a 5x5 matrix, or 25 elements 904. For sake of clarity and explanatory purposes, only reference numerals for a single element 904 and a single cell 1218 of the element 904 are provided. For the other components, the description of Figure 9 can be referenced. In Figure 13, the transducing area of each element 904 is fixed by the number of cells 1218 which populate the element 904. That is, an element 904 with twice the number of cells 1218 as another element 904 will have twice the transducing area as the other element 904.

By way of example, for the row line element 912_1, element 1,1 includes a single cell 1218, element 1,2 includes two cells 1218, the element 1,3 includes three cells 1218, element 1,4 includes two cells 1218, and element 1,5 includes one cell 1218. As such, the elements 1,2 and 1,3 have twice the transducing area as the elements 1,1 and 1,4, and the element 1,3 has three times the transducing area as the elements 1,1 and 1,4. In this embodiment, a similar pattern is followed for the column line element 916_1. That is, the element 1,1 includes a single cell 1218, element 2,1 includes two cells 1218, element 3,1 includes three cells 1218, element 4,1 includes two cells 1218, and element 5,1 includes one cell 1218.

As shown in the illustrated embodiment, the center element 3,3 includes nine cells 1218. The elements (element 3,2; element 2,3; element 4,3; element 3,4) adjacent to the center element 3,3 each include five cells 1218. The elements (element 2,2; element 4,2; element 2,4; element 4,4) at the corners of the element 3,3 each include four cells 1218. The elements along the periphery and at the corners include less than four cells 1218. With this configuration, the apodization rolls off from the center element 3,3 to the edge elements as a function of a distance from the center element 3,3 to each of the

other elements 904. Again, this has the effect of down waiting the edge sub-elements, mitigating ghost artifact introduced thereby. The geometry of each element 904 can be the same or different.

Generally, a size of each cell 1218 is determined by the desired fundamental resonant frequency of the transducer array 802. The active or transducing area of an element 904 is adjusted by varying the number of cells 1218 per element 904. With the geometry in Figure 13, the element 3,3 has nine (9) discrete apodization levels, and the other elements 907 have less than nine discrete apodization levels, or a number of discrete apodization levels determined by the number of cells 1218. A given transducer element 904 pitch and cell 1218 pitch defines a maximum number of cells per element 904, and the apodization profile is discretized into a number of levels equal to the maximum number of cells per element 904.

Figure 14 shows an example of dynamic area controlled apodization. In Figure 14, a single element 904 includes a 3x3 arrangement of CMUT cells 1218, including a first row 1402_1 of CMUT cells 1218, a second row 1402_2 of CMUT cells 1218, and a third row 1402_3 of CMUT cells 1218, each row including three CMUT cells 1218, and a first column 1404_1 of CMUT cells 1218, a second column 1404_2 of CMUT cells 1218, and a third column 1404_3 of CMUT cells 1218, each column including three CMUT cells 1218.

A row electrode 1406 is in electrical communication with the cells of the second row 1402_2. A first plurality of switches 1408 and 1410 respectively selectively electrically connect the cells of the first row 1402_1 and the cells of the third row 1402_3 to the row electrode 1406. As such, the area of the illustrated element 904 can be dynamically changed, row-wise, between three different discrete area levels. The levels include: only the second row 1402_2; the second row 1402_2 and either the first row 1402_1 or the third row 1102_3, and all three rows.

A column electrode 1416 is in electrical communication with the cells of the second column 1404_2. A second plurality of switches 1412 and 1414 respectively selectively electrically connect the cells of the first column 1404_1 and the cells of the third column 1404_3 to the column electrode 1416. As such, the area of the illustrated element 904 can be dynamically changed, column-wise, between three different discrete area levels. The levels include: only the second row 1404_2; the second row 1404_2 and either the first row 1404_1 or the third row 1404_3, and all three rows.

Combining the switching of the rows and columns, the area of the illustrated element 904 can be dynamically changed between nine different discrete area levels. This includes only the central CMUT cell 1218 up to all of the CMUT cells 1218. Similar to the piezoelectric element 904 of Figure 11, if the number of enabled switches in row i is denoted ki and the number of enabled switches in column j is denoted kj, the area apodization A of element (i; j) is A(i; j) = ki x kj. As with fixed area-controlled apodization, dynamic area controlled apodization of row-column addressed arrays offers 2N transmit and receive connections to an N x N transducer array since the switches can be operated from a pre-programmed independent circuit.

Figure 15 shows an example of bias controlled apodization in connection with a

CMUT transducer array 802. For sake of clarity and explanatory purposes, this example includes a 6x6 array. However, it is to be understood that smaller and larger arrays, and non-square arrays are also contemplated herein. It is also to be understood that the illustrated voltage levels are also provided for explanatory purposes and are not limiting; other voltage levels are contemplated herein.

The transducer array 802 includes the electrical contacts $906_1, \ldots, 906_6$, each electrically connected to a plurality of the elements 904 via the electrically conductive elements $910_1, \ldots, 910_6$, forming the row line elements $912_1, \ldots, 912_6$. The array 802 further includes the electrical contacts $908_1, \ldots, 908_6$, each electrically connected to a plurality of elements 904 via the electrically conductive elements $914_1, \ldots, 914_6$, forming the column line elements $916_1, \ldots, 916_6$.

In this example, the transducer array 802 further includes a first set of direct current (DC) voltage sources $1502_1, \ldots, 1502_6$, and a second set of DC voltage sources $1504_1, \ldots, 1504_6$. The first set of DC voltage sources $1502_1, \ldots, 1502_6$ respectively are electrically connected to the electrical contacts $906_1, \ldots, 906_6$, and the second set of DC voltage sources $1504_1, \ldots, 1504_6$ respectively are electrically connected to the electrical contacts $908_1, \ldots, 908_6$.

The DC voltages generate a map of voltage differences over the sub-elements of the array 802. In general, if the DC bias voltage applied to the i'th row is denoted r(i) and the DC bias voltage applied to the j'th column is denoted c(j), then the bias voltage of element (i; j) is given by VDC(i; j) = |r(i) - c(j)|. As the apodization of the individual sub-elements in terms of power scaling is a function of only VDC(i; j) for a given operating frequency, DC bias control allows application of any apodization profile over the entire 2D array that can be described as the sum of two arbitrary discrete 1D functions.

Since the number apodization levels are not limited by the number of cells per sub-element, the DC bias voltage can take any level. Bias-controlled apodization can be implemented as either a fixed or a dynamic apodization. In the first case, a simple voltage divider circuit can be implemented next to the transducer, and the apodization profile is fixed, but the apodization levels are continuous. For dynamic DC bias, a slightly more complicated electronic circuit has to be designed; however, usually only a small number of predefined apodization profiles are needed, so these could be pre-programmed and switched between by an external IC.

With dynamic DC bias voltage control apodization, time gain compensation can be directly integrated into the transducer array 802. By ramping up the DC bias voltage during receive, the signals from the transducer array 802 are effectively time gain compensated, and only a weaker subsequent time dependent amplification of the signals are needed.

Figures 16 and 17 illustrate an example of integrated fixed area apodization for the symmetry axis normal to the array 802. In this instance, the suppression of ghost echoes from a point scatterer located on the symmetry axis normal to the transducer is achieved by applying a rotationally symmetric apodization profile to the transducer. For a CMUT array with 9 cells per sub-element, there are nine (9) apodization levels. A discretized version of a 2D Hann window with 9 levels on a 32x32 array is shown in Figure 16, and

the corresponding mask layout for the CMUT array is shown in Figure, 17. Other suitable windows include, but are not limited to, a Hamming, a linear, a Gaussian, and/or other discrete and/or continuous windows.

For point scatterers located away from the symmetry axis normal to the transducer, the main echo will be damped, as the active area of the sub-elements directly beneath it is reduced. Consequently, the resulting image will have a decreasing signal-to-noise ratio (SNR) as a function of the point scatterer's distance from the symmetry axis. In order to address this issue, a second layout is proposed.

Figure 18 illustrates an example of apodization enabling homogeneous rectilinear imaging with optional beam steering. Using fixed area apodization as an example, the layout in Figure 18 consists of a 2-D row-column addressed array 1800 with all elements having the same (maximum) active area. On each end of the line elements, an apodization element 1802 is attached in which the active area is gradually decreased from a full active area next to the line element to zero active area at the opposing end (the edge of the entire array). With this approach, all point scatterers imaged using rectilinear imaging will experience the same apodization and exhibit the same SNR. In general, the layout in Figure 18 can be used in connection with area apodization (e.g., the example of Figure 21), bias apodization, damping material, and/or apodization. Damping materials are discussed in Demore et al., "Real-Time Volume Imaging Using a Crossed Electrode Array," IEEE Transactions on Ultrasonics, Ferroelectrics, and Frequency Control, vol. 56, no. 6, June 2009.

Beam steering can be employed through a modification: If the apodization elements located in the direction of the beam steering are turned off, the main echo from a point scatterer located will reach the non-apodized part of the line elements first, hence resulting in a full amplitude response. The transmitted/received signal from CMUTs is negligible if no DC bias is applied. By providing four separate DC bias supplies to the apodization elements located on the four sides of the array (or providing four switches, using floating ground, etc.), the apodization elements can be turned on and off in these four groups.

Figure 21 illustrates an example mask layout 2100. In contrast to the embodiment discussed in connection with Figures 16 and 17, in which the array includes a rotationally symmetric apodization profile, this layout is not rotationally symmetric to the axis normal to the array 802. Rather, a same apodization pattern is employed apodization elements which are located only at the end of each 1D array.

In the illustrated example, each of the 1D arrays is a line element that includes a first end, a second end and a middle region there between, and apodization is only at the first and second end regions of each of the 1D arrays, and not at the middle region of each of the 1D arrays. The illustrated mask layout 2100 includes column contacts 2102 and row contacts 2104.

The mask layout 2100 further includes a first group 2106 of column apodization elements and a second group 2108 of column apodization elements. The mask layout 2100 further includes a third group 2110 of row apodization elements and a fourth group 2112 of row apodization elements. As shown, the first, second, third and fourth groups

2106, 2108, 2110, and 2112 of apodization elements are located only at the first and second ends of each 1D array, and not at the middle region of the 1D arrays.

The mask layout 2100 further includes first row contacts 2114 to apodization elements in the first group 2106, and second row contacts 2116 to apodization elements in the second group 2108. The mask layout 2100 further includes third column contacts 2118 to apodization elements in the third group 2110, and fourth column contacts 2120 to apodization elements in the fourth group 2112.

The mask layout 2100 further includes a non-apodized region 2122, which corresponds to only the middle regions of the 1D arrays, and not the first and second ends of the 1D arrays. In this example, the non-apodized region 2122 is a rectangular region about a center of the array, in a central region within the boundary of the first, second, third and fourth groups 2106, 2108, 2110, and 2112 of the apodization elements.

The mask layout 2100 is shown inside of a chip border 2124. Corner regions 2126 do not include any elements. The corner regions 2126 are rectangular shaped. One side of each corner regions 2126 is adjacent to apodized rows elements. Another side of each corner regions 2126 is adjacent to apodized column elements. The two sides intersect at a corner at which the corresponding corner region 2126 is adjacent to the non-apodized region 2122.

Figure 19 graphically illustrates the output of the transducer array 208 in connection with the row-column addressing of described herein, for example, in connection with Figures 8-18. From Figure 19, the output includes only a main lobe 1900 (and no ghost lobes). For comparative purposes, Figure 7 graphically illustrates the row-column addressing of discussed in connection with Figures 1 and 2. In Figure 7, the output includes a main lobe 702 as well as ghost lobes 704 and 706.

In the above, the focus has been on 2-D transducer arrays utilizing row-column addressing. However, as 2-D row-column addressed arrays are essentially two 1-D arrays orthogonal to each other, the described apodization techniques and time gain compensation can also be applied to 1-D arrays. For low-end ultrasound scanners that do not incorporate the extra electronics needed to apply transmit apodization, a static apodization can be implemented directly in the transducer using these techniques.

Another possible use of these techniques is to improve the out-of-plane performance by apodizing 1-D arrays in the out-of-plane direction. This out-of-plane apodization could either be fixed or dynamic. If the apodization is fixed, it would not influence how the ultrasound scanner uses the transducer nor would it lead to extra connections. Fixed area-controlled apodization can be incorporated in both CMUTs and piezoelectric transducers. In 1-D piezoelectric arrays the fixed area apodization can be changed by e.g. widening the dicing trenches in the crystal.

Figure 20 illustrates an example method.

It is to be understood that the following acts are provided for explanatory purposes and are not limiting. As such, one or more of the acts may be omitted, one or more acts may be added, one or more acts may occur in a different order (including simultaneously with another act), etc.

At 2002, a transmit mode signal is received, placing a transducer array that includes at least one 1D array of transducing elements with integrated apodization in transmit mode.

At 2004, optionally, where the apodization is dynamic, a transmit apodization pattern signal is received setting the transmit apodization pattern.

At 2006, an excitation signal is received by the transducer array.

At 2008, the at least one 1D array of transducing elements transmits an ultrasound wave in response to receiving the excitation signal.

At 2010, a receive mode signal is received placing the transducer array in receive mode.

At 2012, optionally, where the apodization is dynamic, a receive apodization pattern signal is received setting the receive apodization pattern.

At 2014, a reflected wave, generated in response to an interaction of the transmitted ultrasound wave with structure, is received by the at least one 1D array of transducing elements or another the at least one 1D array of transducing elements.

At 2016, the at least one 1D array of transducing elements receiving the reflected wave generates a signal indicative thereof.

At 2018, the generate signal is processed and at least image is generated based thereon.

The methods described herein may be implemented via one or more computer processors (e.g., a micro-processor, a central processing unit (cpu), etc.) executing one or more computer readable instructions encoded or embodied on computer readable storage medium (which excludes transitory medium) such as physical memory which causes the one or more processors to carry out the various acts and/or other functions and/or acts. Additionally or alternatively, the one or more processors can execute instructions carried by transitory medium such as a signal or carrier wave.

The application has been described with reference to various embodiments. Modifications and alterations will occur to others upon reading the application. It is intended that the invention be construed as including all such modifications and alterations, including insofar as they come within the scope of the appended claims and the equivalents thereof.

A.6 Claims

What is claimed is:

1. A transducer array (802), comprising: at least one 1D array of transducing elements (804), the at least one 1D array of transducing elements, including: a plurality of transducing elements (904), wherein a first of the plurality of transducing elements has a first apodization and a second of the plurality of transducing elements has a second apodization, and the first apodization and the second apodization are different; at least one electrically conductive element (910) in electrical communication with each of the plurality of transducing elements; and at least one electrical contact (906) in electrical communication with the at least one electrically conductive element, wherein the at least

one electrical contact concurrently addresses the plurality of transducing elements through the at least one electrically conductive element.

2. The transducer array claim 1, further comprising: a plurality of the 1D array of transducing elements, physically arranged with respect to each other in a 2D array, wherein each of the plurality of 1D array of transducing elements is independently addressable.

3. The transducer array of claim 2, wherein one of the plurality of the 1D array of transducing elements is addressable to transmit ultrasound energy, and a second of the plurality of the 1D array of transducing elements is addressable to receive reflected ultrasound waves.

4. The transducer array of any of claims 2 to 3, wherein each of the plurality of the 1D array of transducing elements includes a first end, a second end and a middle region there between, each of the plurality of the 1D array of transducing elements has a same apodization pattern, and the apodization of each of the plurality of the 1D array of transducing elements is only at the first and second ends, and not at the middle region.

5. The transducer array of claim 1, wherein the first of the plurality of transducing elements has a first transducing surface area and the second of the plurality of transducing elements has a second transducing surface area, and a first value of the first transducing surface area and a second value of the second transducing surface area are different.

6. The transducer array of claim 5, wherein the first apodization is proportional to the first value and the second apodization is proportional to the second value.

7. The transducer array of any of claims 5 to 6, wherein the first of the plurality of transducing elements has a first geometric surface area and the second of the plurality of transducing elements has a second geometric surface area, and the first geometric surface area and the first transducing surface area are approximately the same and the second geometric surface area and the second transducing surface area are approximately the same.

8. The transducer array of any of claims 2 to 4, wherein the first value is a fixed single value and the second value is a fixed single value.

9. The transducer array of any of claims 2 to 3, wherein at least one of the plurality of transducing elements includes a plurality of sub-elements (1102), each of the plurality of sub-elements having a transducing surface area, and a value of a transducing surface area of the at least one of the plurality of transducing elements is a summation of the transducing surface areas of each of the plurality of sub-elements.

10. The transducer array of claim 9, wherein at least one of the first value or the second value is dynamically changeable between at least two different values.

11. The transducer array of claim 10, further comprising: a switch (1110, 1112, 1116, 1118) that electrically connects and disconnects at least one of the plurality of sub-elements with the other of the plurality of sub-elements, wherein the value of the transducing surface area of the at least one of the plurality of transducing elements is a summation of the transducing surface areas of each of the electrically connected plurality of sub-elements.

12. The transducer array of claim 11, wherein the value of the transducing surface area of the at least one of the plurality of transducing elements does not include a transducing surface area of a sub-element not electrically connected to the plurality of sub-elements.

13. The transducer array of any of claims 1 to 12, wherein the plurality of transducing elements includes piezoelectric transducing elements.

14. The transducer array of any of claims 5 to 6, wherein a transducing element of at least one of the first or second of the plurality of transducing elements includes a first number of transducing cells, each of the transducing cells having a transducing area, and at least one of the first or second values is a summation of the areas of the transducing cells.

15. The transducer array of claim 14, wherein the at least one of the first or second values is a fixed single value.

16. The transducer array of claim 14, wherein the at least one of the first or second values is a fixed single value is dynamically changeable between at least two different values.

17. The transducer array of claim 16, further comprising: a switch (1408, 1410, 1412, 1414) that electrically connects and disconnects at least one of the transducing cells with the other of the transducing cells, wherein the first or second value is a summation of the transducing surface areas of each of the electrically connected transducing cells.

18. The transducer array of any of claims 14 to 16, wherein the plurality of transducing elements includes capacitive micro machined ultrasonic transducer transducing elements.

19. The transducer array of any of claims 5 to 18, wherein at least one of the first transducing surface area or the second transducing surface area is dynamically variable and performs time gain compensation.

20. The transducer array of claim 1, further comprising: a first voltage source (1500) that applies a first bias voltage to the first of the plurality of transducing elements, wherein a first value of the first bias voltage provides the first apodization; and a second voltage source (1500) that applies a second bias voltage to the second of the plurality of transducing elements, wherein a second value of the second bias voltage provides the second apodization, wherein the first and second values are different values.

21. The transducer array of claim 20, wherein the first and second voltage sources have fixed voltages, and the first value is a fixed single value and the second value is a fixed single value.

22. The transducer array of claim 20, wherein the first and second voltage sources have variable voltages, and at least one of the first value or the second value is switchable between two different values.

23. The transducer array of any of claims 20 to 22, wherein the plurality of transducing elements includes capacitive micro machined ultrasonic transducer transducing elements.

24. The transducer array of any of claims 20 to 23, wherein at least one of the first and second values of the first and second bias voltages includes a time-gain compensation voltage.

25. The transducer array of any of claims 1 to 24, wherein the at least one 1D array of transducing elements includes a central region and at least one end region, the first apodization is less than the second apodization, and the first of the plurality of transducing elements is disposed at the central region and the second of the plurality of transducing elements is disposed at the at least one end region.

26. A method, comprising: transmitting an ultrasound waveform with a transducer array that includes apodization that is integrated into physical elements of the transducer array; receiving a reflected wave with the transducer array; and processing the received reflected wave to generate at least one image.

27. The method of claim 26, further comprising: using a different apodization, for the same transducer array, for transmit and receive operations.

28. The method of any of claims 26 to 27, further comprising: changing the apodization, of the same transducer array, for transmit and receive operations.

29. The method of any of claims 26 to 28, further comprising: controlling a transducing area to control the apodization.

30. The method of any of claims 26 to 29, further comprising: controlling a voltage bias applied to each element to control the apodization.

31. An ultrasound imaging system (800), comprising: a transducer array (802) with an array-wise addressable array of elements that includes at least two elements with a different apodization, wherein the apodization is one of a fixed area controlled apodization, a dynamic area controlled apodization, a fixed bias controlled apodization or a dynamic bias controlled apodization; transmit circuitry (806) that conveys an excitation pulse to the transducer array; receive circuitry (808) that receives a signal indicative of an ultrasound echo from the transducer array; and a beamformer (812) that processes the received signal, generating ultrasound image data.

32. The ultrasound imaging system of claim 31, wherein the transducer array includes a 2D array of transducing elements, and the apodization of the 2D array is not rotationally symmetric.

A.7 Abstract

A transducer array (802) includes at least one 1D array of transducing elements (804). The at least one 1D array of transducing elements includes a plurality of transducing elements (904). A first of the plurality of transducing elements has a first apodization and a second of the plurality of transducing elements has a second apodization. The first apodization and the second apodization are different. The transducer array further includes at least one electrically conductive element (910) in electrical communication with each of the plurality of transducing elements. The transducer array further includes at least one electrical contact (906) in electrical communication with the at least one electrically conductive element. The at least one electrical contact concurrently addresses

the plurality of transducing elements through the at least one electrically conductive element.

A.8 Drawings

1/13

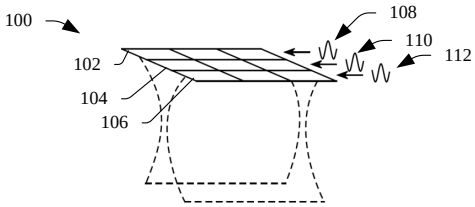

FIGURE 1
(PRIOR ART)

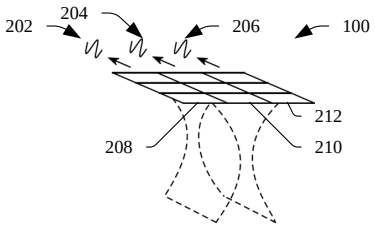

FIGURE 2
(PRIOR ART)

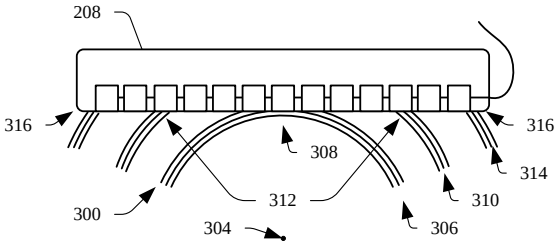

FIGURE 3
(PRIOR ART)

2/13

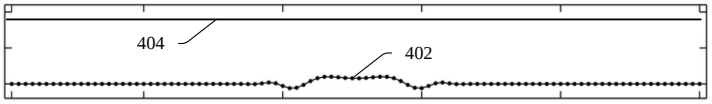

FIGURE 4
(PRIOR ART)

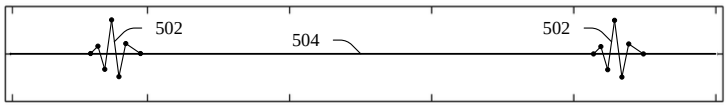

FIGURE 5
(PRIOR ART)

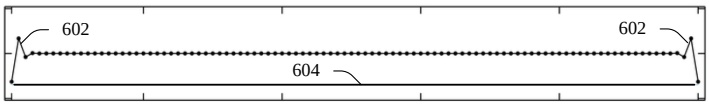

FIGURE 6
(PRIOR ART)

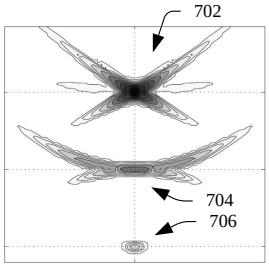

FIGURE 7
(PRIOR ART)

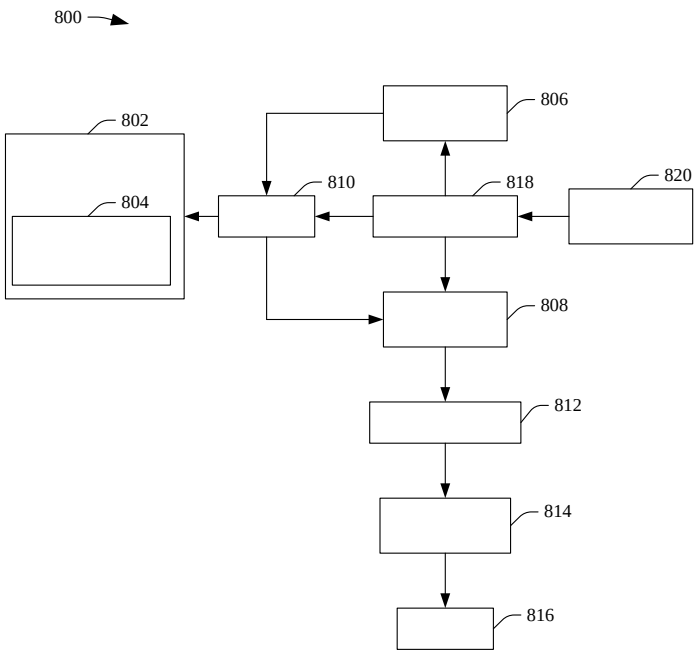

FIGURE 8

4/13

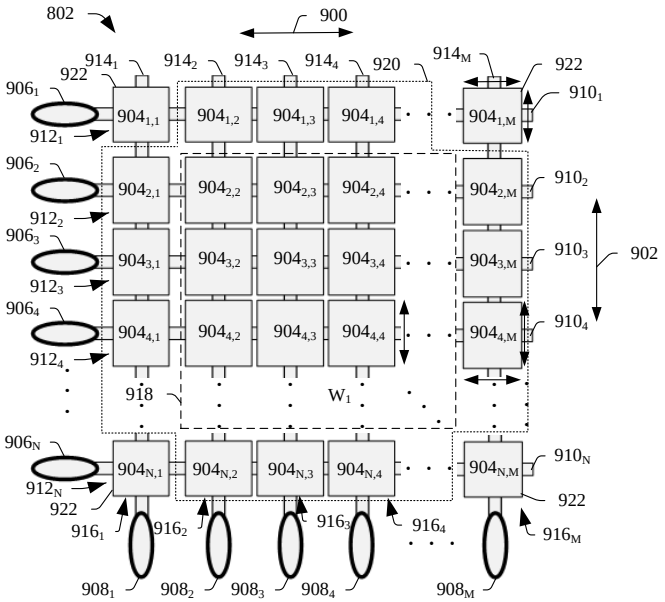
802
900
914$_1$
914$_2$
914$_3$
914$_4$
920
914$_M$
922
906$_1$
912$_1$
910$_1$
906$_2$
912$_2$
910$_2$
906$_3$
912$_3$
910$_3$
902
906$_4$
912$_4$
910$_4$
918
W$_1$
906$_N$
912$_N$
910$_N$
922
916$_1$
916$_2$
916$_3$
916$_4$
916$_M$
908$_1$
908$_2$
908$_3$
908$_4$
908$_M$
904$_{1,1}$ 904$_{1,2}$ 904$_{1,3}$ 904$_{1,4}$ 904$_{1,M}$
904$_{2,1}$ 904$_{2,2}$ 904$_{2,3}$ 904$_{2,4}$ 904$_{2,M}$
904$_{3,1}$ 904$_{3,2}$ 904$_{3,3}$ 904$_{3,4}$ 904$_{3,M}$
904$_{4,1}$ 904$_{4,2}$ 904$_{4,3}$ 904$_{4,4}$ 904$_{4,M}$
904$_{N,1}$ 904$_{N,2}$ 904$_{N,3}$ 904$_{N,4}$ 904$_{N,M}$

FIGURE 9

5/13

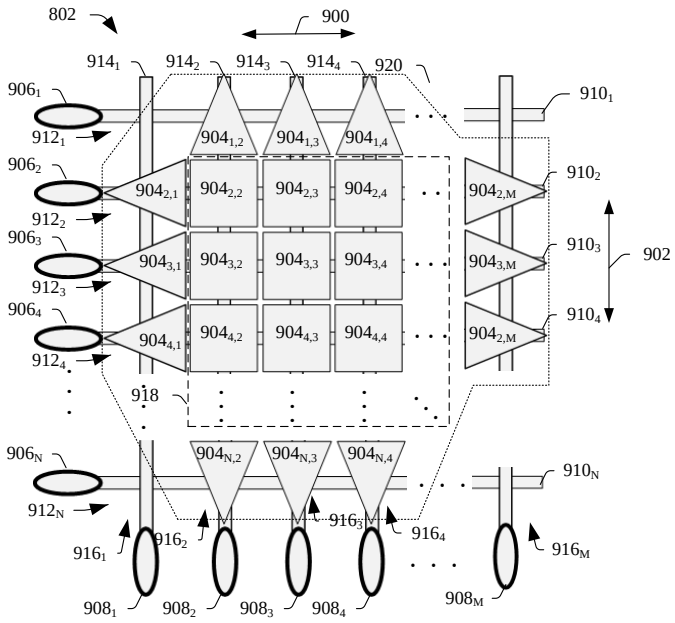

FIGURE 10

6/13

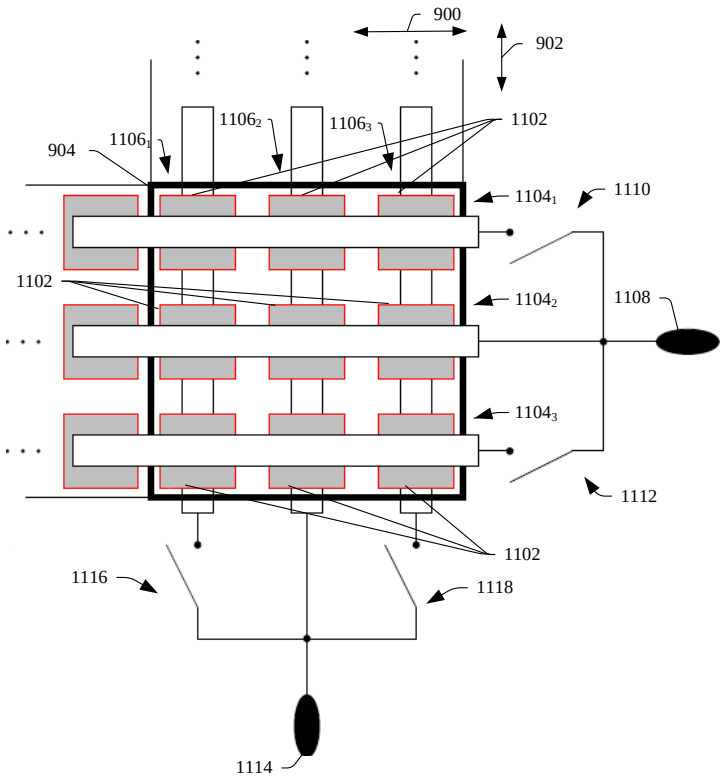

FIGURE 11

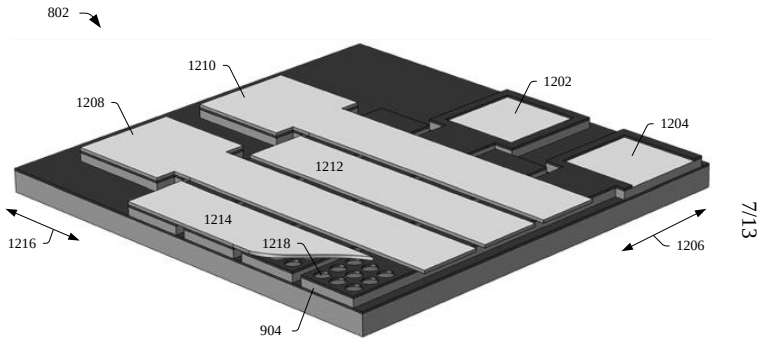

FIGURE 12

8/13

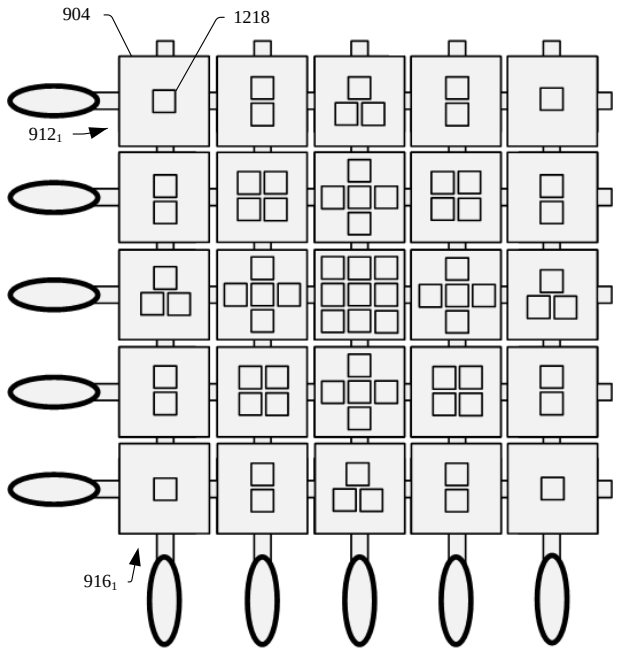

FIGURE 13

9/13

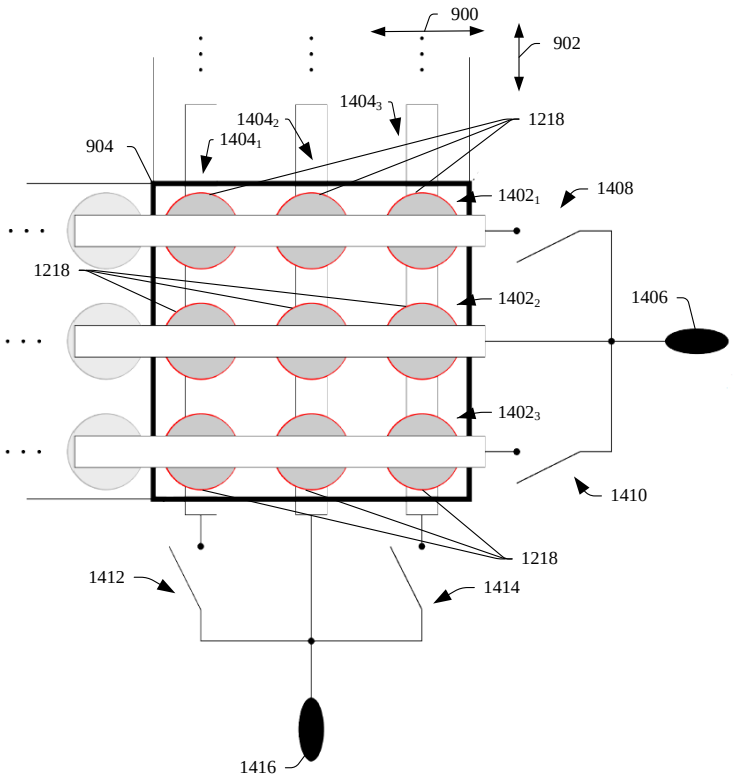

FIGURE 14

10/13

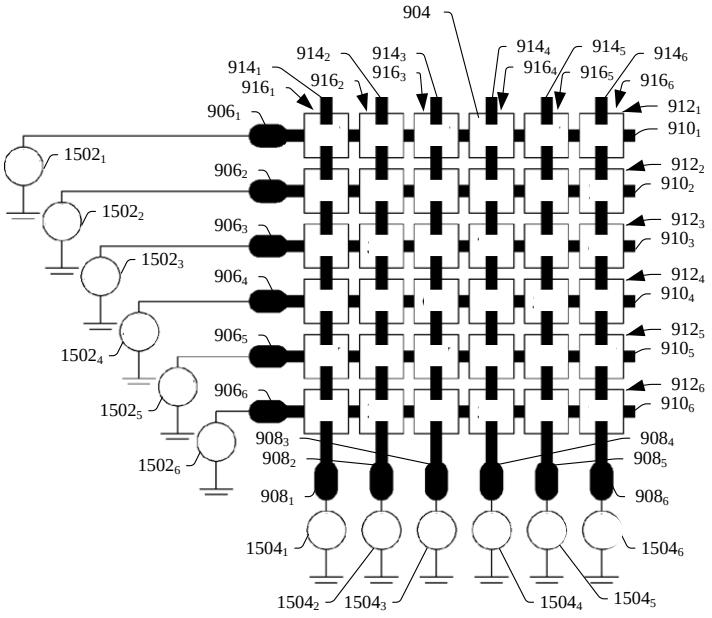

FIGURE 15

11/13

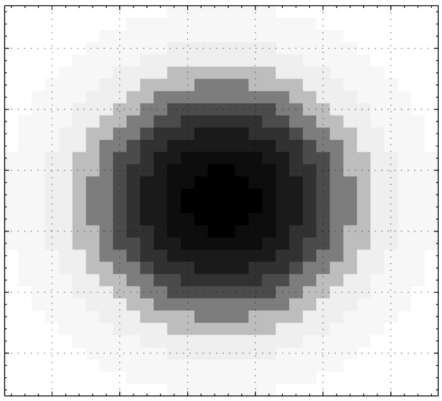

FIGURE 16

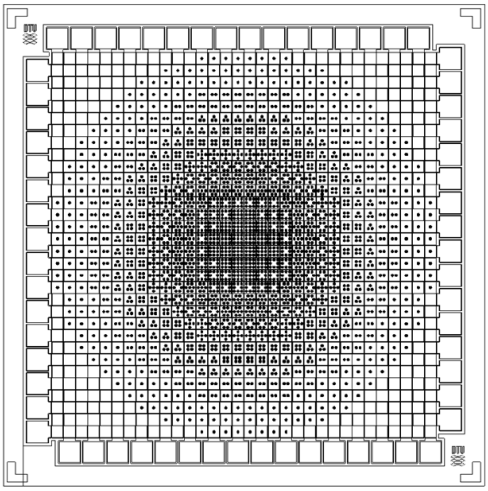

FIGURE 17

12/13

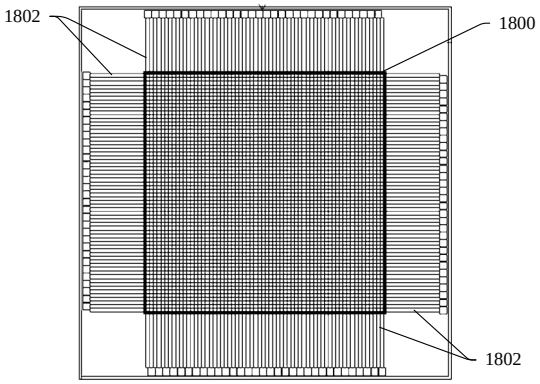

FIGURE 18

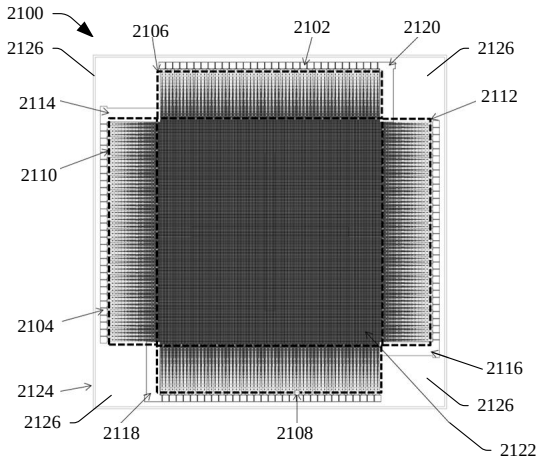

FIGURE 21

13/13

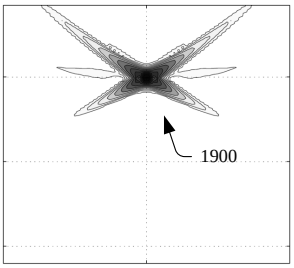

FIGURE 19

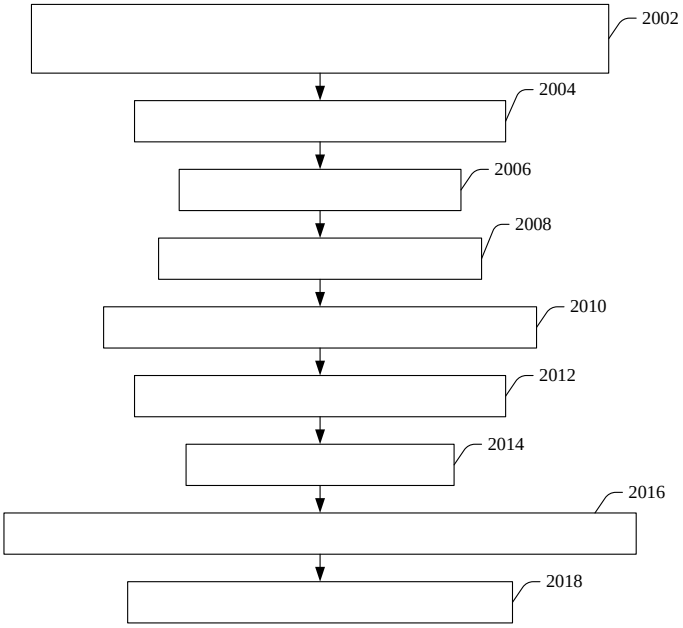

FIGURE 20

Combined Bibliography

References from Chapter 2

Augustine, L. J. (1987). *High resolution multiline ultrasonic beamformer*. U.S. Patent 4,644,795 (cit. on p. 16).

Bae, M. H. and M. K. Jeong (2000). "A study of synthetic-aperture imaging with virtual source elements in B-mode ultrasound imaging systems". In: *IEEE Trans. Ultrason., Ferroelec., Freq. Contr.* Vol. 47, pp. 1510–1519 (cit. on pp. 8, 9).

Bennett, S., D. K. Peterson, D. Corl, and G. S. Kino (1982). "A real-time synthetic aperture digital acoustic imaging system". In: *Acoust. Imaging*. Ed. by P. Alais and A. F. Metherell. Vol. 10, pp. 669–692 (cit. on p. 7).

Burckhardt, C. B., P.-A. Grandchamp, and H. Hoffmann (1974). "An Experimental 2 MHz Synthetic Aperture Sonar System Intended for Medical Use". In: *IEEE Trans. Son. Ultrason.* 21.1, pp. 1–6 (cit. on p. 7).

Flaherty, J. J., K. R. Erikson, and V. M. Lund (1967). *Synthetic Aperture Ultrasound Imaging Systems*. United States Patent, US 3,548,642. United States Patent, US 3,548,642, 1967, Published 22 Dec 1970 (cit. on p. 8).

Frazier, C. H. and W. D. O'Brien (1998). "Synthetic aperture techniques with a virtual source element". In: *IEEE Trans. Ultrason., Ferroelec., Freq. Contr.* 45, pp. 196–207 (cit. on pp. 8, 18).

Hergum, T., T. Bjåstad, K. Kristoffersen, and H. Torp (2007). "Parallel Beamforming Using Synthetic Transmit Beams". In: *IEEE Trans. Ultrason., Ferroelec., Freq. Contr.* 54.2, pp. 271–280 (cit. on p. 16).

Hoctor, R. T. and S. A. Kassam (1990). "The unifying role of the coarray in aperture synthesis for coherent and incoherent imaging". In: *IEEE Proc.* Vol. 78, pp. 735–752 (cit. on p. 14).

Johnson, J., M. Karaman, and B. Khuri-Yakub (2005). "Coherent-array imaging using phased subarrays. Part I: basic principles". In: *IEEE Trans. Ultrason., Ferroelec., Freq. Contr.* 52.1, pp. 37–50. DOI: 10.1109/TUFFC.2005.1397349 (cit. on p. 9).

Johnson, J., O. Oralkan, S. Ergun, U. Demirci, M. Karaman, and B. Khuri-Yakub (2005). "Coherent array imaging using phased subarrays. Part II: simulations and experimental results". In: *IEEE Trans. Ultrason., Ferroelec., Freq. Contr.* 52.1, pp. 51–64. DOI: 10.1109/TUFFC.2005.1397350 (cit. on p. 9).

Karaman, M., P. C. Li, and M. O'Donnell (1995). "Synthetic aperture imaging for small scale systems". In: *IEEE Trans. Ultrason., Ferroelec., Freq. Contr.* 42, pp. 429–442 (cit. on pp. 8, 9).

Karaman, M., I. O. Wygant, O. Oralkan, and B. T. Khuri-Yakub (2009). "Minimally Redundant 2-D Array Designs for 3-D Medical Ultrasound Imaging". In: *IEEE Trans. Med. Imag.* 7, pp. 1051–1061 (cit. on p. 14).

Kim, J.-J. and T.-K. Song (2008). "Real-Time 3D Imaging Methods using 2D Phased Arrays Based on Synthetic Focusing Techniques". In: *Ultrasonic Imaging* 30.3, pp. 169–188 (cit. on p. 10).

Kino, G. S., D. Corl, S. Bennett, and K. Peterson (1980). "Real Time Synthetic Aperture Imaging System". In: *Proc. IEEE Ultrason. Symp.* Pp. 722–731 (cit. on p. 7).

Liu, D.-L. D., J. C. Lazenby, Z. Banjanin, and B. A. McDermott (2002). *System and method for reduction of parallel beamforming artifacts*. U.S. Patent 6447452 (cit. on p. 16).

Lockwood, G. R., J. R. Talman, and S. S. Brunke (1998). "Real-time 3-D ultrasound imaging using sparse synthetic aperture beamforming". In: *IEEE Trans. Ultrason., Ferroelec., Freq. Contr.* 45, pp. 980–988 (cit. on p. 9).

Nikolov, S. I. and J. A. Jensen (2000). "3D synthetic aperture imaging using a virtual source element in the elevation plane". In: *Proc. IEEE Ultrason. Symp.* Vol. 2, pp. 1743–1747 (cit. on p. 9).

— (2002). "Virtual ultrasound sources in high-resolution ultrasound imaging". In: *Proc. SPIE - Progress in biomedical optics and imaging*. Vol. 3, pp. 395–405 (cit. on pp. 8, 9).

Pedersen, M. H., K. L. Gammelmark, and J. A. Jensen (2004). "Preliminary in-vivo evaluation of convex array synthetic aperture imaging". In: *Proc. SPIE - Progress in biomedical optics and imaging*, pp. 33–43 (cit. on p. 8).

Peterson, D. K. and G. S. Kino (1984). "Real-Time Digital Image Reconstruction: A Description of Imaging Hardware and an Analysis of Quantization Errors". In: *IEEE Trans. Son. Ultrason.* 31, pp. 337–351 (cit. on p. 7).

Ranganathan, K. and W. F. Walker (2007). "Cystic Resolution: A Performance Metric for Ultrasound Imaging Systems". In: *IEEE Trans. Ultrason., Ferroelec., Freq. Contr.* 54.4, pp. 782–792 (cit. on p. 11).

Sherwin, C. W., J. P. Ruina, and D. Rawcliffe (1962). "Some early developements in synthetic aperture radar systems". In: *IRE Trans. Mil. Elect.* MIL-6.2, pp. 111–115 (cit. on p. 7).

Smith, S. W., H. G. Pavy, and O. T. von Ramm (1991). "High speed ultrasound volumetric imaging system – Part I: Transducer design and beam steering". In: *IEEE Trans. Ultrason., Ferroelec., Freq. Contr.* 38, pp. 100–108 (cit. on p. 14).

Steinberg, B. D. (1976). *Principles of aperture and array system design*. New York: John Wiley & Sons (cit. on p. 14).

Vilkomerson, D., J. Greenleaf, and V. Dutt (1995). “Towards a Resolution Metric for Medical Ultrasound Imaging”. In: *Proc. IEEE Ultrason. Symp.* Pp. 1405–1410 (cit. on p. 11).

Ylitalo, J. T. (1995). “Synthetic aperture ultrasound imaging using a convex array”. In: *Proc. IEEE Ultrason. Symp.* Pp. 1337–1340 (cit. on p. 8).

Ylitalo, J. T. and H. Ermert (1994). “Ultrasound synthetic aperture imaging: Monostatic approach”. In: *IEEE Trans. Ultrason., Ferroelec., Freq. Contr.* 41, pp. 333–339 (cit. on p. 7).

References from Chapter 3

Austeng, A. and S. Holm (2002). “Sparse 2-D arrays for 3-D phased array imaging - design methods”. In: *IEEE Trans. Ultrason., Ferroelec., Freq. Contr.* 49.8, pp. 1073–1086 (cit. on p. 31).

Bates, K. N. (1995). “A high acuity 3-D acoustic imaging system”. In: *Proc. IEEE Ultrason. Symp.* Pp. 1245–1250 (cit. on p. 34).

Blaak, S., Z. Yu, G. Meijer, C. Prins, C. Lancee, J. Bosch, and N. de Jong (2009). “Design of a micro-beamformer for a 2D piezoelectric ultrasound transducer”. In: *Proc. IEEE Ultrason. Symp.* Pp. 1338–1341. DOI: 10.1109/ULTSYM.2009.5441534 (cit. on p. 31).

Brunke, S. S. and G. R. Lockwood (1997). “Broad-bandwidth radiation patterns of sparse two-dimensional vernier arrays”. In: *IEEE Trans. Ultrason., Ferroelec., Freq. Contr.* 44.5, pp. 1101–1109 (cit. on p. 31).

Chen, A. I. H., L. L. Wong, A. S. Logan, and J. T. W. Yeow (2011). “A CMUT-based real-time volumetric ultrasound imaging system with row-column addressing”. In: *Proc. IEEE Ultrason. Symp.* Pp. 1755–1758 (cit. on p. 34).

Chen, Y., M. Nguyen, and J. T. Yen (2010). “Recent results from dual-layer array transducers for 3-D imaging”. In: *Proc. IEEE Ultrason. Symp.* Pp. 2400–2403 (cit. on p. 34).

— (2011). “Real-time rectilinear volumetric acquisition with a 7.5 MHz dual-layer array transducer - Data acquisition and signal processing”. In: *Proc. IEEE Ultrason. Symp.* Pp. 1759–1761 (cit. on p. 34).

Daher, N. M. and J. T. Yen (2004). “Rectilinear 3-D ultrasound imaging using synthetic aperture techniques”. In: *Proc. IEEE Ultrason. Symp.* Vol. 2, pp. 1270–1273 (cit. on p. 34).

— (2006). “2-D Array for 3-D Ultrasound Imaging Using Synthetic Aperture Techniques”. In: *IEEE Trans. Ultrason., Ferroelec., Freq. Contr.* 53.5, pp. 912–924 (cit. on p. 34).

Davidsen, R. E., J. A. Jensen, and S. W. Smith (1994). “Two-Dimensional Random Arrays for Real Time Volumetric Imaging”. In: *Ultrasonic Imaging* 16.3, pp. 143–163 (cit. on p. 31).

Démoré, C. E. M., A. Joyce, K. Wall, and G. Lockwood (2009). "Real-time volume imaging using a crossed electrode array". In: *IEEE Trans. Ultrason., Ferroelec., Freq. Contr.* 56.6, pp. 1252–1261 (cit. on pp. 34, 35, 38, 44, 50, 53).

Halvorsrod, T., W. Luzi, and T. Lande (2005). "A log-domain µbeamformer for medical ultrasound imaging systems". In: *IEEE Trans. Circuits Syst. I, Reg. Papers* 52.12, pp. 2563–2575. DOI: 10.1109/TCSI.2005.857544 (cit. on p. 31).

Jensen, J. A. (1991). "A Model for the Propagation and Scattering of Ultrasound in Tissue". In: *J. Acoust. Soc. Am.* 89, pp. 182–191 (cit. on p. 36).

Jeong, J. S., C. H. Seo, and J. T. Yen (2007). "Dual-Layer Transducer Array for 3-D Imaging". In: *Proc. IEEE Ultrason. Symp.* Pp. 2371–2374 (cit. on p. 34).

Karaman, M., I. O. Wygant, O. Oralkan, and B. T. Khuri-Yakub (2009). "Minimally Redundant 2-D Array Designs for 3-D Medical Ultrasound Imaging". In: *IEEE Trans. Med. Imag.* 7, pp. 1051–1061 (cit. on p. 31).

Logan, A. S., L. L. P. Wong, A. I. H. Chen, and J. T. W. Yeow (2011). "A 32 x 32 element row-column addressed capacitive micromachined ultrasonic transducer". In: *IEEE Trans. Ultrason., Ferroelec., Freq. Contr.* 58.6, pp. 1266–1271 (cit. on p. 34).

Logan, A. S., L. L. P. Wong, and J. T. W. Yeow (2009). "2-D CMUT wafer bonded imaging arrays with a row-column addressing scheme". In: *Proc. IEEE Ultrason. Symp.* Pp. 984–987 (cit. on p. 34).

Morton, C. E. and G. R. Lockwood (2003). "Theoretical assessment of a crossed electrode 2-D array for 3-D imaging". In: *Proc. IEEE Ultrason. Symp.* Pp. 968–971 (cit. on p. 34).

Rasmussen, M. F. and J. A. Jensen (2013). "3D ultrasound imaging performance of a row-column addressed 2D array transducer: a simulation study". In: *Proc. SPIE Med. Imag.* 86750C, pp. 1–11 (cit. on p. 44).

Sampaleanu, A., P. Zhang, A. Kshirsagar, W. Moussa, and R. Zemp (2014). "Top-orthogonal-to-bottom-electrode (TOBE) CMUT arrays for 3-D ultrasound imaging." In: *IEEE Trans. Ultrason., Ferroelec., Freq. Contr.* 61.2, pp. 266–276. DOI: 10.1109/TUFFC.2014.6722612 (cit. on p. 35).

Savord, B. and R. Solomon (2003). "Fully sampled matrix transducer for real time 3D ultrasonic imaging". In: *Proc. IEEE Ultrason. Symp.* Vol. 1, pp. 945–953 (cit. on p. 31).

Senturia, S. D. (2004). *Microsystem Design*. 6th ed. Kluwer Academic Publishers (cit. on p. 42).

Seo, C. H. and J. T. Yen (2006). "64 x 64 2-D array transducer with row-column addressing". In: *Proc. IEEE Ultrason. Symp.* Vol. 1, pp. 74–77 (cit. on p. 34).

— (2007). "256 x 256 2-D array transducer with row-column addressing for 3-D imaging". In: *Proc. IEEE Ultrason. Symp.* Pp. 2381–2384 (cit. on p. 34).

— (2008). "Recent results using a 256 x 256 2-D array transducer for 3-D Rectilinear Imaging". In: *Proc. IEEE Ultrason. Symp.* Vol. 1-4, pp. 1146–1149 (cit. on p. 34).

— (2009). “A 256 x 256 2-D array transducer with row-column addressing for 3-D rectilinear imaging”. In: *IEEE Trans. Ultrason., Ferroelec., Freq. Contr.* 56.4, pp. 837–847 (cit. on p. 34).

Yen, J. T., C. H. Seo, S. I. Awad, and J. S. Jeong (2008). “A PZT-P[VDF-TrFE] dual-layer transducer for 3-D rectilinear imaging”. In: *Proc. IEEE Ultrason. Symp.* Pp. 1138–1141 (cit. on p. 34).

— (2009). “A dual-layer transducer array for 3-D rectilinear imaging”. In: *IEEE Trans. Ultrason., Ferroelec., Freq. Contr.* 56.1, pp. 204–212 (cit. on p. 34).

Yen, J. T., J. P. Steinberg, and S. W. Smith (2000). “Sparse 2-D array design for real time rectilinear volumetric imaging”. In: *IEEE Trans. Ultrason., Ferroelec., Freq. Contr.* 47.1, pp. 93–110 (cit. on p. 31).

Yen, J. T. (2013). “Beamforming of sound from two-dimensional arrays using spatial matched filters”. In: *J. Acoust. Soc. Am.* 134.5, pp. 3697–704. DOI: 10.1121/1.4821988 (cit. on p. 34).

Zemp, R. J., W. Zheng, and P. Zhang (2011). “Feasibility of Top-Orthogonal-to-Bottom Electrode (TOBE) 2D CMUT arrays for low-channel-count 3D imaging”. In: *Proc. IEEE Ultrason. Symp.* Pp. 498–502 (cit. on p. 35).

References from Paper A

Burckhardt, C. B., P.-A. Grandchamp, and H. Hoffmann (1974). “An Experimental 2 MHz Synthetic Aperture Sonar System Intended for Medical Use”. In: *IEEE Trans. Son. Ultrason.* 21.1, pp. 1–6 (cit. on p. 62).

Chiao, R. Y., L. J. Thomas, and S. D. Silverstein (1997). “Sparse array imaging with spatially-encoded transmits”. In: *Proc. IEEE Ultrason. Symp.* Pp. 1679–1682 (cit. on p. 62).

Flaherty, J. J., K. R. Erikson, and V. M. Lund (1967). *Synthetic Aperture Ultrasound Imaging Systems*. United States Patent, US 3,548,642. United States Patent, US 3,548,642, 1967, Published 22 Dec 1970 (cit. on p. 62).

Hansen, J. M., M. C. Hemmsen, and J. A. Jensen (2011). “An object-oriented multi-threaded software beamformation toolbox”. In: *Proc. SPIE Med. Imag.* Vol. 7968, pages. URL: http://dx.doi.org/10.1117/12.878178 (cit. on p. 67).

Jensen, J. A. (1996). “Field: A Program for Simulating Ultrasound Systems”. In: *Med. Biol. Eng. Comp.* 10th Nordic-Baltic Conference on Biomedical Imaging, Vol. 4, Supplement 1, Part 1, pp. 351–353 (cit. on p. 67).

Jensen, J. A., S. Nikolov, K. L. Gammelmark, and M. H. Pedersen (2006). “Synthetic Aperture Ultrasound Imaging”. In: *Ultrasonics* 44, e5–e15 (cit. on p. 62).

Jensen, J. A. and N. B. Svendsen (1992). “Calculation of Pressure Fields from Arbitrarily Shaped, Apodized, and Excited Ultrasound Transducers”. In: *IEEE Trans. Ultrason., Ferroelec., Freq. Contr.* 39, pp. 262–267 (cit. on p. 67).

Nagai, K. (1985). "A New Synthetic-Aperture Focusing Method for Ultrasonic B-Scan Imaging by the Fourier Transform". In: *IEEE Trans. Son. Ultrason.* SU-32.4, pp. 531–536 (cit. on p. 62).

Ramm, O. T. von, S. W. Smith, and H. G. Pavy (1991). "High speed ultrasound volumetric imaging system – Part II: Parallel processing and image display". In: *IEEE Trans. Ultrason., Ferroelec., Freq. Contr.* 38, pp. 109–115 (cit. on pp. 62, 66).

Ranganathan, K. and W. F. Walker (2007). "Cystic Resolution: A Performance Metric for Ultrasound Imaging Systems". In: *IEEE Trans. Ultrason., Ferroelec., Freq. Contr.* 54.4, pp. 782–792 (cit. on p. 63).

Shattuck, D. P., M. D. Weinshenker, S. W. Smith, and O. T. von Ramm (1984). "Explososcan: A parallel processing technique for high speed ultrasound imaging with linear phased arrays". In: *J. Acoust. Soc. Am.* 75, pp. 1273–1282 (cit. on p. 62).

Smith, S. W., H. G. Pavy, and O. T. von Ramm (1991). "High speed ultrasound volumetric imaging system – Part I: Transducer design and beam steering". In: *IEEE Trans. Ultrason., Ferroelec., Freq. Contr.* 38, pp. 100–108 (cit. on pp. 62, 68).

Soumekh, M. (1999). *Synthetic aperture radar. Signal processing with MATLAB algorithms*. New York: John Wiley & Sons, Inc. (cit. on p. 62).

Vilkomerson, D., J. Greenleaf, and V. Dutt (1995). "Towards a Resolution Metric for Medical Ultrasound Imaging". In: *Proc. IEEE Ultrason. Symp.* Pp. 1405–1410 (cit. on p. 63).

References from Paper B

Karaman, M., I. O. Wygant, O. Oralkan, and B. T. Khuri-Yakub (2009). "Minimally Redundant 2-D Array Designs for 3-D Medical Ultrasound Imaging". In: *IEEE Trans. Med. Imag.* 7, pp. 1051–1061 (cit. on p. 75).

Ramm, O. T. von, S. W. Smith, and H. G. Pavy (1991). "High speed ultrasound volumetric imaging system – Part II: Parallel processing and image display". In: *IEEE Trans. Ultrason., Ferroelec., Freq. Contr.* 38, pp. 109–115 (cit. on p. 74).

Ranganathan, K. and W. F. Walker (2007). "Cystic Resolution: A Performance Metric for Ultrasound Imaging Systems". In: *IEEE Trans. Ultrason., Ferroelec., Freq. Contr.* 54.4, pp. 782–792 (cit. on p. 79).

Rasmussen, M. F., J. M. Hansen, G. Férin, R. Dufait, and J. A. Jensen (2012). "Preliminary comparison of 3D synthetic aperture imaging with Explososcan". In: *Proc. SPIE Med. Imag.* Ed. by J. G. Bosch and M. M. Doyley. Vol. 8320. 83200F. SPIE, pp. 1–9 (cit. on p. 74).

Shattuck, D. P., M. D. Weinshenker, S. W. Smith, and O. T. von Ramm (1984). "Explososcan: A parallel processing technique for high speed ultrasound imaging with linear phased arrays". In: *J. Acoust. Soc. Am.* 75, pp. 1273–1282 (cit. on p. 74).

Smith, S. W., H. G. Pavy, and O. T. von Ramm (1991). "High speed ultrasound volumetric imaging system – Part I: Transducer design and beam steering". In: *IEEE Trans. Ultrason., Ferroelec., Freq. Contr.* 38, pp. 100–108 (cit. on p. 75).

Vilkomerson, D., J. Greenleaf, and V. Dutt (1995). "Towards a Resolution Metric for Medical Ultrasound Imaging". In: *Proc. IEEE Ultrason. Symp.* Pp. 1405–1410 (cit. on p. 79).

References from Paper C

Augustine, L. J. (1987). *High resolution multiline ultrasonic beamformer*. U.S. Patent 4,644,795 (cit. on p. 84).

Bae, M. H. and M. K. Jeong (2000). "A study of synthetic-aperture imaging with virtual source elements in B-mode ultrasound imaging systems". In: *IEEE Trans. Ultrason., Ferroelec., Freq. Contr.* Vol. 47, pp. 1510–1519 (cit. on p. 84).

Bae, M., H. Lee, S. B. Park, R. Yoon, M. H. Jeong, D. G. Kim, M. Jeong, and Y. Kim (2008). "A new ultrasonic synthetic aperture tissue harmonic imaging system". In: *Proc. IEEE Ultrason. Symp.* Pp. 1258–1261 (cit. on p. 85).

Bennett, S., D. K. Peterson, D. Corl, and G. S. Kino (1982). "A real-time synthetic aperture digital acoustic imaging system". In: *Acoust. Imaging*. Ed. by P. Alais and A. F. Metherell. Vol. 10, pp. 669–692 (cit. on p. 84).

Bilge, H. S., M. Karaman, and M. O'Donnell (1996). "Motion estimation using common spatial frequencies in synthetic aperture imaging". In: *Proc. IEEE Ultrason. Symp.* Pp. 1551–1554 (cit. on p. 85).

Burckhardt, C. B., P.-A. Grandchamp, and H. Hoffmann (1974). "An Experimental 2 MHz Synthetic Aperture Sonar System Intended for Medical Use". In: *IEEE Trans. Son. Ultrason.* 21.1, pp. 1–6 (cit. on p. 84).

Delannoy, B., R. Torguet, C. Bruneel, E. Bridoux, J. M. Rouvaen, and H. Lasota (1979). "Acoustical image reconstructions in parallel-processing analog electronic systems". In: *J. Appl. Phys.* 50, pp. 3153–3159 (cit. on p. 84).

Flaherty, J. J., K. R. Erikson, and V. M. Lund (1967). *Synthetic Aperture Ultrasound Imaging Systems*. United States Patent, US 3,548,642. United States Patent, US 3,548,642, 1967, Published 22 Dec 1970 (cit. on p. 84).

Frazier, C. H. and W. D. O'Brien (1998). "Synthetic aperture techniques with a virtual source element". In: *IEEE Trans. Ultrason., Ferroelec., Freq. Contr.* 45, pp. 196–207 (cit. on pp. 84, 93).

Gammelmark, K. L. and J. A. Jensen (2003a). "Duplex Synthetic Aperture Imaging with Tissue Motion Compensation". In: *Proc. IEEE Ultrason. Symp.* Pp. 1569–1573 (cit. on p. 85).

— (2003b). "Multielement Synthetic Transmit Aperture Imaging using Temporal Encoding". In: *IEEE Trans. Med. Imag.* 22.4, pp. 552–563 (cit. on p. 84).

Gammelmark, K. L. and J. A. Jensen (2014). "2-D Tissue Motion Compensation of Synthetic Transmit Aperture Images". In: *IEEE Trans. Ultrason., Ferroelec., Freq. Contr.* Pp. 594–610. DOI: http://dx.doi.org/10.1109/TUFFC.2014.2948 (cit. on p. 85).

Hansen, J. M., M. C. Hemmsen, and J. A. Jensen (2011). "An object-oriented multi-threaded software beamformation toolbox". In: *Proc. SPIE Med. Imag.* Vol. 7968, pages. URL: http://dx.doi.org/10.1117/12.878178 (cit. on p. 99).

Hergum, T., T. Bjåstad, K. Kristoffersen, and H. Torp (2007). "Parallel Beamforming Using Synthetic Transmit Beams". In: *IEEE Trans. Ultrason., Ferroelec., Freq. Contr.* 54.2, pp. 271–280 (cit. on p. 84).

Ho, K.-Y., Y.-H. Chen, C.-Z. Zhan, and A.-Y. Wu (2013). "VLSI implementation of real-time motion compensated beamforming in synthetic transmit aperture imaging". In: *IEEE Int. Symp. Circ. & Sys.* Pp. 1893–1896 (cit. on p. 85).

Hoctor, R. T. and S. A. Kassam (1990). "The unifying role of the coarray in aperture synthesis for coherent and incoherent imaging". In: *IEEE Proc.* Vol. 78, pp. 735–752 (cit. on p. 89).

Jensen, J. A. (1996). "Field: A Program for Simulating Ultrasound Systems". In: *Med. Biol. Eng. Comp.* 10th Nordic-Baltic Conference on Biomedical Imaging, Vol. 4, Supplement 1, Part 1, pp. 351–353 (cit. on p. 89).

Jensen, J. A., H. Holten-Lund, R. T. Nilsson, M. Hansen, U. D. Larsen, R. P. Domsten, B. G. Tomov, M. B. Stuart, S. I. Nikolov, M. J. Pihl, Y. Du, J. H. Rasmussen, and M. F. Rasmussen (2013). "SARUS: A Synthetic Aperture Real-time Ultrasound System". In: *IEEE Trans. Ultrason., Ferroelec., Freq. Contr.* 60.9, pp. 1838–1852 (cit. on p. 99).

Jensen, J. A. and N. B. Svendsen (1992). "Calculation of Pressure Fields from Arbitrarily Shaped, Apodized, and Excited Ultrasound Transducers". In: *IEEE Trans. Ultrason., Ferroelec., Freq. Contr.* 39, pp. 262–267 (cit. on p. 89).

Johnson, J., M. Karaman, and B. Khuri-Yakub (2005). "Coherent-array imaging using phased subarrays. Part I: basic principles". In: *IEEE Trans. Ultrason., Ferroelec., Freq. Contr.* 52.1, pp. 37–50. DOI: 10.1109/TUFFC.2005.1397349 (cit. on p. 85).

Johnson, J., O. Oralkan, S. Ergun, U. Demirci, M. Karaman, and B. Khuri-Yakub (2005). "Coherent array imaging using phased subarrays. Part II: simulations and experimental results". In: *IEEE Trans. Ultrason., Ferroelec., Freq. Contr.* 52.1, pp. 51–64. DOI: 10.1109/TUFFC.2005.1397350 (cit. on p. 85).

Karaman, M., P. C. Li, and M. O'Donnell (1995). "Synthetic aperture imaging for small scale systems". In: *IEEE Trans. Ultrason., Ferroelec., Freq. Contr.* 42, pp. 429–442 (cit. on pp. 84, 85).

Karaman, M. and M. O'Donnell (1998). "Subaperture processing for ultrasonic imaging". In: *IEEE Trans. Ultrason., Ferroelec., Freq. Contr.* 45, pp. 126–135 (cit. on p. 84).

Karaman, M., H. Ş. Bilge, and M. O'Donnell (1998). "Adaptive multi-element synthetic aperture imaging with motion and phase aberation correction". In: *IEEE Trans. Ultrason., Ferroelec., Freq. Contr.* 42, pp. 1077–1087 (cit. on pp. 84, 85).

Karaman, M., I. O. Wygant, O. Oralkan, and B. T. Khuri-Yakub (2009). "Minimally Redundant 2-D Array Designs for 3-D Medical Ultrasound Imaging". In: *IEEE Trans. Med. Imag.* 7, pp. 1051–1061 (cit. on p. 88).

Kim, J.-J. and T.-K. Song (2008). "Real-Time 3D Imaging Methods using 2D Phased Arrays Based on Synthetic Focusing Techniques". In: *Ultrasonic Imaging* 30.3, pp. 169–188 (cit. on p. 85).

Liu, D.-L. D., J. C. Lazenby, Z. Banjanin, and B. A. McDermott (2002). *System and method for reduction of parallel beamforming artifacts*. U.S. Patent 6447452 (cit. on p. 84).

Lockwood, G. R., J. R. Talman, and S. S. Brunke (1998). "Real-time 3-D ultrasound imaging using sparse synthetic aperture beamforming". In: *IEEE Trans. Ultrason., Ferroelec., Freq. Contr.* 45, pp. 980–988 (cit. on p. 85).

Nikolov, S. I. and J. A. Jensen (2000). "3D synthetic aperture imaging using a virtual source element in the elevation plane". In: *Proc. IEEE Ultrason. Symp.* Vol. 2, pp. 1743–1747 (cit. on p. 85).

Nock, L. F. and G. E. Trahey (1992). "Synthetic receive aperture imaging with phase correction for motion and for tissue inhomogenities - part I: basic principles". In: *IEEE Trans. Ultrason., Ferroelec., Freq. Contr.* 39, pp. 489–495 (cit. on p. 84).

Ramm, O. T. von, S. W. Smith, and H. G. Pavy (1991). "High speed ultrasound volumetric imaging system – Part II: Parallel processing and image display". In: *IEEE Trans. Ultrason., Ferroelec., Freq. Contr.* 38, pp. 109–115 (cit. on p. 84).

Ranganathan, K. and W. F. Walker (2007). "Cystic Resolution: A Performance Metric for Ultrasound Imaging Systems". In: *IEEE Trans. Ultrason., Ferroelec., Freq. Contr.* 54.4, pp. 782–792 (cit. on p. 87).

Rasmussen, J. H., M. C. Hemmsen, S. S. Madsen, P. M. Hansen, M. B. Nielsen, and J. A. Jensen (2013). "Preliminary study of synthetic aperture tissue harmonic imaging on in-vivo data". In: *Proc. SPIE Med. Imag.* Vol. 8675, pp. 1–10. DOI: dx.doi.org/10.1117/12.2006363 (cit. on p. 85).

Rasmussen, M. F., G. Férin, R. Dufait, and J. A. Jensen (2012). "Comparison of 3D Synthetic Aperture Imaging and Explososcan using Phantom Measurements". In: *Proc. IEEE Ultrason. Symp.* Pp. 113–116. DOI: 10.1109/ULTSYM.2012.0028 (cit. on p. 84).

Rasmussen, M. F., J. M. Hansen, G. Férin, R. Dufait, and J. A. Jensen (2012). "Preliminary comparison of 3D synthetic aperture imaging with Explososcan". In: *Proc. SPIE Med. Imag.* Ed. by J. G. Bosch and M. M. Doyley. Vol. 8320. 83200F. SPIE, pp. 1–9 (cit. on p. 84).

Shattuck, D. P., M. D. Weinshenker, S. W. Smith, and O. T. von Ramm (1984). "Explososcan: A parallel processing technique for high speed ultrasound imaging with linear phased arrays". In: *J. Acoust. Soc. Am.* 75, pp. 1273–1282 (cit. on p. 84).

Smith, S. W., H. G. Pavy, and O. T. von Ramm (1991). "High speed ultrasound volumetric imaging system – Part I: Transducer design and beam steering". In: *IEEE Trans. Ultrason., Ferroelec., Freq. Contr.* 38, pp. 100–108 (cit. on p. 88).

Steinberg, B. D. (1976). *Principles of aperture and array system design*. New York: John Wiley & Sons (cit. on p. 89).

Trahey, G. E. and L. F. Nock (1992). "Synthetic receive aperture imaging with phase correction for motion and for tissue inhomogenities - part II: effects of and correction for motion". In: *IEEE Trans. Ultrason., Ferroelec., Freq. Contr.* 39, pp. 496–501 (cit. on p. 85).

Vilkomerson, D., J. Greenleaf, and V. Dutt (1995). "Towards a Resolution Metric for Medical Ultrasound Imaging". In: *Proc. IEEE Ultrason. Symp.* Pp. 1405–1410 (cit. on p. 86).

Wild, J. J. (1950). "The use of ultrasonic pulses for the measurement of biologic tissues and the detection of tissue density changes". In: *Surgery* 27, pp. 183–188 (cit. on p. 84).

Ylitalo, J. T. and H. Ermert (1994). "Ultrasound synthetic aperture imaging: Monostatic approach". In: *IEEE Trans. Ultrason., Ferroelec., Freq. Contr.* 41, pp. 333–339 (cit. on p. 84).

References from Paper D

Austeng, A. and S. Holm (2002). "Sparse 2-D arrays for 3-D phased array imaging - design methods". In: *IEEE Trans. Ultrason., Ferroelec., Freq. Contr.* 49.8, pp. 1073–1086 (cit. on p. 112).

Brunke, S. S. and G. R. Lockwood (1997). "Broad-bandwidth radiation patterns of sparse two-dimensional vernier arrays". In: *IEEE Trans. Ultrason., Ferroelec., Freq. Contr.* 44.5, pp. 1101–1109 (cit. on p. 112).

Chen, A. I. H., L. L. Wong, A. S. Logan, and J. T. W. Yeow (2011). "A CMUT-based real-time volumetric ultrasound imaging system with row-column addressing". In: *Proc. IEEE Ultrason. Symp.* Pp. 1755–1758 (cit. on p. 112).

Davidsen, R. E., J. A. Jensen, and S. W. Smith (1994). "Two-Dimensional Random Arrays for Real Time Volumetric Imaging". In: *Ultrasonic Imaging* 16.3, pp. 143–163 (cit. on p. 112).

Hansen, J. M., M. C. Hemmsen, and J. A. Jensen (2011). "An object-oriented multi-threaded software beamformation toolbox". In: *Proc. SPIE Med. Imag.* Vol. 7968, pages. URL: `http://dx.doi.org/10.1117/12.878178` (cit. on p. 118).

Jensen, J. A. (1996). "Field: A Program for Simulating Ultrasound Systems". In: *Med. Biol. Eng. Comp.* 10th Nordic-Baltic Conference on Biomedical Imaging, Vol. 4, Supplement 1, Part 1, pp. 351–353 (cit. on p. 118).

Jensen, J. A. and N. B. Svendsen (1992). "Calculation of Pressure Fields from Arbitrarily Shaped, Apodized, and Excited Ultrasound Transducers". In: *IEEE Trans. Ultrason., Ferroelec., Freq. Contr.* 39, pp. 262–267 (cit. on p. 118).

Karaman, M., I. O. Wygant, O. Oralkan, and B. T. Khuri-Yakub (2009). "Minimally Redundant 2-D Array Designs for 3-D Medical Ultrasound Imaging". In: *IEEE Trans. Med. Imag.* 7, pp. 1051–1061 (cit. on p. 112).

Kim, K. S. and T. K. Song (2004). "High volume rate 3-D ultrasound imaging using cross array based on synthetic transmit focusing". In: *Proc. IEEE Ultrason. Symp.* Vol. 2, pp. 1409–1412 (cit. on p. 116).

Logan, A. S., L. L. P. Wong, A. I. H. Chen, and J. T. W. Yeow (2011). "A 32 x 32 element row-column addressed capacitive micromachined ultrasonic transducer". In: *IEEE Trans. Ultrason., Ferroelec., Freq. Contr.* 58.6, pp. 1266–1271 (cit. on p. 112).

Logan, A. S., L. L. P. Wong, and J. T. W. Yeow (2009). "2-D CMUT wafer bonded imaging arrays with a row-column addressing scheme". In: *Proc. IEEE Ultrason. Symp.* Pp. 984–987 (cit. on p. 112).

Ramm, O. T. von, S. W. Smith, and H. G. Pavy (1991). "High speed ultrasound volumetric imaging system – Part II: Parallel processing and image display". In: *IEEE Trans. Ultrason., Ferroelec., Freq. Contr.* 38, pp. 109–115 (cit. on p. 112).

Ranganathan, K. and W. F. Walker (2007). "Cystic Resolution: A Performance Metric for Ultrasound Imaging Systems". In: *IEEE Trans. Ultrason., Ferroelec., Freq. Contr.* 54.4, pp. 782–792 (cit. on p. 120).

Rasmussen, M. F., G. Férin, R. Dufait, and J. A. Jensen (2012). "Comparison of 3D Synthetic Aperture Imaging and Explososcan using Phantom Measurements". In: *Proc. IEEE Ultrason. Symp.* Pp. 113–116. DOI: 10.1109/ULTSYM.2012.0028 (cit. on p. 112).

Rasmussen, M. F., J. M. Hansen, G. Férin, R. Dufait, and J. A. Jensen (2012). "Preliminary comparison of 3D synthetic aperture imaging with Explososcan". In: *Proc. SPIE Med. Imag.* Ed. by J. G. Bosch and M. M. Doyley. Vol. 8320. 83200F. SPIE, pp. 1–9 (cit. on p. 112).

Seo, C. H. and J. T. Yen (2009). "A 256 x 256 2-D array transducer with row-column addressing for 3-D rectilinear imaging". In: *IEEE Trans. Ultrason., Ferroelec., Freq. Contr.* 56.4, pp. 837–847 (cit. on p. 112).

Smith, S. W., H. G. Pavy, and O. T. von Ramm (1991). "High speed ultrasound volumetric imaging system – Part I: Transducer design and beam steering". In: *IEEE Trans. Ultrason., Ferroelec., Freq. Contr.* 38, pp. 100–108 (cit. on p. 116).

Turnbull, D. H. and F. S. Foster (1991). "Beam steering with pulsed two-dimensional transducer arrays". In: *IEEE Trans. Ultrason., Ferroelec., Freq. Contr.* 38.4, pp. 320–333 (cit. on p. 112).

Vilkomerson, D., J. Greenleaf, and V. Dutt (1995). "Towards a Resolution Metric for Medical Ultrasound Imaging". In: *Proc. IEEE Ultrason. Symp.* Pp. 1405–1410 (cit. on p. 120).

Yen, J. T., J. P. Steinberg, and S. W. Smith (2000). "Sparse 2-D array design for real time rectilinear volumetric imaging". In: *IEEE Trans. Ultrason., Ferroelec., Freq. Contr.* 47.1, pp. 93–110 (cit. on p. 112).

References from Paper E

Daher, N. M. and J. T. Yen (2004). "Rectilinear 3-D ultrasound imaging using synthetic aperture techniques". In: *Proc. IEEE Ultrason. Symp.* Vol. 2, pp. 1270–1273 (cit. on p. 126).

Démoré, C. E. M., A. Joyce, K. Wall, and G. Lockwood (2009). "Real-time volume imaging using a crossed electrode array". In: *IEEE Trans. Ultrason., Ferroelec., Freq. Contr.* 56.6, pp. 1252–1261 (cit. on p. 126).

Hansen, J. M., M. C. Hemmsen, and J. A. Jensen (2011). "An object-oriented multi-threaded software beamformation toolbox". In: *Proc. SPIE Med. Imag.* Vol. 7968, pages. URL: http://dx.doi.org/10.1117/12.878178 (cit. on p. 131).

Jensen, J. A. (1996). "Field: A Program for Simulating Ultrasound Systems". In: *Med. Biol. Eng. Comp.* 10th Nordic-Baltic Conference on Biomedical Imaging, Vol. 4, Supplement 1, Part 1, pp. 351–353 (cit. on p. 132).

Jensen, J. A., H. Holten-Lund, R. T. Nilsson, M. Hansen, U. D. Larsen, R. P. Domsten, B. G. Tomov, M. B. Stuart, S. I. Nikolov, M. J. Pihl, Y. Du, J. H. Rasmussen, and M. F. Rasmussen (2013). "SARUS: A Synthetic Aperture Real-time Ultrasound System". In: *IEEE Trans. Ultrason., Ferroelec., Freq. Contr.* 60.9, pp. 1838–1852 (cit. on p. 131).

Jensen, J. A. and N. B. Svendsen (1992). "Calculation of Pressure Fields from Arbitrarily Shaped, Apodized, and Excited Ultrasound Transducers". In: *IEEE Trans. Ultrason., Ferroelec., Freq. Contr.* 39, pp. 262–267 (cit. on p. 132).

Morton, C. E. and G. R. Lockwood (2003). "Theoretical assessment of a crossed electrode 2-D array for 3-D imaging". In: *Proc. IEEE Ultrason. Symp.* Pp. 968–971 (cit. on p. 126).

Ramm, O. T. von, S. W. Smith, and H. G. Pavy (1991). "High speed ultrasound volumetric imaging system – Part II: Parallel processing and image display". In: *IEEE Trans. Ultrason., Ferroelec., Freq. Contr.* 38, pp. 109–115 (cit. on pp. 126, 129).

Ranganathan, K. and W. F. Walker (2007). "Cystic Resolution: A Performance Metric for Ultrasound Imaging Systems". In: *IEEE Trans. Ultrason., Ferroelec., Freq. Contr.* 54.4, pp. 782–792 (cit. on p. 129).

Rasmussen, M. F. and J. A. Jensen (2013). "3D ultrasound imaging performance of a row-column addressed 2D array transducer: a simulation study". In: *Proc. SPIE Med. Imag.* 86750C, pp. 1–11 (cit. on pp. 126, 128).

Seo, C. H. and J. T. Yen (2009). "A 256 x 256 2-D array transducer with row-column addressing for 3-D rectilinear imaging". In: *IEEE Trans. Ultrason., Ferroelec., Freq. Contr.* 56.4, pp. 837–847 (cit. on p. 126).

Shattuck, D. P., M. D. Weinshenker, S. W. Smith, and O. T. von Ramm (1984). "Explososcan: A parallel processing technique for high speed ultrasound imaging with linear phased arrays". In: *J. Acoust. Soc. Am.* 75, pp. 1273–1282 (cit. on p. 129).

Turnbull, D. H. and F. S. Foster (1991). "Beam steering with pulsed two-dimensional transducer arrays". In: *IEEE Trans. Ultrason., Ferroelec., Freq. Contr.* 38.4, pp. 320–333 (cit. on p. 126).

Vilkomerson, D., J. Greenleaf, and V. Dutt (1995). “Towards a Resolution Metric for Medical Ultrasound Imaging”. In: *Proc. IEEE Ultrason. Symp.* Pp. 1405–1410 (cit. on p. 129).

References from Paper F

Démoré, C. E. M., A. Joyce, K. Wall, and G. Lockwood (2009). “Real-time volume imaging using a crossed electrode array”. In: *IEEE Trans. Ultrason., Ferroelec., Freq. Contr.* 56.6, pp. 1252–1261 (cit. on pp. 135, 136).

Huang, Y., A. S. Ergun, E. Hæggström, M. H. Badi, and B. T. Khuri-Yakub (2003). “Fabricating capacitive micromachined ultrasonic transducers with wafer-bonding technology”. In: *J. Microelectromech. Syst* 12.2, pp. 128–137 (cit. on p. 138).

Jensen, J. A. (1996). “Field: A Program for Simulating Ultrasound Systems”. In: *Med. Biol. Eng. Comp.* 10th Nordic-Baltic Conference on Biomedical Imaging, Vol. 4, Supplement 1, Part 1, pp. 351–353 (cit. on pp. 136, 139).

Jensen, J. A. and N. B. Svendsen (1992). “Calculation of Pressure Fields from Arbitrarily Shaped, Apodized, and Excited Ultrasound Transducers”. In: *IEEE Trans. Ultrason., Ferroelec., Freq. Contr.* 39, pp. 262–267 (cit. on pp. 136, 139).

Kern, W. (1990). “The Evolution of Silicon Wafer Cleaning Technology”. In: *J. Electrochem. Soc.* 137.6, pp. 1887–1892 (cit. on p. 139).

Logan, A. S., L. L. P. Wong, A. I. H. Chen, and J. T. W. Yeow (2011). “A 32 x 32 element row-column addressed capacitive micromachined ultrasonic transducer”. In: *IEEE Trans. Ultrason., Ferroelec., Freq. Contr.* 58.6, pp. 1266–1271 (cit. on p. 135).

Rasmussen, M. F., T. L. Christiansen, E. V. Thomsen, and J. A. Jensen. “Ultrasound Imaging Transducer Array with Integrated Apodization”. PCT/IB2013/002838 (cit. on p. 136).

Rasmussen, M. F. and J. A. Jensen (2013). “3-D Ultrasound Imaging Performance of a Row-Column Addressed 2-D Array Transducer: A Measurement Study”. In: *Proc. IEEE Ultrason. Symp.* Pp. 1460–1463 (cit. on p. 136).

Sampaleanu, A., P. Zhang, A. Kshirsagar, W. Moussa, and R. Zemp (2014). “Top-orthogonal-to-bottom-electrode (TOBE) CMUT arrays for 3-D ultrasound imaging.” In: *IEEE Trans. Ultrason., Ferroelec., Freq. Contr.* 61.2, pp. 266–276. DOI: 10.1109/TUFFC.2014.6722612 (cit. on p. 135).

Seo, C. H. and J. T. Yen (2009). “A 256 x 256 2-D array transducer with row-column addressing for 3-D rectilinear imaging”. In: *IEEE Trans. Ultrason., Ferroelec., Freq. Contr.* 56.4, pp. 837–847 (cit. on p. 135).

Zhang, P., G. Fitzpatrick, T. Harrison, W. A. Moussa, and R. J. Zemp (2012). “Double-SOI Wafer-Bonded CMUTs With Improved Electrical Safety and Minimal Roughness of Dielectric and Electrode Surfaces”. In: *J. Microelectromech. Syst.* 21.3, pp. 668–680 (cit. on p. 138).

References from Paper G

Austeng, A. and S. Holm (2002). "Sparse 2-D arrays for 3-D phased array imaging - design methods". In: *IEEE Trans. Ultrason., Ferroelec., Freq. Contr.* 49.8, pp. 1073–1086 (cit. on p. 146).

Awad, S. I. and J. T. Yen (2009). "3-D spatial compounding using a row-column array". In: *Ultrason. Imaging* 31.2, pp. 120–130 (cit. on p. 146).

Brunke, S. S. and G. R. Lockwood (1997). "Broad-bandwidth radiation patterns of sparse two-dimensional vernier arrays". In: *IEEE Trans. Ultrason., Ferroelec., Freq. Contr.* 44.5, pp. 1101–1109 (cit. on p. 146).

Chen, A. I. H., L. L. Wong, A. S. Logan, and J. T. W. Yeow (2011). "A CMUT-based real-time volumetric ultrasound imaging system with row-column addressing". In: *Proc. IEEE Ultrason. Symp.* Pp. 1755–1758 (cit. on p. 146).

Daher, N. M. and J. T. Yen (2004). "Rectilinear 3-D ultrasound imaging using synthetic aperture techniques". In: *Proc. IEEE Ultrason. Symp.* Vol. 2, pp. 1270–1273 (cit. on p. 146).

— (2006). "2-D Array for 3-D Ultrasound Imaging Using Synthetic Aperture Techniques". In: *IEEE Trans. Ultrason., Ferroelec., Freq. Contr.* 53.5, pp. 912–924 (cit. on p. 146).

Davidsen, R. E., J. A. Jensen, and S. W. Smith (1994). "Two-Dimensional Random Arrays for Real Time Volumetric Imaging". In: *Ultrasonic Imaging* 16.3, pp. 143–163 (cit. on p. 146).

Démoré, C. E. M., A. Joyce, K. Wall, and G. Lockwood (2009). "Real-time volume imaging using a crossed electrode array". In: *IEEE Trans. Ultrason., Ferroelec., Freq. Contr.* 56.6, pp. 1252–1261 (cit. on pp. 146, 148, 154, 157, 162).

Harris, G. R. (1981a). "Review of transient field theory for a baffled planar piston". In: *J. Acoust. Soc. Am.* 70, pp. 10–20 (cit. on p. 149).

— (1981b). "Transient field of a baffled planar piston having an arbitrary vibration amplitude distribution". In: *J. Acoust. Soc. Am.* 70, pp. 186–204 (cit. on p. 149).

Huang, Y., A. S. Ergun, E. Hæggström, M. H. Badi, and B. T. Khuri-Yakub (2003). "Fabricating capacitive micromachined ultrasonic transducers with wafer-bonding technology". In: *J. Microelectromech. Syst* 12.2, pp. 128–137 (cit. on p. 158).

Jensen, J. A. (1991). "A Model for the Propagation and Scattering of Ultrasound in Tissue". In: *J. Acoust. Soc. Am.* 89, pp. 182–191 (cit. on p. 153).

— (1996). "Field: A Program for Simulating Ultrasound Systems". In: *Med. Biol. Eng. Comp.* 10th Nordic-Baltic Conference on Biomedical Imaging, Vol. 4, Supplement 1, Part 1, pp. 351–353 (cit. on p. 153).

Jensen, J. A. and N. B. Svendsen (1992). "Calculation of Pressure Fields from Arbitrarily Shaped, Apodized, and Excited Ultrasound Transducers". In: *IEEE Trans. Ultrason., Ferroelec., Freq. Contr.* 39, pp. 262–267 (cit. on p. 153).

Karaman, M., P. C. Li, and M. O'Donnell (1995). "Synthetic aperture imaging for small scale systems". In: *IEEE Trans. Ultrason., Ferroelec., Freq. Contr.* 42, pp. 429–442 (cit. on p. 146).

Karaman, M., I. O. Wygant, O. Oralkan, and B. T. Khuri-Yakub (2009). "Minimally Redundant 2-D Array Designs for 3-D Medical Ultrasound Imaging". In: *IEEE Trans. Med. Imag.* 7, pp. 1051–1061 (cit. on p. 146).

Kupnik, M., S. Vaithilingam, K. Torashima, I. Wygant, and B. Khuri-Yakub (2010). "CMUT fabrication based on a thick buried oxide layer". In: *Proc. IEEE Ultrason. Symp.* Pp. 547–550. DOI: 10.1109/ULTSYM.2010.5935935 (cit. on p. 158).

Ladabaum, I., X. Jin, H. T. Soh, A. Atalar, and B. T. Khuri-Yakub (1998). "Surface Micromachined Capacitive Ultrasonic Transducers". In: *IEEE Trans. Ultrason., Ferroelec., Freq. Contr.* 45.3, pp. 1–6 (cit. on p. 158).

Logan, A. S., L. L. P. Wong, A. I. H. Chen, and J. T. W. Yeow (2011). "A 32 x 32 element row-column addressed capacitive micromachined ultrasonic transducer". In: *IEEE Trans. Ultrason., Ferroelec., Freq. Contr.* 58.6, pp. 1266–1271 (cit. on p. 146).

Logan, A. S., L. L. P. Wong, and J. T. W. Yeow (2009). "2-D CMUT wafer bonded imaging arrays with a row-column addressing scheme". In: *Proc. IEEE Ultrason. Symp.* Pp. 984–987 (cit. on p. 146).

Lou-Møller, R., C. C. Hindrichsen, L. H. Thamdrup, T. Bove, E. Ringgaard, A. F. Pedersen, and E. V. Thomsen (2007). "Screen-printed piezoceramic thick films for miniaturised devices". In: *J. Electroceram.* 19.7, pp. 333–338 (cit. on p. 157).

Morton, C. E. and G. R. Lockwood (2003). "Theoretical assessment of a crossed electrode 2-D array for 3-D imaging". In: *Proc. IEEE Ultrason. Symp.* Pp. 968–971 (cit. on pp. 146, 162).

Naik, P. (2010). *Principles of Physics*. 4th ed. PHI (cit. on p. 156).

Pierce, A. D. (1989). *Acoustics, An Introduction to Physical Principles and Applications*. New York: Acoustical Society of America (cit. on p. 149).

Ramm, O. T. von, S. W. Smith, and H. G. Pavy (1991). "High speed ultrasound volumetric imaging system – Part II: Parallel processing and image display". In: *IEEE Trans. Ultrason., Ferroelec., Freq. Contr.* 38, pp. 109–115 (cit. on p. 146).

Rasmussen, M. F. (2014). *A Row-column beamformer*. URL: www.rc-beamformer.mofi.dk (cit. on p. 153).

Rasmussen, M. F., T. L. Christiansen, E. V. Thomsen, and J. A. Jensen. "Ultrasound Imaging Transducer Array with Integrated Apodization". PCT/IB2013/002838 (cit. on p. 157).

Rasmussen, M. F. and J. A. Jensen (2013a). "3-D Ultrasound Imaging Performance of a Row-Column Addressed 2-D Array Transducer: A Measurement Study". In: *Proc. IEEE Ultrason. Symp.* Pp. 1460–1463 (cit. on p. 146).

— (2013b). "3D ultrasound imaging performance of a row-column addressed 2D array transducer: a simulation study". In: *Proc. SPIE Med. Imag.* 86750C, pp. 1–11 (cit. on pp. 146–148, 154, 162).

Sampaleanu, A., P. Zhang, A. Kshirsagar, W. Moussa, and R. Zemp (2014). "Top-orthogonal-to-bottom-electrode (TOBE) CMUT arrays for 3-D ultrasound imaging." In: *IEEE Trans. Ultrason., Ferroelec., Freq. Contr.* 61.2, pp. 266–276. DOI: 10.1109/TUFFC.2014.6722612 (cit. on p. 146).

Savoia, A. S., G. Caliano, and M. Pappalardo (2012). "A CMUT Probe for Medical Ultrasonography: From Microfabrication to System Integration". In: *IEEE Trans. Ultrason., Ferroelec., Freq. Contr.* 59.6, pp. 1127–1138 (cit. on p. 158).

Seo, C. H. and J. T. Yen (2006). "64 x 64 2-D array transducer with row-column addressing". In: *Proc. IEEE Ultrason. Symp.* Vol. 1, pp. 74–77 (cit. on p. 146).

— (2007). "256 x 256 2-D array transducer with row-column addressing for 3-D imaging". In: *Proc. IEEE Ultrason. Symp.* Pp. 2381–2384 (cit. on p. 146).

— (2008). "Recent results using a 256 x 256 2-D array transducer for 3-D Rectilinear Imaging". In: *Proc. IEEE Ultrason. Symp.* Vol. 1-4, pp. 1146–1149 (cit. on p. 146).

— (2009). "A 256 x 256 2-D array transducer with row-column addressing for 3-D rectilinear imaging". In: *IEEE Trans. Ultrason., Ferroelec., Freq. Contr.* 56.4, pp. 837–847 (cit. on pp. 146, 162).

Stepanishen, P. R. (1971). "Transient radiation from pistons in an infinite planar baffle". In: *J. Acoust. Soc. Am.* 49, pp. 1629–1638 (cit. on p. 149).

— (1981). "Acoustic transients from planar axisymmetric vibrators using the impulse response approach". In: *J. Acoust. Soc. Am.* 70, pp. 1176–1181 (cit. on p. 149).

Thomenius, K. E. (1996). "Evolution of ultrasound beamformers". In: *Proc. IEEE Ultrason. Symp.* Vol. 2, pp. 1615–1621 (cit. on p. 146).

Tjøtta, J. N. and S. Tjøtta (1982). "Nearfield and farfield of pulsed acoustic radiators". In: *J. Acoust. Soc. Am.* 71, pp. 824–834 (cit. on p. 149).

Turnbull, D. H. and F. S. Foster (1991). "Beam steering with pulsed two-dimensional transducer arrays". In: *IEEE Trans. Ultrason., Ferroelec., Freq. Contr.* 38.4, pp. 320–333 (cit. on p. 146).

Yen, J. T., J. P. Steinberg, and S. W. Smith (2000). "Sparse 2-D array design for real time rectilinear volumetric imaging". In: *IEEE Trans. Ultrason., Ferroelec., Freq. Contr.* 47.1, pp. 93–110 (cit. on p. 146).

Yen, J. T. (2013). "Beamforming of sound from two-dimensional arrays using spatial matched filters". In: *J. Acoust. Soc. Am.* 134.5, pp. 3697–704. DOI: 10.1121/1.4821988 (cit. on pp. 146, 162).

Zhang, P., G. Fitzpatrick, T. Harrison, W. A. Moussa, and R. J. Zemp (2012). "Double-SOI Wafer-Bonded CMUTs With Improved Electrical Safety and Minimal Roughness of Dielectric and Electrode Surfaces". In: *J. Microelectromech. Syst.* 21.3, pp. 668–680 (cit. on p. 158).

References from Paper H

Austeng, A. and S. Holm (2002). "Sparse 2-D arrays for 3-D phased array imaging - design methods". In: *IEEE Trans. Ultrason., Ferroelec., Freq. Contr.* 49.8, pp. 1073–1086 (cit. on p. 174).

Bayram, B., M. Kupnik, C. G. Yaralioglu, Ö. Oralkan, A. S. Ergun, D.-S. Lin, S. H. Wong, and B. T. Khuri-Yakub (2007). "Finite element modeling and experimental characterization of crosstalk in 1-D CMUT arrays". In: *IEEE Trans. Ultrason., Ferroelec., Freq. Contr.* 54.2, pp. 418–430. DOI: 10.1109/TUFFC.2007.256 (cit. on p. 187).

Blaak, S., Z. Yu, G. Meijer, C. Prins, C. Lancee, J. Bosch, and N. de Jong (2009). "Design of a micro-beamformer for a 2D piezoelectric ultrasound transducer". In: *Proc. IEEE Ultrason. Symp.* Pp. 1338–1341. DOI: 10.1109/ULTSYM.2009.5441534 (cit. on p. 174).

Brunke, S. S. and G. R. Lockwood (1997). "Broad-bandwidth radiation patterns of sparse two-dimensional vernier arrays". In: *IEEE Trans. Ultrason., Ferroelec., Freq. Contr.* 44.5, pp. 1101–1109 (cit. on p. 174).

Chen, A. I. H., L. L. Wong, A. S. Logan, and J. T. W. Yeow (2011). "A CMUT-based real-time volumetric ultrasound imaging system with row-column addressing". In: *Proc. IEEE Ultrason. Symp.* Pp. 1755–1758 (cit. on p. 175).

Chen, Y., M. Nguyen, and J. T. Yen (2011). "Real-time rectilinear volumetric acquisition with a 7.5 MHz dual-layer array transducer - Data acquisition and signal processing". In: *Proc. IEEE Ultrason. Symp.* Pp. 1759–1761 (cit. on p. 174).

Christiansen, T. L., O. Hansen, M. D. Johnsen, J. N. Lohse, J. A. Jensen, and E. V. Thomsen (2013). "Void-free direct bonding of CMUT arrays with single crystalline plates and pull-in insulation". In: *Proc. IEEE Ultrason. Symp.* Pp. 1737–1740. DOI: 10.1109/ULTSYM.2013.0443 (cit. on p. 180).

Daher, N. M. and J. T. Yen (2004). "Rectilinear 3-D ultrasound imaging using synthetic aperture techniques". In: *Proc. IEEE Ultrason. Symp.* Vol. 2, pp. 1270–1273 (cit. on p. 174).

— (2006). "2-D Array for 3-D Ultrasound Imaging Using Synthetic Aperture Techniques". In: *IEEE Trans. Ultrason., Ferroelec., Freq. Contr.* 53.5, pp. 912–924 (cit. on p. 174).

Davidsen, R. E., J. A. Jensen, and S. W. Smith (1994). "Two-Dimensional Random Arrays for Real Time Volumetric Imaging". In: *Ultrasonic Imaging* 16.3, pp. 143–163 (cit. on p. 174).

Démoré, C. E. M., A. Joyce, K. Wall, and G. Lockwood (2009). "Real-time volume imaging using a crossed electrode array". In: *IEEE Trans. Ultrason., Ferroelec., Freq. Contr.* 56.6, pp. 1252–1261 (cit. on pp. 174, 175).

Halvorsrod, T., W. Luzi, and T. Lande (2005). "A log-domain µbeamformer for medical ultrasound imaging systems". In: *IEEE Trans. Circuits Syst. I, Reg. Papers* 52.12, pp. 2563–2575. DOI: 10.1109/TCSI.2005.857544 (cit. on p. 174).

Huang, Y. L., E. O. Hæggström, X. F. Zhuang, A. S. Ergun, and B. T. Khuri-Yakub (2005). "A solution to the charging problems in capacitive micromachined ultrasonic transducers". In: *IEEE Trans. Ultrason., Ferroelec., Freq. Contr.* 52.4, pp. 578–580. DOI: 10.1109/TUFFC.2005.1428039 (cit. on p. 184).

Huang, Y., A. S. Ergun, E. Hæggström, M. H. Badi, and B. T. Khuri-Yakub (2003). "Fabricating capacitive micromachined ultrasonic transducers with wafer-bonding technology". In: *J. Microelectromech. Syst* 12.2, pp. 128–137 (cit. on p. 178).

Jensen, J. A. (1996). "Field: A Program for Simulating Ultrasound Systems". In: *Med. Biol. Eng. Comp.* 10th Nordic-Baltic Conference on Biomedical Imaging, Vol. 4, Supplement 1, Part 1, pp. 351–353 (cit. on p. 190).

Jensen, J. A., H. Holten-Lund, R. T. Nilsson, M. Hansen, U. D. Larsen, R. P. Domsten, B. G. Tomov, M. B. Stuart, S. I. Nikolov, M. J. Pihl, Y. Du, J. H. Rasmussen, and M. F. Rasmussen (2013). "SARUS: A Synthetic Aperture Real-time Ultrasound System". In: *IEEE Trans. Ultrason., Ferroelec., Freq. Contr.* 60.9, pp. 1838–1852 (cit. on pp. 181, 186).

Jensen, J. A. and N. B. Svendsen (1992). "Calculation of Pressure Fields from Arbitrarily Shaped, Apodized, and Excited Ultrasound Transducers". In: *IEEE Trans. Ultrason., Ferroelec., Freq. Contr.* 39, pp. 262–267 (cit. on p. 190).

Karaman, M., I. O. Wygant, O. Oralkan, and B. T. Khuri-Yakub (2009). "Minimally Redundant 2-D Array Designs for 3-D Medical Ultrasound Imaging". In: *IEEE Trans. Med. Imag.* 7, pp. 1051–1061 (cit. on p. 174).

Kern, W. (1990). "The Evolution of Silicon Wafer Cleaning Technology". In: *J. Electrochem. Soc.* 137.6, pp. 1887–1892 (cit. on p. 179).

Logan, A. S., L. L. P. Wong, A. I. H. Chen, and J. T. W. Yeow (2011). "A 32 x 32 element row-column addressed capacitive micromachined ultrasonic transducer". In: *IEEE Trans. Ultrason., Ferroelec., Freq. Contr.* 58.6, pp. 1266–1271 (cit. on p. 175).

Logan, A. S., L. L. P. Wong, and J. T. W. Yeow (2009). "2-D CMUT wafer bonded imaging arrays with a row-column addressing scheme". In: *Proc. IEEE Ultrason. Symp.* Pp. 984–987 (cit. on p. 175).

Morton, C. E. and G. R. Lockwood (2003). "Theoretical assessment of a crossed electrode 2-D array for 3-D imaging". In: *Proc. IEEE Ultrason. Symp.* Pp. 968–971 (cit. on p. 174).

Oralkan, Ö., A. S. Ergun, J. A. Johnson, M. Karaman, U. Demirci, K. Kaviani, T. H. Lee, and B. T. Kuri-Yakub (2002). "Capacitive micromachined ultrasonic transducers: Next-generation arrays for acoustic imaging?" In: *IEEE Trans. Ultrason., Ferroelec., Freq. Contr.* 49, pp. 1596–1610 (cit. on p. 186).

Rasmussen, M. F. (2014). *A Row-column beamformer*. URL: www.rc-beamformer.mofi.dk (cit. on p. 189).

Rasmussen, M. F., T. L. Christiansen, E. V. Thomsen, and J. A. Jensen. "Ultrasound Imaging Transducer Array with Integrated Apodization". PCT/IB2013/002838 (cit. on p. 175).

— (2014). “3-D Imaging with Row-Column Addressed Arrays: Transducer-Integrated Apodization and Line-element Beamforming”. In: *IEEE Trans. Ultrason., Ferroelec., Freq. Contr.* Submitted (cit. on pp. 175, 177, 186, 189, 192).

Rasmussen, M. F. and J. A. Jensen (2013a). “3-D Ultrasound Imaging Performance of a Row-Column Addressed 2-D Array Transducer: A Measurement Study”. In: *Proc. IEEE Ultrason. Symp.* Pp. 1460–1463 (cit. on p. 174).

— (2013b). “3D ultrasound imaging performance of a row-column addressed 2D array transducer: a simulation study”. In: *Proc. SPIE Med. Imag.* 86750C, pp. 1–11 (cit. on p. 175).

Sampaleanu, A., P. Zhang, A. Kshirsagar, W. Moussa, and R. Zemp (2014). “Top-orthogonal-to-bottom-electrode (TOBE) CMUT arrays for 3-D ultrasound imaging.” In: *IEEE Trans. Ultrason., Ferroelec., Freq. Contr.* 61.2, pp. 266–276. DOI: 10.1109/TUFFC.2014.6722612 (cit. on p. 175).

Savoia, A. S., G. Caliano, and M. Pappalardo (2012). “A CMUT Probe for Medical Ultrasonography: From Microfabrication to System Integration”. In: *IEEE Trans. Ultrason., Ferroelec., Freq. Contr.* 59.6, pp. 1127–1138 (cit. on p. 182).

Savord, B. and R. Solomon (2003). “Fully sampled matrix transducer for real time 3D ultrasonic imaging”. In: *Proc. IEEE Ultrason. Symp.* Vol. 1, pp. 945–953 (cit. on p. 174).

Schroeder, M. R. (1979). “Integrated-impulse method measuring sound decay without using impulses”. In: *J. Acoust. Soc. Am.* 66.2, pp. 497–500 (cit. on p. 188).

Seo, C. H. and J. T. Yen (2006). “64 x 64 2-D array transducer with row-column addressing”. In: *Proc. IEEE Ultrason. Symp.* Vol. 1, pp. 74–77 (cit. on p. 174).

— (2007). “256 x 256 2-D array transducer with row-column addressing for 3-D imaging”. In: *Proc. IEEE Ultrason. Symp.* Pp. 2381–2384 (cit. on p. 174).

— (2008). “Recent results using a 256 x 256 2-D array transducer for 3-D Rectilinear Imaging”. In: *Proc. IEEE Ultrason. Symp.* Vol. 1-4, pp. 1146–1149 (cit. on p. 174).

— (2009). “A 256 x 256 2-D array transducer with row-column addressing for 3-D rectilinear imaging”. In: *IEEE Trans. Ultrason., Ferroelec., Freq. Contr.* 56.4, pp. 837–847 (cit. on p. 174).

Ventsel, E. and T. Krauthammer (2001). *Thin plates and shells: theory, analysis, and applications*. Dekker (cit. on pp. 176, 184).

Yaralioglu, G. G., A. S. Ergun, B. Bayram, E. Hæggström, and B. T. Khuri-Yakub (2003). “Calculation and measurement of electromechanical coupling coefficient of capacitive micromachined ultrasonic transducers”. In: *IEEE Trans. Ultrason., Ferroelec., Freq. Contr.* 50.4, pp. 449–456. DOI: 10.1109/TUFFC.2003.1197968 (cit. on p. 190).

Yen, J. T., C. H. Seo, S. I. Awad, and J. S. Jeong (2009). “A dual-layer transducer array for 3-D rectilinear imaging”. In: *IEEE Trans. Ultrason., Ferroelec., Freq. Contr.* 56.1, pp. 204–212 (cit. on p. 174).

Yen, J. T., J. P. Steinberg, and S. W. Smith (2000). “Sparse 2-D array design for real time rectilinear volumetric imaging”. In: *IEEE Trans. Ultrason., Ferroelec., Freq. Contr.* 47.1, pp. 93–110 (cit. on p. 174).

Yen, J. T. (2013). “Beamforming of sound from two-dimensional arrays using spatial matched filters”. In: *J. Acoust. Soc. Am.* 134.5, pp. 3697–704. DOI: 10.1121/1.4821988 (cit. on p. 174).

Zemp, R. J., W. Zheng, and P. Zhang (2011). “Feasibility of Top-Orthogonal-to-Bottom Electrode (TOBE) 2D CMUT arrays for low-channel-count 3D imaging”. In: *Proc. IEEE Ultrason. Symp.* Pp. 498–502 (cit. on p. 174).

Zhang, P., G. Fitzpatrick, T. Harrison, W. A. Moussa, and R. J. Zemp (2012). “Double-SOI Wafer-Bonded CMUTs With Improved Electrical Safety and Minimal Roughness of Dielectric and Electrode Surfaces”. In: *J. Microelectromech. Syst.* 21.3, pp. 668–680 (cit. on p. 178).